MODELING, IMPLEMENTATION AND CONTROL OF A CVT BASED PTO FOR A SMALL SCALE MHK-TURBINE IN LOW FLOW SPEED OPERATION

by

Hugo Pimentel

A Dissertation Submitted to the Faculty of

College of Engineering and Computer Science

In Partial Fulfillment of the Requirements for the Degree of

Doctor of Philosophy

Florida Atlantic University

Boca Raton, FL

May 2024

MODELING, IMPLEMENTATION AND CONTROL OF A CVT BASED PTO FOR A SMALL SCALE MHK-TURBINE IN LOW FLOW SPEED OPERATION

by

Hugo Pimentel

This dissertation was prepared under the direction of the candidate's dissertation advisor, Dr. Manhar Dhanak, Department of Ocean and Mechanical Engineering, and has been approved by all members of the supervisory committee. It was submitted to the faculty of the College of Engineering and Computer Science and was accepted in partial fulfillment of the requirements for the degree of Doctor of Philosophy.

SUPERVISORY COMMITTEE:

Manhar Dhanak

Manhar Dhanak, Ph.D.
Dissertation Advisor

Pierre Philippe Beaujean

Pierre-Philippe Beaujean, Ph.D.

Hassan Mahfuz

Hassan Mahfuz, Ph.D.

James VanZwieten

James VanZwieten, Ph.D.

Pierre Philippe Beaujean

Pierre-Philippe Beaujean, Ph.D.
Chair, Department of Ocean and Mechanical Engineering

Stella Batalama

Stella Batalama, Ph.D.
Dean, College of Engineering and Computer Science

Robert W. Stackman Jr.
Robert W. Stackman Jr. (Apr 12, 2024 09:15 EDT)

Robert W. Stackman Jr., Ph.D.
Dean, Graduate College

April 12, 2024
Date

ACKNOWLEDGEMENTS

I am grateful for my advisor, Dr. Manhar Dhanak, who gave me the opportunity to contribute to the body of knowledge of renewable energy and push forward the frontiers of human understanding. I would like to thank the committee members, Dr. Pierre-Philippe Beaujean, Dr. Hassan Mahfuz and Dr. James VanZwieten, for their invaluable time and feedback. Special thanks to Edward Henderson and John Frankenfield, who provided relentless support on the technical aspects of my work. My extended thanks to Adriana McKinney, who provided technical and administrative support throughout my work. I would like to thank the US Department of Energy and the Office of Naval Research for supporting this research.

ABSTRACT

Author: Hugo Pimentel

Title: Modeling, Implementation and Control of a CVT Based PTO for a Small Scale MHK-Turbine in Low Flow Speed Operation

Institution: Florida Atlantic University

Dissertation Advisor: Dr. Manhar Dhanak

Degree: Doctor of Philosophy

Year: 2024

Modeling, implementation, field testing and control of a power takeoff (PTO) device equipped with a ball-type continuously variable transmission (B-CVT) for a small marine hydrokinetic (MHK) turbine deployed from a floating unmanned autonomous mobile catamaran platform is described. The turbine is a partially submerged multi-blade undershot waterwheel (USWW). A validated numerical torque model for the MHK turbine has been derived and a speed controller has been developed, implemented and tested in the field. The dependance of the power generated as a function of number and submergence level of turbine blades has been investigated and the number of blades that maximizes power production is determined. Bench and field testing in support of characterizing the power conversion capabilities of MHK turbine and PTO are described. Detailed results of the final torque and power coefficient models, the controls architecture, and the MHK turbine performance with varying numbers of blades are provided.

DEDICATION

To my wife, Leticia Cantarelli, whose unwavering support, companionship and understanding made this work possible. To my family, for their encouragement, appreciation and kind words of advice.

MODELING, IMPLEMENTATION AND CONTROL OF A CVT BASED PTO
FOR A SMALL SCALE MHK-TURBINE IN LOWFLOE SPEED OPERATION

LIST OF TABLES

LIST OF FIGURES

LIST OF EQUATIONS

1. PROBLEM STATEMENT, MOTIVATION AND GOALS AND OBJECTIVES

A novel system has been developed in support of potential efforts in remote coastal monitoring. The system is comprised of a Wave Adaptive Modular Vehicle (WAM-V) unmanned surface vehicle (USV) equipped with a drone landing platform and Wi-fi recharging pad, self-anchoring capabilities, a Marine-Hydrokinetic (MHK) turbine onboard the vehicle, which may be deployed in low-current ocean or river sites to harness power from water flow for conversion to electric power and its storage in onboard batteries. The turbine is comprised of an undershot waterwheel attached to deployment arms connected to the surface vehicle and houses a power take-off (PTO) device within its hub. The PTO consists of a planetary gearbox, a Continuously-Variable Transmission (CVT), a generator, a charge controller and a 12V lead-acid battery.

Little is known about the dynamic behavior of the waterwheel itself, the PTO system as a whole and how the system produces power under different flow conditions. Furthermore, the natural oscillation of renewable power sources leads to several different conditions and the magnitude of the available power, which makes it important to have renewable energy systems that can deal with those different scenarios while maximizing their power production. Maximizing power production and operation time is not only important from an engineering perspective, but also from an economical perspective, as it allows systems like the one discussed in this work to be economically feasible and lucrative, creating more competitive, cuttingedge solution for renewable energy, generating more jobs and contributing to the growth of the sector as a whole.

Because of the novelty of this MHK system, there is a need to undertake studies to provide proof of concept of the system, and consider means for optimizing its power generation capabilities. This work focuses on developing and implementing a control algorithm for the PTO that will allow the system to operate at its optimal efficiency region based on the incoming water flow. As the system is deployed and begins operation it will regulate the loads on the turbine shaft and maintain it operating at its optimal speed setpoint. Furthermore, torque and power coefficient models will be derived to aid parametric design of MHK turbines based on available flow speeds and power production requirements.

2. APPROACH

2.1 Literature Review

The energy that can be harnessed from a moving fluid is proportional to the water density, the cross-section capture area the flow interacts with the turbine, and the cube of the speed of the water current. Moving fluids, whether fresh water, sea water or air, are a reliable source of power that can be tapped world-wide. The primary way of capturing that energy is by utilizing turbines to convert the energy contained in a fluid flow into mechanical power. Although design modifications are usually needed, the same principles utilized in wind turbines to extract power from an air flow can be utilized for underwater turbines. The first classification of turbines is based on how they convert hydro-kinetic flow energy into mechanical energy of the turbines. Lift turbines rely on lift forces to generate power, whereas drag turbines rely on drag forces to produce power (Manwell, Mcgowan and Rogers 2009). Lift-type blades have higher efficiency in areas with high flow velocity, and are usually used as wind power generators. Drag-type blades have high torque and excellent efficiency in low-speed flow fields, so they are more suitable for ocean current power generation (Min-Hsiung Yang 2023).

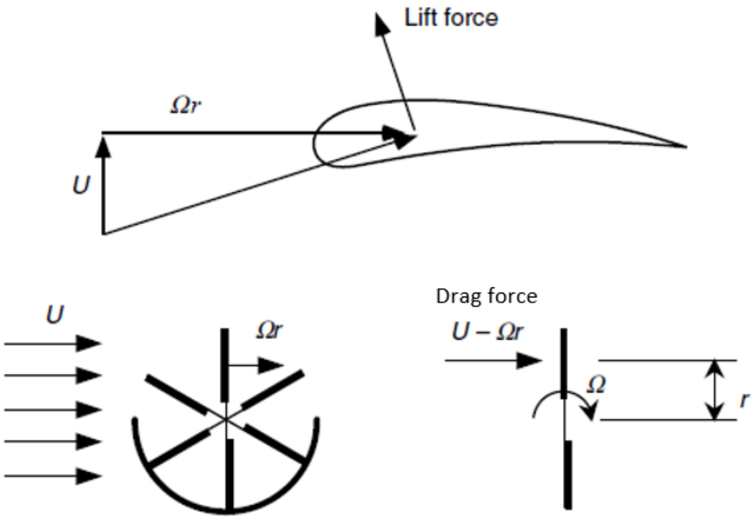

Figure 1: Basic difference between lift and drag-based turbines (Manwell, Mcgowan and Rogers 2009).

Turbines operating with the axis aligned with the current are referred to as horizontal axis turbines to distinguish them from cross-flow turbines in which the axis is orthogonal to the current direction. Vertical-axis turbines represent a particular case of cross-flow turbines (A.H. Day 2015). There are also other ways to capture that power without utilizing turbines, such as oscillating flaps or vibrating cylinders. Some of those concepts are overviewed below (M. J. Khan 2009).

2.1.1 Turbine Systems

A turbine system can be classified as horizontal, vertical, or cross flow axis turbine. These are briefly described below together with existing examples.

Axial, horizontal – usually called Horizontal Axis Wind Turbines (HAWT) in the wind energy field, the rotor axis of a HAWT is parallel to the incoming flow. Figure 2 shows an example of a 3-blade HAWT.

Figure 2: Horizontal axis underwater turbine (Verdant Power n.d.)

Vertical – usually called Vertical Axis Wind Turbines (VAWT) in the wind energy field, the rotor axis is vertical to water or ground surface and orthogonal to flow direction. Those turbines can be subcategorized according to their working principle. Lift type VAWT area also called Darrieus turbines, whereas drag type VAWT are called Savonius (Van Bang Nguyen 2017).

Figure 3: Vertical axis wind turbine (Van Bang Nguyen 2017)

Some of the advances in drag-based vertical axis turbines include the ability to control the angle of the blades for fully submerged turbines, which drastically increases its efficiency. The system retracts part of its blades at specific sections during its rotation to minimize losses due to opposing motion between fluid flow and blades, and extends them as the blades begin to be able to contribute to the rotation of the turbine.

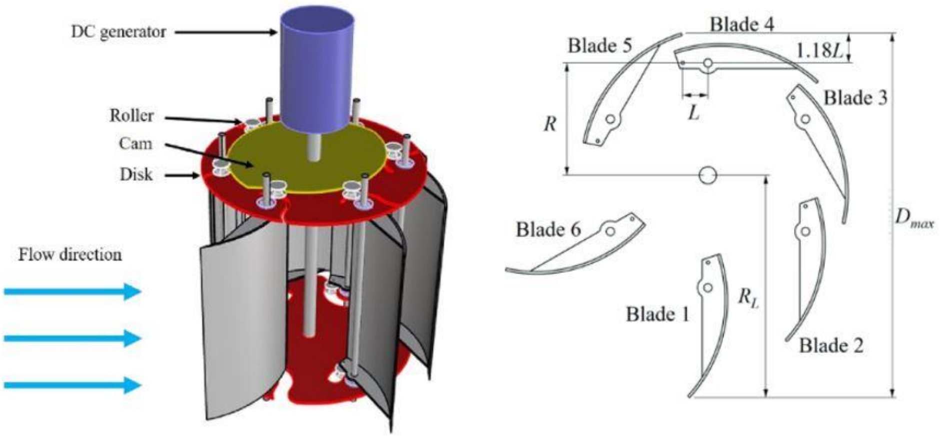

Figure 4: Fully submerged vertical axis turbine with controllable blade angle (Min-Hsiung Yang 2023)

Cross-flow – the rotor axis of a cross-flow turbine is parallel to water surface and perpendicular to flow direction. Figure 5 shows a cross-flow turbine being deployed.

Figure 5: Cross-flow underwater turbine (Tethys Engineering n.d.)

2.1.2 Non-turbine systems

Flutter vane with piezoelectric material – systems that rely on aero or hydroelastic resonance, or flutter, caused by the interaction of the flowing fluid and the vane structure. The induced vibration on the structure flexes the piezoelectric material, causing a voltage differential.

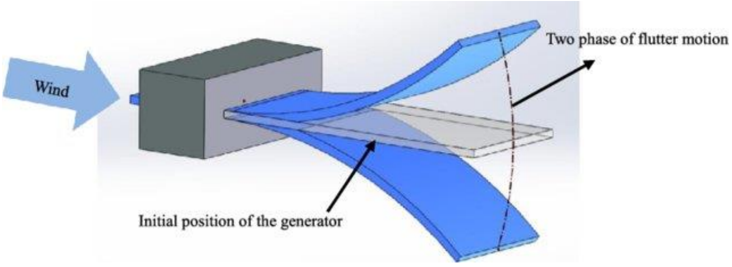

Figure 6: Flutter structure schematic (Pengyingkai Wang 2016)

Vortex-induced vibration – power conversion technique that relies on the vibrations induced in a submerged bluff body by a flow stream. Those vibrations are captured by a PTO, such as a linear generator or an alternator connected to the bluff body via a transmission system.

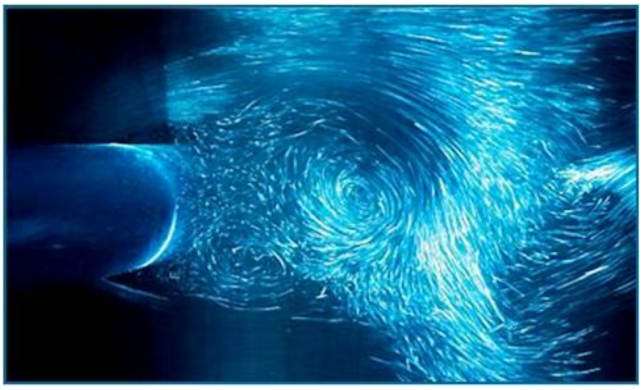

Figure 7: Vortex shedding on a submerged bluff body (Vortex Hydro Energy n.d.)

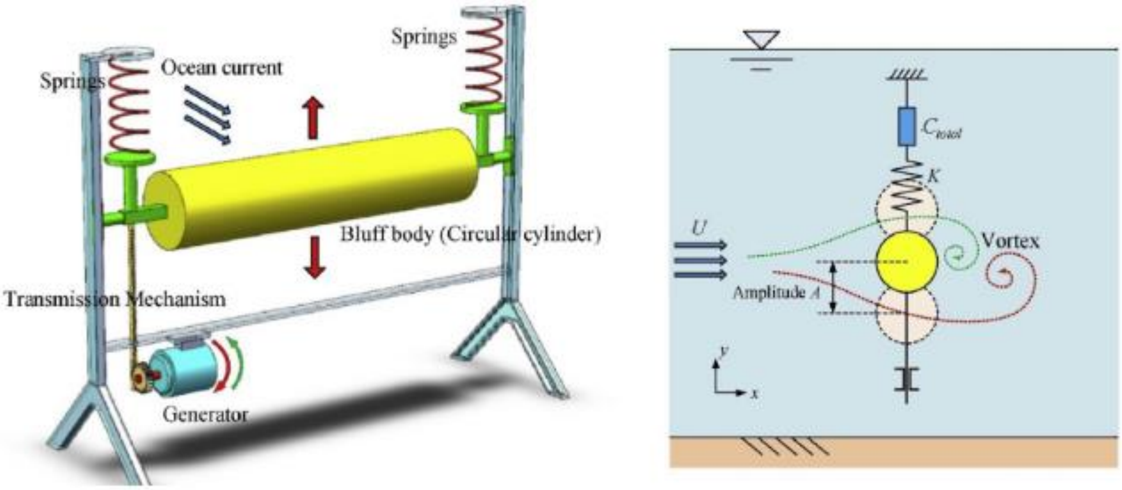

Figure 8: Vortex-induced vibrations on a submerged bluff body and possible PTO arrangement (Baoshou Zhang 2017)

Oscillating hydrofoil – those systems rely on lift and drag forces due to differences in pressure on the foils, and can be passively or actively operated. They can be positioned vertically or horizontally (Tethys Engineering n.d.).

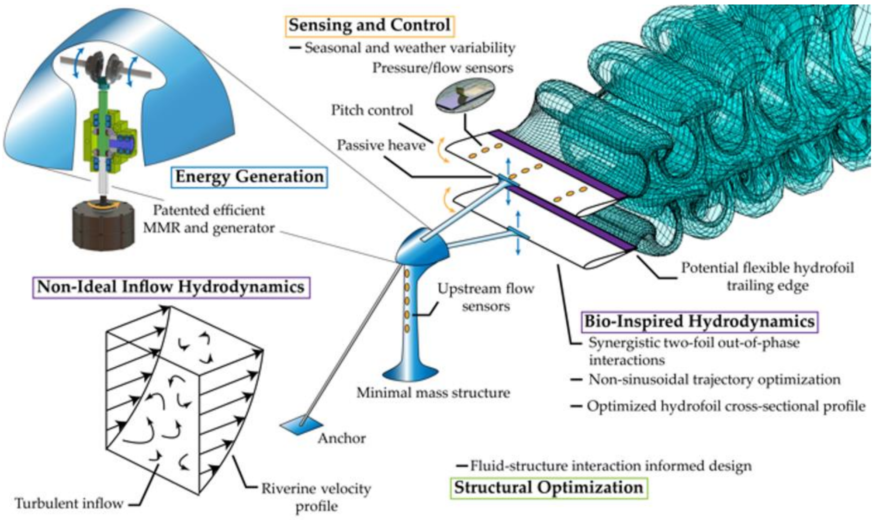

Figure 9: Oscillating hydrofoil schematic (Kackenmeister 2021)

Sail systems – the same concept used to propel vessels thousands of years ago is reimagined and used to power a generator and produce electricity. More details as to how energy is produced in the PTO section.

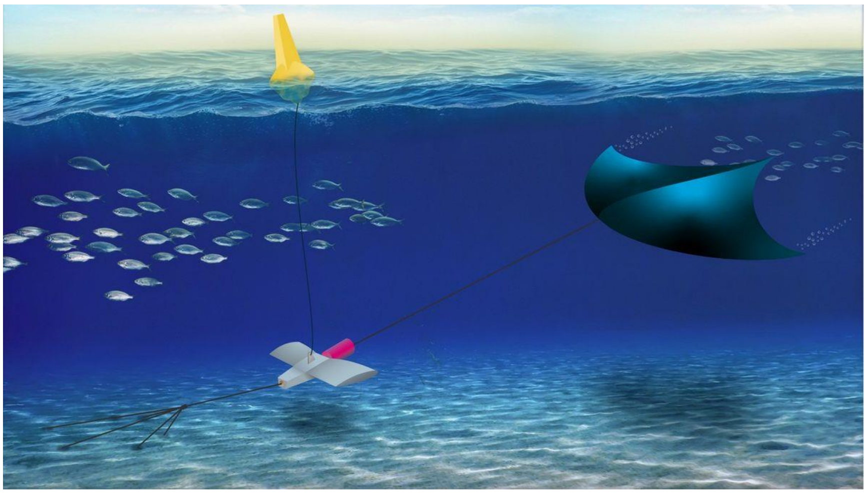

Figure 10: Manta Kite concept, converting flow power into kinetic energy and then electricity (Ackerman 2021)

Another interesting concept, also under the sail/kite subcategory is the kite designed by Makani Technologies. A plane-like energy kite set vertically on top of a tower and connected to it via a chord, utilizes small propellers to lift the kite off the tower, and a larger set of wing-like airfoils to keep the chord taut. Once the energy kite reaches its maximum altitude, the propellers are shut off and become wind turbines, while “figure 8” motion patterns of the kite generate lift as air passes through the wings and keeps it in the air (Anderson 2019). Power is then transferred to a generator located at the tower via connecting chord.

Figure 11: Energy kite under field testing (Anderson 2019)

2.1.3 Review of Power Take-off Devices

Power take-off (PTO) is the term coined for a set of components that work together to convert one type of energy to another. As an example, in the wave energy field, a PTO is a system that transforms the energy absorbed by the prime mover (e.g., point absorber buoy) of the Wave Energy Converter (WEC) into useable electricity (José F. Gaspar 2021). For the flow energy field (whether air or water) a PTO converts the power captured from the flow to usable power in the form of electricity. In a broader, more applicable sense, a PTO can be defined as a conversion system that transforms energy from one type to another. Wind/underwater turbines can convert power either via connecting the turbine rotor to a planetary gearbox and then generator, but can also feature a direct connection to the generator (direct drive connection) or feature a hydraulic connection between the rotor and a hydraulic pump and then a hydraulic motor (sometimes at the bottom of the tower) that is connected to a generator.

A novel patented hydraulic transmission concept is called the Delft Offshore Turbine (DOT). A single water pump brings water from the ocean, pressurizes it, and sends it back down to a central Pelton wheel connected to a generator (TUDelft n.d.). Several of those turbines can be deployed at the same site and power one single generator.

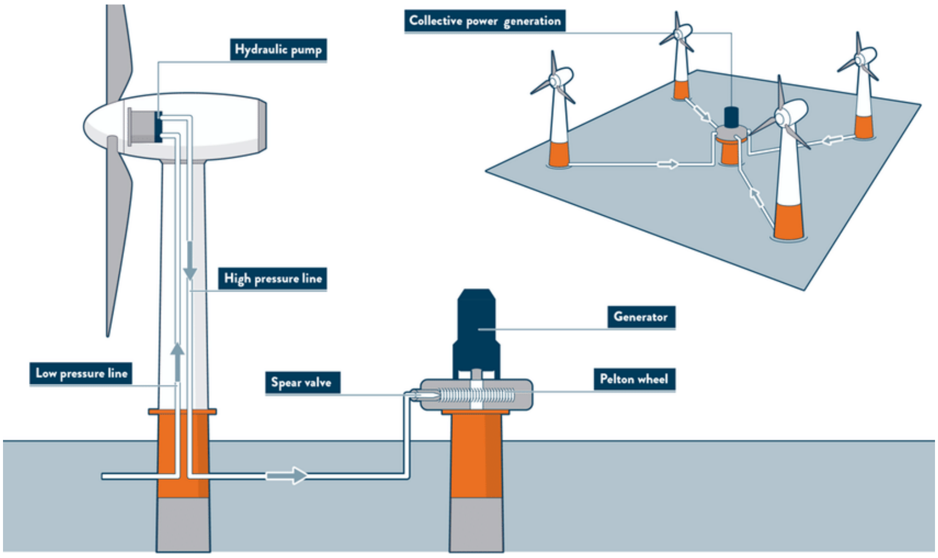

Figure 12: Working principle of DOT turbines and their implementation (TUDelft n.d.)

As HAWT can feature a direct drive connection to the generator, so can non-turbines systems, such as the PTO for the VIVACE vortex-induced vibration systems (Michael M. Bernitsas 2008). However, those systems feature a linear version of the direct drive, where the vertical movement of the bluff body underwater due to vibrations caused by a passing flow drive linear generators on both sides of the body, converting flow power into electricity.

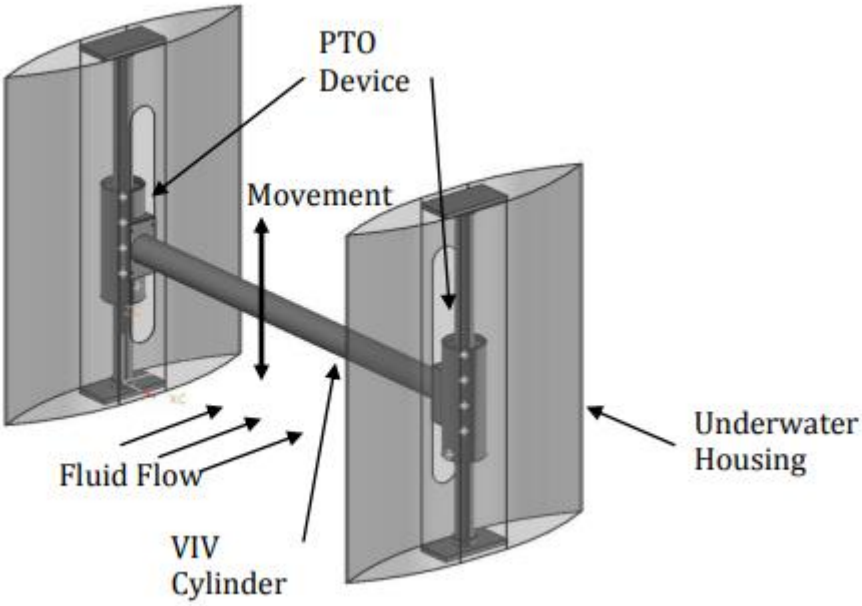

Figure 13: VIVACE's working principle detailed (Peter Avram n.d.)

PTOs can also be of frictional nature, such as the proposed PTO for a floating VAWT. The turbine rotor shaft has five generators contacting it via friction tires (Maura, et al. 2019). That configuration allows for misalignment between turbine rotor and generators while still transferring power.

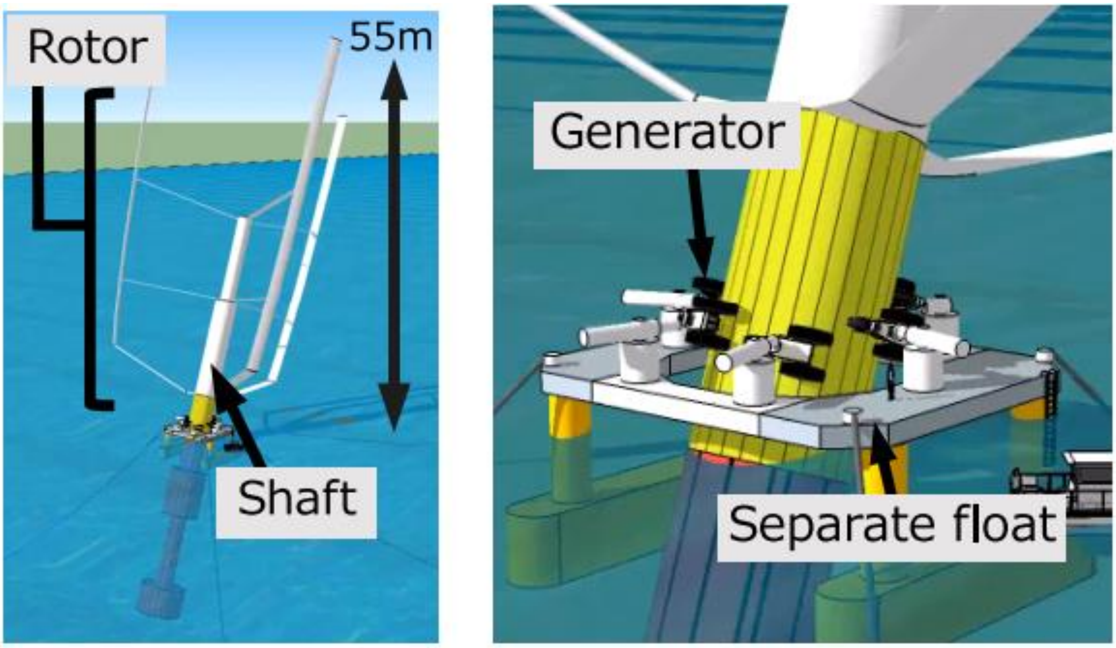

Figure 14: Floating VAWT with friction-driven PTO (Maura, et al. 2019)

Another interesting configuration of the power conversion principle is the flutter vane system, which has a piezoelectric material cantilevered on a structure fixed to a bluff body. As the flow passes by the structure and induces vibration, the vane vibrates and deforms the piezoelectric material, which generates a voltage differential that is then converted to power.

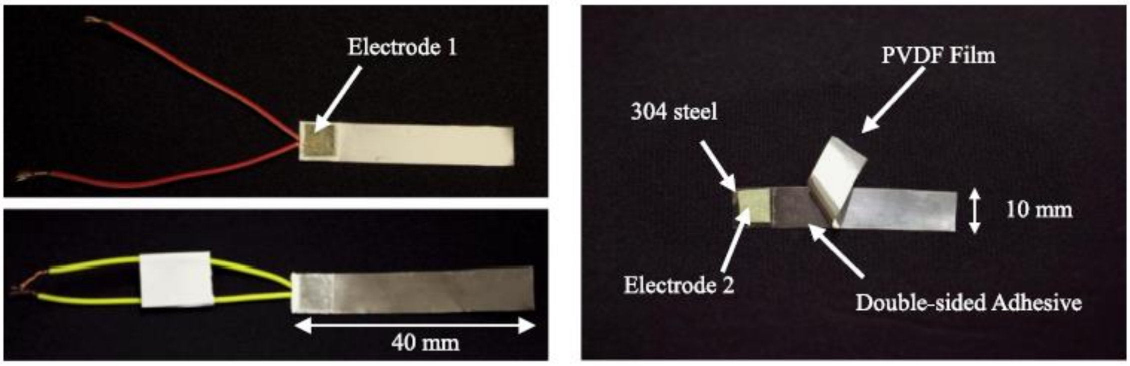

Figure 15: Configuration of piezoelectric material of vane (Pengyingkai Wang 2016)

Sail or kite generators, depending on whether they operate underwater or in the air, convert the fluid flow power into kinetic energy, which is used to reel out the generator spool and thus produce electricity. After the maximum extension of the chord is reached, the sail or kite takes on a more aerodynamic shape so it can be reeled back in, take back its original shape, and restart the cycle.

2.1.4 Turbine Performance Parameters and Controls

Turbines in general have their performance characterized by two dimensionless parameters: power coefficient – also known as Cp – and tip speed ratio (TSR). The first parameter quantifies how efficiently a given turbine converts flow power into mechanical power and is defined as the turbine mechanical power over the available flow power, or:

$$C_p = \frac{P_m}{P_f} = \frac{T_r \omega_r}{1/2 \rho A U^3} \tag{1}$$

Where:

- P_m: mechanical power on turbine
- P_f: available flow power
- T_r: torque on turbine rotor
- ω_r: rotor angular velocity
- ρ: fluid density
- A: blade swept area (Watson n.d.)
- U: flow speed

The second parameter quantifies the ratio between the linear speed at the tip of the turbine blade and the flow speed, or:

$$\lambda = \frac{\omega_r . r}{U} \tag{2}$$

Where r is the blade tip radius to the center of the rotor

For each turbine there is a value for TSR for a given flow speed that yields maximum power capture, or maximum Cp, called optimal TSR. For renewable energy applications, regardless of what kind of turbine is used and whether it is an air or underwater system, maximum power extraction from the flow is of utmost interest so that the system can operate at its optimal state. This is achieved by controlling the torque in the system, which speeds up or slows down the rotor, maintaining both the torque and angular velocity of the rotor at their optimal values. Figure 16 shows a typical plot of TSR vs. Cp for a 3-blade, 20 kW wind turbine. It can be noticed that the optimal TSR is approximately 5.5 times the wind speed, yielding a Cp of approximately 0.5. Figure 17 shows an equivalent plot but for a waterwheel. It can be noticed that the optimal TSR is much lower than that of a wind turbine due to the different working principles of those two machines. While horizontal axis turbines (or lift-based machines in general) rely on lift forces to operate and count with the effect of relative speed (relative speed between fluid speed and angular speed of blade), waterwheels (or drag-based machines in general) rely on drag forces, directly proportional to the square of the velocity difference between flow and blade, and can never rotate faster than the flow speed. This is why lift-based machines are operationally superior in areas with high flow velocity, and drag-based machines excel in low-speed flows, which makes them more suitable for ocean current power generation.

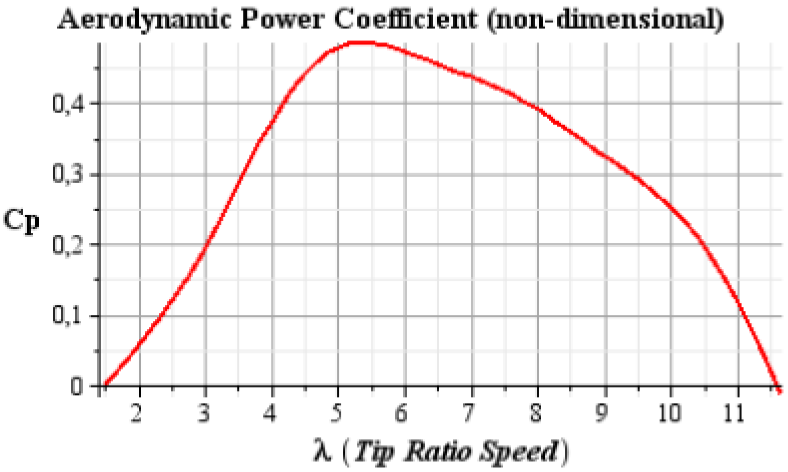

Figure 16: Typical TSR vs. Cp plot (K.E. Johnson 2003)

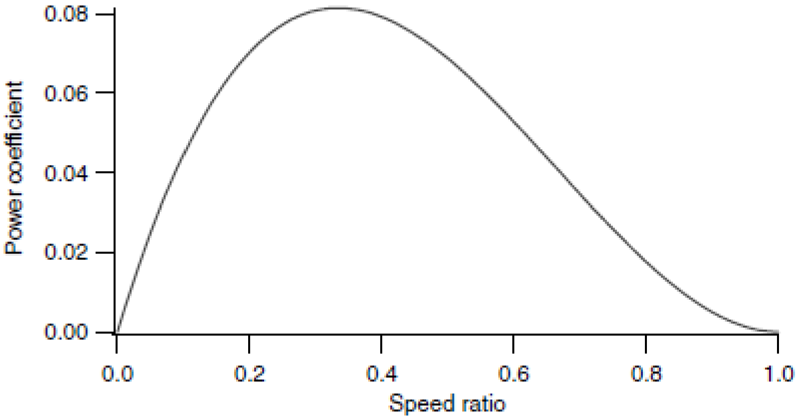

Figure 17: TSR vs. Cp of a horizontal cross-flow wind turbine equipped with flat blades (Manwell, Mcgowan and Rogers 2009)

The TSR and Cp are important parameters that indicate the optimal operating conditions for a turbine, which provides the control system operational setpoints to keep the system on for maximum power capture. In a turbine-based renewable energy system, the controller operates to keep the TSR within its optimal value during operation by regulating the load on the turbine rotor to speed up or slow down its axle, depending on conditions.

The basic dynamic equation is derived from the interaction between the flow, the blades and the load as:

$$\dot{\omega}_r = \frac{1}{J_{eq}}(T_r - T_L) \tag{3}$$

Where:

- $\dot{\omega}_r$: rotor angular acceleration
- J_{eq}: equivalent inertia of the whole system reflected on the turbine
- T_r: torque on rotor
- T_L: torque due to load

The controller regulates the term T_L of the equation based on readings of angular speed and rotor torque, with an optimal TSR as setpoint. For vertical axis turbines the expression for available rotor torque is derived as:

$$T_r = \frac{P_m}{\omega_r} = \frac{1}{2}\frac{\rho A C_p U^3}{\omega_r}$$

Utilizing the expression for TSR and substituting for U:

$$T_r = \frac{1}{2}\rho A r \frac{C_p}{\lambda}\left(\frac{\omega_r r}{\lambda}\right)^2 \tag{4}$$

For the load torque term, the main control law utilized to regulate that quantity during region 2 operation is (K.E. Johnson 2003):

$$T_L = k\omega_r^2 \tag{5}$$

$$k = \frac{1}{2}\rho A r^3 \frac{C_{p,max}}{\lambda_{opt}^3} \tag{6}$$

Where:

- k: torque load gain

- $C_{p,max}$: maximum turbine Cp

- - λ_{opt}: optimal TSR

$$\dot{\omega}_r = \frac{1}{J_{eq}}\left(\frac{1}{2}\rho A r \frac{C_p}{\lambda}\left(\frac{\omega_r r}{\lambda}\right)^2 - \frac{1}{2}\rho A r^3 \frac{C_{p,max}}{\lambda_{opt}^3}\omega_r^2\right)$$

$$\dot{\omega}_r = \frac{1}{2J_{eq}}\rho A r^3 \omega_r^2 \left(\frac{C_p}{\lambda^3} - \frac{C_{p,max}}{\lambda_{opt}^3}\right) \tag{7}$$

The sign of the angular acceleration of the rotor depends on $\lambda - \lambda_{opt}$:

- If $\lambda > \lambda_{opt} \rightarrow \dot{\omega}_r < 0$ – turbine decelerates

- If $\lambda < \lambda_{opt} \rightarrow \dot{\omega}_r > 0$ – turbine accelerates

The main issue with this approach is the difficulty of capturing precise values of Cp and TSR, since those rely on measurements of wind speed across the rotor area, and those measurements, especially for larger turbines, tend to vary considerably throughout its area and contain excessive noise (K.E. Johnson 2003).

A method frequently utilized in renewable energy systems that taps into photovoltaic power is called Maximum Power Point Tracking (Hall 2022). One of the most common MPPT routines is called Perturb and Observe (P&O), where the voltage is perturbed and power is observed. The algorithm changes the output voltage by a small amount (also called a step change) and observes changes in power output. Voltage increments cause power output to increase if the system is operating to the left of the maximum power point on the power curve, and decrease power output if the system is operating to the right of the MPP (A. S. Mahdi 2019). In other words, the MPPT seeks voltage and current values that maximize power output as conditions vary (Richard C. Dorf 2011). This method is also called Hill-Climb Search (HCS) as it seems to "climb" the power curve looking for its peak. The mechanical equivalent of maximizing power output through control of voltage and current is the control of rotor speed and mechanical load. The HCS algorithm seeks the peak power point of the turbine and computes the optimal signal to drive the system to the MPP (Ouhrouche 2011).

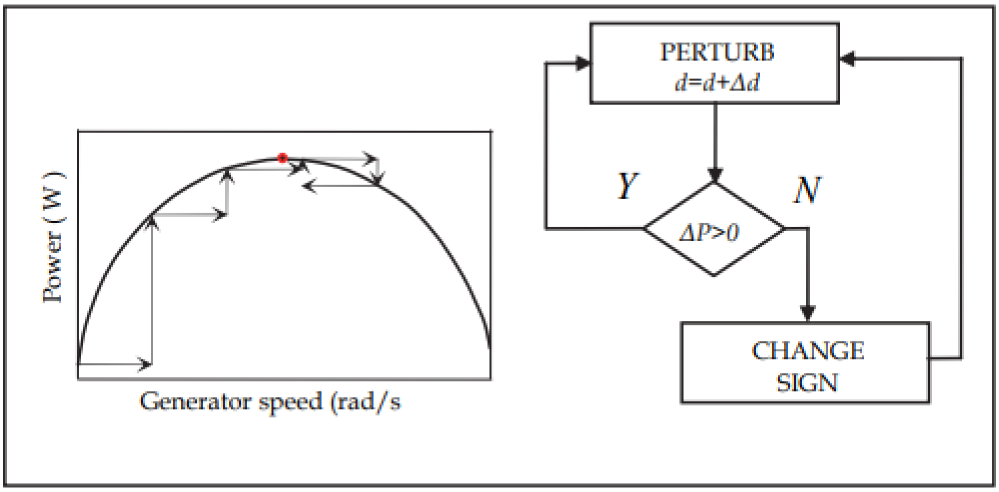

Figure 18: P&O principle - mechanical load is disturbed, power is observed and controller decides next step based on observations (Ouhrouche 2011)

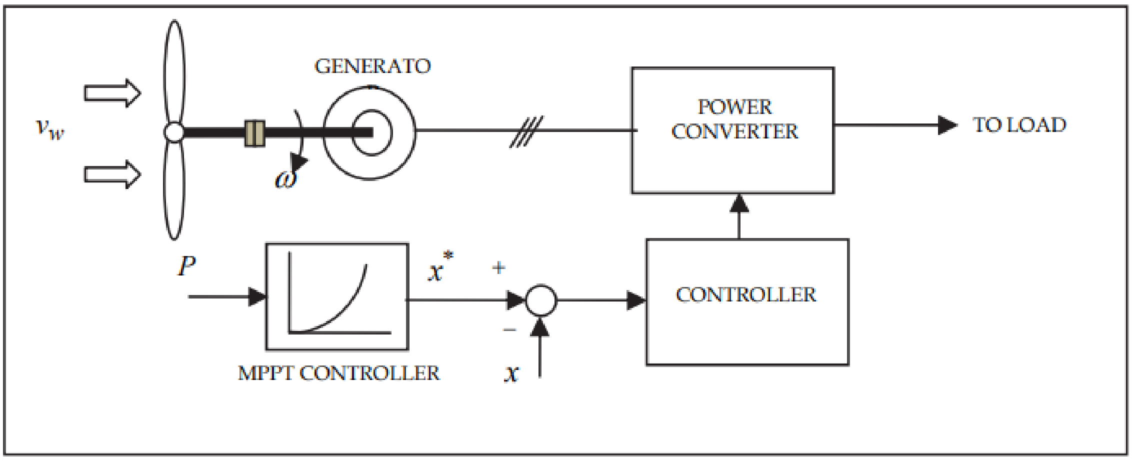

Figure 19: schematic of a HAWT equipped with HCS control (Ouhrouche 2011)

It is important to notice that standard HCS MPPT works very well when the turbine inertia is very small and it reacts to changes in wind speed almost instantaneously (Wang e Chang 2004). An option to overcome this issue is to measure parameters from the power electronics section of the system as opposed to reading rotor and wind speeds. In other words, after a small, intentional disturbance in the system cause by a change in the inverter current demand, the change in electrical power output is measured and the controller then makes a decision regarding its next action. After the direction of change of power output (if it increases or decreases) is detected, the direction of the inverter current demand control signal can be decided according to rules set based on the HCS principle, as shown in Table 1 (Wang e Chang 2004).

Table 1: Rules for HCS controller based on power output readings (Niassati, et al. 2012)

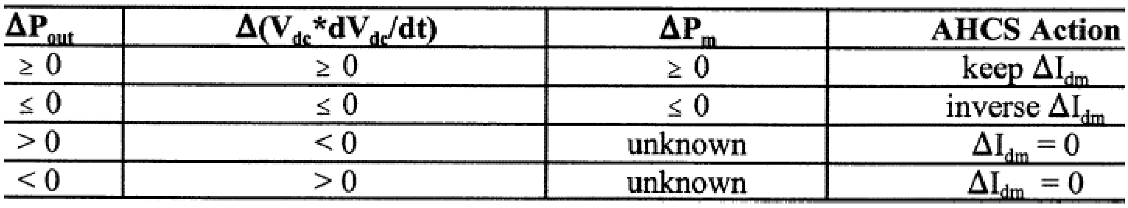

ΔP_{out}	$\Delta(V_{dc} * dV_{dc}/dt)$	ΔP_m	AHCS Action
≥ 0	≥ 0	≥ 0	keep ΔI_{dm}
≤ 0	≤ 0	≤ 0	inverse ΔI_{dm}
> 0	< 0	unknown	$\Delta I_{dm} = 0$
< 0	> 0	unknown	$\Delta I_{dm} = 0$

This approach uses the “search-remember-reuse” technique that recycles itself until an accurate memory of system characteristics is established (Ouhrouche 2011). The method has 3 phases: initial mode, training mode and application mode. When the system memory is empty and the system is under a transient state, the controller enters the initial mode, where the inverter current demand is determined by max-power error driven (MPED) control, where the system tries to minimize the error between maximum power for a given wind speed and the current power output. Upon reaching steady-state operation, the controller enters the training mode and AHCS is used, varying the inverter current demand searching for the MPP and training the memory by saving those points in it, as well as the control parameters and state parameters (such as current demand and voltage output). If the system is operating in a transient state and the memory already has data for the voltages being measured, the controller enters the application mode and the inverter current demand is immediately determined by Direct Current Demand Control (DCDC) so that the turbine can operate at its highest efficiency (Wang e Chang 2004). Figure 21 shows an overview of the modes.

Other issues with HCS include the time it takes to converge due to fixed step size disturbances or due to unstable oscillating behavior around a point, where the system oscillates around but never really reaches the maximum power point. To solve that, much like variable step size numerical methods to solve ODEs faster and more precise, alternative HCS methods utilize variable step sizes to reach the MPP faster and avoid unstable behavior. As one of the strategies to achieve adaptive step size, constant monitoring the variation of power. When the perturbation step passes the maximum point of the power curve ($\Delta P_{out} < 0$) the perturbation direction reverses and the step size is reduced to half of the previous step size. This process repeats itself every time the perturbation causes the power output to decrease, which causes the oscillation around the MPP to decrease quickly (Niassati, et al. 2012).

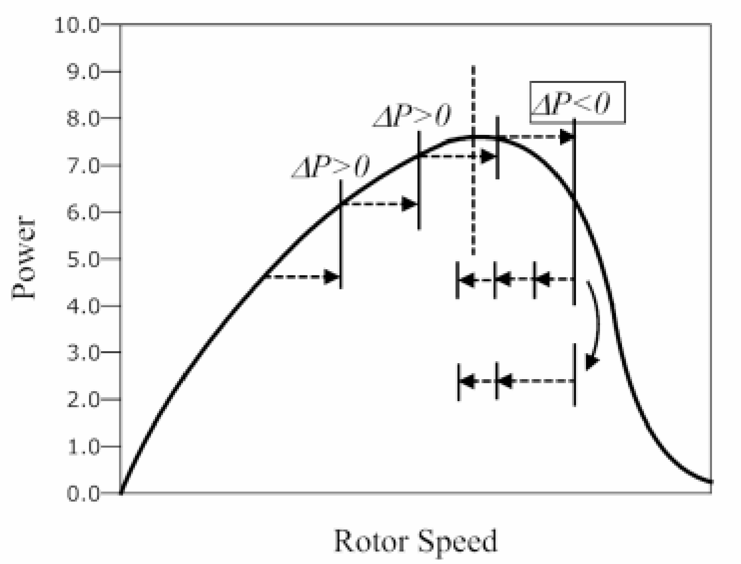

Figure 20: Schematic of adaptive HCS (Niassati, et al. 2012).

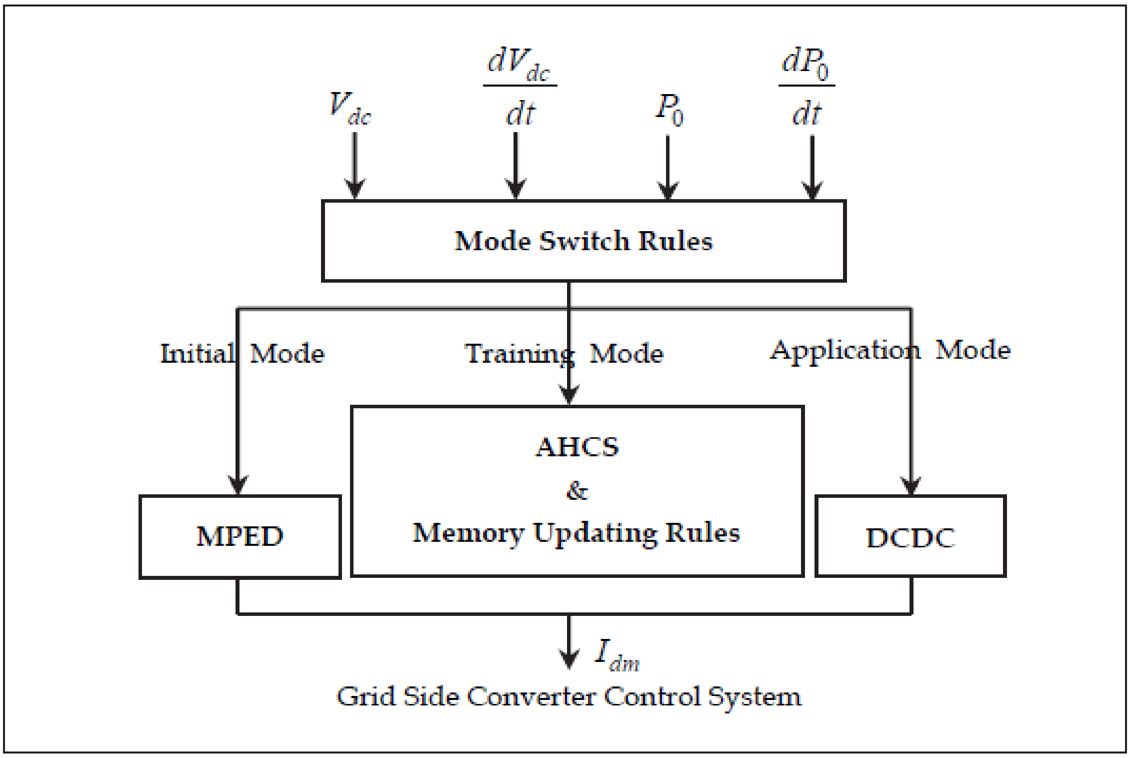

Figure 21: Operation modes for AHCS (Ouhrouche 2011)

2.1.5 System Overview

The system consists of a waterwheel, a PTO, and associated electronics onboard an unmanned mobile surface vessel (a Wave Adaptive Modular Vehicle, or WAM-V USV). The concept of operation requires that the WAM-V self-anchors in specific locations where flow speed is ideal for the marine hydrokinetic (MHK) turbine to produce power. Figure 22 shows the basic dimensions of the waterwheel and Figure 23 shows the waterwheel and PTO onboard WAM-V during field testing. The PTO consists of (Figure 24) (Hall 2022):

1. Input shaft
2. Support disk
3. Planetary gearbox

4. CVT shift stack
5. CVT sub-system support
6. CVT transfer gears
7. NuVinci Ball CVT
8. Encoder plate and encoders
9. Generator
10. Support disk and structure mount

Figure 25 shows the PTO housed within the waterwheel blades. The waterwheel transfers its motion to the input shaft, which takes power through the planetary gearbox, CVT and generator. The CVT shift stack is equipped with a servo motor that changes the gear ratio of the CVT, which allows for speed decoupling between the generator and waterwheel. There are two encoders: one located before the CVT, which captures the angular speed at the output of the planetary gearbox, and another after the CVT, which captures the angular speed of the generator. Although the relationship between servo motor position and CVT ratio has already been obtained (Hall 2022), the two encoders work as a verification setup to add reliability to that relationship and the ratio values it gives. Even though there is no encoder at the waterwheel shaft, by dividing the readings from the first encoder by the fixed (planetary) gearbox ratio the angular speed at the rotor shaft is obtained, which eliminates the need for a third encoder. The fixed gearbox has a 35:1 ratio, whereas the CVT has a variable ratio range of 0.5:1 to 1.9:1. Therefore, the total ratio between the input shaft and the generator ranges from 18.2:1 to 66.8:1. The generator used for initial testing was the Freedom III Permanent Magnet Synchronous Generator (PMSG), with maximum rated power of 1.5kW at 970rpm. Table 2 shows some numbers that characterize the generator performance. The charge controller used for initial testing was the LT8491 High Voltage Buck-Boost Battery Charge Controller with Maximum Power Point Tracking (MPPT) and I^{2}C communication interface (Analog Devices n.d.). The battery used was 12V lead-acid.

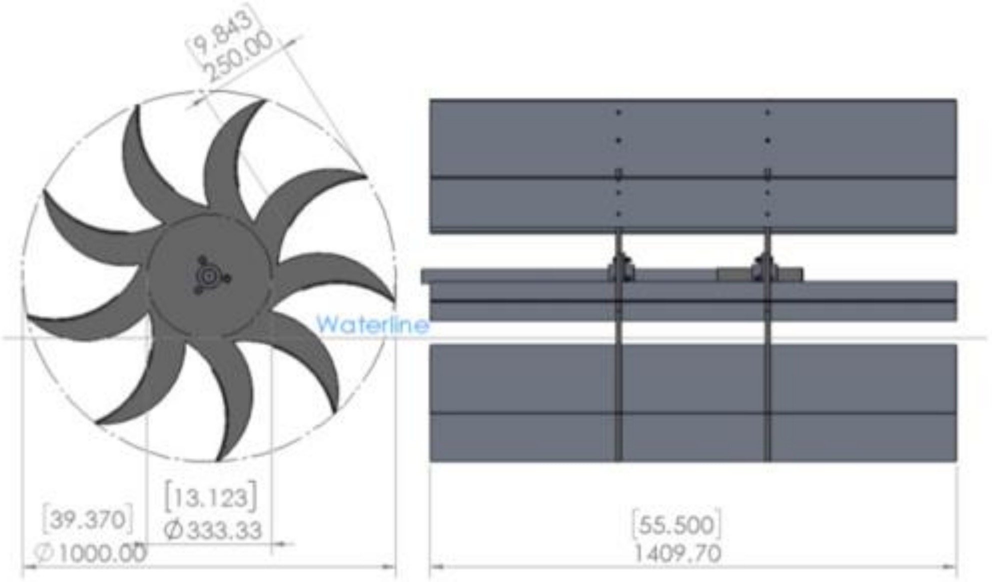

Figure 22: Basic waterwheel dimensions (Hall 2022)

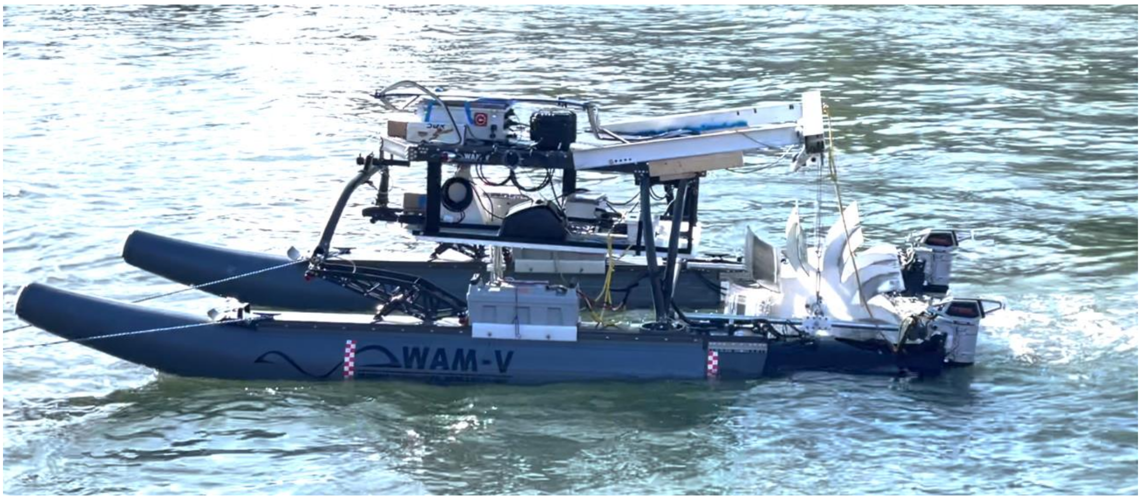

Figure 23: Waterwheel and PTO onboard WAM-V during field testing (Dhanak 2023)

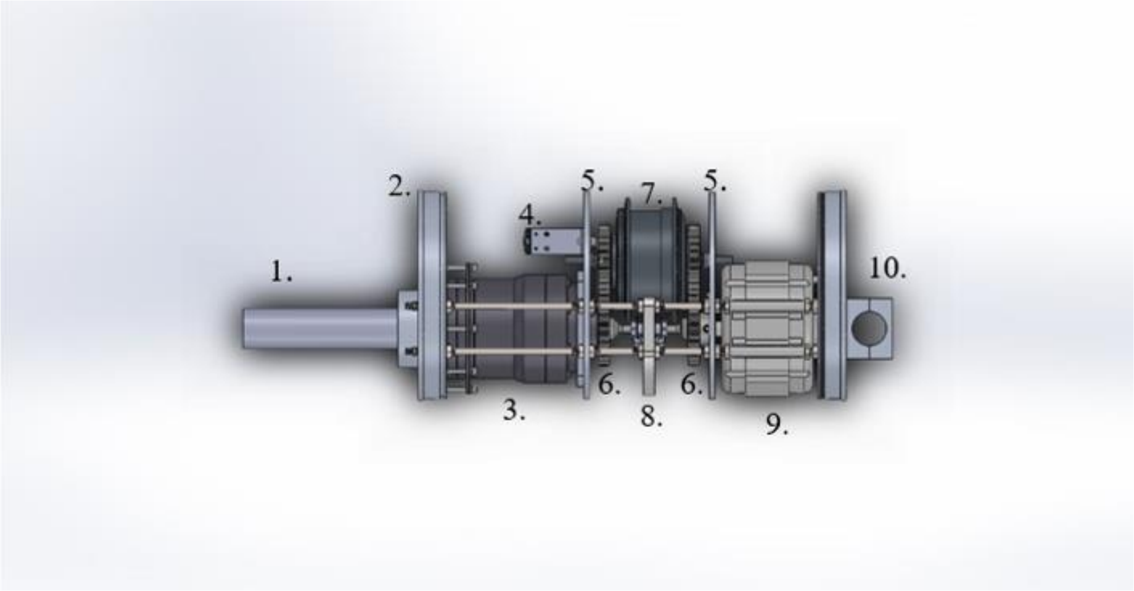

Figure 24: PTO components enumeration (Hall 2022)

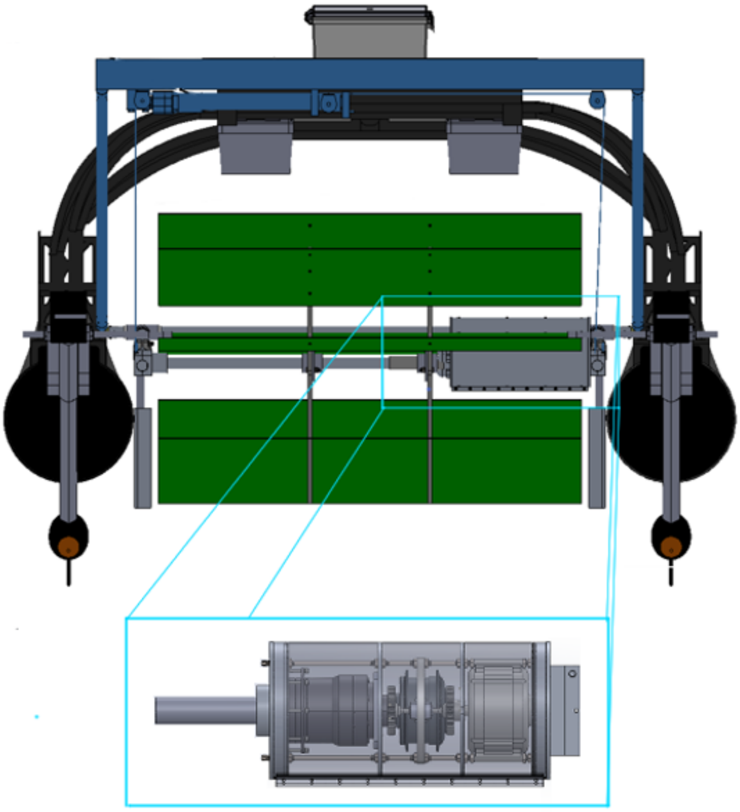

Figure 25: PTO housed within waterwheel, inside watertight aluminum casing (Hall 2022)

Table 2: Freedom III generator characteristics (Missouri Wind and Solar n.d.)

RPM	Voltage (V)	Power (W)	Current (A)
250	12	420	35
490	24	800	33.3
970	48	1500	31.2

2.2 Overview

For Section 3, field tests and device proof of concept will be discussed, the results analyzed and further data derived from obtained dataset in order to understand the behavior of the MHK system and derive conclusion regarding its power production, torque capabilities and generator sizing. Upon completion of that phase, the need for a new generator will be evaluated to better fit power production capabilities of the system and a charge controller capable of communicating with the PTO control board and receiving commands will be discussed. To manage control variables (CVT ratio and generator current) an algorithm will be developed and tested on MATLAB’s Simulink using a dynamic model of the system, currently under development. Different cost functions and optimization algorithms will be studied and tested on the system model and the options yielding satisfactory results will be picked.

The MHK system is essentially a MISO system (Multiple Inputs Single Outputs) that consists of the CVT ratio and the generator current as inputs and turbine speed as output. Flow and waterwheel speeds are measured variables used in the control system to set turbine speed setpoints. The goal of this work is to implement a suitable speed controller on the waterwheel’s PTO system without prior knowledge of the waterwheel’s optimal TSR setpoint, but an estimation based on analytical model. This will be achieved by regulating the generator electrical current demand through the charge controller, ultimately regulating the torque load on the waterwheel shaft. That control action will be paired with the control of the CVT ratio that decouples the generator speed from the waterwheel speed. In other words, the system can look for a more efficient speed and load for the generator to operate at while maintaining the waterwheel speed within the desired limits, as it can also decrease the reflected inertia on the turbine’s shaft when minimum torque load is achieved but cannot meet the speed setpoint.

To accomplish that, an algorithm will be developed to effectively control both the CVT and the generator current demand via control of the charge controller. The charge controller and the CVT will work together to maintain the turbine speed at its optimal TSR setpoint while trying to optimize flow power extraction and generation of electrical power.

To obtain an estimate for the optimal TSR setpoint, a waterwheel analytical torque model will be developed and analyzed both analytically and numerically. That model will then be used on Simulink simulations, where an appropriate algorithm to control both CVT and electrical current will be developed and simulated. Benchtop tests will be conducted to validate the control strategy, with the developed analytical torque model used as a base to program the benchtop DC motor. Modifications on the charge controller will be detailed in order to achieve electrical current control and consequently torque control. Data stemming from rounds of field test in-between bench tests will be utilized to update the analytical torque model and improve the waterwheel emulation accuracy. After a final control schematic is developed, one last set of field tests will be carried out to validate the proposed algorithm. Furthermore, overall waterwheel torque and power coefficient models will be derived based on the number of blades and diameter of the turbine operating at full depth, where maximum power coefficient estimations will be obtained based on the number of blades. The performance of different turbine configurations regarding number of blades and operating depths will be evaluated and conclusions will be drawn from test data. Lastly, discussions regarding the overall results and scope of future work will be carried.

3. FIELD TESTS – ROUND 1

The entire waterwheel system with PTO and electronics was tested on 02/23/2023, 02/24/2023 and 02/28/2023 at the Intercoastal Waterway (ICW), Dania Beach, Florida. During testing the electro-mechanical performance of the system was observed in an effort to optimize its mechanical-to-electrical power conversion capabilities for future testing. Before initiating tests, the encoders were damaged and could not be used for speed measurements. The basic test routine consisted of first deploying the waterwheel in the water with the CVT set to its lowest, with different submergences tested per test day: 8in, 10in (full blade) and 12in. As the wheel started turning, the generator created a voltage output. The charge controller was then manually enabled by the user when the voltage was on average above 10V, which allowed current to flow to the battery. If the wheel was moving fast enough, the user then begun increasing the CVT ratio to speed up the generator and increase power output. If the waterwheel slowed down too much, the user decreased the CVT ratio to avoid stalling the wheel. It was important to avoid stalling the wheel since the CVT ratio can only be changed when the wheel is in motion. The user visually monitored the speed of the waterwheel and decided whether to increase or decrease the CVT ratio.

An important point to mention is that the charge controller, upon detecting voltage below a certain threshold for a while, disabled itself and did not reenable itself unless it either sensed a high enough voltage for a specific period or the user manually commanded it to. The user had to notice that, in case the generator output voltage was high and the current output was zero, that meant the charge controller was disabled and the user then sent the command to reenable it. In summary, while the wheel is deployed, the user checks for the wheel speed (visually) while monitoring the generator output voltage and current, the charge controller status (enabled/disabled) and the CVT position (ratio) to make necessary adjustments as needed. Figure 26, Figure 27 and Figure 28 show flow speed and electrical power output over time. Those values are obtained through a moving average, with a window size of 200 samples. The actual charge controller current demand is depicted in Figure 29.

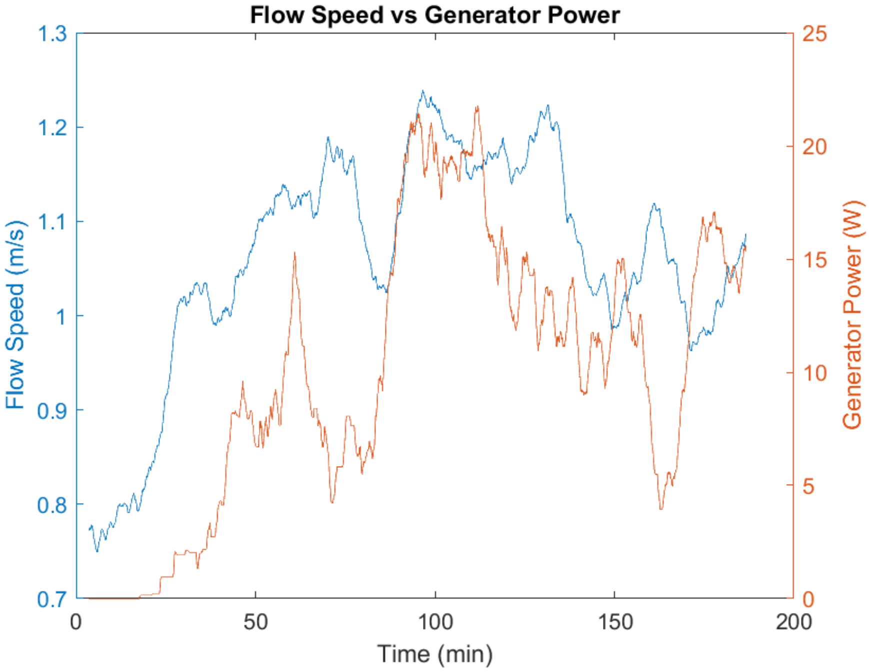

Figure 26: Flow speed and power output over time - 9 blades, 10in submergence – field test (2/23/2023)

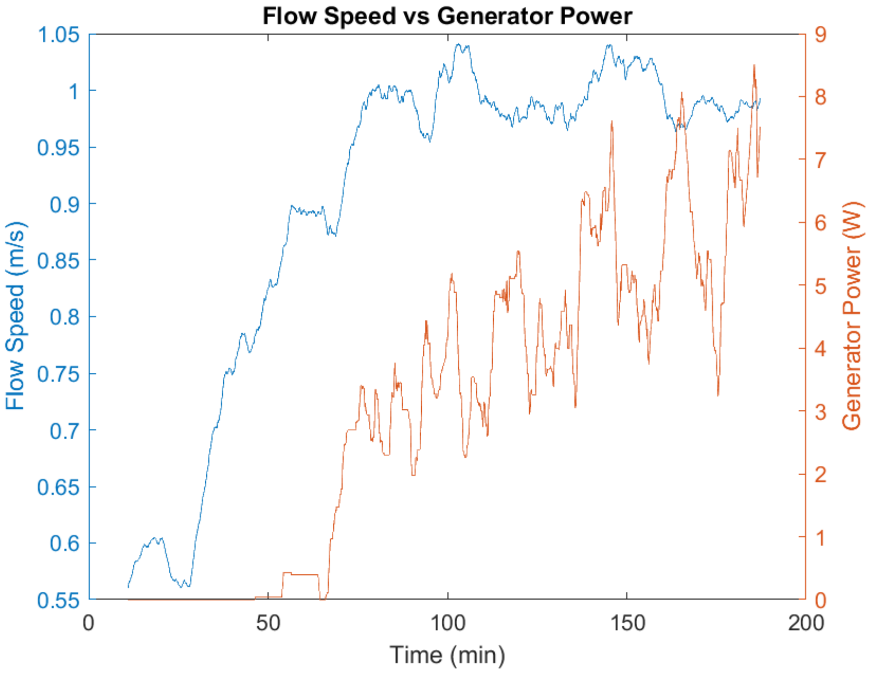

Figure 27: Flow speed and power output over time - 9 blades, 12in submergence – field test (2/24/2023)

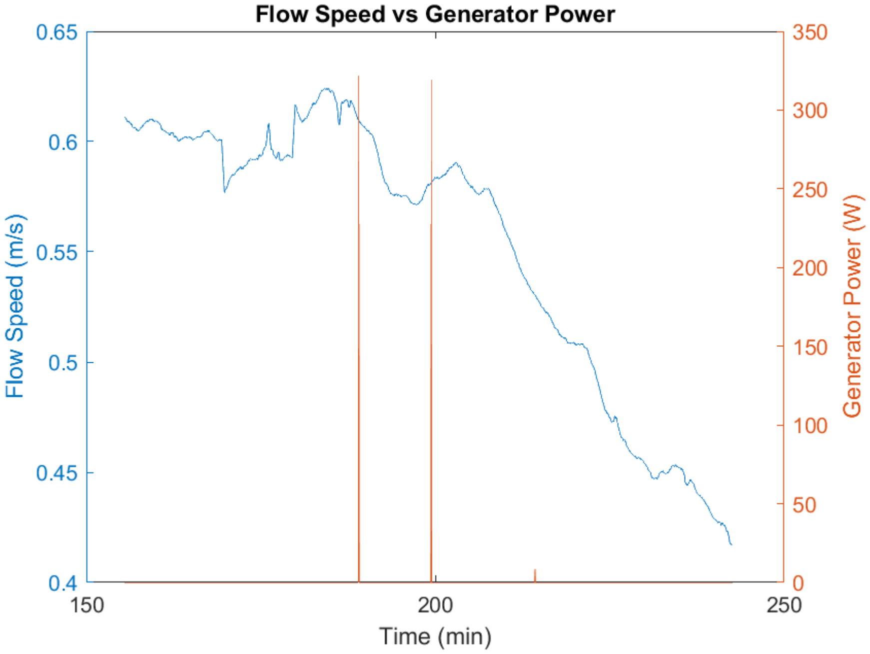

Figure 28: Flow speed and power output over time - 7 blades, 10in submergence – field test (2/28/2023)

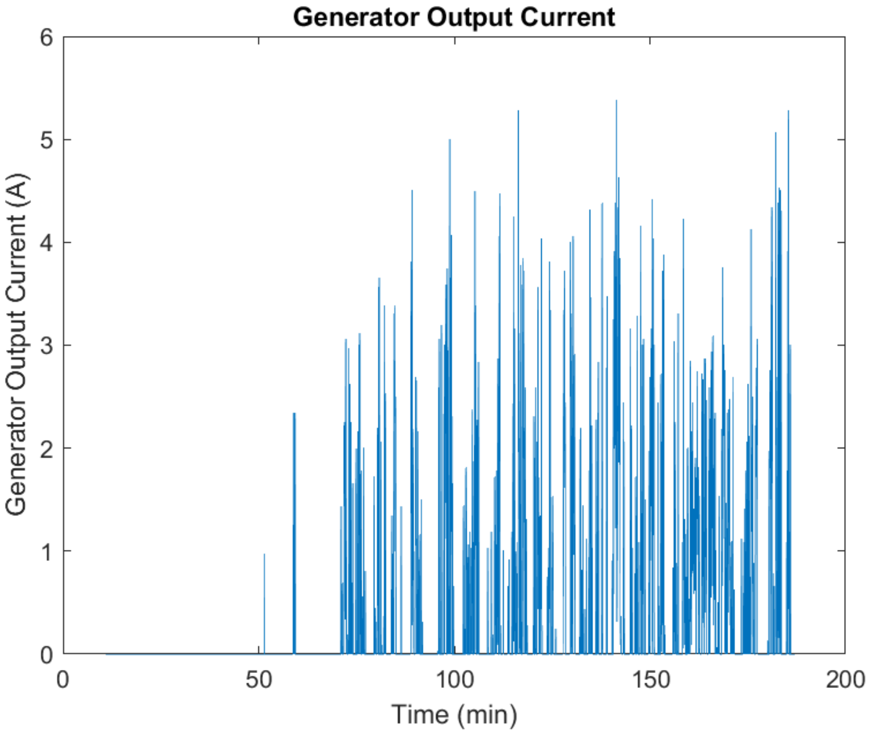

Figure 29: Actual charge controller current demand - 9 blades, 12in submergence – field test (2/24/2023)

The first and most immediate conclusion drawn from field tests is that the load demand at the wheel rotor was too large, which caused it to decelerate and bring the generator voltage below the threshold of the charge controller, causing itself to disable (i.e., generator output current becomes zero – no electrical power output). The charge controller demanded certain current values, with demand spikes shown in Figure 29. Those spikes immediately caused an excessive torque on the system, causing a sudden deceleration. That cycle repeated itself multiple times during testing. Only for flow speeds over 1m/s was the system able to exit that cycle and maintain wheel rotation. Moreover, the charge controller draws current based on the battery charging state, as seen in Figure 30. Since the battery was not completely depleted, the charge controller was operating under stage 1 and trying to bring the current to charging limit, which caused excessive load demand on the system and decelerated the wheel. With such performance, the main conclusions drawn from tests are two:

1) Current generator might be too large for the system, which may cause excessive loads upon small current demands from charge controller

2) Charge controller and PTO control system have to communicate so successful generator torque control can occur and a MPPT technique can be utilized.

Furthermore, the CVT was only activated for brief moments during testing on 2/23/2023, since the wheel did not develop enough speed to have the user increase the ratio on the other test days. On 2/28/2023, the tidal flow was too low to produce power, which caused the data set to be disregarded. Table 3 shows the summary of field test results.

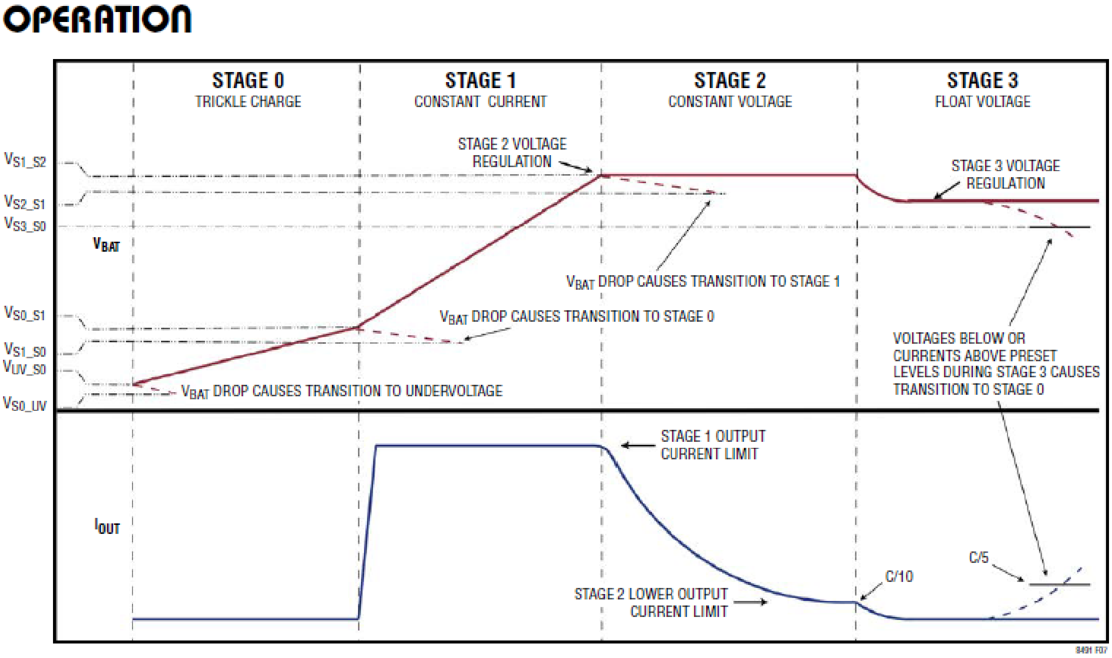

Figure 30: Charging states for lead-acid battery (Analog Devices n.d.)

Table 3: Summary of field test results

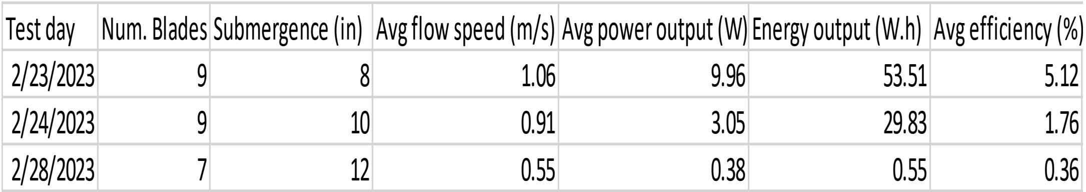

Test day	Num. Blades	Submergence (in)	Avg flow speed (m/s)	Avg power output (W)	Energy output (W.h)	Avg efficiency (%)
2/23/2023	9	8	1.06	9.96	53.51	5.12
2/24/2023	9	10	0.91	3.05	29.83	1.76
2/28/2023	7	12	0.55	0.38	0.55	0.36

3.1 Inferred Field Test Results

As mentioned earlier, the encoders sustained damage prior to testing and could not gather data. Also, there was no torque sensor in the system, which renders live torque reading on the powertrain impossible. This means that there was no torque reading during all tests and thus no way of calculating waterwheel torque, power, Cp and TSR. However, a strategy to obtain those data was put in action. It essentially consisted of characterizing the generator and PTO under different speeds and electrical loads, obtaining mathematical models of those components. After obtaining the models, it is possible to go back to field test data and apply those models to obtain data not directly measured. This technique does not replace proper measurements during tests and was only performed as an alternative to obtain more information about the performance of the system.

First, the generator alone was characterized, where both generator speed and electrical resistance were varied and values for resistive torque and efficiency were computed. Table 4 and Table 5 show the values obtained and Figure 31 shows the configuration for running the characterization. It can be noticed that some data points are missing, which is due to the fact that the characterization pushed the laboratory power supply to its maximum current output limit (it is a 48V, 7A power supply, totaling 336W of available power). Next, the values for RPM were kept fixed and the measurements were plotted against electrical resistance. Plots for torque and efficiency can be seen in Figure 32 and Figure 33, where the main mathematical relationship between those quantities was obtained for each group of plots through fitted trendlines. It is noticeable that the relationship resistance-torque and resistance-efficiency are of the following form:

$$T_{g,m} = a_1(\omega)R^{b_1(\omega)} \tag{8}$$

$$\varepsilon_m = a_2(\omega)\, ln(R) + b_2(\omega) \tag{9}$$

Where:

- $T_{g,m}$: generator model torque
- $\varepsilon_{g,m}$: efficiency model
- R: electrical resistance
- a_1, b_1, a_2, b_2: speed-dependent coefficients
- ω: generator angular speed, RPM

For each fixed angular speed value, the coefficients took new values. By plotting the coefficients a_1, b_1, a_2, b_2, it was possible to derive a relationship between those coefficients and angular speed, as shown in figures. The expressions for the coefficients were:

$$a_1(\omega) = -4 \cdot 10^{-6}\omega^2 + 0.0127\omega - 0.794 \tag{10}$$

$$b_1(\omega) = 1 \cdot 10^{-6}\omega^2 - 1.4 \cdot 10^{-3}\omega - 0.2143 \tag{11}$$

$$a_2(\omega) = -7 \cdot 10^{-7}\omega^3 + 1 \cdot 10^{-6}\omega^2 - 7 \cdot 10^{-4}\omega - 5.12 \cdot 10^{-2} \tag{12}$$

$$b_2(\omega) = 4 \cdot 10^{-9}\omega^3 - 8 \cdot 10^{-6}\omega^2 + 4.5 \cdot 10^{-3}\omega + 0.2902 \tag{13}$$

Table 4: Generator torques as function of angular speed and electrical resistance

		RPM									
		86	174	263	352	443	531	616	826	1034	1233
Load (Ω)	250	0.12	0.12	0.12	0.16	0.18	0.2	0.22	0.26	0.32	0.36
	100	0.12	0.14	0.16	0.22	0.24	0.28	0.32	0.38	0.44	0.52
	50	0.14	0.18	0.24	0.3	0.34	0.4	0.44	0.58	0.68	0.8
	25	0.16	0.24	0.32	0.42	0.5	0.6	0.7	0.9	1.12	1.3
	10	0.24	0.4	0.6	0.82	1.02	1.24	1.4	1.82		
	5	0.36	0.68	1.04	1.4	1.74	2.1	2.4			

Table 5: Generator efficiencies as function of angular speed and electrical resistance

		RPM									
		86	174	263	352	443	531	616	826	1034	1233
Load (Ω)	250	0.078353	0.126421	0.161776	0.251297	0.24861	0.25731	0.293352	0.55803	0.507762	0.512616
	100	0.17933	0.259292	0.336243	0.328971	0.383398	0.414355	0.684791	0.707774	0.674736	0.67088
	50	0.175253	0.333467	0.408283	0.504789	0.544318	0.555921	0.629451	0.744386	0.757626	0.748603
	25	0.254874	0.474079	0.577031	0.622516	0.666002	0.687337	0.828226	0.838379	0.815307	0.831263
	10	0.4066	0.63662	0.715234	0.746644	0.776704	0.794711	0.86786	0.876795		
	5	0.430564	0.660851	0.723967	0.776461	0.798269	0.804966	0.866286			

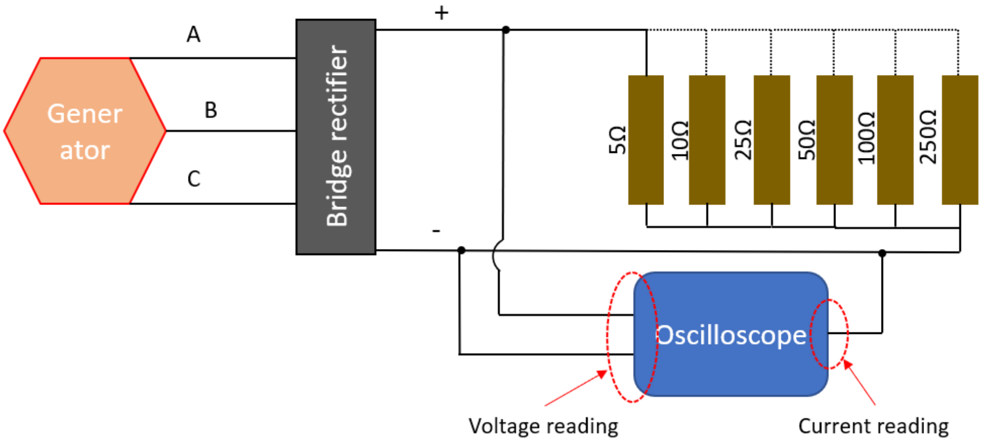

Figure 31: Electrical setup schematic with resistances varied manually

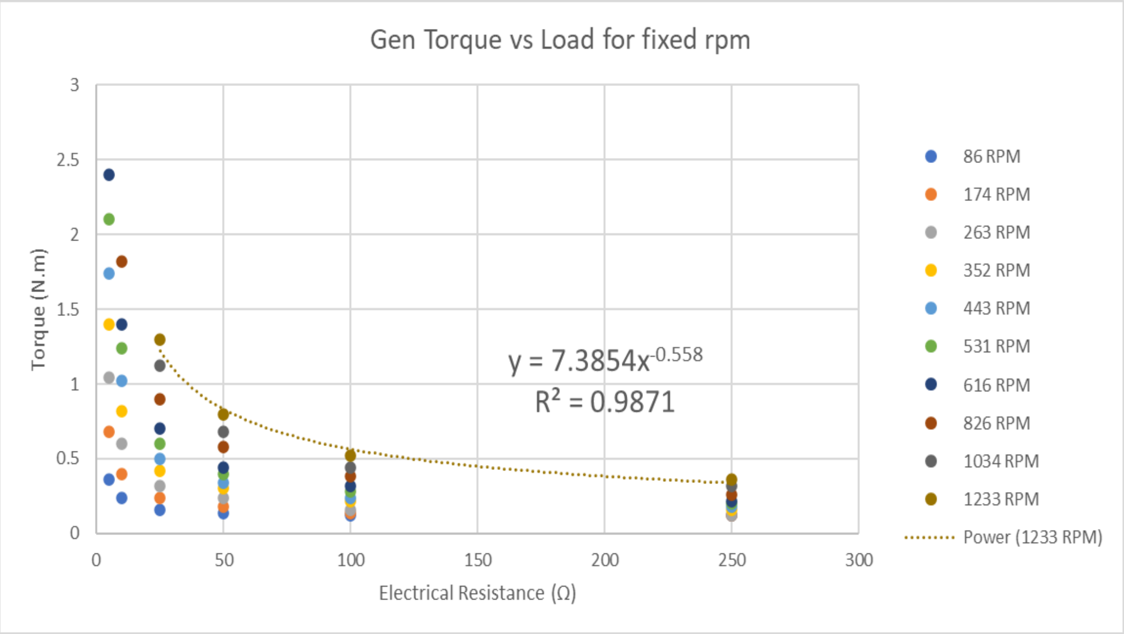

Figure 32: Plots for generator electrical resistance vs. torque for fixed angular speeds

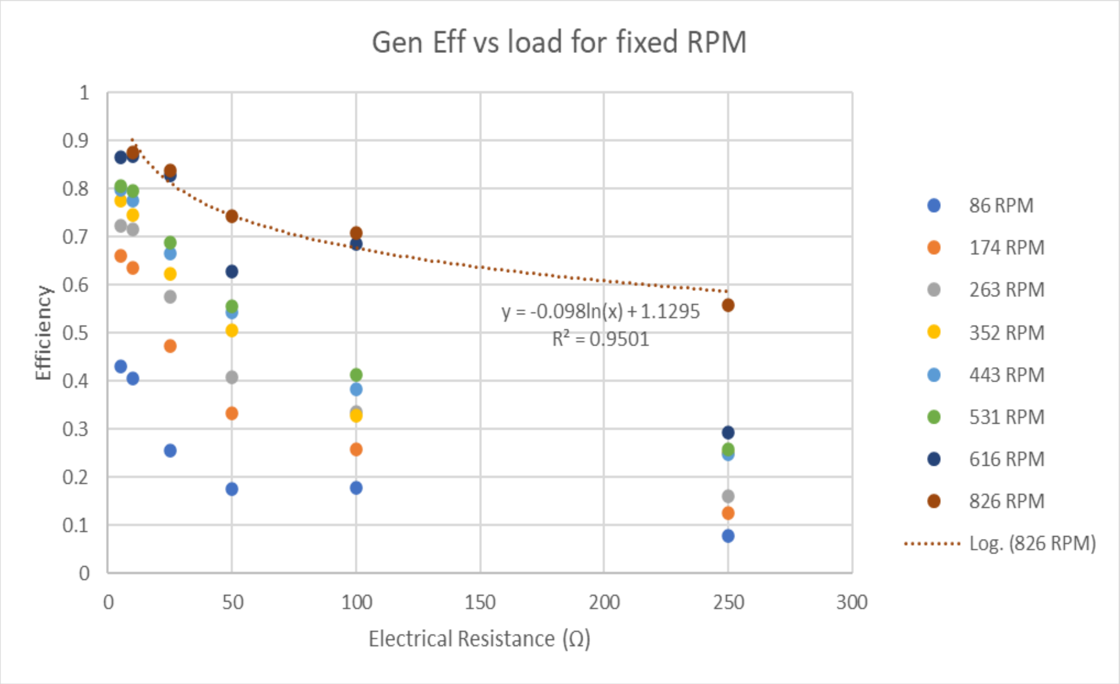

Figure 33: Plots for generator electrical resistance vs. efficiency for fixed angular speeds

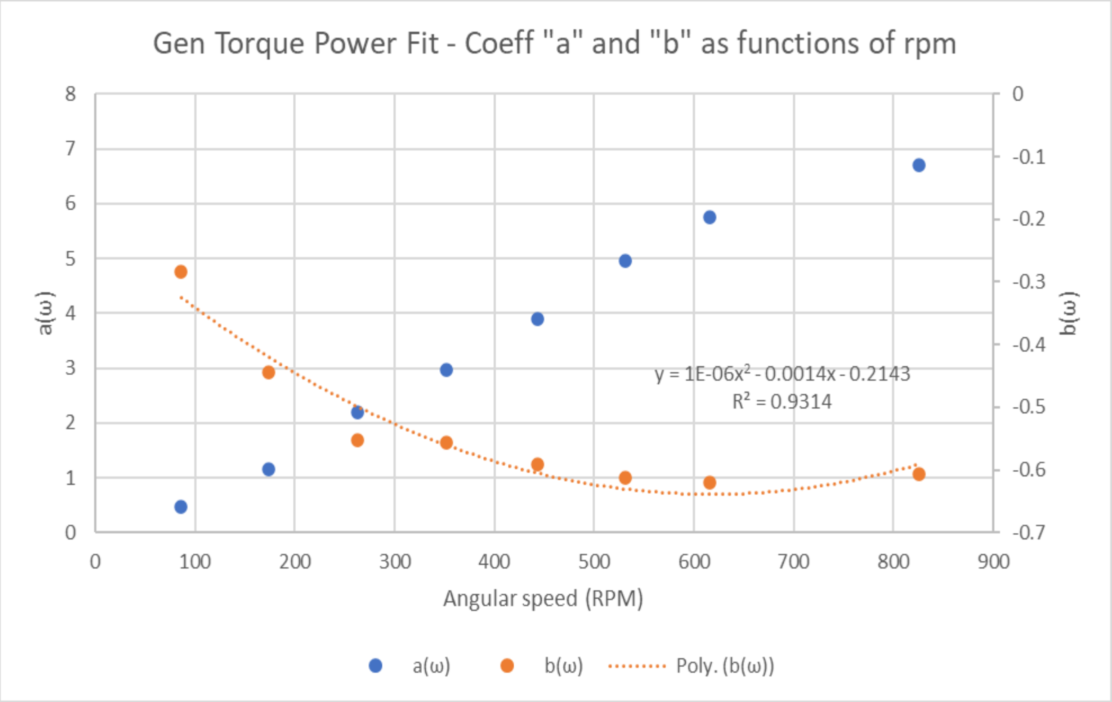

Figure 34: Torque curve fit coefficients as a function of generator angular speed

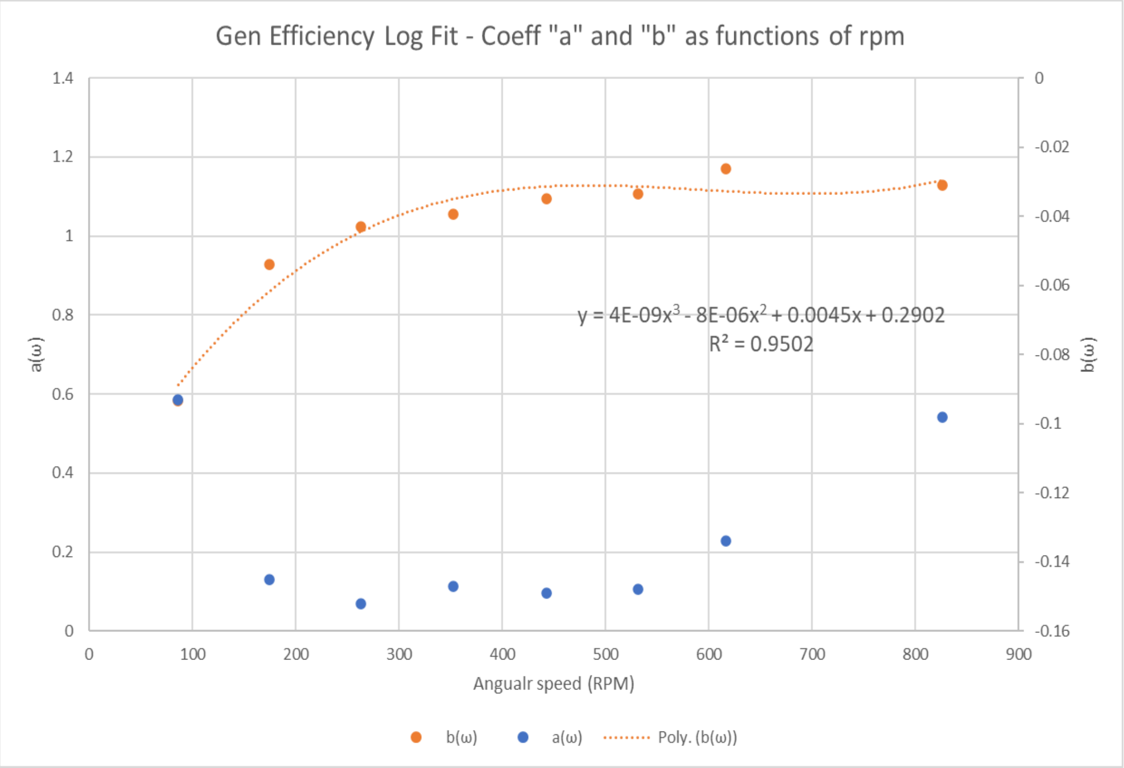

Figure 35: Efficiency curve fit coefficients as a function of generator angular speed

After obtaining the mathematical model for the generator torque and efficiency as functions of generator angular speed and electrical load, the same process was performed for the PTO as a whole, beginning on the input shaft and ending on the generator. The measured parameters for the PTO were generator voltage, input shaft torque and PTO total efficiency. Figure 36 shows the setup for running the PTO characterization. This time, a variable load source was used, such that it can sustain constant resistance while power changes.

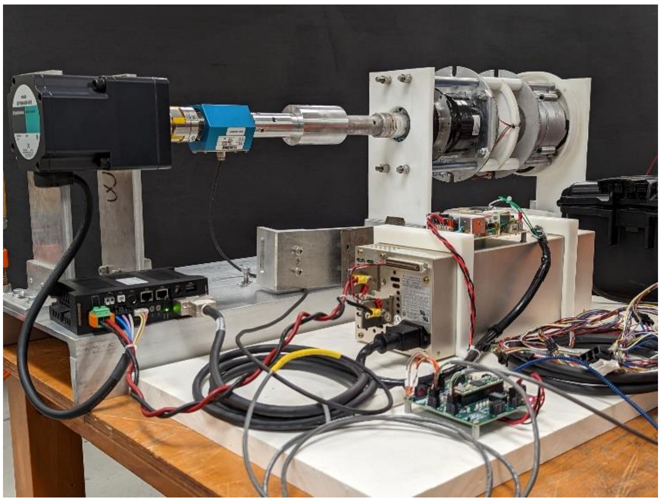

Figure 36: PTO characterization setup in laboratory

Starting with the generator voltage, it may be questioned the need to obtain such model if during field tests voltage data at the generator output is readily available. That model is necessary because voltage (available from field tests) will be modeled as a function of equivalent resistance (voltage divided by current, both available from field tests) and generator angular speed (not available during field tests). After obtaining that model, the mathematical relationship can be solved for the angular speed, thus obtaining a model for the generator speed as function of both voltage and equivalent electrical resistance. Table 6 shows the PTO voltage output as a function of load and RPM. It can be noticed that the bottom parameters are highlighted. The same issue that happened with the power supply when characterizing the generator happened during the PTO characterization, where the power supply output power was maximized. The highlighted numbers are extrapolations based on previous values. When the voltage output values are plotted, it can be seen (Figure 37) that the relationship between voltage and load follows a logarithmic equation.

$$V_{PTOm} = a_3(\omega)\, ln(R) + b_3(\omega) \tag{14}$$

Similar to the generator characterization, by plotting the coefficients a and b it was possible to derive a relationship between those coefficients and angular speed (Figure 38).

$$a_3(\omega) = 0.002\omega + 0.025 \tag{15}$$

$$b_3(\omega) = 0.0433\omega - 1.5383 \tag{16}$$

By substituting the coefficients in the voltage model and solving for ω:

$$\omega_m = (V_{PTOm} - 0.025\, ln(R) + 1.5383)/(0.002\, ln(R) + 0.0433) \tag{17}$$

For the PTO total efficiency (electrical power output over mechanical power input):

$$\varepsilon_{PTOm} = a_5(\omega)\, ln(R) + b_5(\omega) \tag{18}$$

$$a_5(\omega) = 3 \cdot 10^{-7}\omega^2 - 4 \cdot 10^{-4}\omega - 0.0209 \tag{19}$$

$$b_5(\omega) = -2 \cdot 10^{-6}\omega^2 + 2.4 \cdot 10^{-3}\omega + 0.0674 \tag{20}$$

Going back to field test data, it is possible to obtain the equivalent generator resistance by dividing the output voltage by the output current, utilizing the moving average dataset used for plotting power on Figure 26, Figure 27 and Figure 28. After obtaining that dataset and combining it with the voltage output data, the generator angular speeds (RPM) can be obtained. After obtaining the basis for all other models (generator angular speed and resistance) further data can be obtained.

By multiplying the generator speed by the gear ratios, the waterwheel angular speed (RPM) can be obtained, which allows for the TSR to be obtained. The generator torque can be obtained by applying its torque model. To infer the waterwheel power, the output electrical power is divided by the PTO total efficiency:

$$P_{ww} = P_e / \varepsilon_{PTOm}$$

For the wheel torque, its power is divided by its angular speed:

$$T_{ww} = \frac{P_{ww}}{\omega_{ww}} = \frac{P_{ww}}{\varphi \varphi_{cvt} \omega_m}$$

Where:

- φ: fixed gearbox ratio
- φ_{cvt}: CVT ratio

The PTO mechanical efficiency is obtained by dividing the total PTO efficiency by the generator efficiency:

$$\varepsilon_{PTO,mec} = \varepsilon_{PTOm} / \varepsilon_m$$

Lastly, for calculating Cp, the flow power is obtained by multiplying flow speed readings by $1/2\rho A$ and Cp is calculated by dividing the mechanical power of the waterwheel by the flow power:

$$C_p = \frac{P_{ww}}{P_F} = \frac{P_{ww}}{1/2\rho A U^3}$$

Where the area is calculated as the blade width times the blade underwater depth.

Figure 39 and Figure 40 show flow speed, Cp and TSR for both tests on 2/23 and 2/24 respectively. Figure 41 and Figure 42 show the overall system efficiency in converting flow power to electrical power. Figure 43 and Figure 44 show the PTO mechanical efficiency, from the rotor shaft of the waterwheel to the input shaft of the generator.

Table 6: PTO voltage output as function of generator angular speed and electrical resistance

		RPM						
		100	**200**	**300**	**400**	**500**	**600**	**700**
Load (Ω)	**NO LOAD**	4.3	10	15.1	21.2	26.4	32.5	37.6
	200	3.80	9.50	14.30	20.20	25.00	30.70	35.70
	180	3.70	9.40	14.40	20.10	25.00	30.70	35.60
	160	3.60	9.40	14.30	20.00	24.80	30.60	35.40
	140	3.60	9.40	14.20	20.00	24.80	30.50	35.50
	120	3.60	9.40	14.10	19.90	24.70	30.40	35.30
	100	3.60	9.30	14.10	19.90	24.50	30.30	35.10
	90	3.60	9.30	14.00	19.80	24.60	30.10	35.10
	80	3.60	9.30	14.00	19.80	24.50	30.20	34.90
	70	3.60	9.30	14.00	19.70	24.40	30.00	34.90
	60	3.50	9.20	13.90	19.60	24.30	29.90	34.60
	50	3.50	9.10	13.90	19.40	24.10	29.70	34.40
	40	3.50	9.10	13.80	19.30	24.00	29.50	34.00
	30	3.40	9.00	13.50	19.10	23.60	29.20	33.70
	20	3.30	8.80	13.40	18.80	23.30	28.60	33.00
	10	3.20	8.30	12.70	17.80	22.00	27.10	31.20
	8	3.10	8.10	12.40	17.50	21.70	26.60	31.63
	6	3.00	7.90	12.10	16.90	21.00	26.85	31.24
	4	2.99	7.95	12.16	17.06	21.14	26.36	30.68
	2	2.86	7.65	11.74	16.46	20.40	25.52	29.74

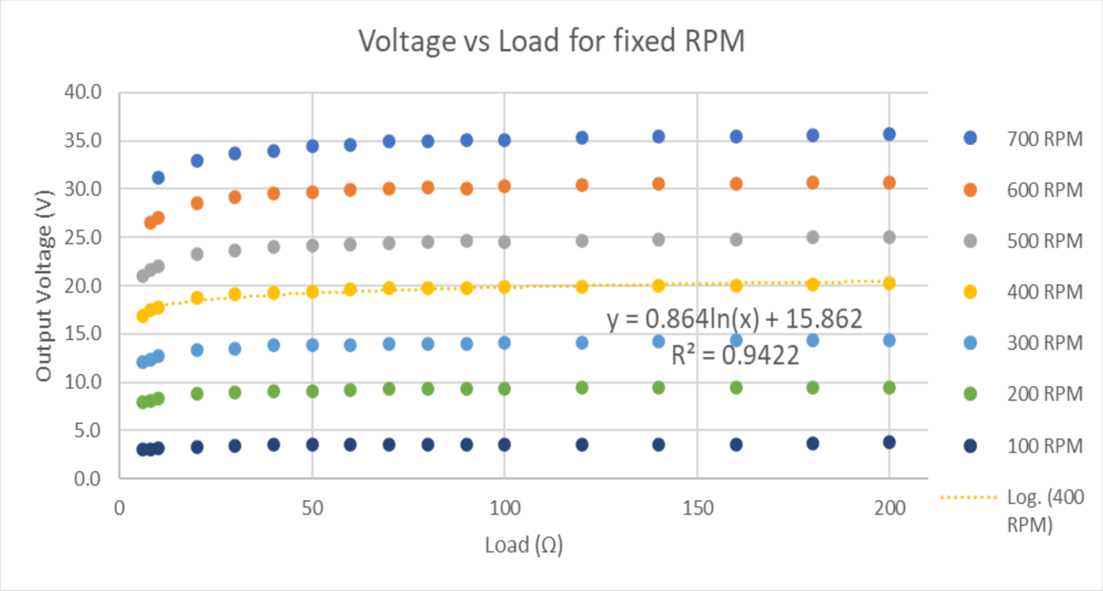

Figure 37: PTO output voltage as function of electrical load for fixed speeds

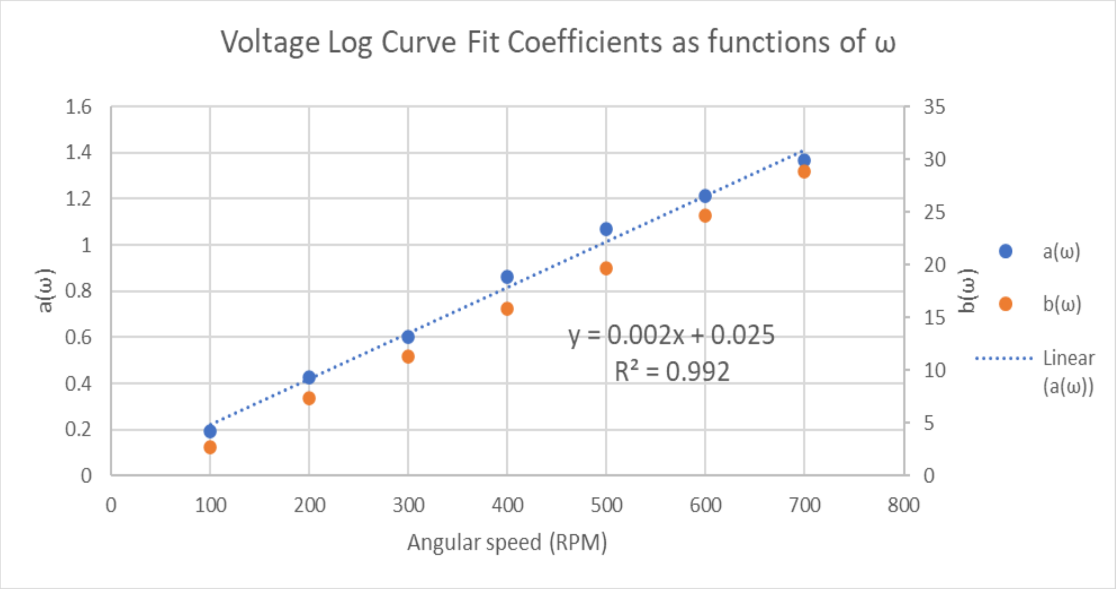

Figure 38: Voltage curve fit coefficients as a function of generator angular speed

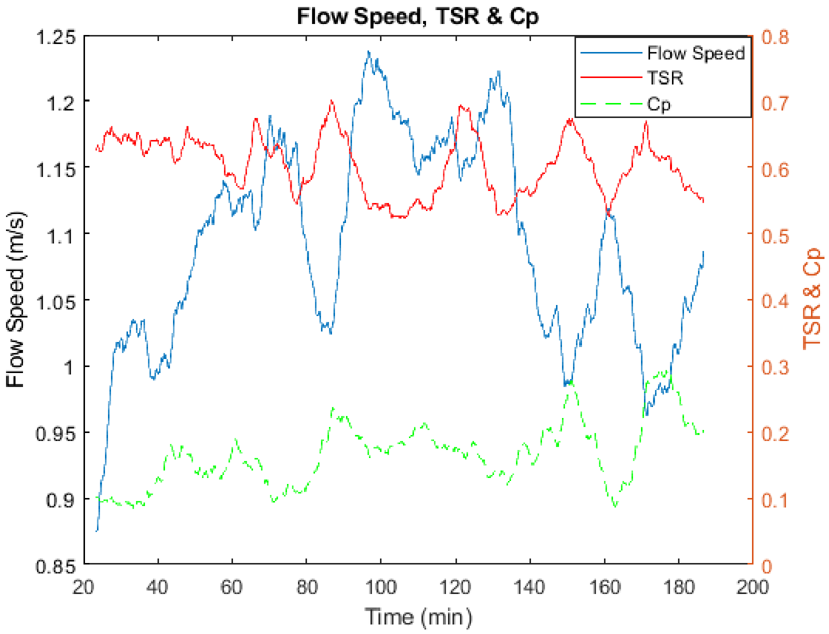

Figure 39: Flow speed, TSR and Cp over time – field test 2/23/2023

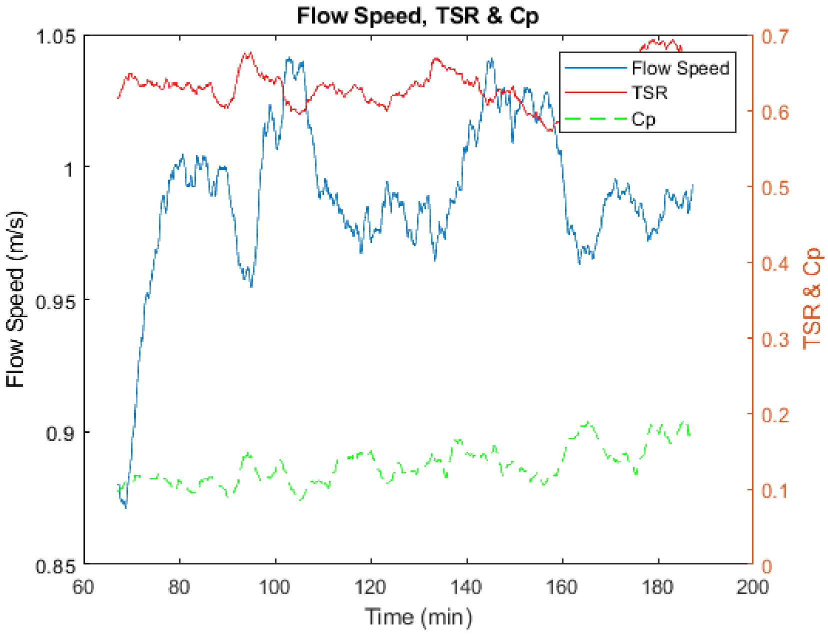

Figure 40: Flow speed, TSR and Cp over time – field test 2/24/2023

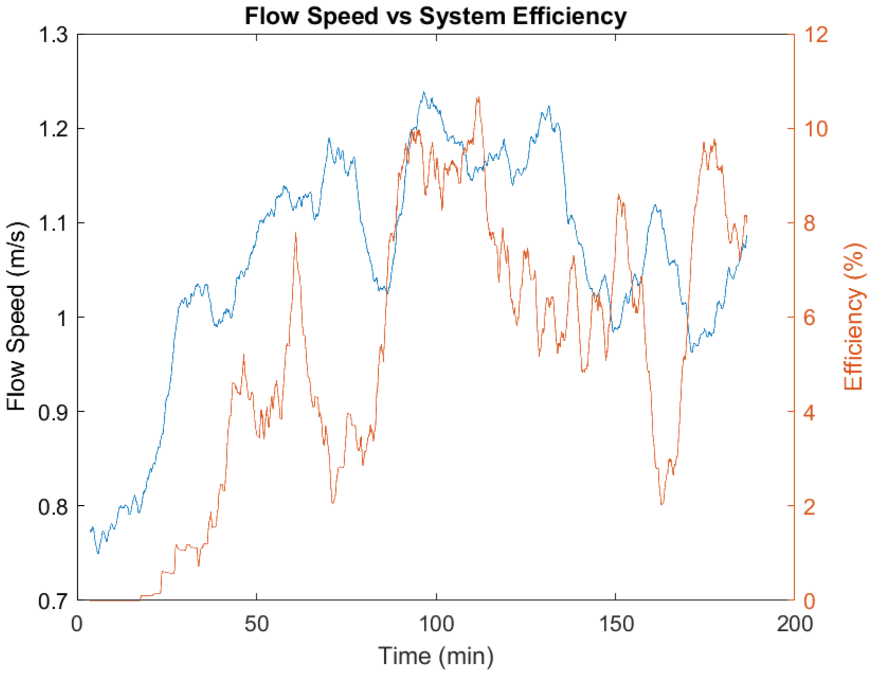

Figure 41: Flow speed and system efficiency over time – field test 2/23/2023

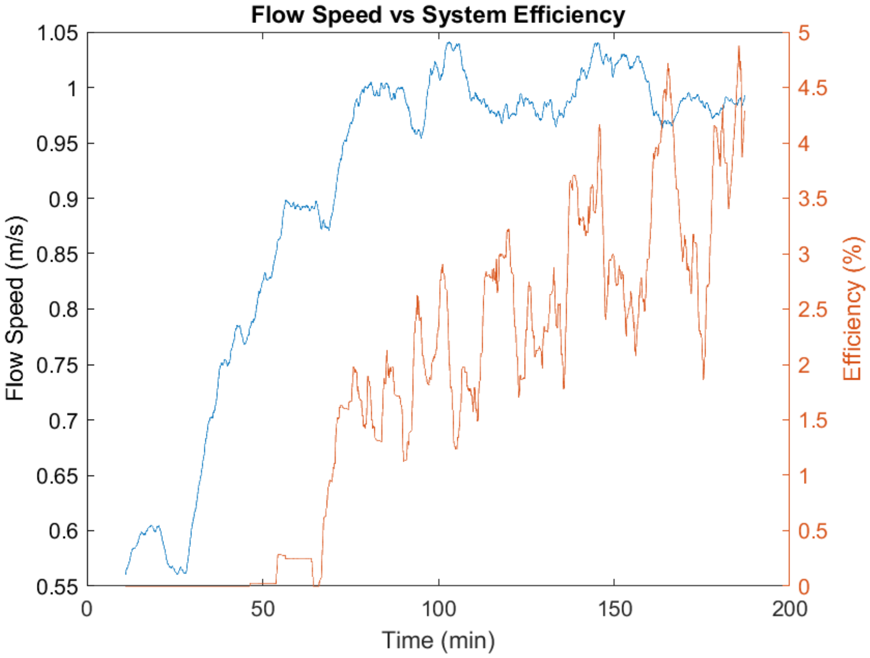

Figure 42: Flow speed and system efficiency over time – field test 2/24/2023

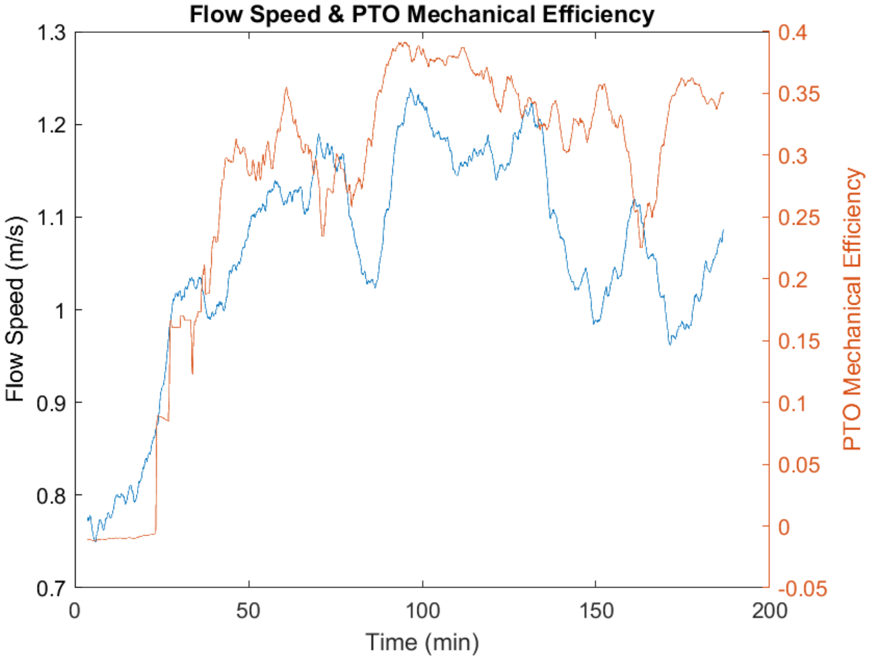

Figure 43: Flow speed and PTO mechanical efficiency over time – field test 2/23/2023

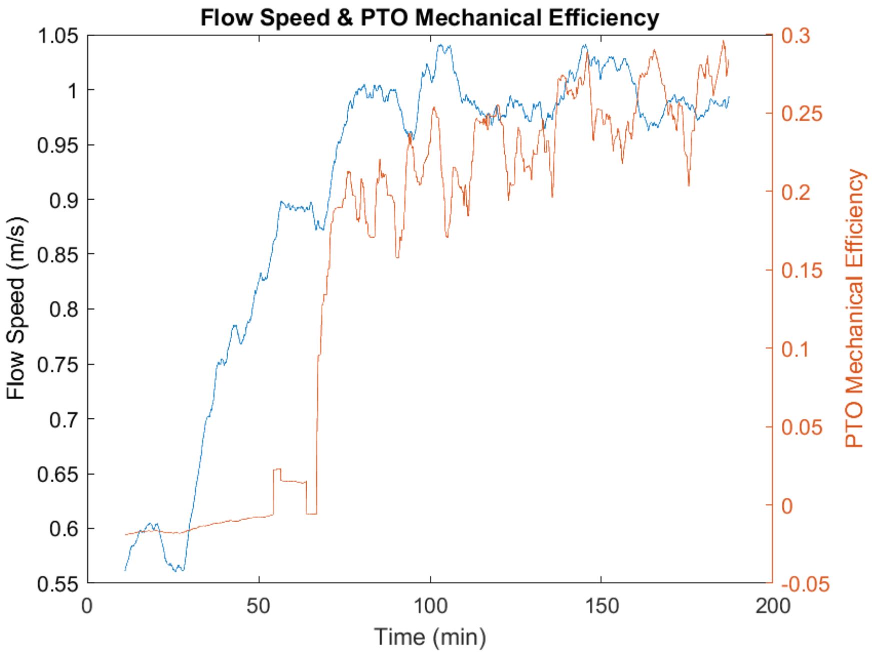

Figure 44: Flow speed and PTO mechanical efficiency over time – field test 2/24/2023

The results reveal important information about the system:

1) Communication between charge controller and PTO controller – if proper communication was established between the PTO controller and the charge controller, load monitoring in the system could regulate how much amperage was send to the battery, which would improve the efficiency of the system. Previous works on wind turbines and torque control show the importance of controlling the torque in the system to achieve optimal operating points. Therefore, work on that front will be detailed in later section.

2) PTO manufacturing precision – as show in Figure 43 and Figure 44 the mechanical efficiency of the PTO, which is a function of speed and load, does not surpass 40% at best. Due to the non-continuous nature of renewable energy sources, it is extremely important to have a high-efficiency PTO, so that power is efficiently utilized to produce electrical energy. It can be seen that, even with the issues

previously mentioned in points 1 and 2, a considerable amount of power is being dissipated through the PTO.

3) Proper sensors – encoders, flow speed and torque sensors are important to capture the behavior of the system reliably and are required. Flow speed, voltage and current sensors worked well, but there was no provision for torque sensors inside the system and the encoders did not work. The methods used for inferring additional data have errors associated and are limited in their precision.

3.2 Generator Sizing

To understand what generator power rating would be a match for the system, it is useful to start with the theoretical flow power. The following approach is mean to be an approximation and not an accurate calculation, with the goal of providing an estimation for the power specification of the generator. The flow power contained in a fluid moving across an area is given by:

$$P_f = 1/2\rho A U^3 \tag{21}$$

From field data, the maximum flow speed measured was 1.2m/s. With a wheel blade area and water density of $0.345m^2$ (full submergence) and $1000kg/m^3$:

$$P_f = 298\,W$$

Although the following assumption is assumed ideal and not realistic, by adopting the Betz limit for lift machines of 0.593, the maximum power that can be captured by the waterwheel is:

$$P_{ww} = C_{p,max} P_f \tag{22}$$

$$P_{ww} = 177\ W$$

While bench testing the PTO, it was found that its maximum mechanical efficiency was 58%. Thus, the total power available at the generator input shaft is:

$$P_g = \varepsilon_{PTOmech} P_{ww} \tag{23}$$

$$P_g = 102\ W$$

Therefore, a 100W generator fits the system well. The model chosen for next iterations is the Marsrock 600RPM, 100W, 24V PMSG. Figure 45shows the generator model. A comparative study between both generators will be detailed in later section.

Figure 45: Marsrock 100W generator sourced for next tests (Power Take Off Generators n.d.)

4. SYSTEM MODEL

Prior to detailing the system modeling, a literature survey shows several different studies yielding important results when it comes to waterwheel performance. The most useful studies pair CFD simulations with experiments to bridge the gap between computational and experimental analyses, obtain a model and apply it to simulate larger systems with similar characteristics.

(Olivier Cleynen 2018) performed experiments on a free-stream waterwheel comprised of 10 curved blades, followed by a CFD study to compare and validate computational results to experimental ones. After validating CFD simulations, 2D simulations of a full-size wheel were carried out, where power delivery and power coefficient throughout a blade stroke were analyzed. The study found out that, as the turbine depth increases, the blade peak power delivery increases and the power delivery peak increases. However, from a certain depth forward the blade power delivery becomes negative as the blade enters and exits the water, the power peak occurs earlier in the stroke and is more. The same effects were observed with increase in free-stream flow speed. Furthermore, it was also mentioned that, at high TSR values, a negative blade power delivery occurs when the blade nears its exit point unstable.

(S K Teoh 2022) investigated design parameters on self-floating waterwheels through laboratory testing utilizing PLA-manufactured turbines and a flow tank. The authors varied the number of blades (4, 6 and 8 blades) and the immersed radius ratio (ratio between the underwater portion of the blade over the entire wheel radius). The results indicated that curved blades yield higher power generation than flat blades. The same conclusion was drawn for increasing number of blades, with maximum power obtained for the 6-blade turbine configuration. Furthermore, although the 4-blade and 6-blade turbines increased their power output with increase in immersed radius ratio, the 8-blade turbine saw a decrease in its power output with increased depth due to the increase in the blade entry and exit splash. This might indicate that the optimal number of blades for a waterwheel lies between 6 or 7.

(Yucheng Liu 2012) developed an analytical model to predict the performance of a 16-blade waterwheel, followed by model validation via CFD. On that model the authors considered not only the driving force of the flow, but the resistive force of the flow behind the blades, considering the flow stationary behind the blades and utilizing the absolute angular speed of the blades to generate the resistive force. The analytical models agreed well with CFD simulations for lower angular speeds, but overestimated power output at higher angular speeds. The trigonometry used to calculate forces and torques contributed greatly to the development of the model in this work, which is detailed in later section.

(Quaranta 2018) conducted a review on stream waterwheels as a renewable energy supply, with performance assessment and design recommendations. The author concluded that the maximum expected C_p values range from 0.3 to 0.4 at a TSR 0f 0.5. It was also concluded that the waterwheel power can be improved by using curved blades, which better captures flow power. That finding could mean improved power coefficients for curved blades when compared to flat blades, which was also conclude by (S K Teoh 2022).

(Müller, Jenkins and Batten 2010) analyzed a 1:10 scale waterwheel under constrained flow regime (narrow channel with wall and bottom blockage effects) via in-lab experiments in a flow tank to quantify the turbine's efficiency as a function of the number of blades. Results show that a higher number of blades yields higher efficiency, with maximum power coefficient values of 0.42 at TSR ranging from 0.4 to 0.55. The authors also compared experimental efficiency results with theoretical calculations and found agreeable results at 8 blades, but the theoretical model overestimates efficiencies for higher blade numbers.

(Scott Baker 2015) performed flow tank experiments on a 8-flat-blade waterwheel supported by a stationary floating barge at a relatively shallow depth such that bottom effects affected turbine performance. The researchers also varied the trim angle of the barge to quantify the change in flow speed across the barge and the power produced by the turbine for each trim. Results showed that the 0° trim yielded the highest power output due to the constant high flow speed across the barge, while 1° and 2° trims caused an immediate slow down followed by acceleration of the flow across the barge, yielding lower power outputs. The investigation also quantified the current velocity at free stream, barge intake, turbine intake and turbine outlet under different turbine speeds, which concluded that the flow speed at the barge intake, turbine intake and turbine outlet decreased linearly with decrease in turbine speed. Finally, the authors investigated the effects of flow speed in wheel power production, ranging from 0.75 m/s to 2.75 m/s, and found maximum efficiency at a TSR of 0.7 between 1.25 m/s and 2.5 m/s. Efficiencies were lower for flow speeds below 1m/s and above 2.5 m/s.

(Al-Dabbagh 2018) investigated the performance of stream, 12-blade Waterwheel equipped with curved blades, by means of CFD techniques (Ansys-CFX package), utilizing the Reynolds stress-omega transport turbulence model at flow speeds of 1m/s and 2 m/s. That model is capable of analyzing the flow around the turbine and account for flow separation and vortices, making it suitable for the study. The blades were 0.5m tall, with a radius of curvature of 0.33m and a wheel diameter of 3m. The turbine's behavior was simulated for TSR values of 0.2, 0.4, 0.6, 0.8 and 0.9. The results showed a maximum power coefficient of 0.15 at a TSR of 0.42 and flow speed of 2m/s. All other power coefficient values for both flow speeds were similar.

(Nguyen Manh Hung 2018) conducted CFD and experimental studies on a waterwheel equipped with 3, 6, 9, 11 and 12 flat blades and solid disk plates on the laterals of the turbine, decreasing sideways flow. The turbine had a 1.5m diameter, 0.9m width and a bottom clearance of 0.15m. The setup also included local flow speed augmentation profiles to locally increase flow speed and decrease environmental effects of the turbine in river beds. For the CFD study, a three-dimensional model of the turbine within a domain of flow fields was elaborated. Mesh refinement tests were caried out utilizing a tetrahedral mesh to determine minimum number of mesh elements to preserve accuracy and save computational time. The study found that, although the experimental results for the 3-blade turbine found maximum C_p at a TSR of 0.45, all other tests, both experimental and numerical, found maximum power coefficients at a TSR of 0.4. Furthermore, the 6-blade turbine shows the best performance, with a C_p value of 0.424, followed by the 9-blade turbine ($C_p = 0.41$), 11-blade turbine ($C_p = 0.387$), 12-blade turbine ($C_p = 0.373$) and 3-blade turbine ($C_p = 0.3$).

4.1 Waterwheel Model

As previously mentioned, the ability to maintain a turbine operating at its optimal TSR is achieve through torque control, which regulates the torque load on the system based on the operation point the turbine is at and its current torque being produced, as shown in Eq. 3. It is important to highlight that, since the system has a varying ratio due to the CVT, the equivalent inertia will vary accordingly and will also be modeled. The detailed model is built based on the drag model shown next. The drag model is analogous to the waterwheel, since the shielded portion of the model represents the blades of the wheel out of the water, under no action of flow speed. Moreover, the difference between flow medium is considered to be reflected in its density solely and the immersion depth is neglected at early stages of model development, being considered after a basic model is built. A detailed system model is under development and it begins by considering a basic model for drag machines (Manwell, Mcgowan and Rogers 2009), shown in Figure 46.

$$F_B = 1/2 \rho A C_d (U - \omega_r r)^2 \tag{24}$$

Where:

- F_B: force acting in one blade
- A: blade area perpendicular to flow
- C_d: blade drag coefficient

Torque can be calculated as:

$$T_B = F_B r' \tag{25}$$

$$T_B = 1/2\rho A C_d r'(U - \omega_r r)^2 \tag{26}$$

Where r' is the point where the force is applied, which is smaller the blade radius r.

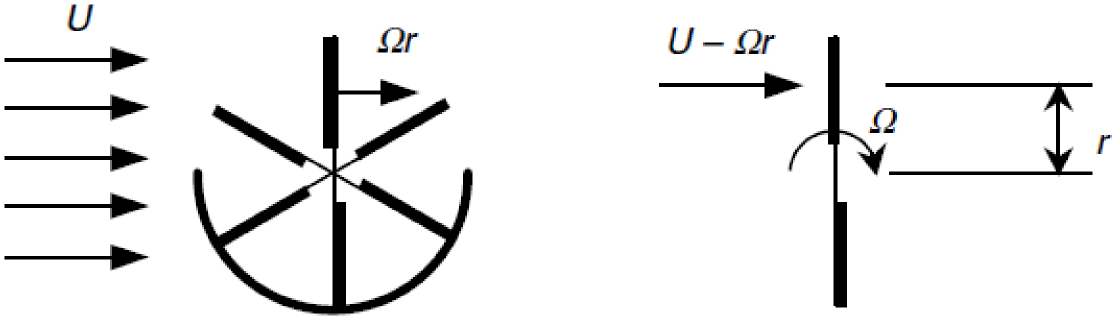

Figure 46: Simplified drag machine model (Manwell, Mcgowan and Rogers 2009)

Power is given by:

$$P_B = T_B.\omega_r \tag{27}$$

$$P_B = \frac{1}{2}.\rho.A.C_d.r'.\omega_r(U - \omega_r.r)^2 \tag{28}$$

Maximum power can be found by deriving the expression for power in one blade by the angular velocity of the blade and equating to zero:

$$\frac{dP_B}{d\omega_r} = \rho.A.C_d.r'(U - \omega_r.r)(-r)\omega_r + \frac{1}{2}\rho.A.C_d.r'(U - \omega_r.r)^2 = 0$$

$$\omega_{r,opt} = U/3r \tag{29}$$

Using $\lambda = \omega_r . r/U$:

$$\lambda_{opt} = 1/3 \tag{30}$$

For a simplified model of a drag machine, the optimal TSR is 1/3 or 33.33% of the flow speed. That result allows for estimation of an expression for maximum torque, power and Cp of the wheel as:

$$T_{B,max} = 1/2. \rho. A. Cd. r'(U - U/3)^2$$

$$T_{B,max} = 2/9 \rho. A. r'. Cd. U^2 \tag{31}$$

$$P_{B,max} = 2/27\ \rho. A. Cd(r'/r)U^3 \tag{32}$$

$$C_{P,max} = \frac{P_{B,max}}{P_{flow}} = \frac{2/27\ \rho. A. Cd(r'/r)U^3}{1/2\rho. A. U^3}$$

$$C_{P,max} = 4/27 C_d(r'/r) \tag{33}$$

This result shows that the higher the drag coefficient on a blade, the more power it can convert, which is obvious given that the turbine works based on the drag of its blades. It also shows that the further away from the center the flow force is applied, the higher the efficiency, which is also obvious. For a long, semi-circular plate, the drag coefficient is 2.3 (Engineers Edge n.d.). Since the blades' section of the waterwheel is not semi-circular (it has approximately 120° as opposed to 180° for a semi-circular section), the drag coefficient is assumed to be close to that of a flat plat, or 1.2 (Nasa n.d.). The blade area is 0.345 m² and assuming that the force is applied at the tip of the blade (purely for estimation purposes), the maximum Cp is:

$$C_{P,max} = 4/27 \cdot 1.2 \cdot (r/r)$$

$$C_{P,max} = 0.18$$

With a very simplified model of the waterwheel, it is possible to arrive at a maximum Cp of approximately 0.2. The comparison between this maximum theoretical value with the Cp values obtained during experiments leads to the belief that a more accurate model of the waterwheel can lead to higher and more accurate values of maximum Cp.

To arrive at a more detailed model, it is useful to start looking at the equation for the force on the blade. For this approach it is assumed that, although the waterwheel blades are curved, the area considered is the are perpendicular to the flow, and any gain in performance relative to a flat blade is reflected in the drag coefficient of the blade. If the flat plate moved parallel to the flow speed only, the expression for the total force would be give as Eq. (24). However, in reality the tangential speed of each blade element varies linearly with the blade radius. To begin further exploring the forces and torques acting on the turbine, it is useful to consider a waterwheel under full blade submergence and a single blade at 90° with respect to incoming flow. Figure 47 shows the basic geometry and parameters for the blade perpendicular to the flow and an infinitesimally small blade element dr.

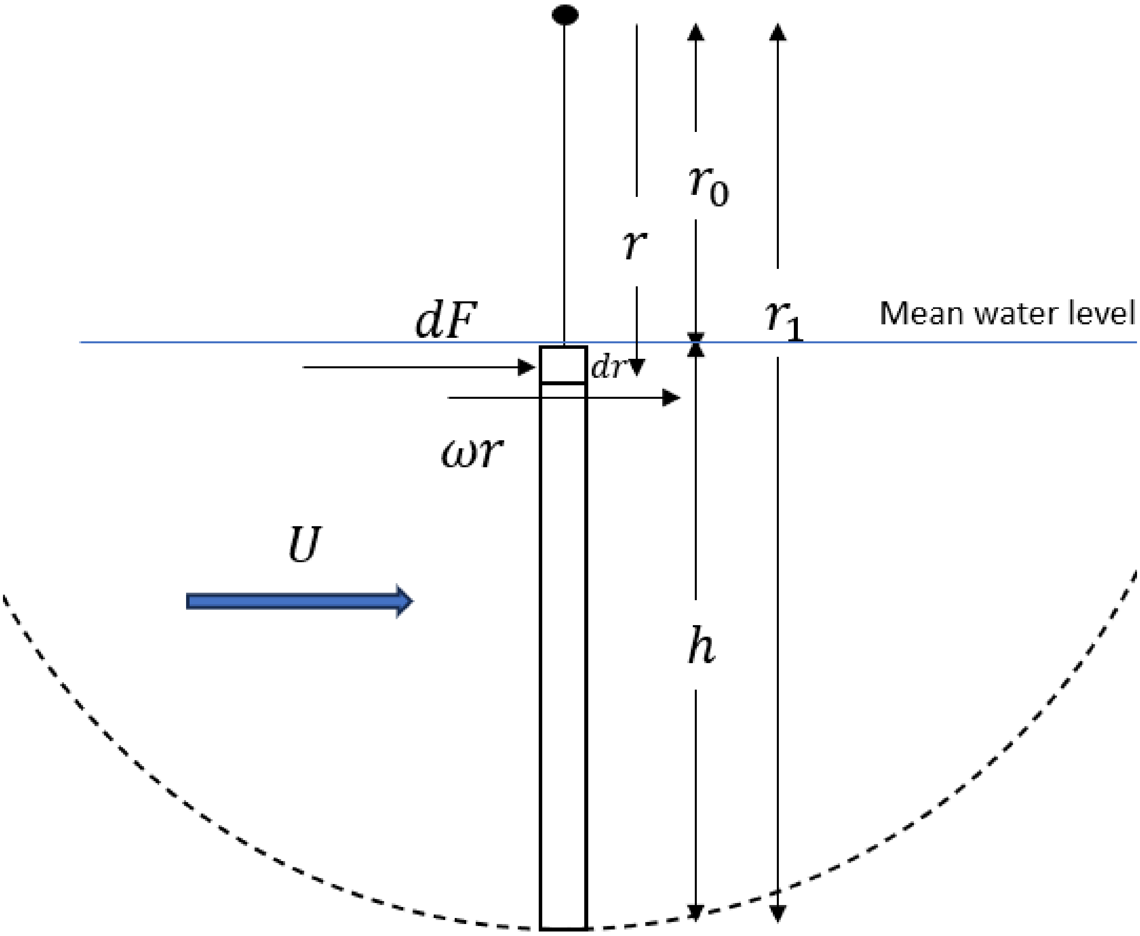

Figure 47: Flat blade and infinitesimal element

Based on the drag model, the total force caused by the uniform flow acting on the blade can be written as:

$$dF = \frac{1}{2}\rho b C_d (U - \omega_r r)^2 dr \tag{34}$$

Torque can then be written as:

$$dT_B = dF_B r \tag{35}$$

$$T_B = 1/2\ \rho b C_d \int_{r_0}^{r_1} (U - \omega_r r)^2 r dr \tag{36}$$

By solving the above equation and taking the blade radius ratio as $\gamma = r_0/r_1$:

$$T_B = \frac{\rho b C_d r_1^2 U^2}{24}[3\lambda^2(1-\gamma^4) - 8\lambda(1-\gamma^3) + 6(1-\gamma^2)] \tag{37}$$

Torque is caused by the force induced by the flow on the blade. In other words, if the total force on the blade was converted to a concentrated force, it would be applied at a specific point at a distance r' from the center. By dividing torque by force and looking at the ratio between the distance to the center of the blade where the force is applied and the blade radius as the TSR increases, it can be noticed that, as the blade rotates faster, the point of application of the concentrated force gets closer to the base of the blade (Figure 48).

:

$$r' = T_B/F_B \tag{38}$$

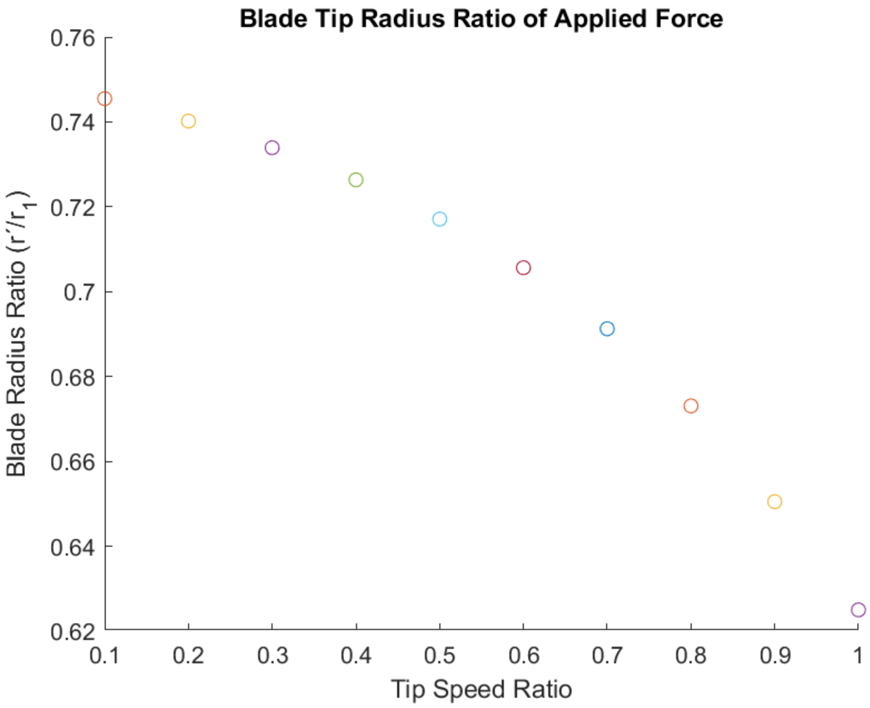

Figure 48: Position ratio of point of application of equivalent concentrated force on the blade

To calculate the blade power, torque is multiplied by the angular velocity of the rotor:

$$P_B = T_B\omega_r = \frac{T_B\lambda U}{r_1}$$

Substituting for T_B using Equation (35):

$$\mathrm{P}_B = \frac{\rho b C_d r_1 \lambda U^3}{24}[3\lambda^2(1-\gamma^4) - 8\lambda(1-\gamma^3) + 6(1-\gamma^2)] \tag{39}$$

The power coefficient of the blade can be found by dividing Equation (39) by the available flow power:

$$C_P = P_{ww}/P_F$$

$$C_p = \frac{C_d\lambda}{12(1-\gamma)}[3\lambda^2(1-\gamma^4) - 8\lambda(1-\gamma^3) + 6(1-\gamma^2)] \tag{40}$$

Therefore, the power coefficient of the blade is only dependent on the drag coefficient, the tip speed ratio and the blade ratio, which is the ratio between the radius of the base of the blade and the tip of the blade. The following figures display the power characteristics of one blade at 90° with respect to the flow speed, and were obtained taking the drag coefficient of a flat plate ($C_d = 1.2$). Figure 49 illustrates the Cp surface, with increase in performance as the blade area decreases (blade ratio approaches 1). Figure 50 shows the blade power surface plot, with maximum power available when the blade area is maximum (blade ratio is zero).

Thus, the most efficient blade geometry possible is that with the least amount of area, yielding highest C_P. However, that configuration produces no power, since there is no area for the flow to act upon. The maximum power output happens when the blade ratio is zero, which means that the blade starts at the center of the wheel. To find the maximum C_p and optimal TSR, the C_p equation can be derived with respect to TSR and gamma and set to zero. However, the calculations are not trivial and the optimal parameters were found instead via numerical evaluation using MATLAB. For the current wheel, with the radius of the tip of the blade $r_1 = 0.5\ m$ and radius of the base of the blade $r_0 = 0.25\ m$ (which gives $\gamma = 0.5$) and taking a drag coefficient of 1.2, the maximum C_P is approximately 0.17 and occurs at $\lambda_{opt} = 0.44$. Figure 51 shows the blade C_p plot with the abovementioned parameters.

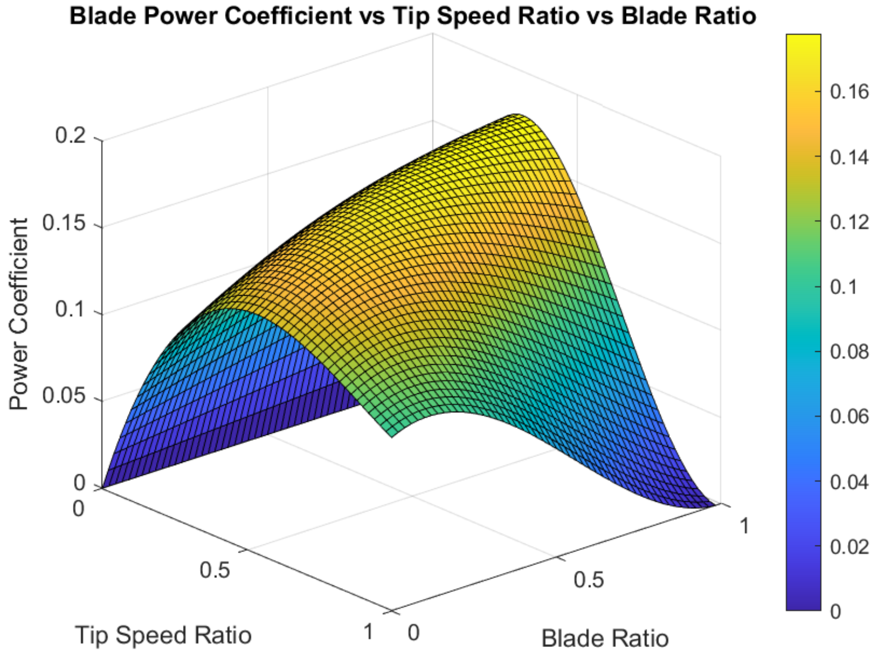

Figure 49: Blade power coefficient as a function of TSR and blade ratio

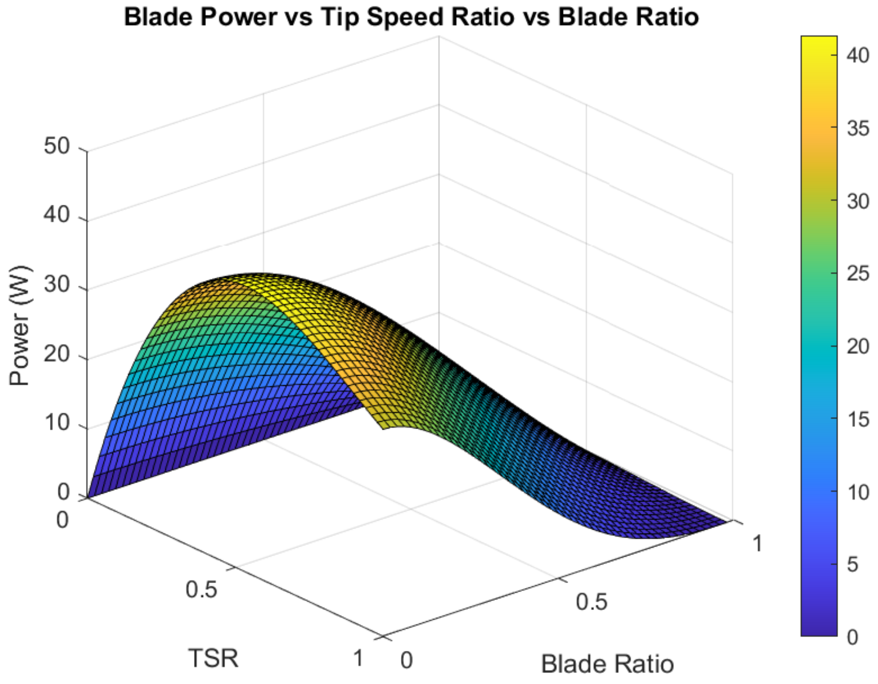

Figure 50: Blade power as a function of tip speed ratio and blade ratio

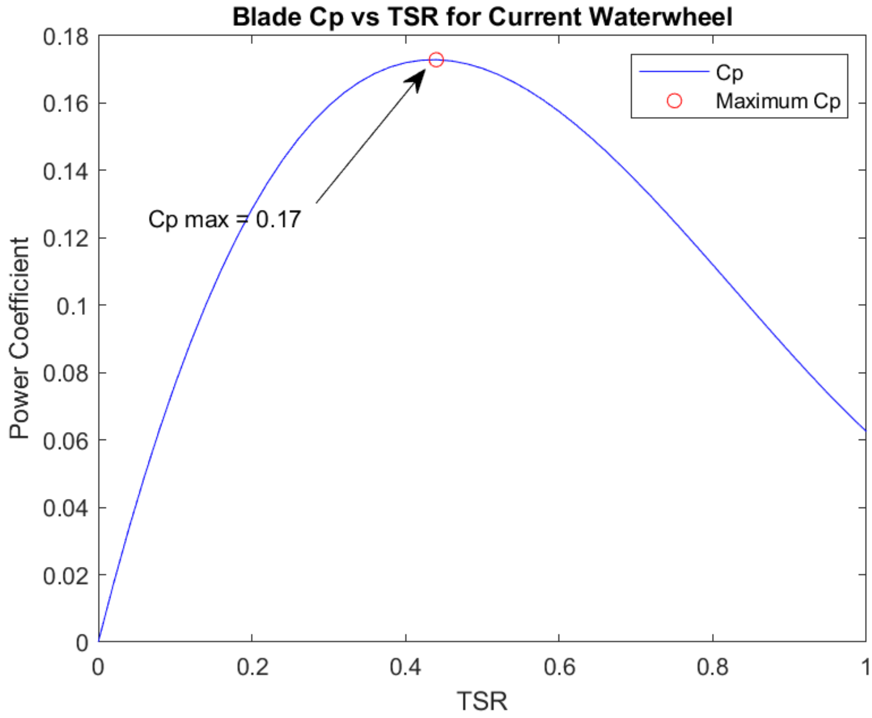

Figure 51: Blade Cp vs TSR curve for current system's blade ratio

After an initial assessment of the forces and torque exerted by the flow on the blade of the waterwheel, it is now time to consider a broader model, which takes into account both the submerged depth of the wheel and the angle of the blade during the stroke. More details on the derivation of that model can be found on Appendix I.

As an illustration of the results yielded by the model, Figure 52 and Figure 53 show the waterwheel's Cp and torque-power plots for the following parameters:

- Blade tip radius: 0.5 m
- Blade base radius: 0.25 m
- Blade width: 1.4m
- Flow speed: 1 m/s
- Drag coefficient: 2
- Number of blades: 7
- Underwater depth: 0.3 m

The results show that for a TSR close to one, the wheel needs external power to move at that speed, shown by the negative values for Cp, torque and power near a TSR of 1. This can be expected at greater depths relative to the radius, since at certain point of the stroke some blades have a close-to-perpendicular relative motion with the flow speed. If, for instance, the wheel was submerged at a depth equal to its radius, the blades near the water surface would have a perpendicular motion with respect to the flow passing through. Assuming a waterwheel is operating at a depth equal to its radius and looking at a blade positioned at nearly 180°, the flow component is zero and the resultant torque on that blade opposes the flow-induced torque.

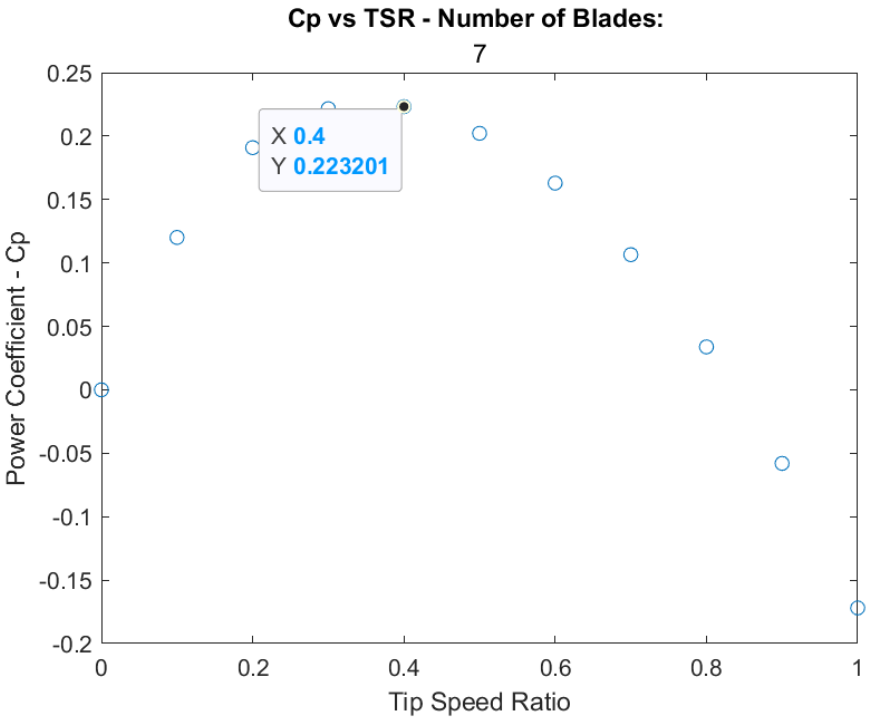

Figure 52: Waterwheel's model-based power coefficient vs TSR

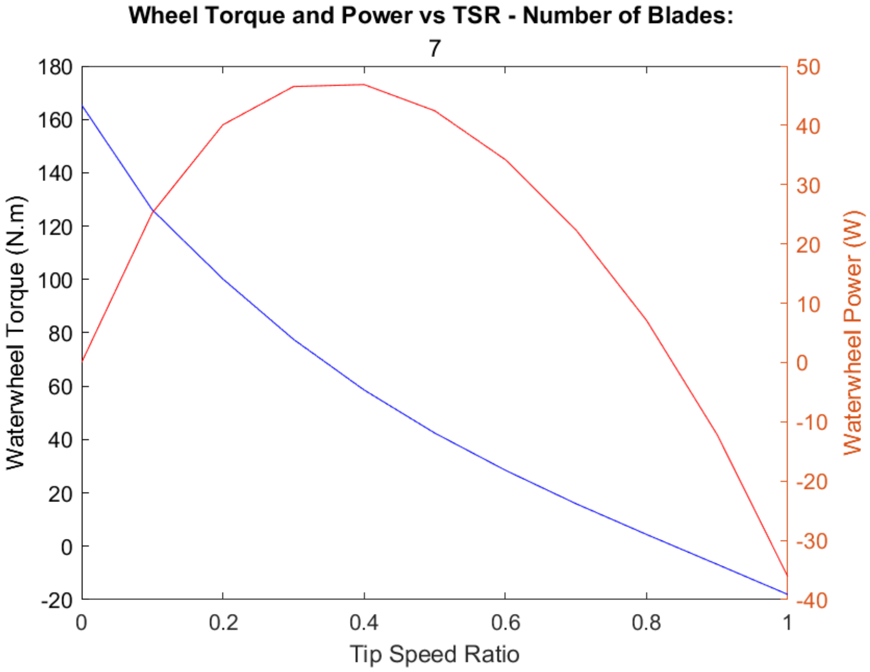

Figure 53: Waterwheel's model-based torque and power characteristics vs TSR

If the wheel rotates at higher speeds relative to the flow speed, those resistive torques increase with the square of the speed and cause the effect observed in the model when TSR nears 1. Based on the model results, the maximum power output occurs at a TSR of 0.4, which was used as a setpoint for simulations and subsequent bench and field tests.

Although this model is a simplified representation of the behavior of the waterwheel, it captures the essential characteristics of its performance and is implemented in the Simulink simulation shown next. The model is also used to program the waterwheel torque characteristics on the DC motor of the test bench. Figure 54 shows the resultant torque model.

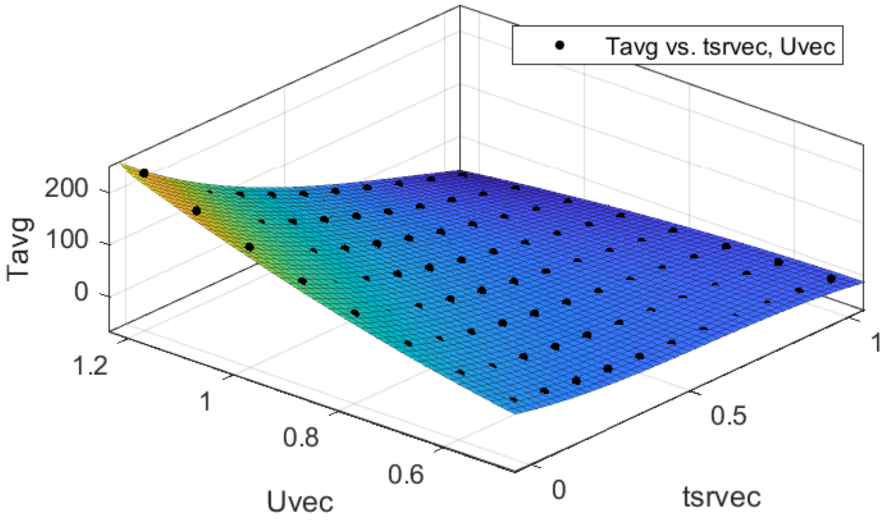

Figure 54: Waterwheel torque surface and fitted curve as a function of flow speed (Uvec) and TSR (tsrvec)

After plotting the torque response surface at discrete points for flow speed and TSR, a polynomial was fit for the 7-blade configuration. The resultant average waterwheel torque equation, represented by Figure 54, is given by:

$$T_{ww,avg} = -120.8\lambda^3 + 164.7U_0\lambda^2 - 207.8U_0^2\lambda + 123\lambda^2 - 135.9U_0\lambda + 142.8U_0^2 - 16.32\lambda + 19.86U_0 - 2.672 \quad (41)$$

4.2 New Generator Characterization and Model

The generator characterization consisted of obtaining its resistive torque and output voltage as functions of the generator speed and current demand by varying the rpms under different resistances. Speeds ranged from 100rpm to 850rpm while resistances ranged from 100Ω to 2.8Ω. The setup was comprised of a 336W power supply (1), a DC motor and motor controller (Oriental Motor BLVM640N-GFS and gear head Oriental Motor GFS6G100FR; motor controller Oriental Motor BLVD40NM) connected to a 35:1 gearbox (Sure Gear PGD 110-35A5) followed by the 3-phase Marsrock 100W PMG. Two encoders were placed at the DC motor shaft and generator shaft and two torque sensors (Interface T8-50-A1A and Interface T8-10-A1A) were placed between the DC motor and gearbox and between the gearbox and generator. Two voltage meters were connected to the first and second torque sensors as a second measurement of torque via their output voltage. The generator output was connected to a bridge rectifier and its output was connected to different sets of resistances to generate varying voltages and currents. A multimeter was connected to the output of the rectifier to measure output voltage and current. A Teensy board with a dedicated power supply was used to gather torque readings and rpm readings. Figure 55 shows the basic hardware setup, while Figure 56 shows the resistances setup on the generator side.

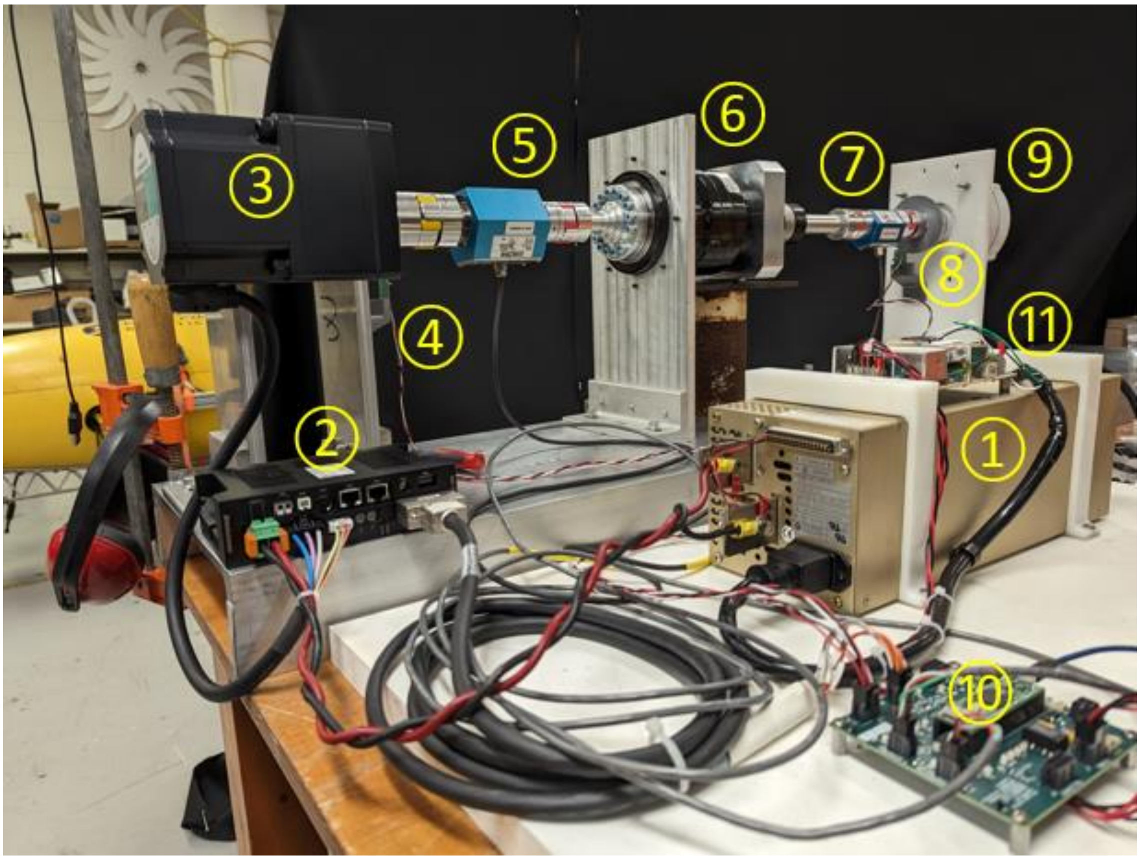

Figure 55: Generator characterization hardware setup

The numbering represents the following components:

1. Power supply
2. DC motor controller
3. DC motor
4. DC motor encoder
5. DC motor torque sensor
6. Gearbox
7. Generator torque sensor
8. Generator encoder
9. Generator
10. Teensy

11. Teensy power supply

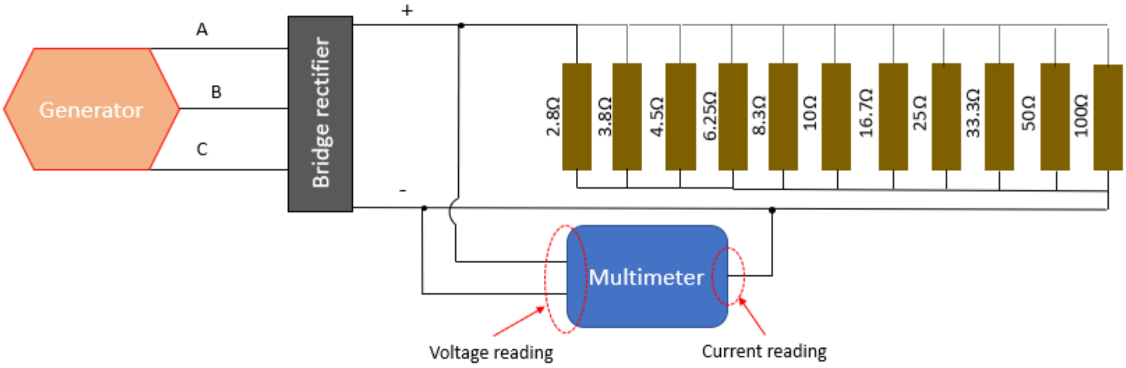

Figure 56: Resistances layout on generator side

For each speed and resistance setpoint, generator voltage, resistive torque, current and power output were measured. Two functions were obtained for the output voltage and resistive torque in terms of current demand and rpms. Those models are valid only for $2.8\,\Omega \leq R \leq 100\,\Omega$. The equation obtained for voltage output is of the form:

$$V(I,\omega_g) = K_V(\omega_g)I_{out} + B_V(\omega_g)$$

Where:

$$K_V(\omega_g) = -4\cdot 10^{-6}\omega_g^2 + 2.2\cdot 10^{-3}\omega_g - 5.0667$$

$$B_V(\omega_g) = 0.058\omega_g$$

A similar approach is used for obtaining the generator resistive torque as a function of the demanded current and the generator rpm.

$$T_g = K_T(\omega_g)I_{out} + B_T(\omega_g)$$

Where:

$$K_T(\omega_g) = -1 \cdot 10^{-4}\omega_g + 0.5526$$

$$B_T(\omega_g) = 2 \cdot 10^{-4}\omega_g + 0.0105$$

Figure 57shows the generator power output for each pair of speed-resistance setpoint, followed by resistive torque and current demand plots in Figure 58 and Figure 59. It can be noticed that, for the same resistive torque, there are several combinations of resistance and generator speed that yield the same result. For example, if the system requires a resistive torque of 0.4 N.m several combinations will yield that torque number. However, the more the rpms increase, the higher the power produced. So, for the example value above, the best-case scenario would be to maintain the generator speed at 845 rpm and bring the resistance to approximately 100 Ω (that is achieved by manipulating the current demand). Therefore, it can be concluded that, regardless of the requested resistive torque, the generator has to rotate as fast as possible to generate maximum power. Although that conclusion seems obvious, it will play an important role when dealing with the controls aspect of the system.

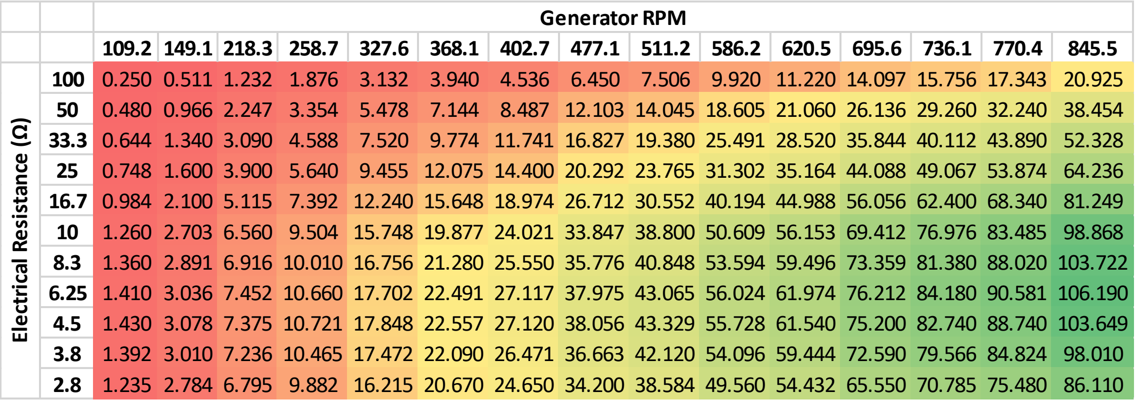

		Generator RPM														
		109.2	**149.1**	**218.3**	**258.7**	**327.6**	**368.1**	**402.7**	**477.1**	**511.2**	**586.2**	**620.5**	**695.6**	**736.1**	**770.4**	**845.5**
Electrical Resistance (Ω)	**100**	0.250	0.511	1.232	1.876	3.132	3.940	4.536	6.450	7.506	9.920	11.220	14.097	15.756	17.343	20.925
	50	0.480	0.966	2.247	3.354	5.478	7.144	8.487	12.103	14.045	18.605	21.060	26.136	29.260	32.240	38.454
	33.3	0.644	1.340	3.090	4.588	7.520	9.774	11.741	16.827	19.380	25.491	28.520	35.844	40.112	43.890	52.328
	25	0.748	1.600	3.900	5.640	9.455	12.075	14.400	20.292	23.765	31.302	35.164	44.088	49.067	53.874	64.236
	16.7	0.984	2.100	5.115	7.392	12.240	15.648	18.974	26.712	30.552	40.194	44.988	56.056	62.400	68.340	81.249
	10	1.260	2.703	6.560	9.504	15.748	19.877	24.021	33.847	38.800	50.609	56.153	69.412	76.976	83.485	98.868
	8.3	1.360	2.891	6.916	10.010	16.756	21.280	25.550	35.776	40.848	53.594	59.496	73.359	81.380	88.020	103.722
	6.25	1.410	3.036	7.452	10.660	17.702	22.491	27.117	37.975	43.065	56.024	61.974	76.212	84.180	90.581	106.190
	4.5	1.430	3.078	7.375	10.721	17.848	22.557	27.120	38.056	43.329	55.728	61.540	75.200	82.740	88.740	103.649
	3.8	1.392	3.010	7.236	10.465	17.472	22.090	26.471	36.663	42.120	54.096	59.444	72.590	79.566	84.824	98.010
	2.8	1.235	2.784	6.795	9.882	16.215	20.670	24.650	34.200	38.584	49.560	54.432	65.550	70.785	75.480	86.110

Figure 57: Generator power plot

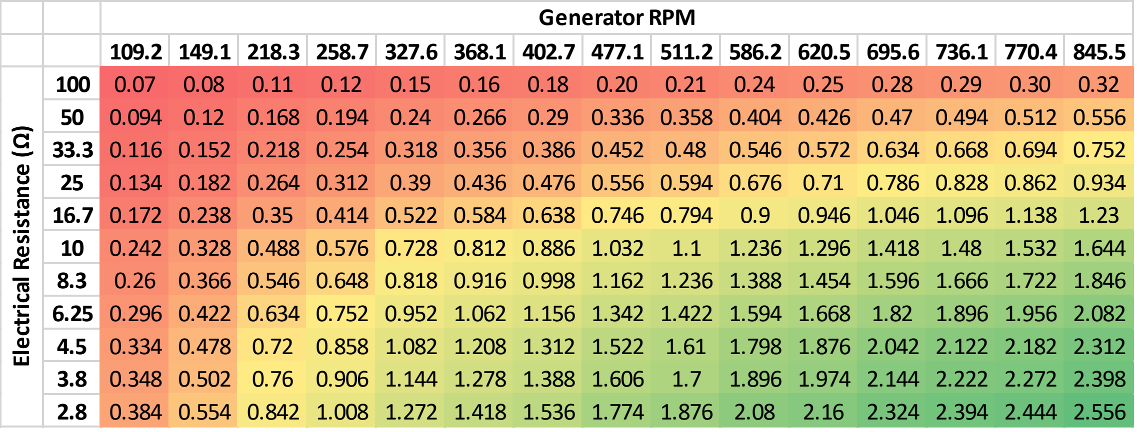

		Generator RPM														
		109.2	**149.1**	**218.3**	**258.7**	**327.6**	**368.1**	**402.7**	**477.1**	**511.2**	**586.2**	**620.5**	**695.6**	**736.1**	**770.4**	**845.5**
Electrical Resistance (Ω)	**100**	0.07	0.08	0.11	0.12	0.15	0.16	0.18	0.20	0.21	0.24	0.25	0.28	0.29	0.30	0.32
	50	0.094	0.12	0.168	0.194	0.24	0.266	0.29	0.336	0.358	0.404	0.426	0.47	0.494	0.512	0.556
	33.3	0.116	0.152	0.218	0.254	0.318	0.356	0.386	0.452	0.48	0.546	0.572	0.634	0.668	0.694	0.752
	25	0.134	0.182	0.264	0.312	0.39	0.436	0.476	0.556	0.594	0.676	0.71	0.786	0.828	0.862	0.934
	16.7	0.172	0.238	0.35	0.414	0.522	0.584	0.638	0.746	0.794	0.9	0.946	1.046	1.096	1.138	1.23
	10	0.242	0.328	0.488	0.576	0.728	0.812	0.886	1.032	1.1	1.236	1.296	1.418	1.48	1.532	1.644
	8.3	0.26	0.366	0.546	0.648	0.818	0.916	0.998	1.162	1.236	1.388	1.454	1.596	1.666	1.722	1.846
	6.25	0.296	0.422	0.634	0.752	0.952	1.062	1.156	1.342	1.422	1.594	1.668	1.82	1.896	1.956	2.082
	4.5	0.334	0.478	0.72	0.858	1.082	1.208	1.312	1.522	1.61	1.798	1.876	2.042	2.122	2.182	2.312
	3.8	0.348	0.502	0.76	0.906	1.144	1.278	1.388	1.606	1.7	1.896	1.974	2.144	2.222	2.272	2.398
	2.8	0.384	0.554	0.842	1.008	1.272	1.418	1.536	1.774	1.876	2.08	2.16	2.324	2.394	2.444	2.556

Figure 58: Generator resistive torque plot

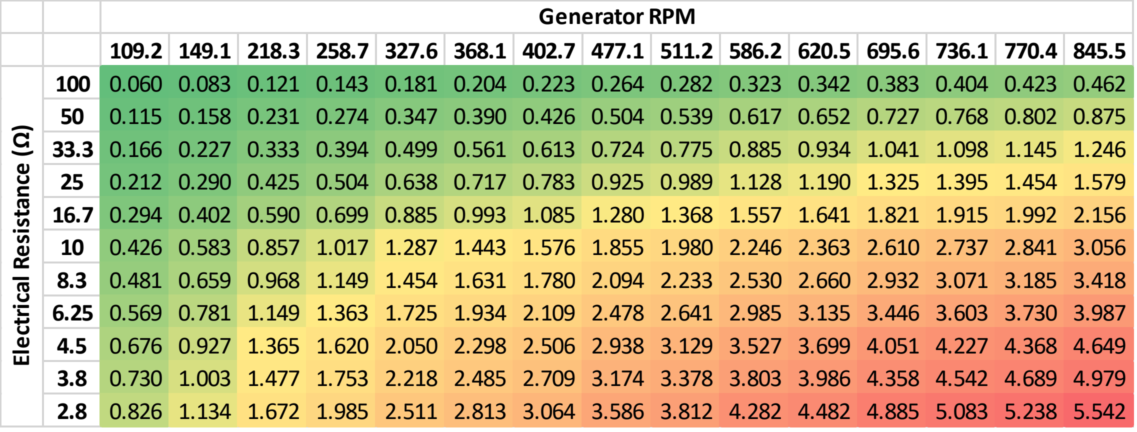

		Generator RPM														
		109.2	**149.1**	**218.3**	**258.7**	**327.6**	**368.1**	**402.7**	**477.1**	**511.2**	**586.2**	**620.5**	**695.6**	**736.1**	**770.4**	**845.5**
Electrical Resistance (Ω)	**100**	0.060	0.083	0.121	0.143	0.181	0.204	0.223	0.264	0.282	0.323	0.342	0.383	0.404	0.423	0.462
	50	0.115	0.158	0.231	0.274	0.347	0.390	0.426	0.504	0.539	0.617	0.652	0.727	0.768	0.802	0.875
	33.3	0.166	0.227	0.333	0.394	0.499	0.561	0.613	0.724	0.775	0.885	0.934	1.041	1.098	1.145	1.246
	25	0.212	0.290	0.425	0.504	0.638	0.717	0.783	0.925	0.989	1.128	1.190	1.325	1.395	1.454	1.579
	16.7	0.294	0.402	0.590	0.699	0.885	0.993	1.085	1.280	1.368	1.557	1.641	1.821	1.915	1.992	2.156
	10	0.426	0.583	0.857	1.017	1.287	1.443	1.576	1.855	1.980	2.246	2.363	2.610	2.737	2.841	3.056
	8.3	0.481	0.659	0.968	1.149	1.454	1.631	1.780	2.094	2.233	2.530	2.660	2.932	3.071	3.185	3.418
	6.25	0.569	0.781	1.149	1.363	1.725	1.934	2.109	2.478	2.641	2.985	3.135	3.446	3.603	3.730	3.987
	4.5	0.676	0.927	1.365	1.620	2.050	2.298	2.506	2.938	3.129	3.527	3.699	4.051	4.227	4.368	4.649
	3.8	0.730	1.003	1.477	1.753	2.218	2.485	2.709	3.174	3.378	3.803	3.986	4.358	4.542	4.689	4.979
	2.8	0.826	1.134	1.672	1.985	2.511	2.813	3.064	3.586	3.812	4.282	4.482	4.885	5.083	5.238	5.542

Figure 59: Generator current demand plot

	109	149	218	258	328	368	403	477	511	587	621	696	736	771	845
100 Ω															
Gen V (V)	5	7.3	11.2	13.4	17.4	19.7	21.6	25.8	27.8	32	34	38.1	40.4	42.3	46.5
Gen C (A)	0.05	0.07	0.11	0.14	0.18	0.2	0.21	0.25	0.27	0.31	0.33	0.37	0.39	0.41	0.45
50 Ω															
Gen V (V)	4.8	6.9	10.7	12.9	16.6	18.8	20.7	24.7	26.5	30.5	32.4	36.3	38.5	40.3	44.2
Gen C (A)	0.1	0.14	0.21	0.26	0.33	0.38	0.41	0.49	0.53	0.61	0.65	0.72	0.76	0.8	0.87
33.3 Ω															
Gen V (V)	4.6	6.7	10.3	12.4	16	18.1	19.9	23.7	25.5	29.3	31	34.8	36.8	38.5	42.2
Gen C (A)	0.14	0.2	0.3	0.37	0.47	0.54	0.59	0.71	0.76	0.87	0.92	1.03	1.09	1.14	1.24
25 Ω															
Gen V (V)	4.4	6.4	10	12	15.5	17.5	19.2	22.8	24.5	28.2	29.8	33.4	35.3	36.9	40.4
Gen C (A)	0.17	0.25	0.39	0.47	0.61	0.69	0.75	0.89	0.97	1.11	1.18	1.32	1.39	1.46	1.59
16.7 Ω															
Gen V (V)	4.1	6	9.3	11.2	14.4	16.3	17.9	21.2	22.8	26.1	27.6	30.8	32.5	34	37.1
Gen C (A)	0.24	0.35	0.55	0.66	0.85	0.96	1.06	1.26	1.34	1.54	1.63	1.82	1.92	2.01	2.19
10 Ω															
Gen V (V)	3.6	5.3	8.2	9.9	12.7	14.3	15.7	18.7	20	22.9	24.1	26.8	28.3	29.5	32.1
Gen C (A)	0.35	0.51	0.8	0.96	1.24	1.39	1.53	1.81	1.94	2.21	2.33	2.59	2.72	2.83	3.08
8.3 Ω															
Gen V (V)	3.4	4.9	7.6	9.1	11.8	13.3	14.6	17.2	18.4	21.1	22.2	24.7	26	27	29.3
Gen C (A)	0.4	0.59	0.91	1.1	1.42	1.6	1.75	2.08	2.22	2.54	2.68	2.97	3.13	3.26	3.54
6.25 Ω															
Gen V (V)	3	4.4	6.9	8.2	10.6	11.9	13.1	15.5	16.5	18.8	19.8	21.9	23	23.9	25.9
Gen C (A)	0.47	0.69	1.08	1.3	1.67	1.89	2.07	2.45	2.61	2.98	3.13	3.48	3.66	3.79	4.1
4.5 Ω															
Gen V (V)	2.6	3.8	5.9	7.1	9.2	10.3	11.3	13.4	14.3	16.2	17	18.8	19.7	20.4	22.1
Gen C (A)	0.55	0.81	1.25	1.51	1.94	2.19	2.4	2.84	3.03	3.44	3.62	4	4.2	4.35	4.69
3.8 Ω															
Gen V (V)	2.4	3.5	5.4	6.5	8.4	9.4	10.3	12.1	13	14.7	15.4	17	17.8	18.4	19.8
Gen C (A)	0.58	0.86	1.34	1.61	2.08	2.35	2.57	3.03	3.24	3.68	3.86	4.27	4.47	4.61	4.95
2.8 Ω															
Gen V (V)	1.9	2.9	4.5	5.4	6.9	7.8	8.5	10	10.6	12	12.6	13.8	14.3	14.8	15.8
Gen C (A)	0.65	0.96	1.51	1.83	2.35	2.65	2.9	3.42	3.64	4.13	4.32	4.75	4.95	5.1	5.45

Figure 60: Generator characterization results

4.4 Simulink System Model

The goal of this section is to develop an algorithm that controls both the CVT ratio and the generator current demand effectively and simulates the behavior of the system in order to verify the effectiveness of the control algorithm. It should also be able to provide insights on the performance of the turbine and PTO setup when different gains for the PID controller are used. Therefore, to better understand the operating behavior of the waterwheel, the PTO and power output, a Simulink model was developed to simulate the behavior of the system when subjected to certain flow conditions. The setup is comprised of a waterwheel torque model, a generator model (torque and voltage models), a PTO friction model, an equivalent inertia model, a charge controller model, a PID controller and what is called a Torque Setpoint Controller module, or TSC. The TSC module also models the charge controller behavior, which impacts its decision-making.

The below section breaks down the models and subsystems utilized in the Simulink file. On this section, the focus is to showcase through simulation that torque control via CVT ratio and output current control yields better performance than purely output current control due to flexible torque range made possible due to CVT's variable gear ratio. The subsystems and models comprising the Simulink file are described next.

1) Waterwheel torque model – the model used to describe the wheel torque as a function of its angular speed and flow speed is the numerical model described in the previous section. For each simulation time step, it divides the blades into small elements and calculates the force and torque on the surface of each element. The total torque on the wheel is the sum of the individual torques on each blade. The simulation

keeps track of the position of each blade according to the simulation time and wheel speed.

2) Generator torque and voltage models – the equations used to describe the generator resistive torque and output voltage were obtained through characterization, as previously mentioned. Since $\omega_g = \varphi\varphi_{cvt}\omega_{ww}$, the generator output voltage and resistive torques are functions of the electrical current output, the CVT ratio and waterwheel angular speed. Direct control can be exerted over the PTO’s gear ratio and generator current demand, whereas indirect control is exerted over waterwheel speed by controlling the torque load on the system by means of manipulating those two variables. Figure 61 illustrate the Simulink subsystem.

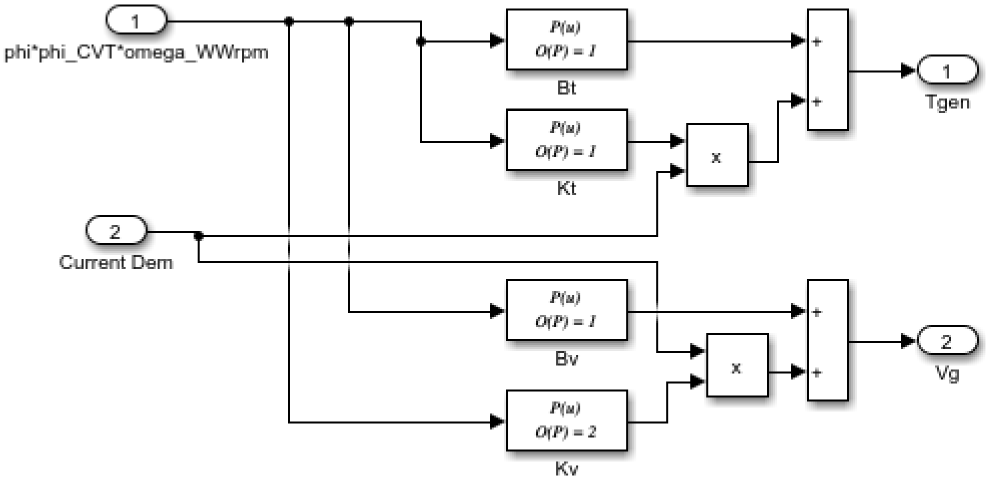

Figure 61: Generator resistive torque and voltage output models

3) Friction model – the friction model is given here as a model of the fixed gearbox connected to the generator only, obtained through benchtop tests and curve fitting. Although the friction model is not complete here (since it does not have the CVT and its gear meshing), it should be sufficient to obtain basic understand of the friction losses in the system. Here, the model is given as:

$$T_f = 0.351\omega_{ww}R^{-0.385} + 2.2925$$

Where the waterwheel speed is expressed in rpms and R is the electrical resistance, given as:

$$R = V_g/I_g$$

4) Equivalent inertia model – The equivalent inertia of the system changes with a change in CVT ratio. The expression for the total energy of the system is:

$$\frac{1}{2}J_{eq}\omega_r^2 = \frac{1}{2}J_{ww}\omega_r^2 + \frac{1}{2}J_{GB}\omega_{GB}^2 + \frac{1}{2}J_G\,\omega_G^2 \tag{42}$$

Where:

- J_{ww}: waterwheel inertia
- J_{GB}: gearbox inertia
- J_G: generator inertia
- ω_{GB}: rotational speed of gearbox output shaft
- ω_G: rotational speed of generator

Knowing that:

$$\omega_{GB} = \varphi_{GB}\omega_r \tag{43}$$

$$\omega_G = \varphi_{GB}\varphi_{CVT}\omega_r \tag{44}$$

The expression for the equivalent inertia is:

$$J_{eq}\omega_r^2 = J_{ww}\omega_r^2 + J_{GB}(\varphi_{GB}\omega_r)^2 + J_G(\varphi_{GB}\varphi_{CVT}\omega_r)^2$$

$$J_{eq} = J_{ww} + J_{GB}{\varphi_{GB}}^2 + J_G(\varphi_{GB}\varphi_{CVT})^2 \tag{45}$$

The equivalent inertia expression is given by Equation (45) and is a function of the square of the total gear ratio of the powertrain. The gain K is simply the square of the product between the fixed gearbox ratio and the generator inertia. The 7-blade waterwheel inertia was calculated based on the waterwheel CAD model and the masses of its components, while the generator rotor inertia was calculated by approximating a solid steel cylinder with dimensions close to those of the generator rotor. Figure 62 illustrates the Simulink block.

$$J_{ww} = 6.8kg.m^2$$

$$J_g = 6.25 \cdot 10^{-3}kg.m^2$$

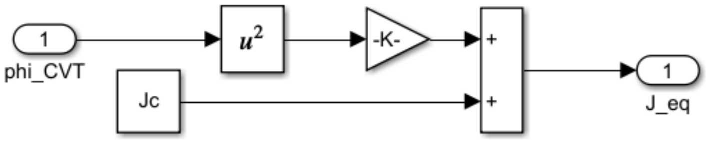

Figure 62: System equivalent inertia model

5) Torque Setpoint Controller Module (TSC) – this controller is the second of two controllers in the system. The first one is a basic PID controller that relates error values to resistive torque setpoints to the system. For initial simulations, the

waterwheel optimal TSR is set to 0.4, based on the waterwheel torque model, which gives a speed setpoint to the system to operate around. The PID controller relates the error between the setpoint and the current wheel speed to a torque load on the turbine shaft and feeds that torque demand to the TSC module, which then calculates the optimal CVT ratio and current demand setpoints. The way those two setpoints are calculated is based on the equation for the resistive torque on the system, expressed as the product between the gear ratios, both fixed and variable, and the generator resistive torque, or:

$$T_r = \varphi\varphi_{cvt}T_g \tag{46}$$

$$T_r = \varphi\varphi_{cvt}(K_T\big(\omega_g\big)I_{out} + B_T(\omega_g))$$

$$T_r = \varphi\varphi_{cvt}((-1 \cdot 10^{-4}\omega_g + 0.5526)I_{out} + 2 \cdot 10^{-4}\omega_g + 0.0105)$$

Since $\omega_g = \varphi\varphi_{cvt}\omega_{ww}$:

$$T_r = \varphi\varphi_{cvt}((-1 \cdot 10^{-4}\varphi\varphi_{cvt}\omega_{ww} + 0.5526)I_{out} + 2 \cdot 10^{-4}\varphi\varphi_{cvt}\omega_{ww} \text{ -} \tag{47}$$

Figure 63 shows the system's resistive torque plot as the CVT ratio and the current demand vary.

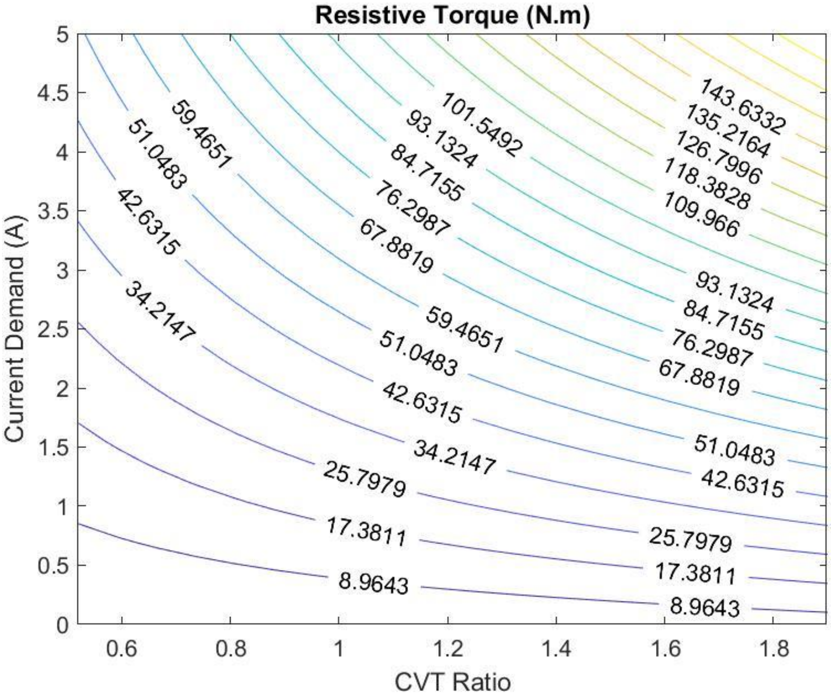

Figure 63: System resistive torque as function of CVT ratio and current demand for a fixed waterwheel speed

As a first attempt to devise an optimal TSC, knowing that the generator efficiency increases at its speed increases, it is desired to rotate the generator as fast as possible. Thus, during steady-state operations the CVT should in most cases stay at its maximum ratio of 1.9 and the current demand vary accordingly to achieve the required torque. Therefore, by using Equation (48) with the CVT ratio fixed at 1.9 and solving for the generator current setpoint (waterwheel speed in rpms):

$$I_{sp} = \frac{T_r/(\varphi\varphi_{cvt}) - 2 \cdot 10^{-4}\varphi\varphi_{cvt}\omega_{ww} - 0.0105}{-1 \cdot 10^{-4}\varphi\varphi_{cvt}\omega_{ww} + 0.5526} \tag{48}$$

If the calculated setpoint current demand lies above the minimum and under the maximum values limited by the charge controller (more details soon) and within the boundaries of the validity region of the model (mentioned below), the setpoint for CVT ratio is then set to maximum ($\varphi_{cvt} = 1.9$) and the current demand setpoint is set to the calculated value above. If, on the other hand, the current demand falls below the minimum value, the CVT ratio decreases by a fixed decrement, a new current setpoint is calculated and the cycle repeats itself until either suitable setpoints are found or the CVT ratio reaches its minimum value of 0.5. If the current demand falls above maximum, it is then set to maximum and the CVT ratio its set to its current value. The minimum and maximum current values in this case are set to 0.4A and 4A respectively, based on the modifications and testing of the charge controller, coming up in next sections.

However, there is a region of validity to the above expression ($2.8\,\Omega \le R \le 100\,\Omega$), which represents the electrical resistance range that the generator models were obtained. The generator voltage model is then used to verify that condition. If the calculated voltage divided by the calculated current demand (which gives resistance) is lower than the minimum resistance value, then the current is set to the calculated voltage over the low end of the resistance. If the opposite happens at the high end of the resistance, the current is set to the calculated voltage over the high end of the resistance. A pseudo-code shows the logic behind the validity region limiting the current demand:

```
if Ig > Vg/Rmin
    Ig = Vg/Rmin
Elseif Ig < Vg/Rmax
```

```
    Ig = Vg/Rmax
End
```

6) Charge controller model – the model for the charge controller is implemented within the TSC controller block previously mentioned, and describes the behavior of that component while affecting the decision-making of the TSC controller. It directly impacts the dynamics of the system, since it handles the current demand to the battery and enables/disables current control when conditions are met. The battery charge controller is implemented using an off-the-shelf LT8491 Battery Charge Controller Evaluation Board from Analog Devices. The default behavior of this device applies a fixed current to the battery during the constant-current portion of a lead-acid battery charge cycle (Figure 30). A hardware modification to the LT8491 Evaluation Board was designed, implemented, and tested that permits control of the charging current. Figure 64 shows the schematic of the added circuitry. A programmable voltage of 0 to 5 volts, developed by the PTO sub-system controller is applied to a filter and buffer amplifier. The amplifier output voltage is injected via resistors RC and RD into the IMON_OUT pin of the LT8491 controller. This creates an offset current that lowers the effective charge current regulation point. A voltage change from 0 to 5 volts results in charge current change from the default charge current of 4 amps to approximately 0.4A respectively. The charge controller maintains regulation of the new programmed current during the constant-current portion of the charge cycle (Stage 1) and limits the maximum charge current during the constant-voltage (Stage 2) portion as well (Henderson 2023).

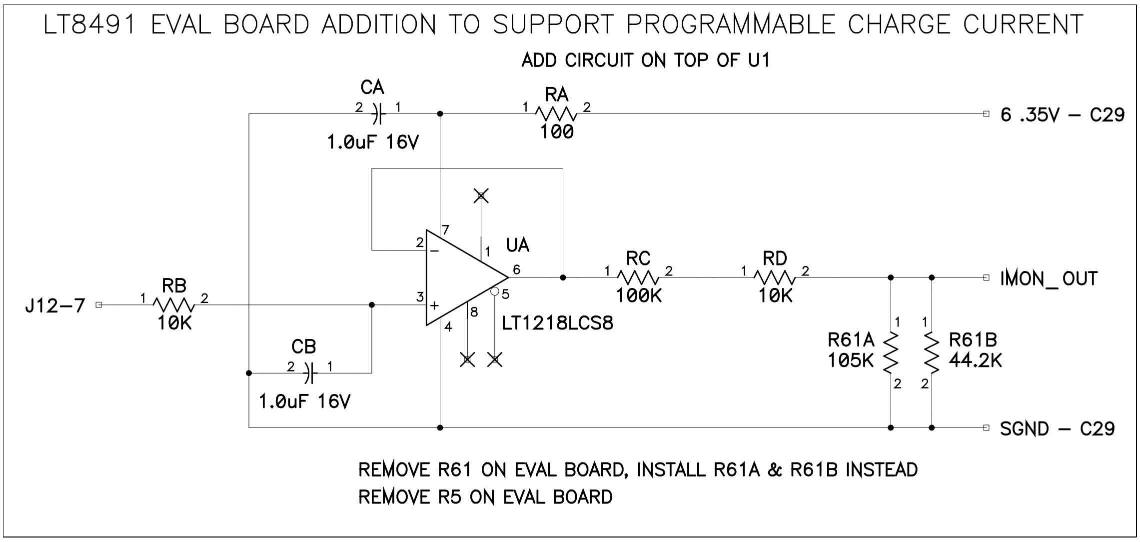

Figure 64: Added circuitry to the LT8491 charge controller

After the abovementioned modifications, some tests were performed on the charge controller to better understand and model its behavior. On the first test, a constant input voltage (emulating the generator input voltage to the charge controller) of 20V was set and a range of PWM signals, from 0% to 100% (at 20% increments) derived from the 0-5V programmable voltage, were sent to the IMON_OUT pin of the controller. The battery voltage was varied from 12.3V to 14.3V and the controller output current to the battery was computed. On the second test, the battery voltage was kept constant at 12.7V while the input voltage varied from 7.5V to 30V.Figure 65 and Figure 66 shows the test plots.

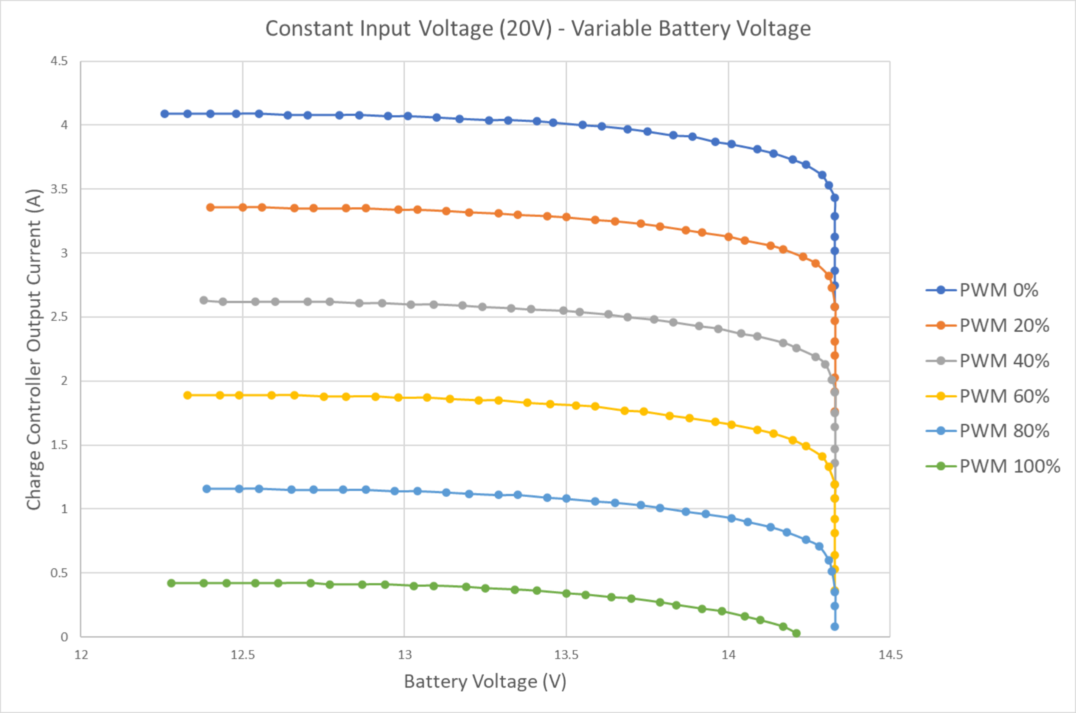

Figure 65: Charge controller current output behavior for constant input voltage and variable battery voltage

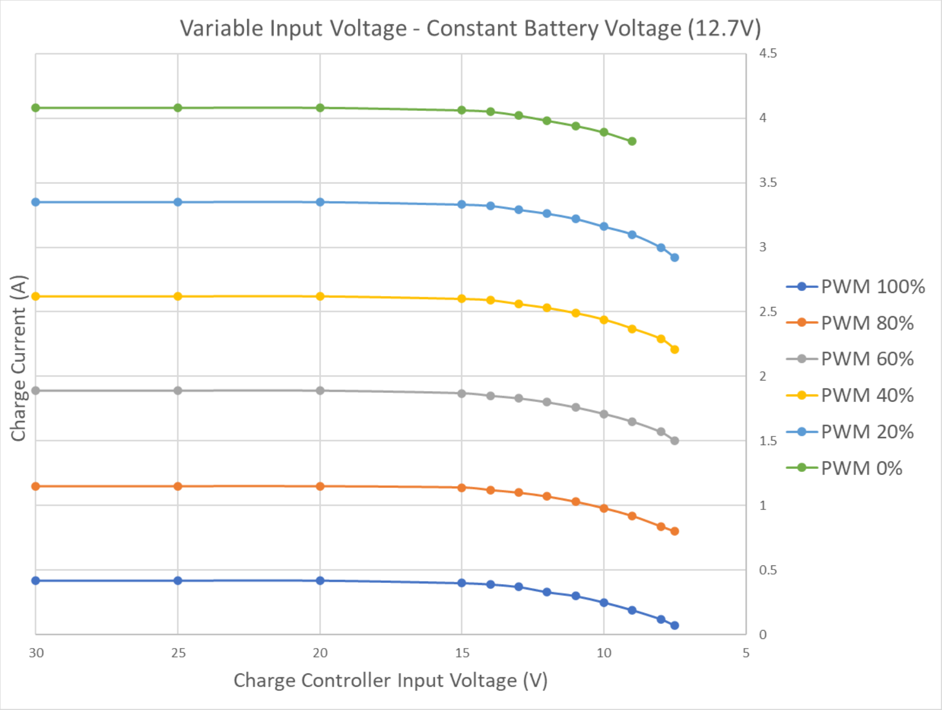

Figure 66: Charge controller current output behavior for variable input voltage and constant battery voltage

In order to model the controller behavior with good accuracy, some assumptions were made as follows:

- $V_{in} \geq 14V$: controller can charge battery with maximum current of 4A. The model for the battery current as function of the PWM signal is:

$$I_b = I_{b,max}(1 - 0.9PWM)$$

Where PWM is written as a decimal number between 0 and 1 (representing 0 to 255).

- $7V < V_{in} < 14V$: the maximum charging current the controller can output begins to drop with the input voltage. While the equation that relates the battery current to the PWM value remains the same as above, the model for the maximum current is written as:

$$I_{b,max} = 0.048V_{in} + 3.4$$

$$I_b = I_{b,max}(1 - 0.9PWM)$$

- $V_{in} \leq 7V$: charge controller is disabled, which means the battery current is zero and the system cannot produce any useful power.

Moreover, the controller turns on whenever the input voltage reaches a minimum required value, which can be set by the user based on the performance of the system. The value used for simulating the system is set to 12V. To calculate the generator current output demand, assuming the Charge Controller efficiency is 100%, the input power to the charge controller equals the output power to the battery, or:

$$V_g I_g = V_b I_b$$

Knowing that V_g (i.e., the generator output voltage) is the input voltage to the charge controller and I_g (i.e., the generator output current) is the output current demand to be regulated:

$$I_g = \frac{V_b I_b}{V_g}$$

$$I_g = \frac{V_b I_{b,max}(1 - 0.9PWM)}{V_g}$$

Since the value of I_g is calculated by utilizing the generator torque model to calculate I_g based on the PID torque demand, the necessary PWM value to supply the required current can be found by resolving for the PWM term in the above expression. Since the result is a decimal number between 0 and 1, the result is multiplied by 255.

$$PWM = 1.11\left(1 - \frac{V_g I_g}{V_b I_{b,max}}\right) \cdot 255 \tag{49}$$

7) Waterwheel speed setpoint, error and control – the speed setpoint of the waterwheel is initially set based on an optimal TSR of 0.4. The simulation calculates the error between current wheel speed and speed setpoint and sends out a new resistive torque setpoint, which will be met by manipulating the CVT ratio and/or

generator current demand through the TSC. The overall control architecture is depicted in Figure 67.

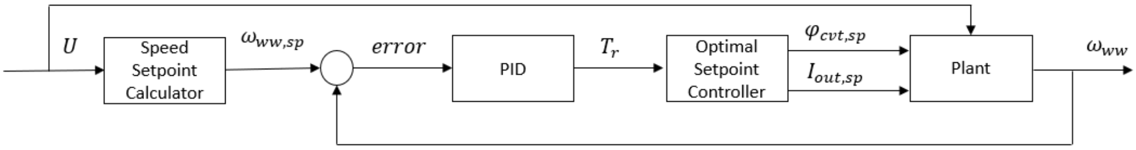

Figure 67: System control - basic architecture

To quantify the performance of the system under simulation, the total mechanical energy captured by the waterwheel and electrical energy produced by the generator are calculated at the end of the simulation. The average wheel mechanical power and generator electrical power output are calculated by dividing the total mechanical and electrical energy by the simulation time. The total efficiency during the simulation is also calculated by dividing the electrical energy by the mechanical energy. The Simulink model is depicted in Figure 68 below.

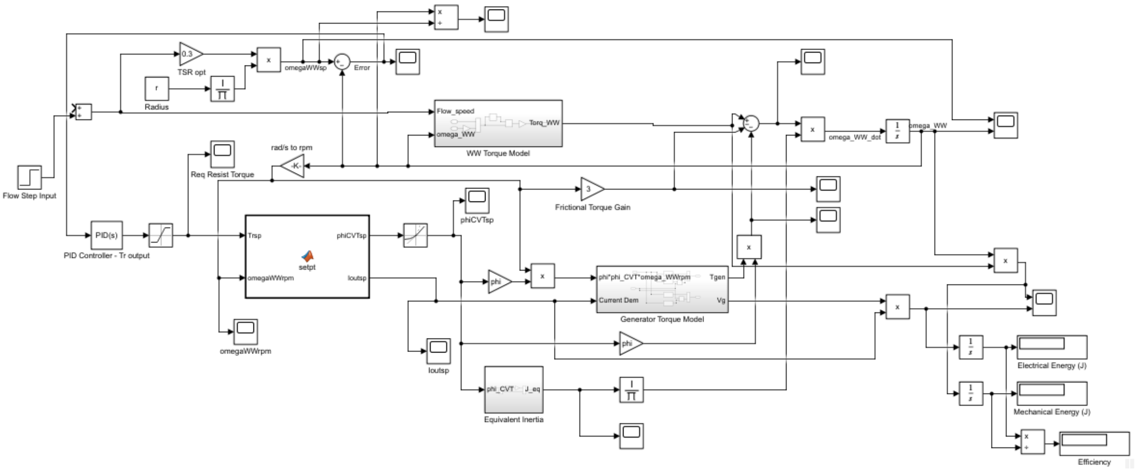

Figure 68: Simplified Simulink model of waterwheel and PTO system

It is important to reiterate that the ability of a turbine-powered energy system to operate efficiently is directly related to how well it can maintain its turbine at its optimal speed by controlling the torque load on the turbine shaft. The purpose of this section is not only to obtain initial results and conduct performance evaluation based on the Simulink model, but to compare how well a CVT and current demand control system versus a pure current demand control system perform under varying conditions (i.e., different flow speeds). This section goes over some initial simulation results, with PI parameters tuned and kept constant for each specific run. Here two Simulink models will be used: one with current demand control only and another with both current demand control and CVT ratio control, with a simulation time of 40 seconds. The first one, current demand control only, will have the CVT set at its maximum ratio of 1.9. The second one will have the CVT ratio set to its minimum ratio of 0.5 and should work its way up to the optimal operating ratio. The modulation of generator current demand will be done by varying PWM values based on current demand and voltage readings. The Simulink solver used was the Dormand-Prince (commonly referred to as ode45), with a maximum step size of 0.01 and a relative tolerance of 0.001.

Before continuing, to better illustrate what is expected in terms of controls and performance, it is useful to draw an analogy, where the expected behavior of the system is similar to that of a car engine and transmission, in which the Engine Control Unit (ECU) upon detecting a torque demand the engine cannot provide at current gearing, decreases the gear ratio (shifts down) to decrease the reflected load on the engine output shaft, allowing the vehicle to keep its speed or accelerate to the desired speed setpoint. That example is analogous to the waterwheel and PTO.

Firstly, similar to an internal combustion engine, turbines in general are able to deliver torque based on the speed they operate at. As waterwheels are drag machines, no speed translates directly to maximum torque for a given flow. As the waterwheel speed increases for a constant flow (i.e., its TSR increases), its ability to generate torque decreases. Generally speaking, the control system modulates the torque load on the waterwheel shaft to keep the waterwheel rotating at its speed setpoint. Thus, the turbine torque delivery is affected by the speed setpoint of the turbine and the flow speed acting on it. The torque load on the turbine shaft is controlled by both the generator output current demand and the CVT ratio. The turbine torque delivery decreases as the turbine speed increases, while it increases with the square of the flow speed. In other words, a lower turbine speed setpoint will demand a higher torque load to keep it rotating at that setpoint, especially at higher flow speeds. It is crucial to recognize that there is an upper and a lower limit for how much torque load can be actually provided by the controller to the PTO, set by the charge controller and generator. If maximum current is demanded and the torque load cannot be met (high torque), CVT ratio is increased. If minimum current is demanded and the torque load cannot be met (low torque), the CVT ratio is decreased. Another important point is that the system does not have to necessarily wait for maximum current demand (PWM is zero) to increase the PTO ratio. It is known from experiments and models that the higher the generator operating speeds are, the more efficient it becomes. Thus, a given current threshold could be set such that, once the system requires values under that limit, the CVT ratio is increased, therefore increasing the generator efficiency. If the torque load and thus the current demand fall within those extreme cases, the CVT is maintained and torque control is performed exclusively via current demand control.

Note that, for low flow speed and high TSR setpoint, torque demands will be extremely low. Thus, assuming that the current demand reaches its minimum value and the CVT decreases, since the flow speed is low, even though in this example the waterwheel speed setpoint is high, the generator output speed yields lower voltage output, especially with lower CVT ratio, causing the voltage to fall below the minimum needed to run the charge controller, which then turns itself off and ceases power production. If the generator could output more voltage, the charge controller could remain on and power could still be produced. Thus, one important conclusion here is that, if the system is to be designed to harness power from low-speed currents, a generator capable of outputting higher voltage at low speeds (when compared to the generator used in this project) is desirable in order to keep the charge controller running.

4.5 PI Derivations and PTO Efficiency Model

The basic control law is based on the error between the turbine speed setpoint and its actual speed. The simulation works by receiving the torque demand from the PI controller, calculating the required current demand and calculating the necessary PWM value to be send to the charge controller to draw that target current from the generator. The calculated current demand has to fall within the generator model limits in order to avoid unexpected results, meaning the electrical resistance has to fall within 2.8Ω and 100Ω. The torque model utilized is derived from the torque model shown in Equation (41). Although the I-gain was obtained through manual testing, the P-gain was obtained based on the fact that the waterwheel torque, considering the average torque written in its simplest form, can be regarded as proportional to the square of the difference between the flow speed and the tangential speed of the blade tip:

$$T_{ww} = 1/2 \rho A r' r_1 C_d (U - \omega_r r_1)^2 \tag{50}$$

On Equation (50), r' (the radius ratio of applied force) varies between 74% of the blade radius when TSR is zero, and 62% of the blade radius when TSR = 1, according the early analytical analysis of the torque integration along the blade at 90° (Figure 48). Even though the blades change angles, the assumption that r' is constant is used here. Thus, taking the average of the two values, $r' = 68\%$. The area is considered to be the blade width times the underwater depth, which in this case is equal to the radius. Therefore:

$$T_{ww} = 1/2\rho b r' r_1^2 C_d (U - \omega_r r_1)^2$$

Rewriting the above equation as a function of the TSR:

$$T_{ww} = 1/2\rho b r' r_1^2 C_d U^2 (1 - \lambda)^2$$

Taking the Taylo expansion of the waterwheel torque and neglecting higher order terms:

$$T_{ww} = T_{ww}|_{U_0,\lambda_0} + \frac{dT_{ww}}{d\lambda}(\lambda - \lambda_0) + \frac{dT_{ww}}{dU}(U - U_0)$$

Although the waterwheel torque is dependent on both the flow speed and the tip speed ratio, since during this simulation step the flow speed is kept relatively constant, the above equation can be rewritten as:

$$T_{ww} = T_{ww}|_{U_0,\lambda_0} + \frac{dT_{ww}}{d\lambda}|_{U_0,\lambda_0}(\lambda - \lambda_0) \tag{51}$$

Taking $\lambda_0 = \lambda_{sp}$ and writing the definition of error:

$$e = \lambda_0 - \lambda = \lambda_{sp} - \lambda$$

Rewriting Equation (51):

$$T_{ww} = T_{ww}|_{U_0,\lambda_0} - \frac{dT_{ww}}{d\lambda}|_{U_0,\lambda_0} e$$

$$T_{ww} = T_{ww}|_{U_0,\lambda_0} - K_p e \tag{52}$$

Therefore, the proportional gain is found to be:

$$K_p = -\rho b r' r_1^2 C_d U_0^2 (1 - \lambda_{sp}) \tag{53}$$

The I-gain was derived based on trial and error for different speed setpoints and flow speeds, and then an analytical function was found to fit those gains as:

$$K_I = K_{I0}/U \tag{54}$$

Where K_{I0} is the I-gain found when calibrating for a unitary flow speed ($U = 1\ m/s$).

Another feature added in this section to enhance the accuracy of the simulations is the mechanical efficiency model of the PTO. Since the PTO is not equipped with a torque sensor, to estimate the torque on the waterwheel, a torque model is derived from the generator torque model and the efficiency of the system as:

$$T_L = \frac{\varphi \varphi_{cvt} T_g}{\eta_{gb}} \tag{55}$$

Where:

- T_L: load torque on waterwheel shaft
- φ: gearbox ratio
- φ_{cvt}: CVT ratio
- η_{gb}: gearbox and CVT efficiency combined

To calculate the CVT ratio more accurately during field and bench tests, the PTO is equipped with two hall effect sensors, one on the input and one on the output of the CVT. To model the efficiency of the gearbox and CVT, bench tests were performed on the PTO with its generator connected to electrical resistances varying from 2.8Ω to 100Ω. It is important to mention that the model also accounts for friction in the PTO, which will simplify the calculations for the waterwheel torque from field test results. The model obtained for the efficiency of the gearbox and CVT as a function of the generator current demand and waterwheel speed in RPM is:

$$\eta_{gb} = c + \frac{I_{out}}{b e^{a I_{out}}} \tag{56}$$

$$c = -0.1253\omega_{ww}^2 + 5.123\omega_{ww} + 7.298 \tag{57}$$

$$a = 2.531\omega_{ww}^{-0.6303} \tag{58}$$

$$b = 0.002529e^{0.2972\omega_{ww}} \tag{59}$$

Figure 69 shows the surface plot for the model as a function of current demand and waterwheel speed in RPM. Note that for lower waterwheel speeds, the generator current demand cannot be much higher than one due to the generator's inherent characteristics. Thus, the portion of the surface where the efficiencies decrease after peaking is never accessed.

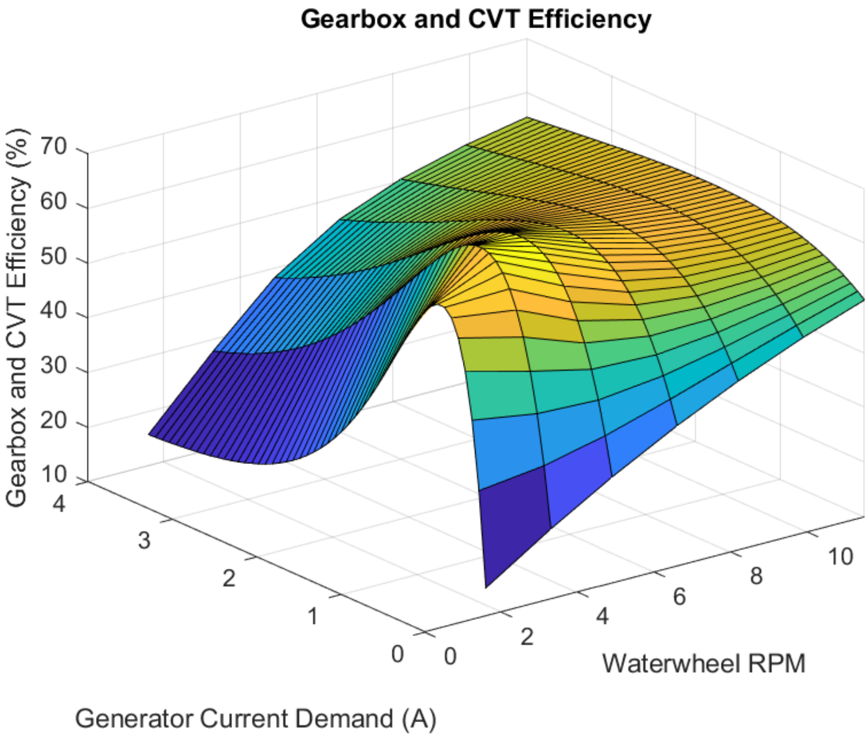

Figure 69: Gearbox and CVT efficiency model plot in percent

Moving back to the simulations, to illustrate the performance differences between the two control systems, some simulations were run. The first simulation subjects both systems to a constant flow speed of 0.8 m/s and changes the TSR setpoint every 20 seconds of simulation time, from 0.2 to 0.8. The second simulation fixes the TSR setpoint at 0.5 and decreases the flow speed every 20 seconds of simulation time until the system cannot maintain the turbine speed setpoint and generate power, varying the flow from 1m/s to 0.6m/s.

1) Simulation Run #1 – for the first run, Figure 70 and Figure 71 show the performance of the pure current demand controller, while Figure 72 and Figure 73 show the performance of the CVT and current demand controller. It can be noticed that, for the first controller, when the TSR setpoint reaches 0.6, it can no longer decrease its torque load to maintain the turbine speed, whereas the second controller can maintain all speeds up to the last setpoint by decreasing the CVT ratio to meet torque load demands.

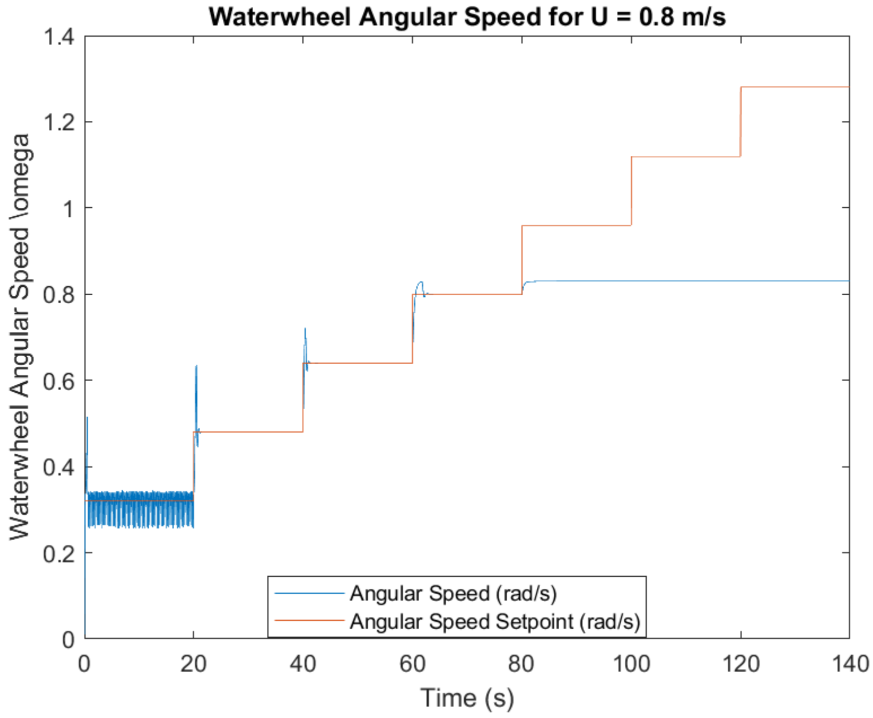

Figure 70: Waterwheel speed and its setpoint for pure current demand controller and U = 0.8 m/s

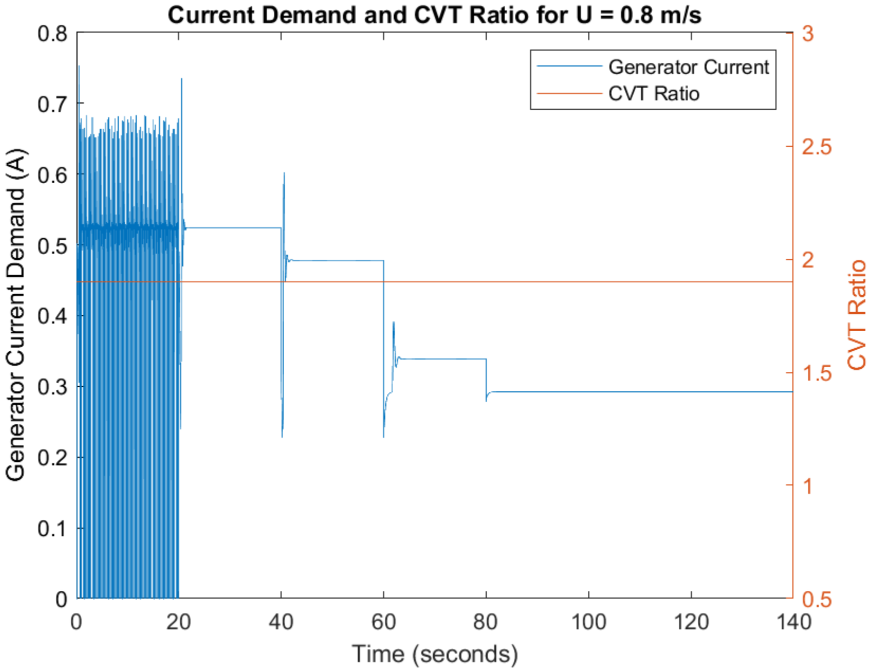

Figure 71: Generator current and CVT ratio (fixed) for pure current demand controller and U = 0.8 m/s

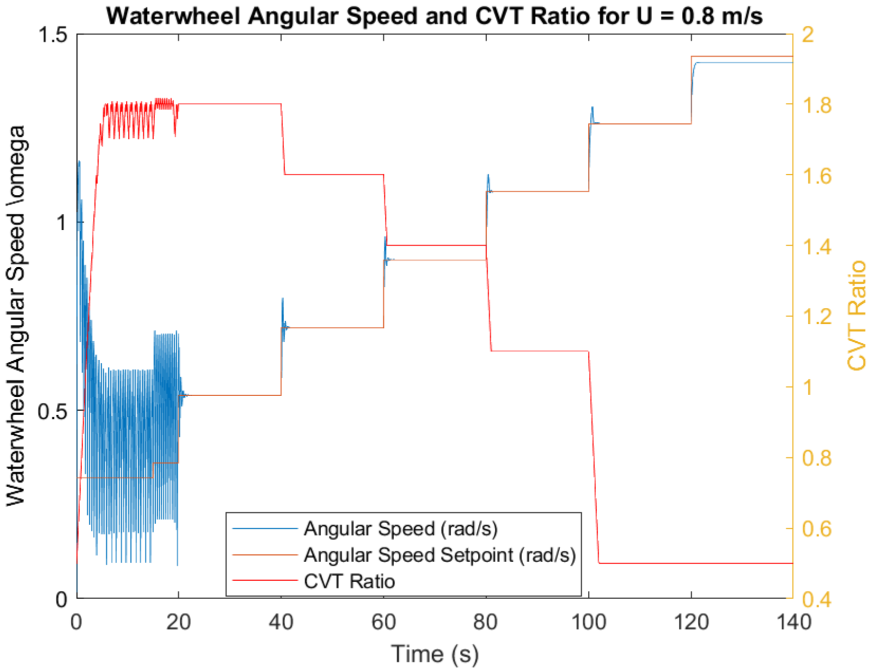

Figure 72: Waterwheel speed, speed setpoint and CVT ratio for CVT and current demand controller and U = 0.8 m/s

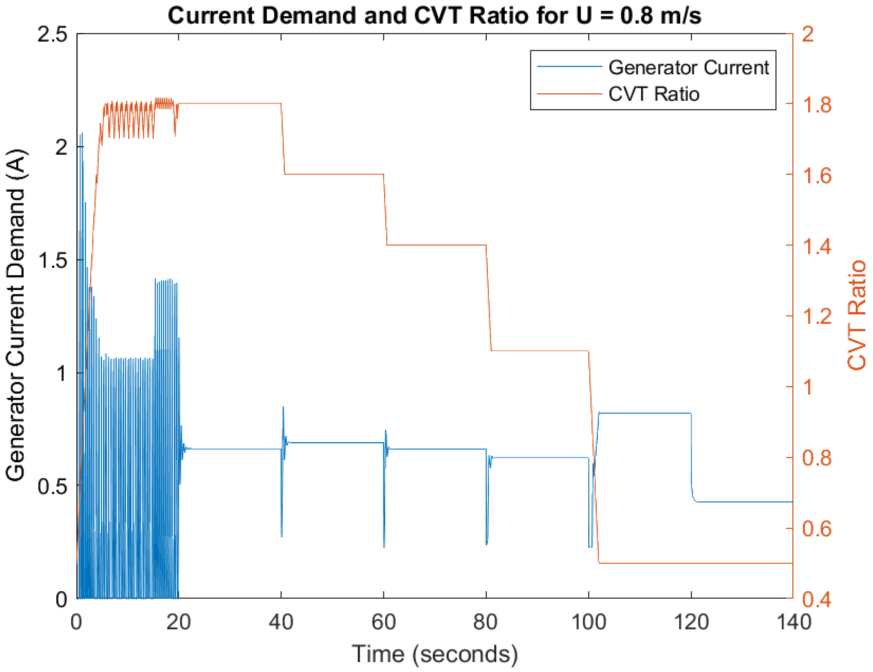

Figure 73: Generator current and CVT ratio for CVT and current demand controller and U = 0.8 m/s

2) Simulation Run #2 – for the second run, Figure 74 and Figure 75 show the performance of the pure current demand controller, while Figure 76 and Figure 77 show the performance of the CVT and current demand controller. Note that the first controller cannot meet the TSR setpoint when the flow speed drops below 0.8 m/s, while the second controller only fails to reach the setpoint at 0.6 m/s. The algorithm to actuate the CVT in conjunction with the current demand is not fully functional in this section and needs improvements, but it can successfully illustrate the advantages of having such setup in a power generation system, especially when trying to harness power from a low-speed source, such as tidal currents.

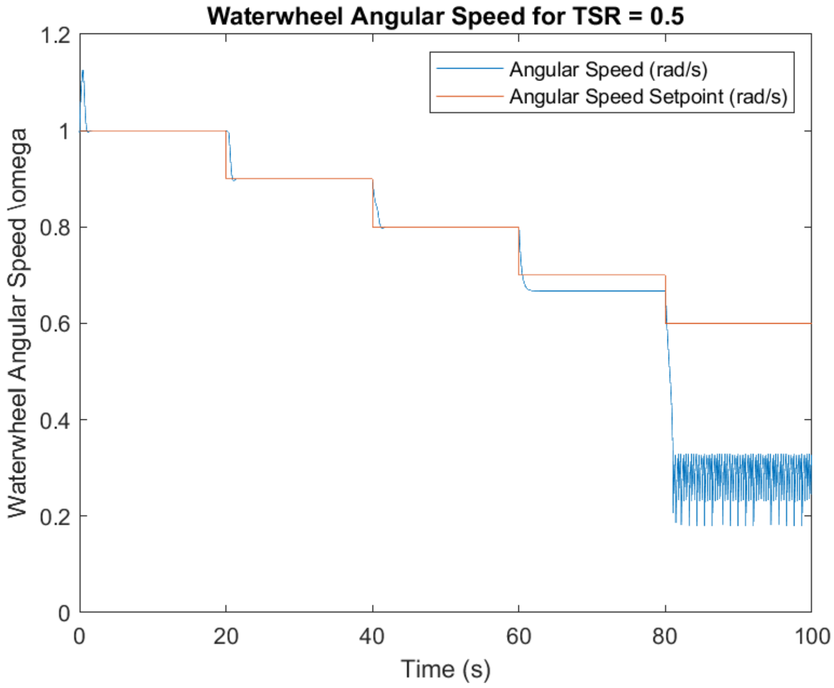

Figure 74: Waterwheel speed and its setpoint for pure current demand controller and TSR setpoints of 0.5

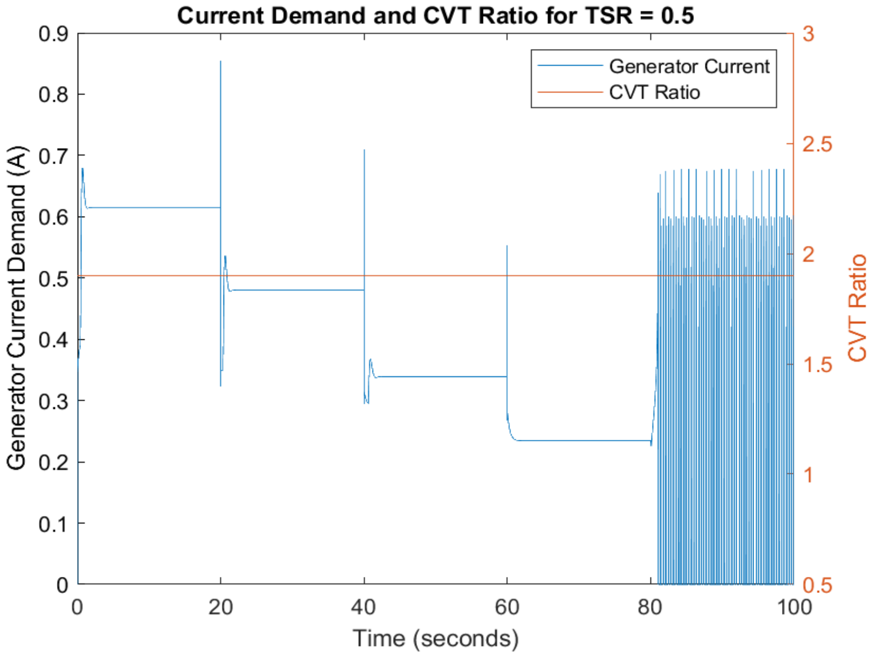

Figure 75: Generator current and CVT ratio for CVT and current demand controller and TSR setpoint of 0.5

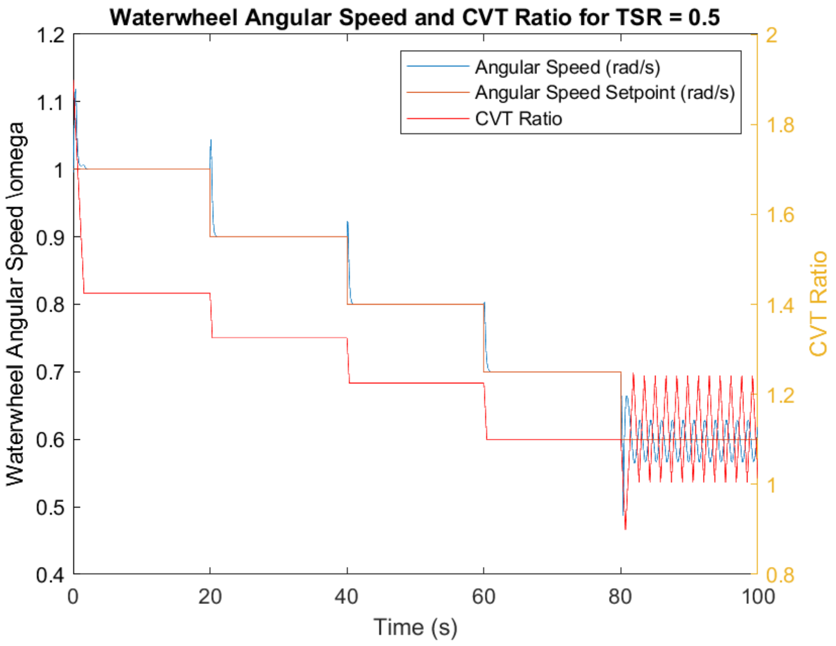

Figure 76: Waterwheel speed, speed setpoint and CVT ratio for CVT and current demand controller and TSR = 0.5

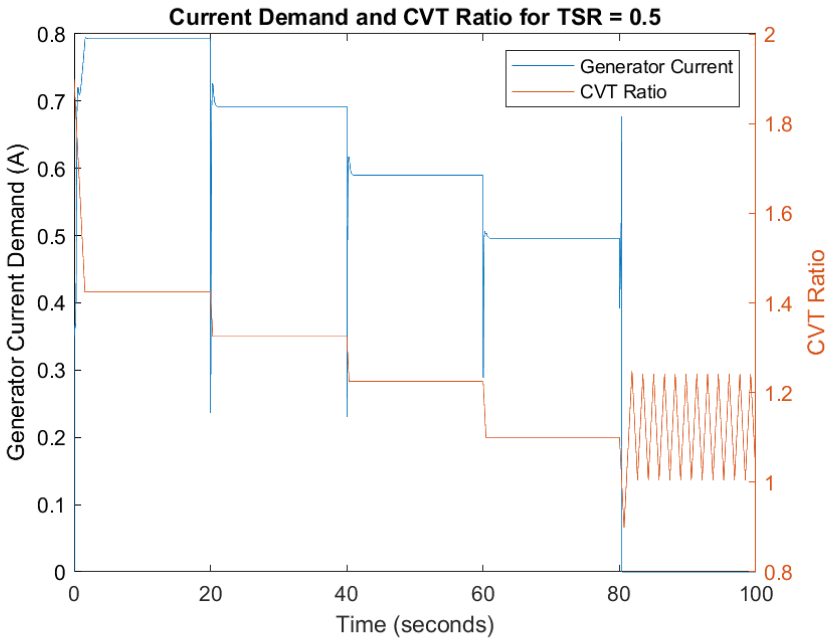

Figure 77: Generator current and CVT ratio for CVT and current demand controller and TSR = 0.5

It is important to realize, however, that the abovementioned results are obtained via modeling the behavior of the turbine via analytical approach. Even though that approach is based on well-established mathematical models of drag forces on objects generated by incoming flow, it is not a comprehensive approach as it simplifies and/or fails to account for all parameters, while assuming others based on theoretical limits. It is expected that the torque properties of the waterwheel generate less force than what was predicted by the model, based on the behavior of the system during the first round of tests. Therefore, further examination and, more importantly, field tests need to be conducted to adjust the waterwheel torque model and better simulate its behavior.

4.6 Notes on Maximum Power Point Tracking and Machine Learning

For the current MHK turbine and the PTO, although the MPPT algorithm was not developed, some notes about how to approach that implementation are shared. The MPPT is a perturb-and-observe method that changes the operating setpoint of a system and observes its output, making its next decision based on the response of the system. For the current system, the algorithm would perturb the speed setpoint of the turbine and observe the power output. If the power output increases, the algorithm then continues the setpoint perturbation in the same direction while building its memory. When the power output decreases for a given perturbation following the same direction as the last one, the algorithm then returns to the previous setpoint and deems it the optimal setpoint for maximum power output. Figure 18 depicts its working principle in detail. Some algorithms utilize variable step size to increase the accuracy of the method in finding the maximum power point. However, since the change in Cp curve with respect to the turbine TSR is not large near the maximum power point, added to the fact that flow speed readings come with a considerable amount of noise, a search resolution of 0.1 when sweeping through the TSR range might be enough. Figure 78 illustrates how the output power behaves when the turbine speed setpoint changes under constant flow speed. The top plot shows a TSR setpoint varying from 0.2 to 0.7, while the bottom plot shows the electrical power output of the generator. It can be noticed that when the TSR reaches a setpoint of 0.4, the output electrical power reaches its maximum. The MPPT algorithm sweeps through the TSR range and looks for the TSR setpoint that yields maximum power output for a specific incoming flow speed range. The algorithm saves that setpoint for that specific flow speed range, so that next time the system is deployed it immediately sets the speed setpoint to the one that yields maximum power output. That routine should be performed for the entire flow speed range, the setpoints saved and the system learns the optimal speeds to run at based on flow speed readings.

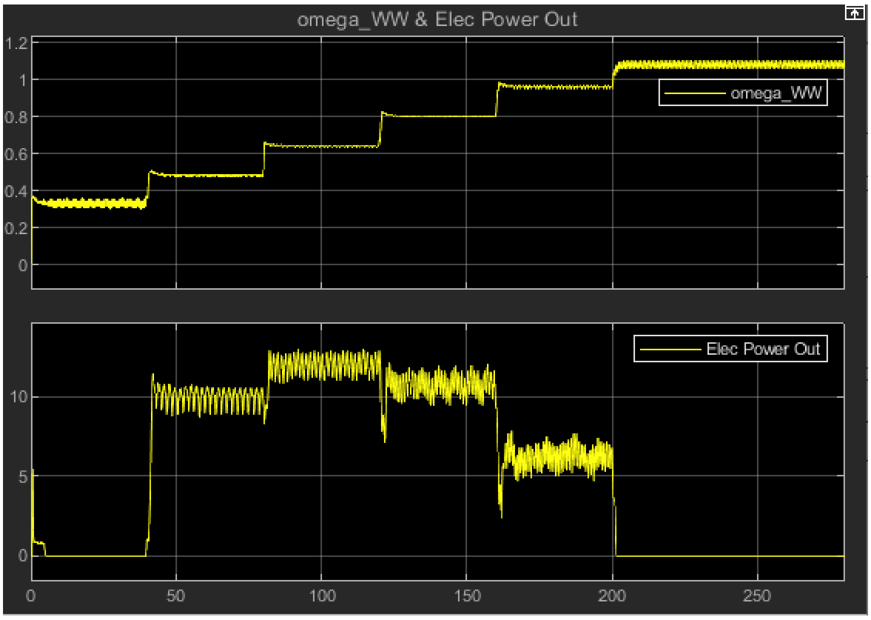

Figure 78: Waterwheel speed and electrical power output for flow speed of 0.8m/s

4.7 New Generators Comparison

During the first round of field tests, an oversized generator was used, which resulted in acceptable results for initial field tests and proof-of-concept. In order to properly match the generator to the available flow power, a generator was sized and picked based on the available power at the generator shaft. The previously used generator was the Missouri Wind and Solar's Freedom III PMSG, rated at 1500W at 970 RPM (discontinued), while the new generator is the Marsrock G100S PMG, rated at 100W at 600RPM. In order to understand the performance of the system when equipped with either of those generators, simulations were run to compare power output and system efficiency. For the simulations comparing both results, the models used were obtained through bench testing. The Freedom III output voltage and resistive torque models were rewritten in a form similar to the Marsrock models, and are shown below. The flow speed was varied from 0.5m/s to 1.2 m/s and the TSR setpoint was set to 0.4. The PI control gains were set according to the control law mentioned in previous section and the simulation time was of 40 seconds. The plots below were obtained by using a moving average filter with a window size of 1200 samples, since the outputs at lower flow speeds are noisy and hard to visualize. The general equations for voltage output and torque load for both generators are written as:

$$V_g = K_V(\omega_g)I_{out} + B_V(\omega_g) \tag{60}$$

$$T_g = K_T\big(\omega_g\big)I_{out} + B_T(\omega_g) \tag{61}$$

The speed-dependent coefficients K_V, B_V, K_T and B_T for each generator are expressed below, where the subscripts MR and F3 represent the Marsrock and Freedom III generators respectively.

$$K_{V,MR}(\omega_g) = -4 \cdot 10^{-6}\omega_g^2 + 2.2 \cdot 10^{-3}\omega_g - 5.0667$$

$$B_{V,MR}(\omega_g) = 0.058\omega_g$$

$$K_{T,MR}(\omega_g) = -1 \cdot 10^{-4}\omega_g + 0.5526$$

$$B_{T,MR}(\omega_g) = 2 \cdot 10^{-4}\omega_g + 0.0105$$

$$K_{V,F3}(\omega_g) = -2 \cdot 10^{-6}\omega_g^2 + 1.4 \cdot 10^{-3}\omega_g - 1.2854$$

$$B_{V,F3}(\omega_g) = 0.0497\omega_g$$

$$K_{T,F3}(\omega_g) = 1 \cdot 10^{-6}\omega_g^2 - 1.13 \cdot 10^{-3}\omega_g + 0.9209$$

$$B_{T,F3} = 0.08$$

Figure 79 and Figure 80 show the total electrical power generated and the total system efficiency (generator power output over turbine mechanical power) for both generators during the 40s simulation time. The Marsrock performs better than the

Freedom III at lower flow speeds (0.9 m/s and below), and the gain in performance becomes almost double at 0.5 m/s. That happens due to the fact that the Freedom III operates well under its efficient region. When flow speeds increase (1m/s and above) the Freedom III outperforms the Marsrock, but not by much. Figure 81 shows the efficiency plot for each generator and the percent increase in efficiency of the Marsrock over the Freedom III, shown by the grey curve. For more than half the flow speed range the Marsrock outperforms the Freedom III, especially at low flow speeds. Conversely, the Freedom III outperforms the Marsrock when flow speeds reach values of 1m/s and beyond, but not by much (maximum of 11% more efficient at 1.2 m/s). It is also known that tidal flows seldom reach high speeds, and the fact that the first field tests read flow speeds of 1m/s and beyond is due to the fact that the testing location works as a bottleneck that narrows the area where the flow passes through, increasing its speeds. In addition, since the Freedom III does not outperform the Marsrock by much at higher flow speeds, it can be concluded that the Marsrock is the best option for the system given.

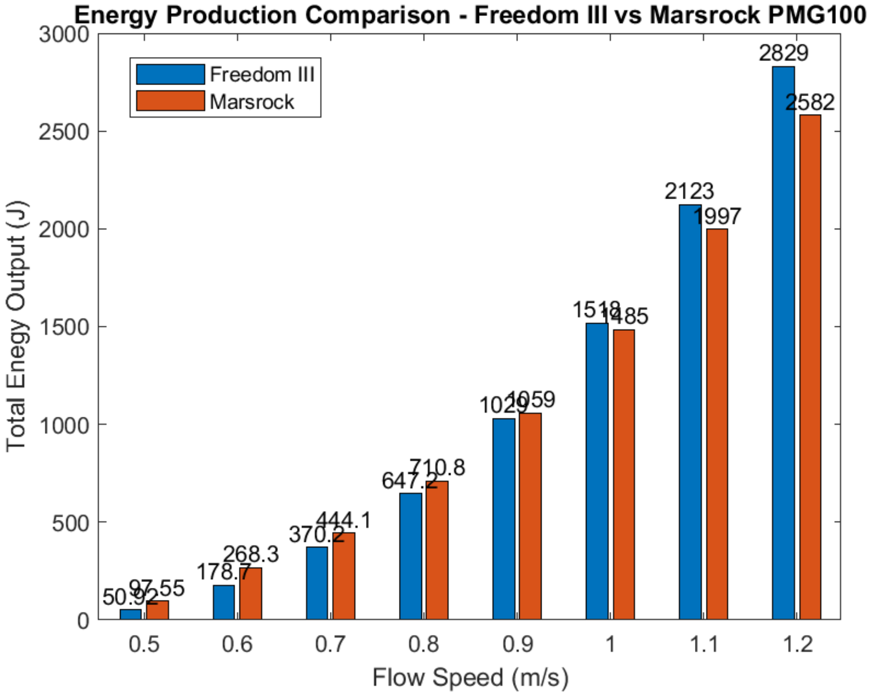

Figure 79: Electrical energy output - Freedom III vs Marsrock

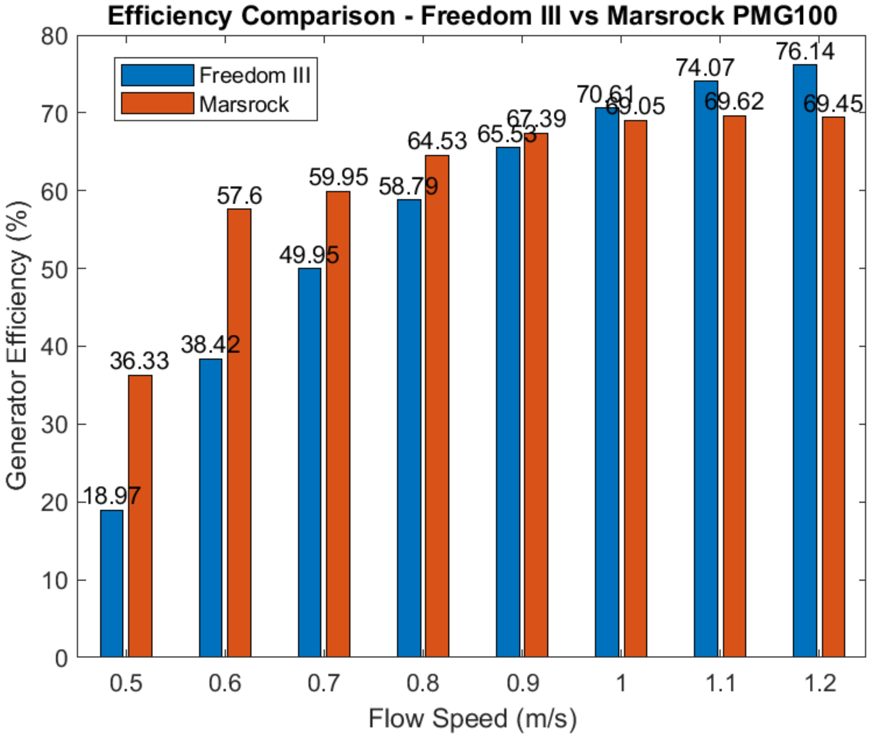

Figure 80: System efficiency - Freedom III vs Marsrock

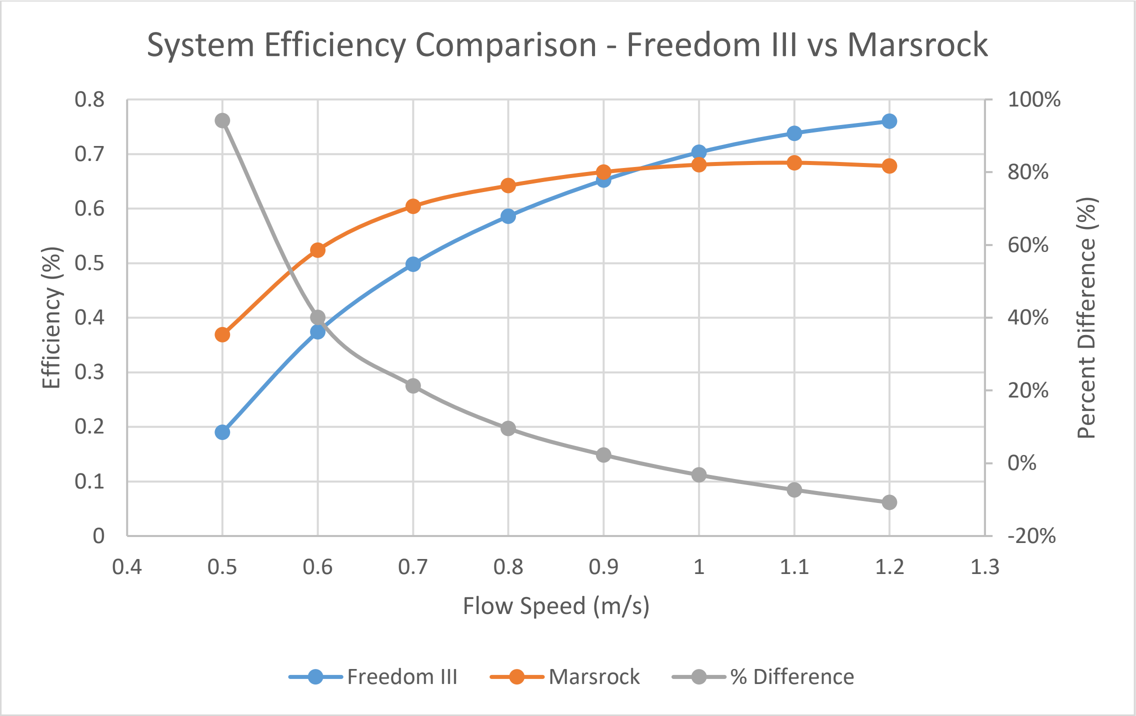

Figure 81: Efficiency of each generator and performance comparison

5. BENCH TEST – ROUND 1

To run bench tests, the DC motor (BLVM640N-GFS) had to be programmed in order to behave as the waterwheel would, based on the previously discussed numerical torque model. More details on bench test programming on Appendix B. Benchtop testing showed a critical characteristic of the PTO that was not accounted for during the simulation phase: it had low torsional rigidity and twisted considerably upon load increase. Not only that, it resonated with the torque fluctuations of the waterwheel (emulated by the DC motor) and caused instabilities to propagate. Figure 82 shows the generator speed and PWM over time for an emulated flow speed of 0.8m/s. Due to the spring-like action of the PTO, instabilities occurred at lower loads and became significantly larger when loads increased (decrease in PWM value). At the very end of the graphic the charge controller was turned off and the instabilities decreased. Figure 83 shows the generator voltage and current over time for the same test. It can be noticed that both quantities are out of phase by approximately 180º, which amplified the twisting motions of the PTO and increased the instability magnitude. Another factor that contributed to instability is the maximum rated torque of the sensor, limited to 53N.m. When the sensor reaches its maximum reading, the difference between torque model values and sensor readings increases, thus increasing the acceleration and therefore the input torque from the DC motor. That is unfortunately a hardware issue and it caused later tests to be conducted at lower flow speeds to avoid that effect.

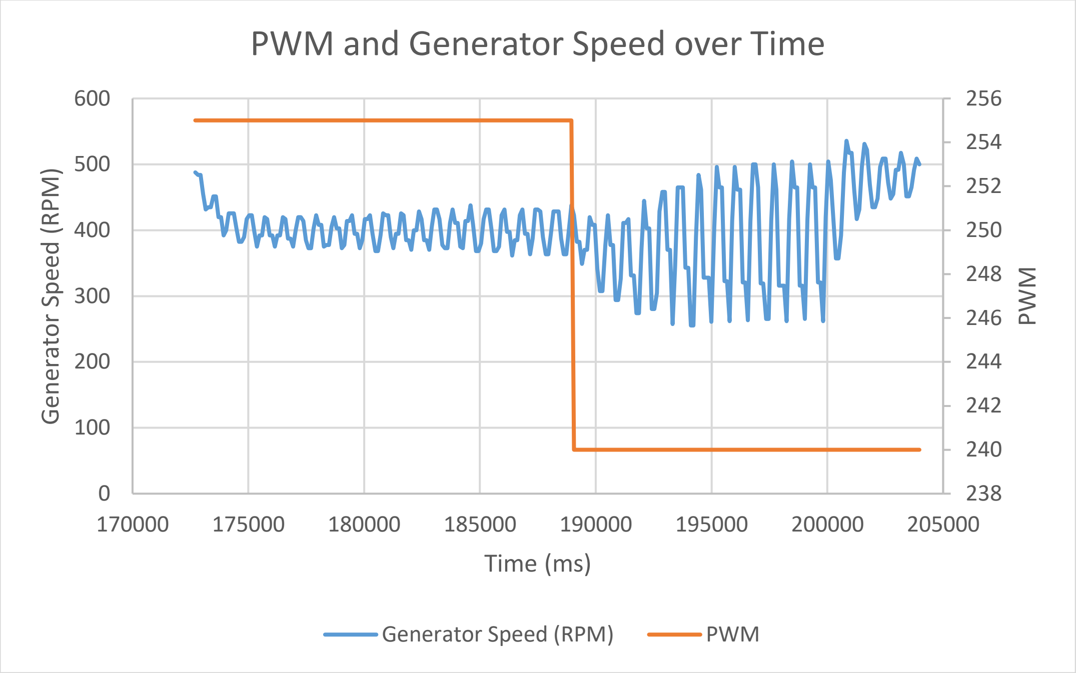

Figure 82: PWM and generator speed over time for an emulated flow speed of 0.8m/s

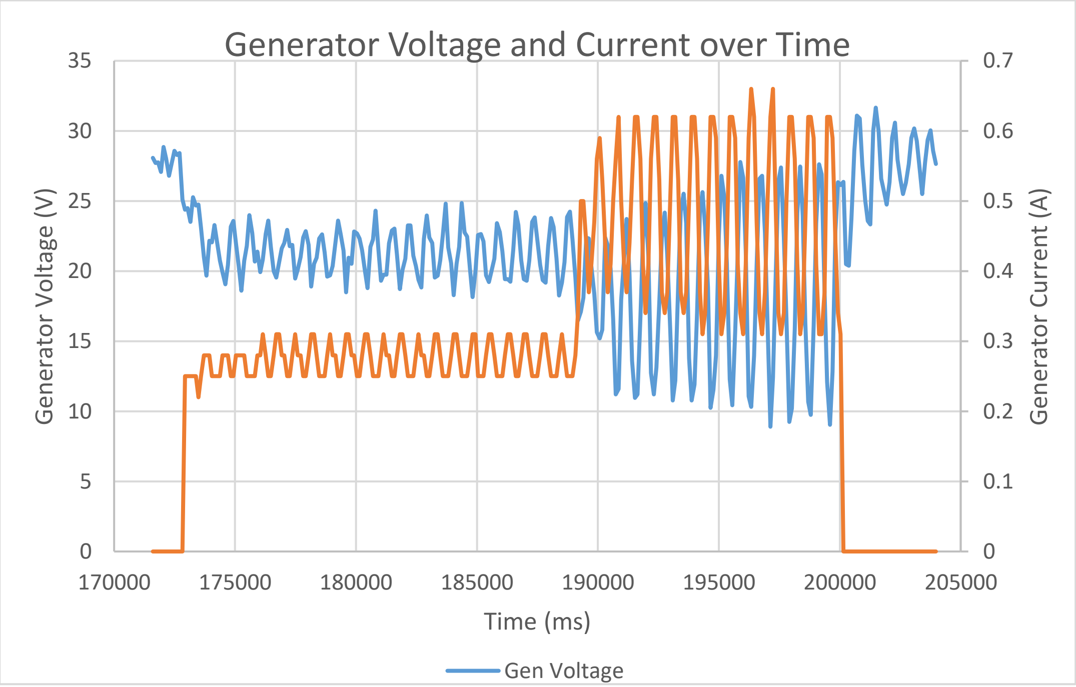

Figure 83: Generator voltage and current over time for an emulated flow speed of 0.8m/s

In an attempt to overcome the instabilities, the PTO was modified to have its stiffness increased so that further testing could be done. However, even with increased torsional stiffness, the oscillations continued to occur, although with a lower amplitude. Tests were run with a constant PWM output to the charge controller and similar behavior was observed, as shown in Figure 84. It is possible to notice that, as the load increased (decrease in PWM), the amplitude of the oscillations increased to a point where the tests had to be interrupted due to risk of structural damage to the PTO.

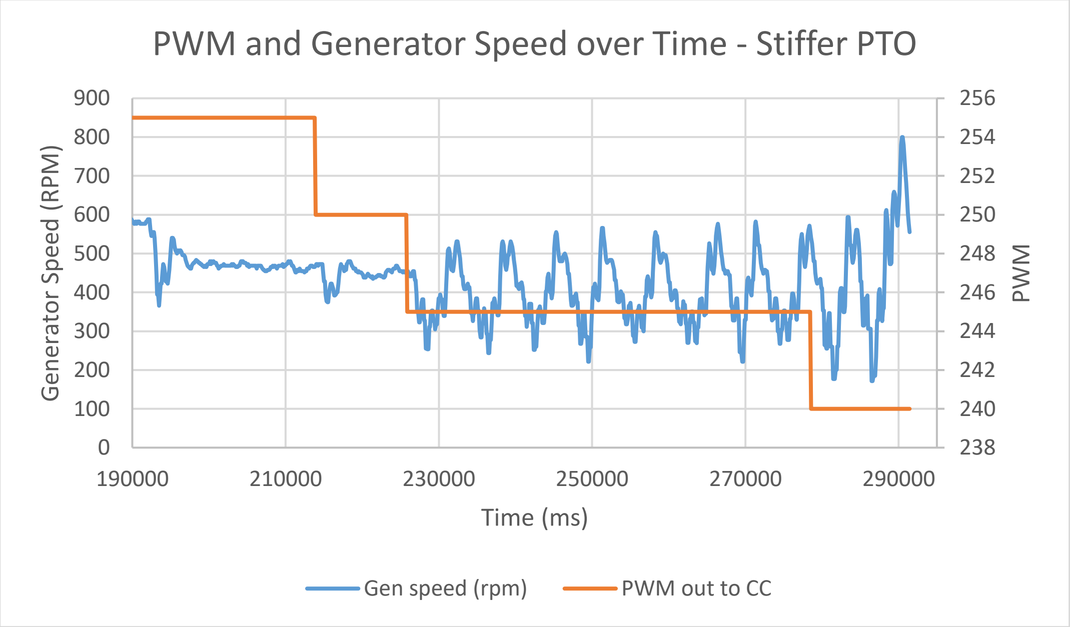

Figure 84: PWM and generator speed over time for an emulated flow speed of 0.8m/s with a stiffer PTO

Upon further examination it was noticed that the charge controller's current regulation was the main responsible for the instabilities observed. That occurred due to the fact that the charge controller is a constant power controller, which means it always tries to input constant power into the battery (50W for the model being discussed). Therefore, upon detecting a decrease in input voltage, it automatically increases the current to maintain the power flow to the battery. The inverse is also true and, upon detecting an increase in input voltage, it decreases the current, which keeps the power constant. The role of the modifications done to the controller is to offset that constant power via PWM by injecting an external current through the resistors of the sensing pin, giving it a false current reading on the battery side. When the PWM is maximum, the current offset is maximum and the charge controller requests minimum current from the generator since it is trying to maintain a low constant power. When the PWM is minimum, the current offset is minimum and the charge controller requests maximum current from the generator, since it is trying to maintain high power.

There is, however, room for regulations within the charge controller, even with a fixed PWM value being sent. Looking back at Equation (49), it can be observed that for a fixed PWM value, if the generator voltage decreases, the generator current will increase and vice versa. Therefore, to overcome the PTO instability issue, a secondary controller was added to the logic and the primary PID controller was modified as follows:

1) Primary controller – the thought process behind this controller lies in the fact that the waterwheel does not respond instantaneously to changes in torque load or flow speed. Therefore, an integral only controller was implemented, with an integral gain of -30, taking the TSR setpoint, relating the TSR error to a torque load, which is then related to a current load on the generator (as before), while running at a frequency of 0.5Hz (1 action every 2 seconds) and averaging measures in between actions. The output of that controller is a generator current demand, which is sent over to the secondary controller.

2) Secondary controller – this controller takes the generator current demand as input and outputs PWM values to the charge controller to keep the current demand the same throughout the averaging cycle of the primary controller. Because small fluctuations on the generator voltage cause the charge controller to vary its current demand (which causes the instability on the PTO), the secondary controller runs at 10Hz (1 action every 0.1 second) and the main program loop updates readings at 40Hz. That gives the secondary controller 4 readings to average between actions.

Figure 85 shows the stability of the system when a sequence of flow speed step inputs is run (0.8m/s, 0.9m/s and 1m/s). It can be noticed that the PWM oscillates to compensate for the corrections done by the charge controller in order to keep the current demand of the primary controller as constant as possible. Although the system stabilizes for the first and second flow speed values, it is noticeable that the oscillations in PWM and generator speed increase at 1m/s. One of the reason for the oscillation is due to the fact that the averaging time (2 seconds) was too long, which caused slow responses of the primary controller when compared to the acceleration of the waterwheel, resulting in the controller falling out of phase with the plant. Moreover, the fact the waterwheel torques are higher at higher flow speeds combined with the saturation of the torque sensor, contributed to the instability increase considerably. Since field tests had to be conducted shortly after the tests described in this section were carried out, the field test control algorithm utilized the latest control configuration ran during this round of bench tests, with an averaging time of 2 seconds and a Ki gain of -30. After the field test results section, more work on the controllability of the system is explored.

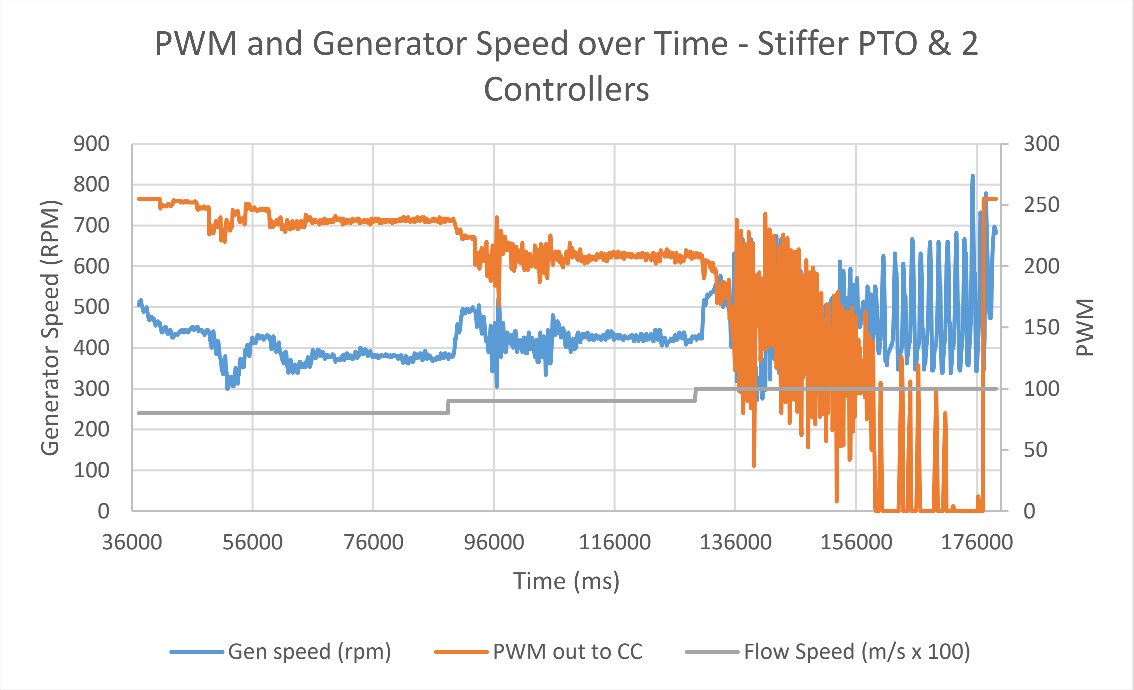

Figure 85: Stability of system with primary and secondary controllers for emulated flow speed step sequence of 0.8, 0.9 and 1m/s with TSR setpoint of 0.4

6. FIELD TESTS – ROUND 2

This section goes over the second round of field tests, where the turbine speed controller is implemented and tested. Field tests were ran utilizing a sampling frequency of 10Hz and an averaging time of 2 seconds, yielding 20 samples per averaging (the controller calculated torque demands after averaging readings for 2 seconds). The TSR setpoints were set to 0.4 and the CVT ratio was changed by the user based on the generator voltage and the PWM limits. If the generator voltage fell below 7V the charge controller shut off and no power was produced. If the PWM reached its highest value (minimum load demand) and the wheel speed was still below its speed setpoint, the CVT ratio was decreased. If the PWM reached its minimum value (highest load demand) and the wheel speed was still above its speed setpoint, the CVT ratio was increased. In addition, if the PWM was fluctuating under a certain threshold (for example 100), the CVT ratio was increased in order to increase efficiency due to faster generator speed and lower current demands. Although the actuations of the CVT were manually performed by the user during the current round of field tests, the insights gained from doing so were invaluable and crucial for a better understanding of what the controller needs to accomplish.

On the post-processing end, a moving average filter with a window size of 1000 samples was applied to the dataset. To obtain the turbine Cp values throughout the entire test duration, two calculation methods were utilized:

1) Calculate turbine torque utilizing generator torque and PTO efficiency models, multiply the calculated torque by the turbine angular speed (obtaining turbine

mechanical power) and divide that quantity by the respective flow power (obtained by computing $1/2\rho A U^3$, where U is all the flow speed readings:

$$C_{p1} = \frac{P_{ww}}{P_{flow}} = \frac{T_{ww}\omega_{ww}}{P_{flow}} = \frac{\varphi\varphi_{cvt}T_{g,model}\omega_{ww}}{1/2\rho A\varepsilon_{model}U^3} \tag{62}$$

2) Calculate turbine power by dividing the generator electrical power output readings by the PTO efficiency model (obtaining the waterwheel power), and divide that quantity by the respective flow power as done above:

$$C_{p2} = \frac{P_{ww}}{P_{flow}} = \frac{P_{gen}}{\varepsilon_{model}P_{flow}} = \frac{V_{gen}I_{gen}}{1/2\rho A\varepsilon_{model}U^3} \tag{63}$$

The abovementioned calculations were implemented to minimize errors due to model inaccuracies, especially the first method, where the generator torque and PTO efficiency models are multiplied by one another, potentially increasing the overall error in estimating the power coefficient. After obtaining the two Cp curves, an average Cp is calculated by averaging the two curves over time. As it will be demonstrated in analytical torque derivation section, the power coefficient of a drag-based machine such as the waterwheel is not dependent of flow speed, which allows for a final Cp curve to be obtained. However, although the power coefficient is, in theory, independent of flow speed, another set of curves is obtained to show the performance of the turbine under varying flow speeds, as a Cp vs TSR plot for a range of flow speeds experience during testing. Both the final Cp curve and the Cp curves per flow speeds were obtained by sweeping through the TSR data array, allocating its values within pre-defined TSR bins and allocating the respective Cp values for the current iteration index into Cp matrices, in which the number of rows equals the number of time increments in data, and the number of columns equals the TSR bins (from 0.1 to 0.8).

6.1 Field Test (01/10/2024)

For this field test day, the 7-blade, full submergence waterwheel was tested, and the control system tracked its speed setpoints relatively well, although some bugs in the code still had to be addressed. Figure 86 shows the waterwheel speed, both setpoint and measured, which displays a moderate speed tracking performance starting at around 4000 seconds, when flow speed increased to values that allow for speed tracking. Figure 87 displays the flow speed and electrical power output, and the clear increase in power is noticeable with increased flow speed, while Figure 88 shows the overall system efficiency in converting flow power to electrical power. Figure 89 illustrated the two Cp curves obtained through both calculation methods, as well as the resulting average Cp curve. Note that the first curve in blue seems to overshoot Cp values from the 6000-second marc forward. The average Cp curve allows for the plot of an overall Cp curve for the turbine on that test day, displayed in Figure 90. Furthermore, Figure 91 shows the performance of the turbine per flow speed for that test day, where it can be seen that the best performance occurred at a flow speed of 0.8 m/s.

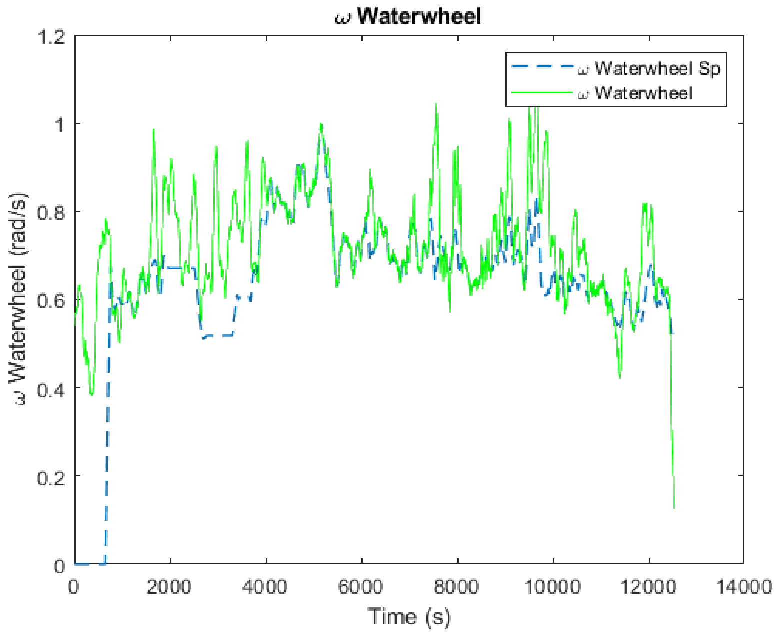

Figure 86: Waterwheel speed - setpoint vs measured – 01/10/24

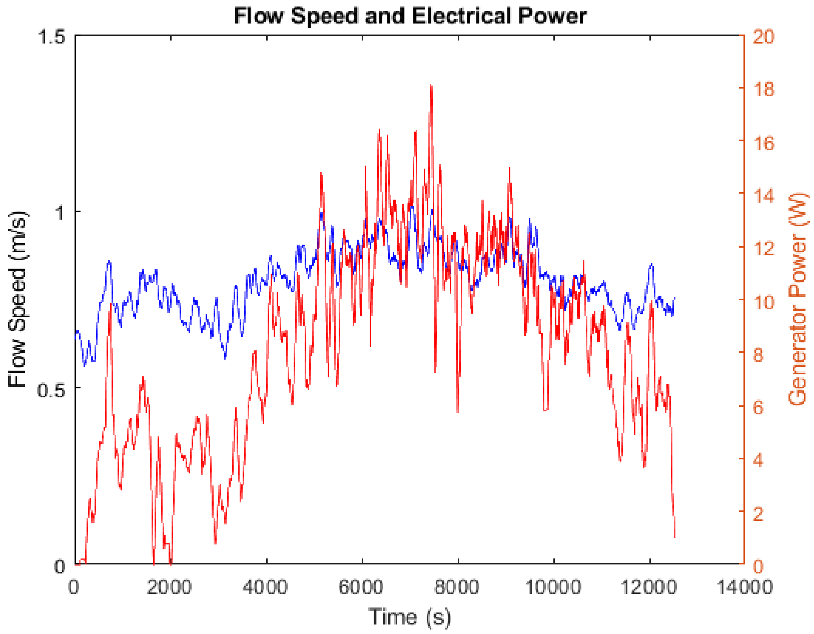

Figure 87: Flow speed vs electrical power – 01/10/24

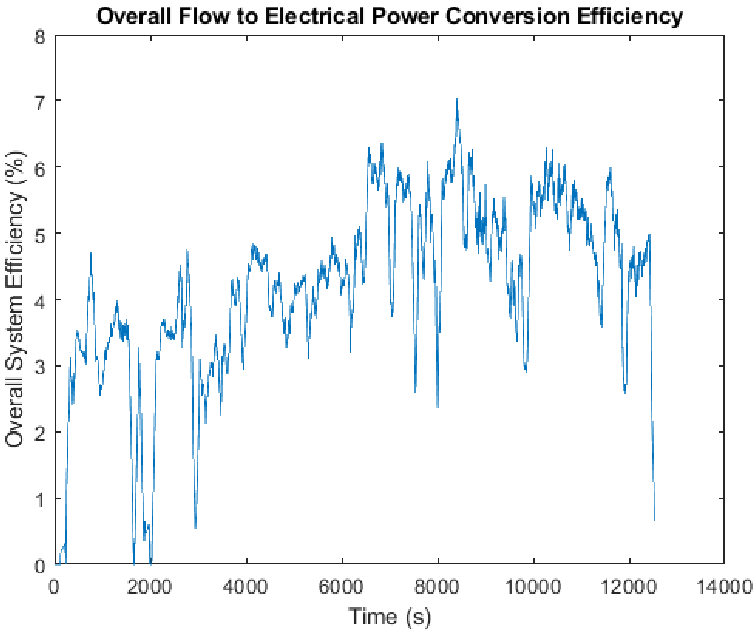

Figure 88: Overall system efficiency - from flow to electrical power – 01/10/24

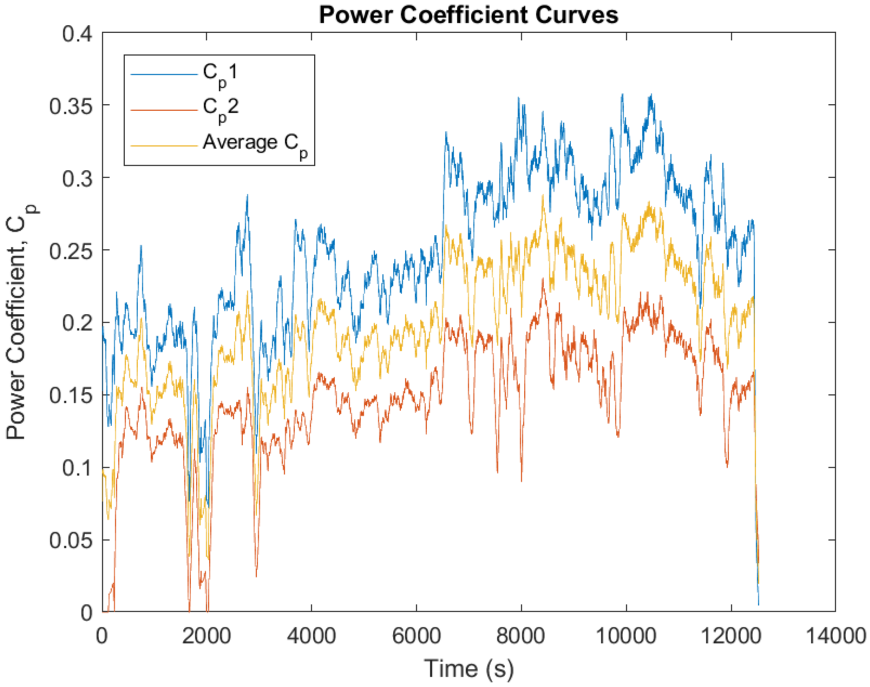

Figure 89: Power coefficient curves obtained via two calculation methods, and the resulting average curve - field test 1/10/24

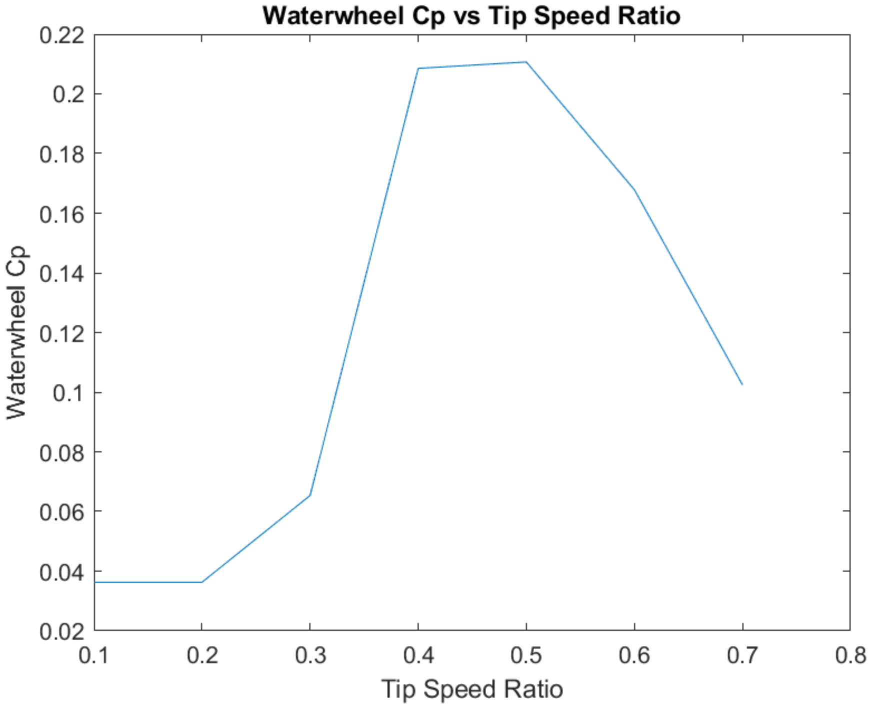

Figure 90: Resulting Cp curve - field test 01/10/24

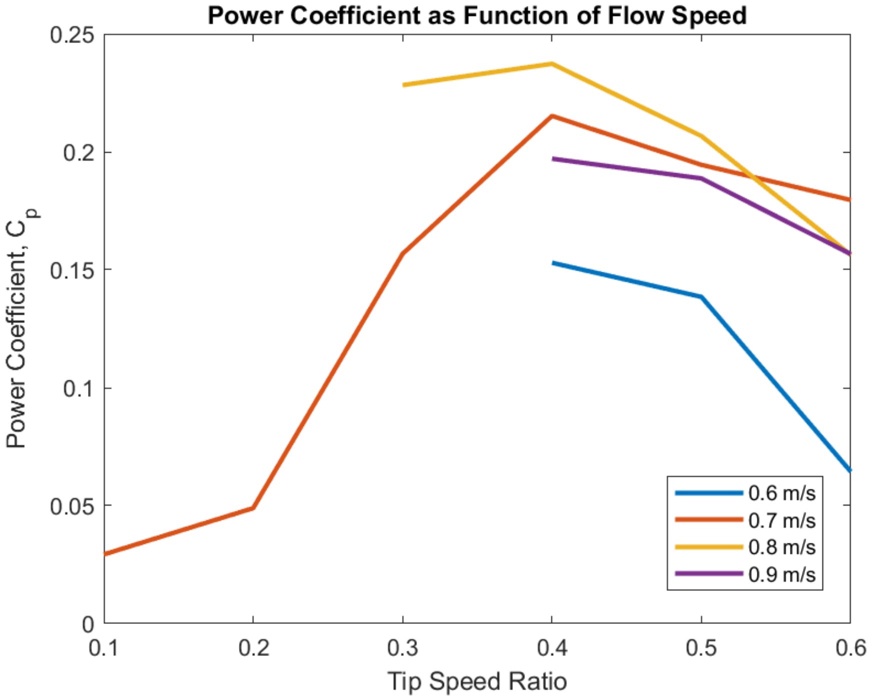

Figure 91: Cp vs TSR curves per flow speed – field test 01/10/24

6.2 Field Test (01/11/2024)

For this field test day, the 7-blade, half submergence waterwheel was tested, and the results in terms of speed control were not satisfactory as the waterwheel did not follow the speed setpoints set by the controller, as illustrated in Figure 92. The main reason is not fully understood, but the dataset obtained for PWM values, shown in Figure 93, show that no speed control was performed, which could have been a software issue, since the generator voltage achieved high enough values to perform speed control. Figure 94 shows the flow speed and generator electrical power output for that test day, while Figure 95 illustrated the overall system efficiency in converting flow power to electrical power. Figure 96 shows the two calculated Cp curves and the average Cp curve obtained, where it is noticeable that the first curve overshoots Cp values, especially at approximately 3500 seconds. The average Cp curve delivers more reasonable performance metrics of the turbine and allows the plot of an overall Cp curve as shown in Figure 97. Figure 98 shows the performance of the as a Cp curve per flow speed, where it can be noticed that the turbine had its best performance at 1.2 m/s.

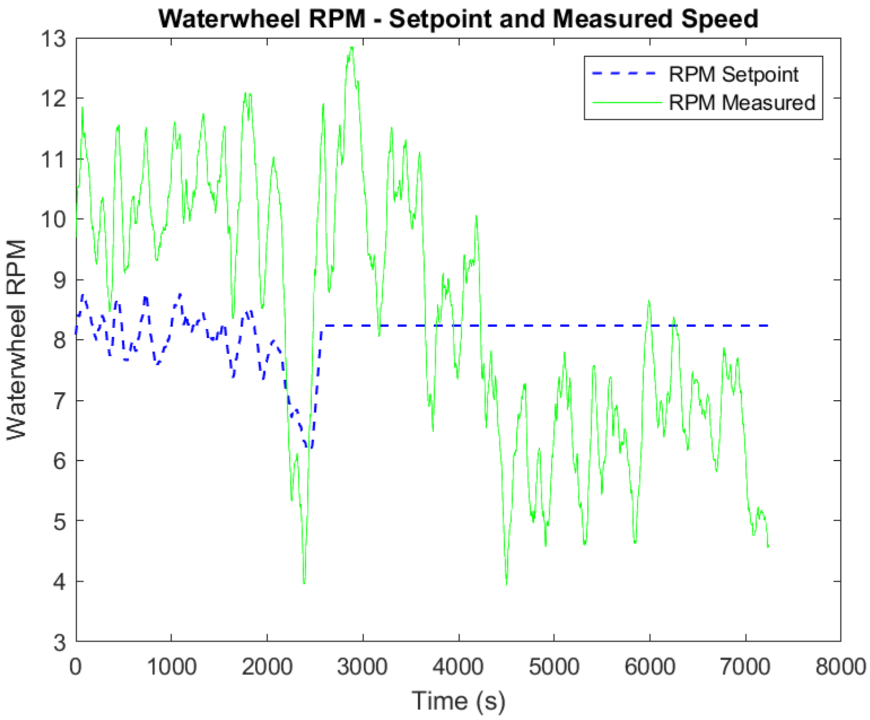

Figure 92: Waterwheel speed - setpoint vs measured – field test 01/11/24

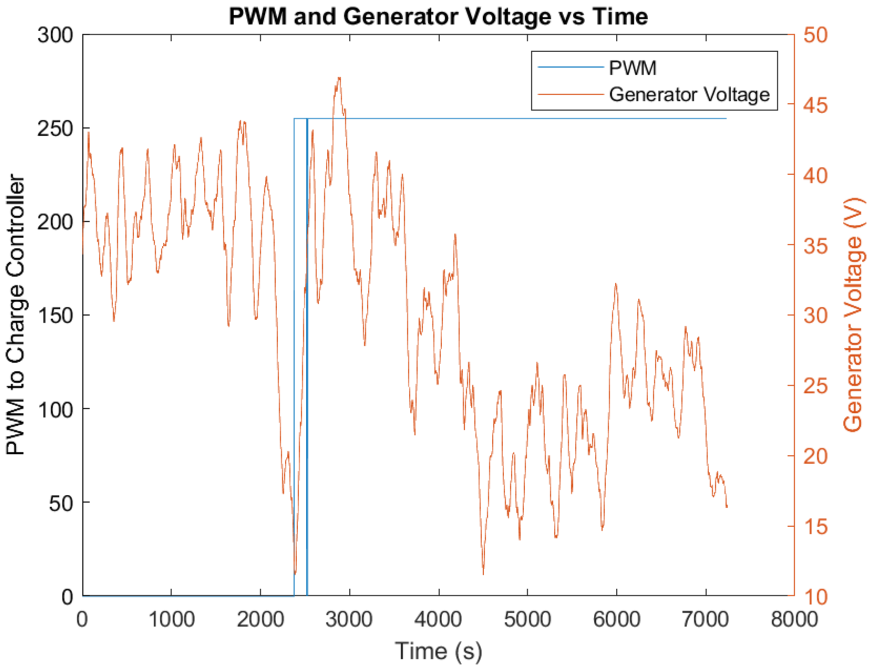

Figure 93: PWM and generator voltage – field test 01/11/24

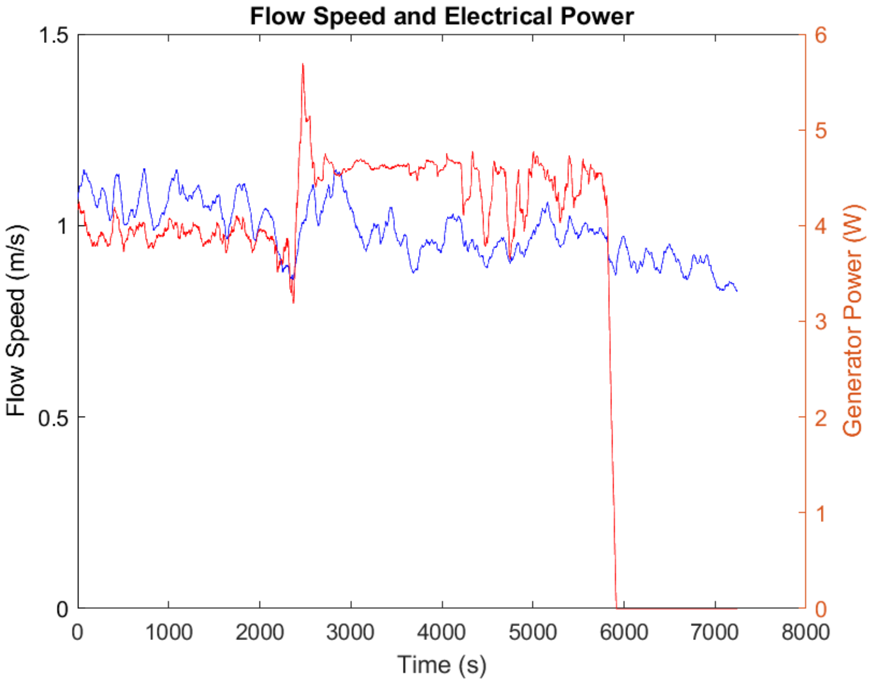

Figure 94: Flow speed vs electrical power – field test 01/11/24

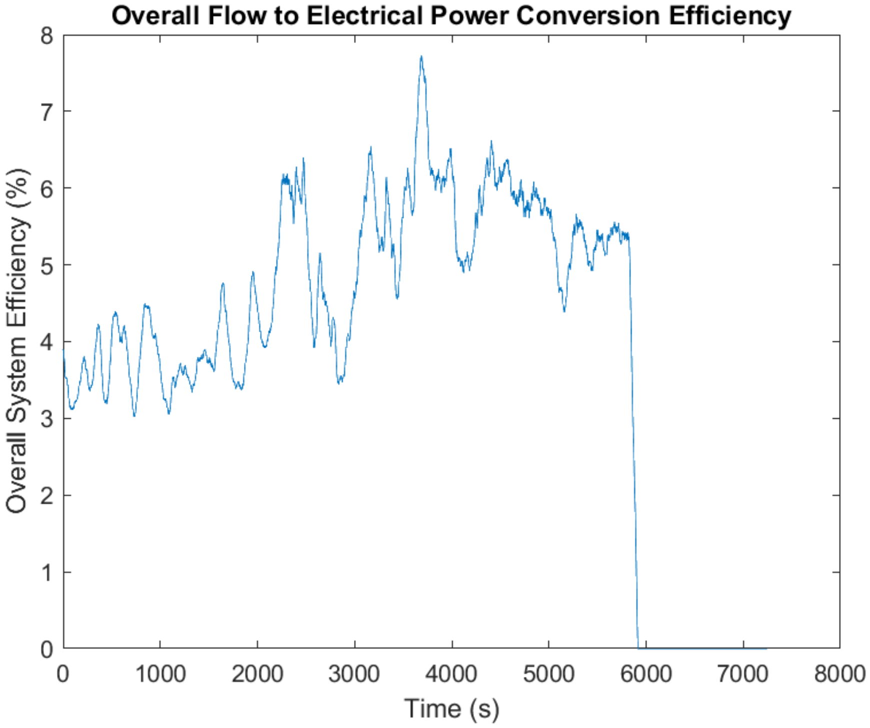

Figure 95: Overall system efficiency - from flow to electrical power – field test 01/11/24

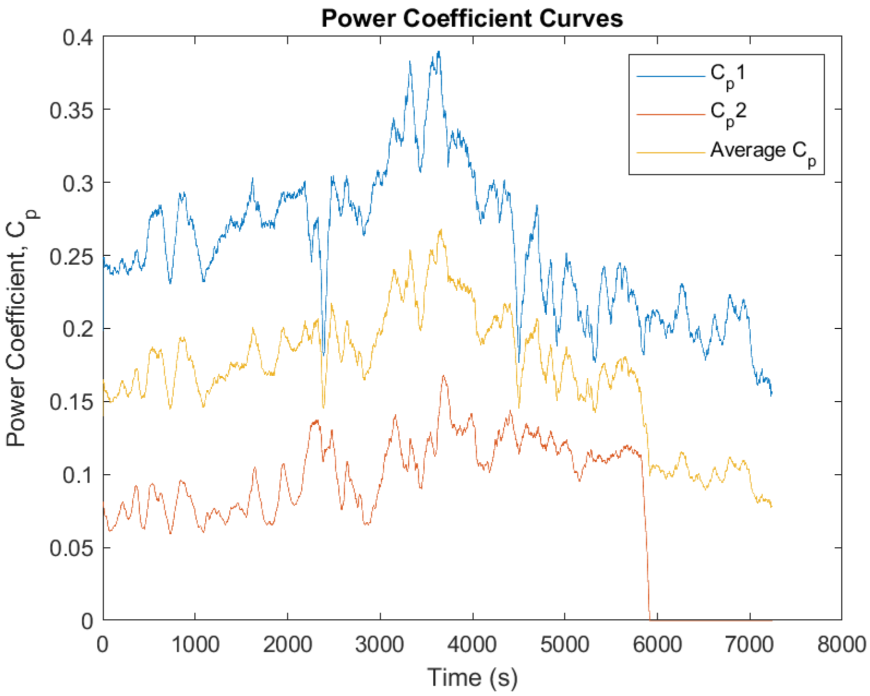

Figure 96: Power coefficient curves obtained via two calculation methods, and the resulting average curve - field test 1/11/24

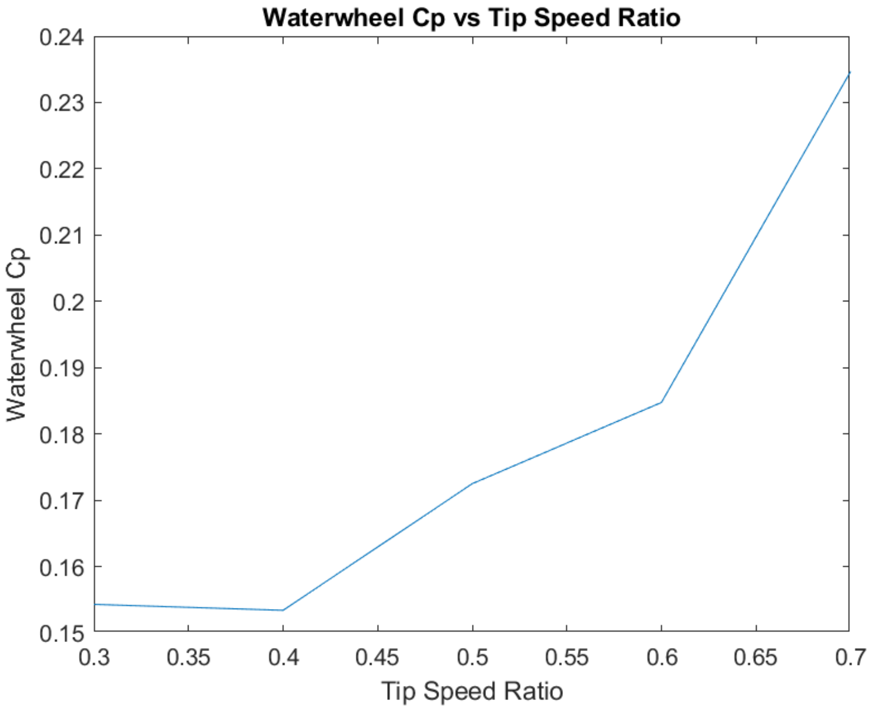

Figure 97: Resulting Cp curve - field test 01/11/24

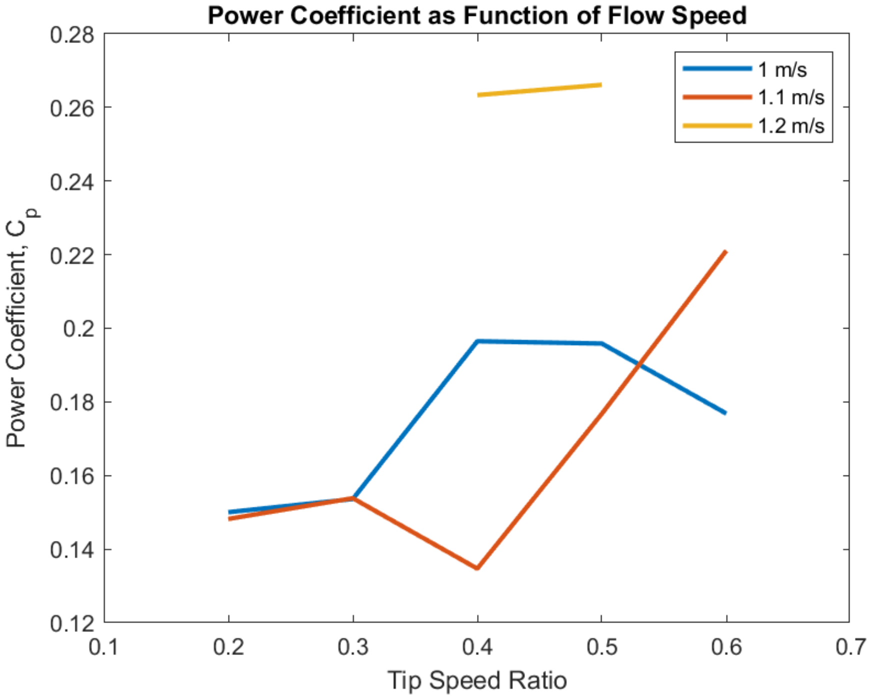

Figure 98: Cp vs TSR curves per flow speed – field test 01/11/24

6.3 Field Test (01/16/2024)

For this field test day, once again the 7-blade, half submergence waterwheel was tested, and the speed control performance was poor, as illustrated in Figure 99. The waterwheel did not follow the speed setpoints as set by the controller, even though PWM values were constantly sent to the charge controller for current demand modulation, as shown in Figure 100. The main hypothesis here is that the measurement averaging frequency used to make decisions on torque load was too slow when compared to the average flow speed and the speed setpoints of the wheel, which caused delayed decision-making by the control system (this round of tests utilized 2-second averaging time and 10Hz sampling frequency). Figure 101 shows the flow speeds generator output power for that test day, while Figure 102 shows the overall system efficiency in converting flow power to electrical power. It can be noticed that poor speed control results in poor system performance. Figure 103,

Figure 104 and Figure 105 give further information on the performance of the turbine during that field test day, which evidences the low performance of the turbine due to lack of controllability.

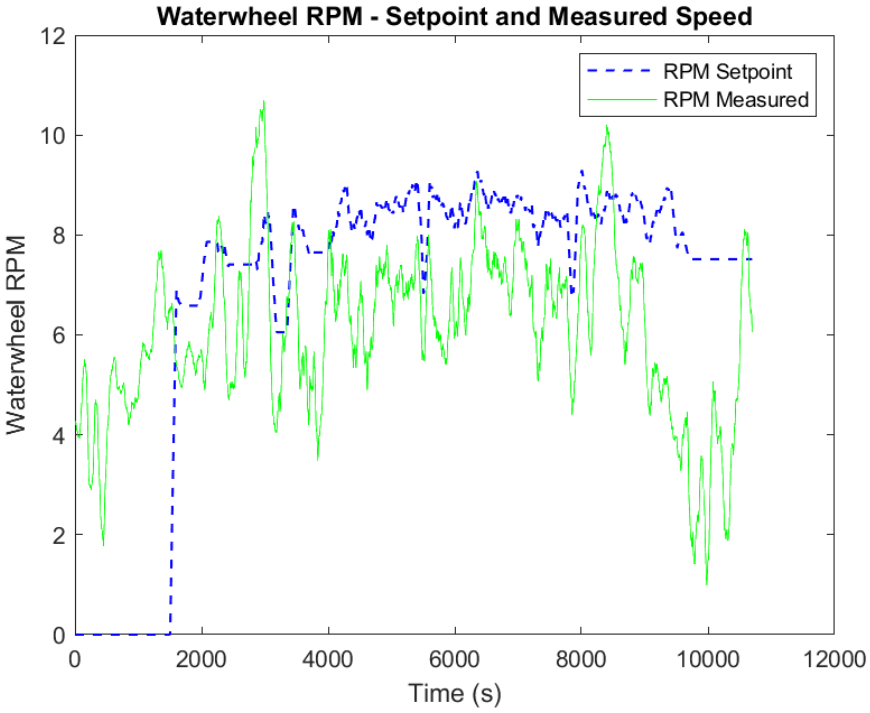

Figure 99: Waterwheel speed - setpoint vs measured – field test 01/16/24

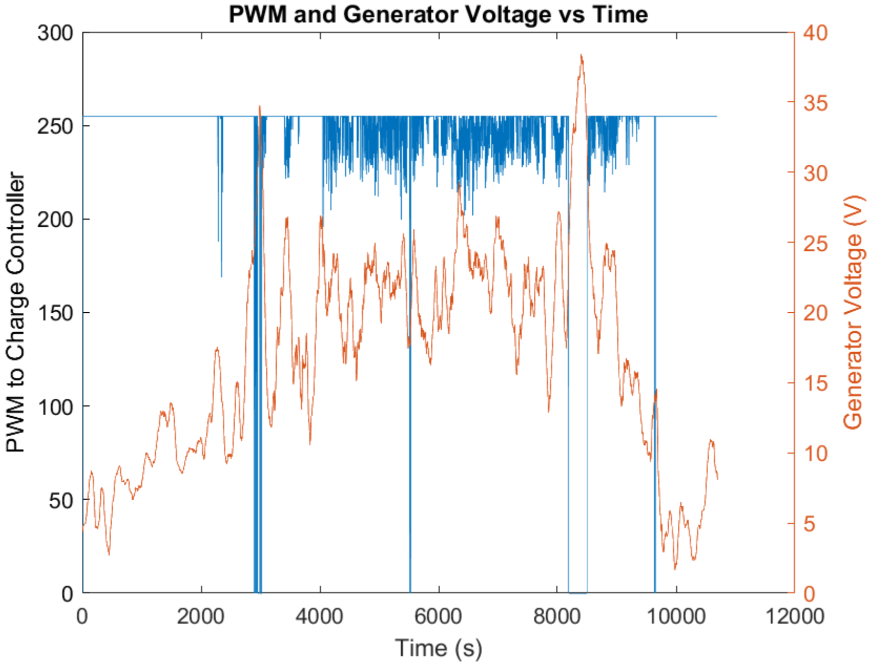

Figure 100: PWM and generator voltage – field test 01/16/24

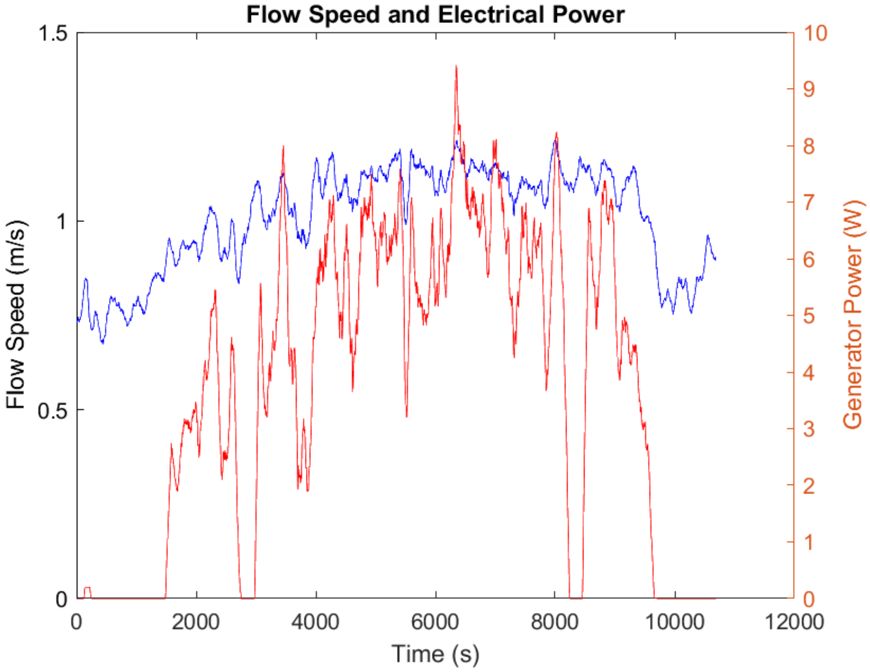

Figure 101: Flow speed vs electrical power – field test 01/16/24

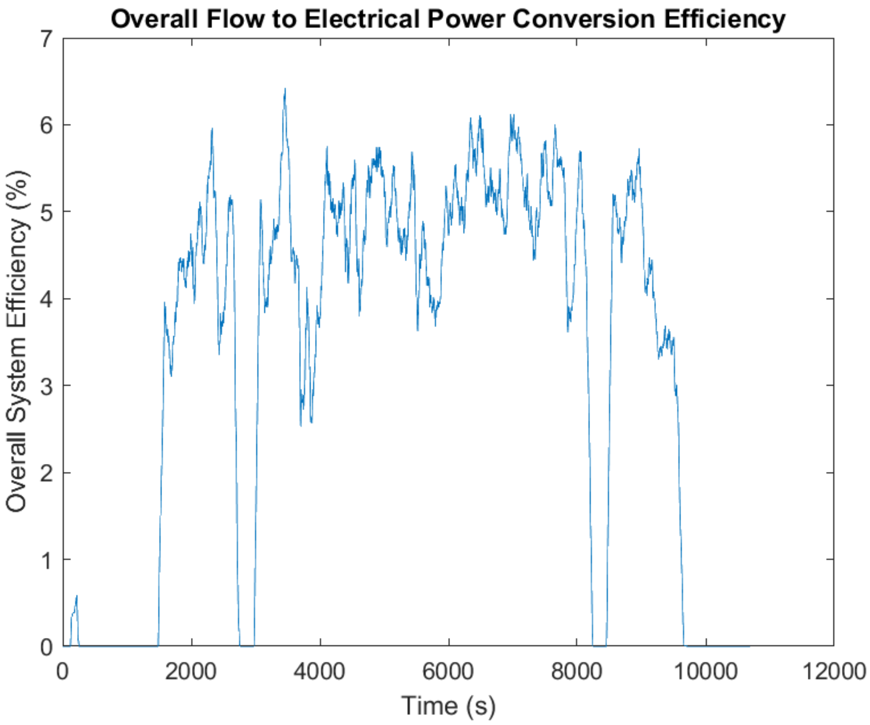

Figure 102: Overall system efficiency - from flow to electrical power – field test 01/16/24

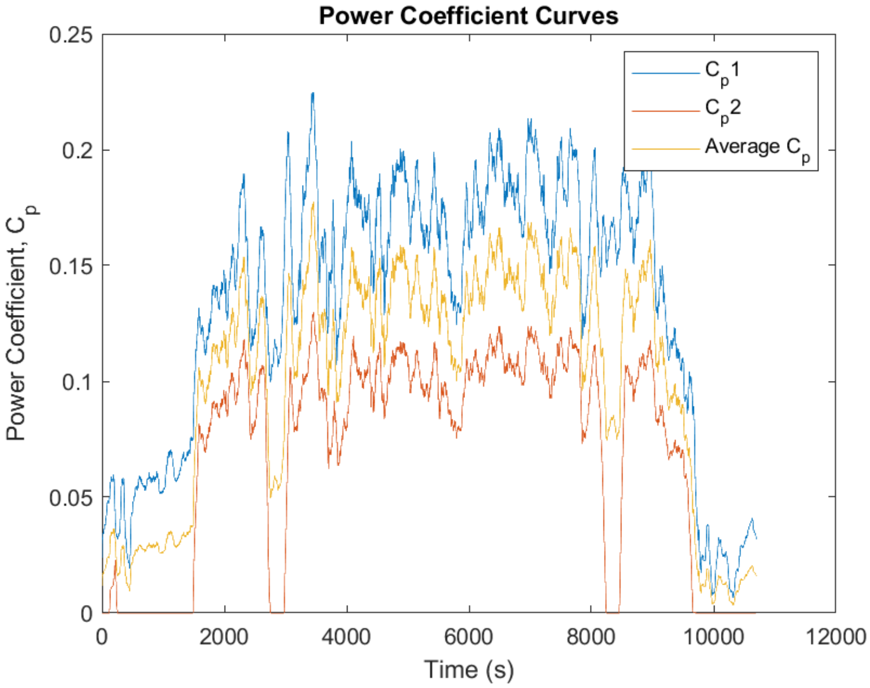

Figure 103: Power coefficient curves obtained via two calculation methods, and the resulting average curve - field test 1/16/24

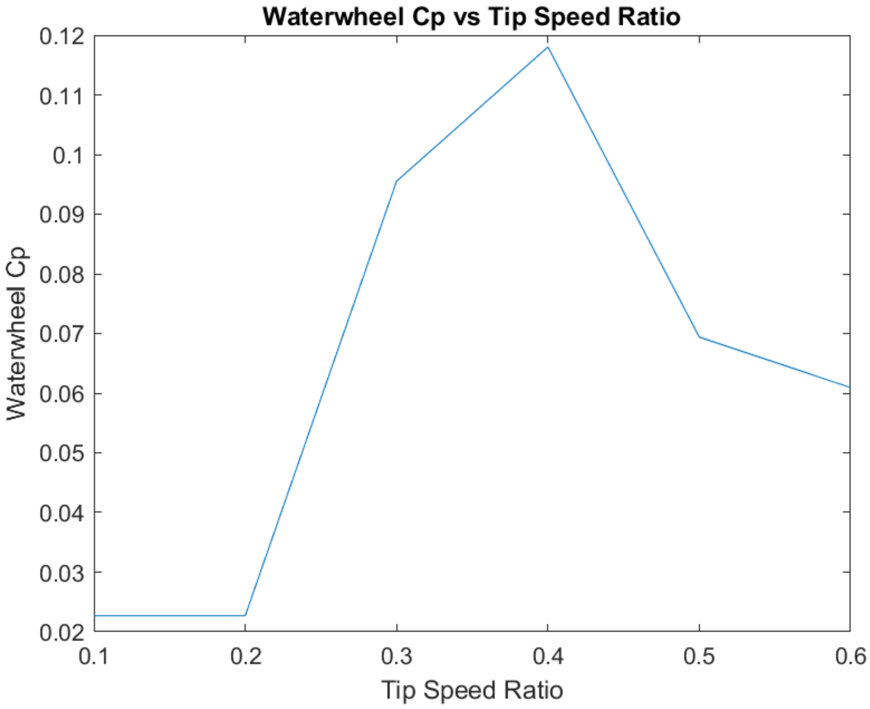

Figure 104: Resulting Cp curve - field test 01/16/24

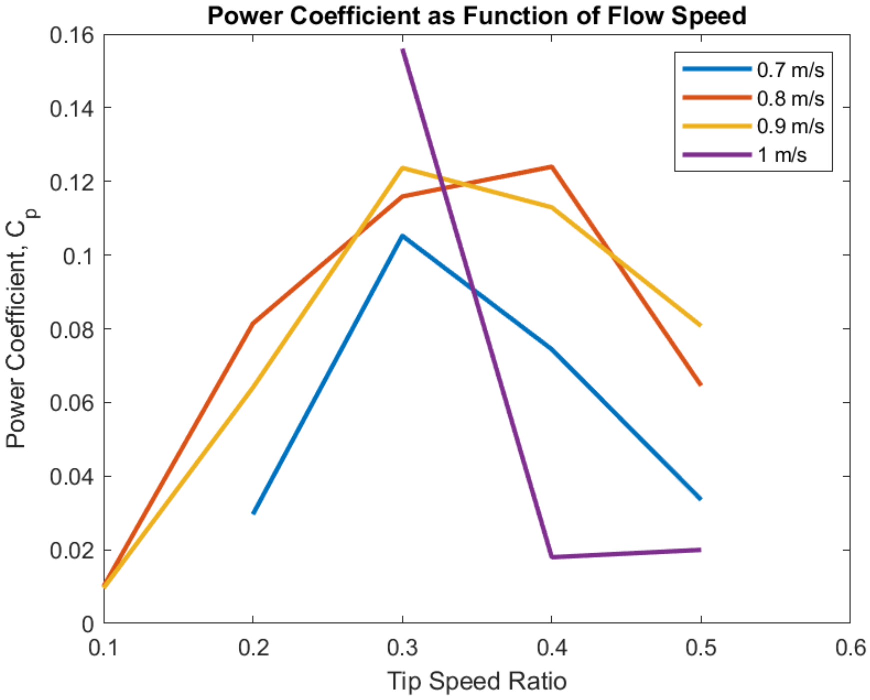

Figure 105: Cp vs TSR curves per flow speed – field test 01/16/24

6.4 Field Test (01/17/2024)

For this field test day, the 9-blade, full submergence waterwheel was tested, and the speed control performance showed relatively good performance, shown in Figure 106. As the flow speed increased, it became impossible for the waterwheel to hold the designated TSR setpoint, with PWM values constantly reaching zero (i.e., maximum current demand) and CVT positioned at its highest ratio, as shown in Figure 107, with the PWM plotted after a 800-sample window-size moving average filter. This phenomenon happened as explained for other field tests conducted on 01/11/24 and 01/16/24, when the flow and turbine speed setpoints become too fast for the controller to take action in a timely manner. Figure 108 shows the flow speed and output electrical power, with output power peaking at 30W and maximum flow speeds reaching over 1.3 m/s. Figure 109 illustrated the overall system efficiency in converting flow power to electrical power, with peak efficiency nearing 16%. Figure 110 depicts the turbine's power coefficient throughout the complete test, with an average C_p over 0.2. By sweeping through the C_p data and plotting it against TSR, Figure 111 is obtained, which illustrated the resulting C_p curve for that test day. Finally, Figure 112 shows the power coefficient curves per flow speed.

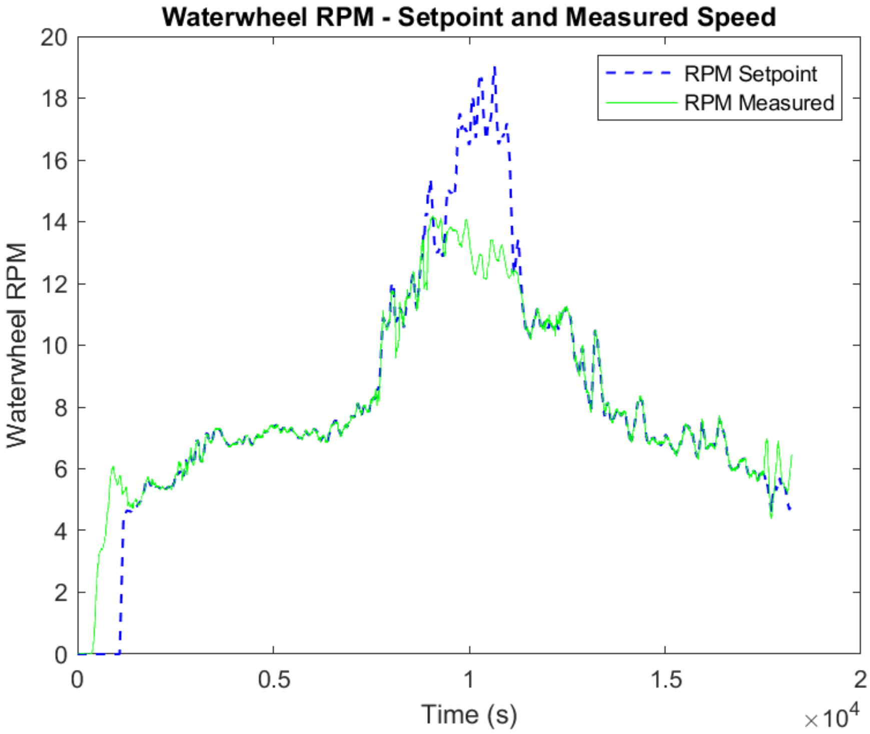

Figure 106: Waterwheel speed - setpoint vs measured - field test 01/17/24

Figure 107: PWM, CVT's servo position and user-set TSR setpoint - field test 1/17/24

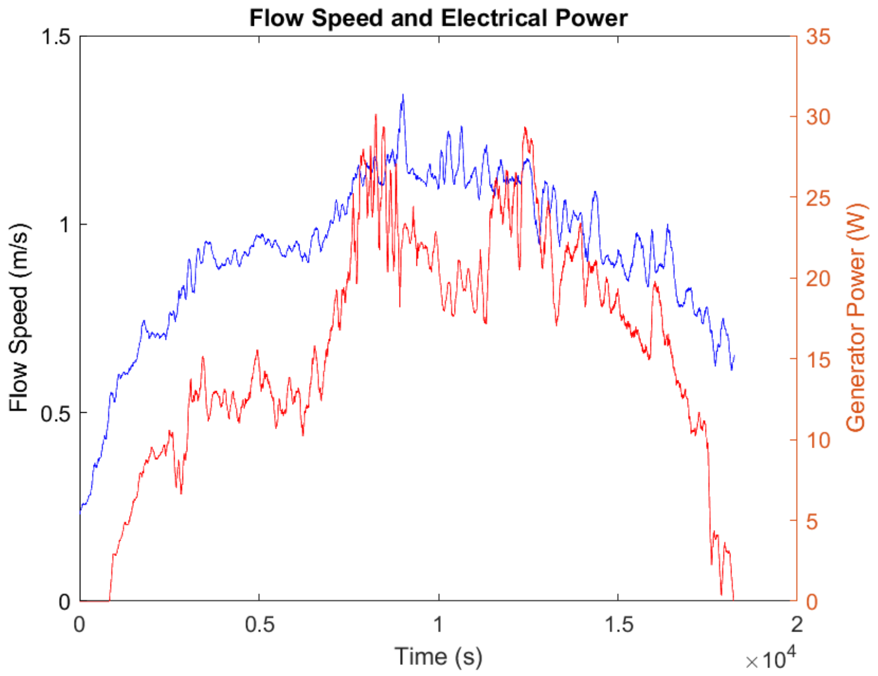

Figure 108: Flow speed vs electrical power - field test 01/17/24

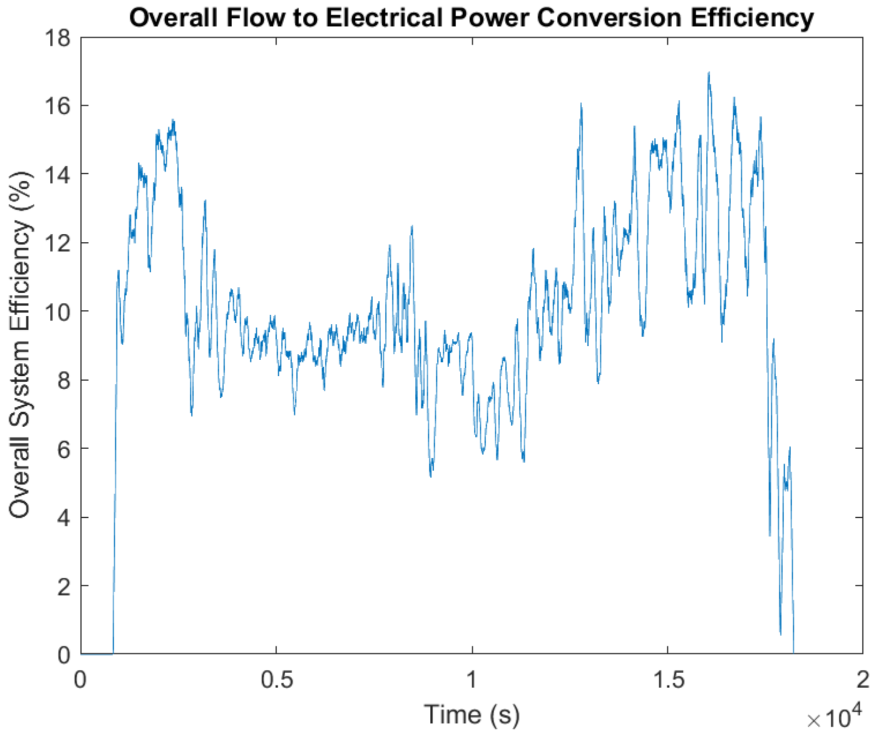

Figure 109: Overall system efficiency - from flow to electrical power – 01/17/24

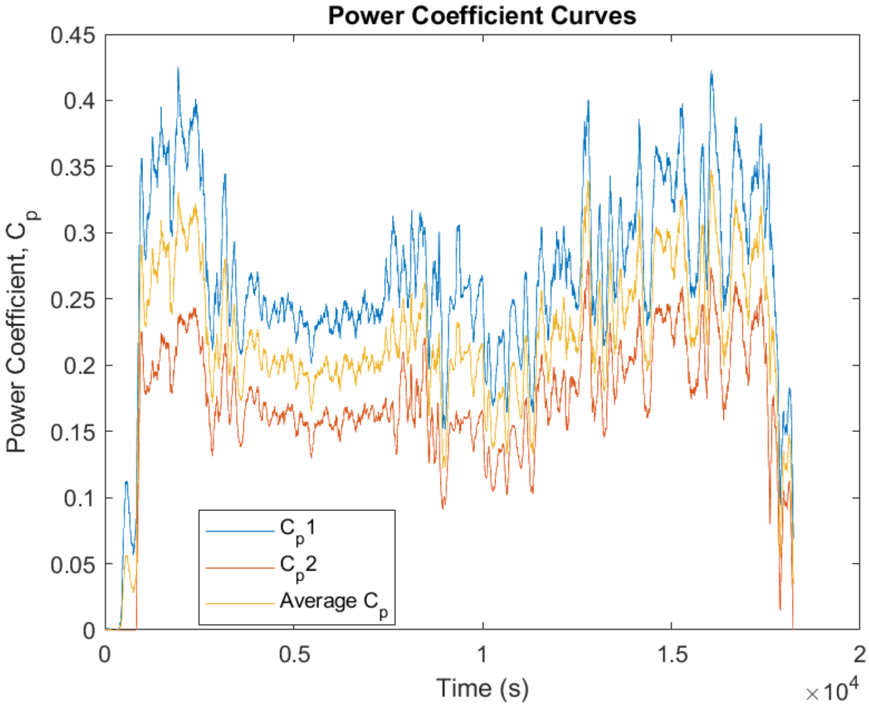

Figure 110: Power coefficient curves obtained via two calculation methods, and the resulting average curve - field test 1/17/24

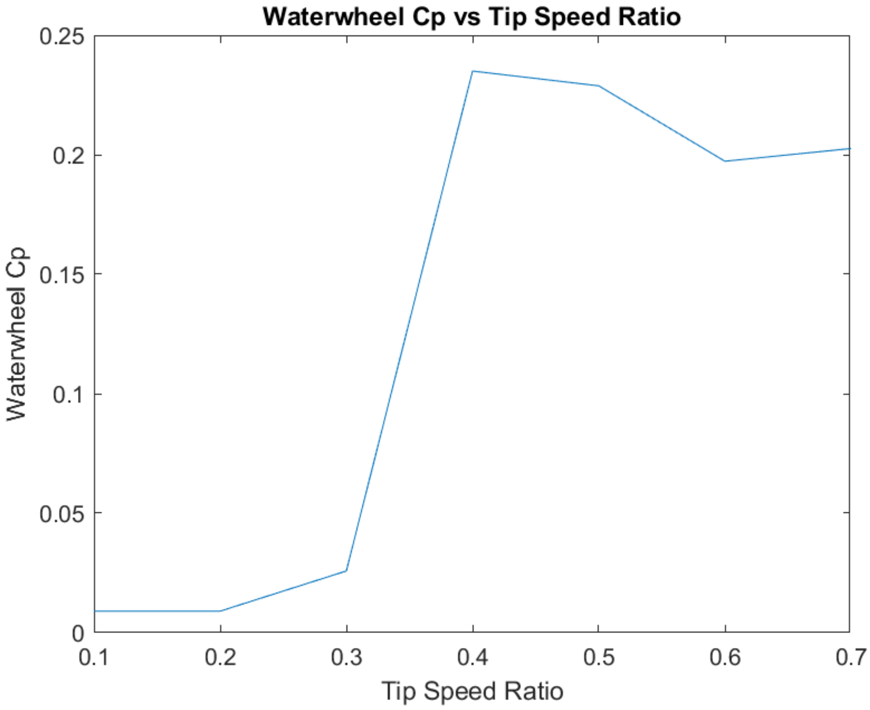

Figure 111: Resulting Cp curve - field test 01/17/24

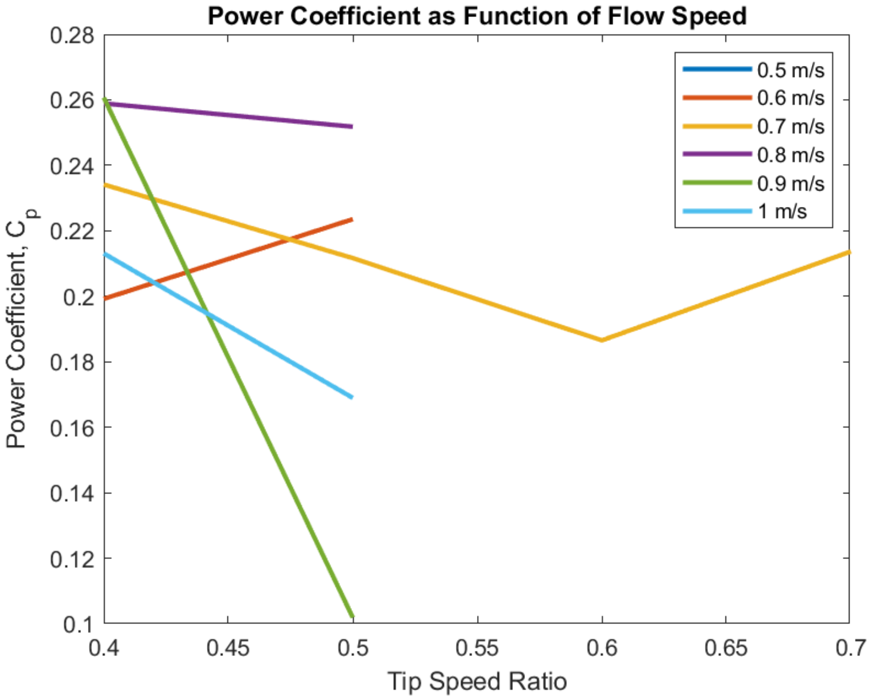

Figure 112: Cp vs TSR curves per flow speed – 01/17/24

6.5 Field Test (01/19/2024)

For this field test day, the 9-blade, half submergence waterwheel was tested, and the speed control performance was relatively good, as illustrated in Figure 113, which shows the waterwheel speed, both setpoint and measured, and a moderate-to-satisfactory speed tracking performance starting at around 3000 seconds, when flow speed increased to values that allow for speed tracking. Figure 114 shows flow speed and electrical power output, while Figure 115 shows the overall system performance in converting flow power to electrical power. It is noticeable the increase in performance, especially when compared to test days when the speed tracking controller did not perform well, with gains in efficiency of almost twice the previous efficiencies. Those results illustrate the importance of proper speed control in order to maximize the performance of the turbine. Figure 116 displays the Cp curves obtained by utilizing the two calculation methods previously mentioned, as well as the average Cp curve, resulting in the turbine Cp vs TSR curve displayed in Figure 117. The increase in turbine efficiency is perceptible when comparing the Cp curve obtained in Figure 117 with other curves for other test days, especially days in which the speed control algorithm did not perform well. Finally, Figure 118 shows the performance of the turbine per flow speed as Cp curves for each flow speed where power was produced.

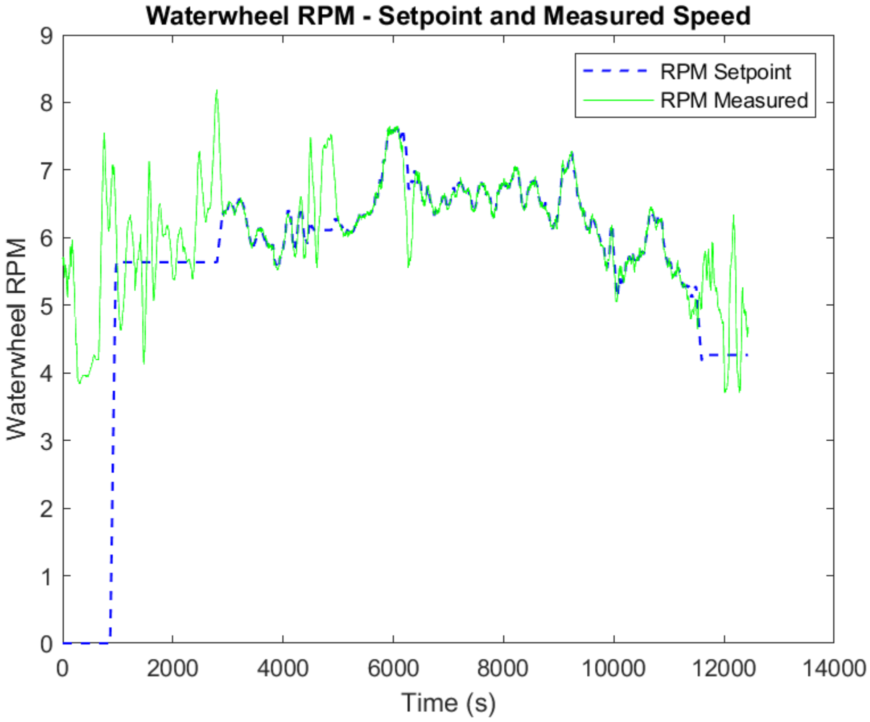

Figure 113: Waterwheel speed - setpoint vs measured – field test 01/19/24

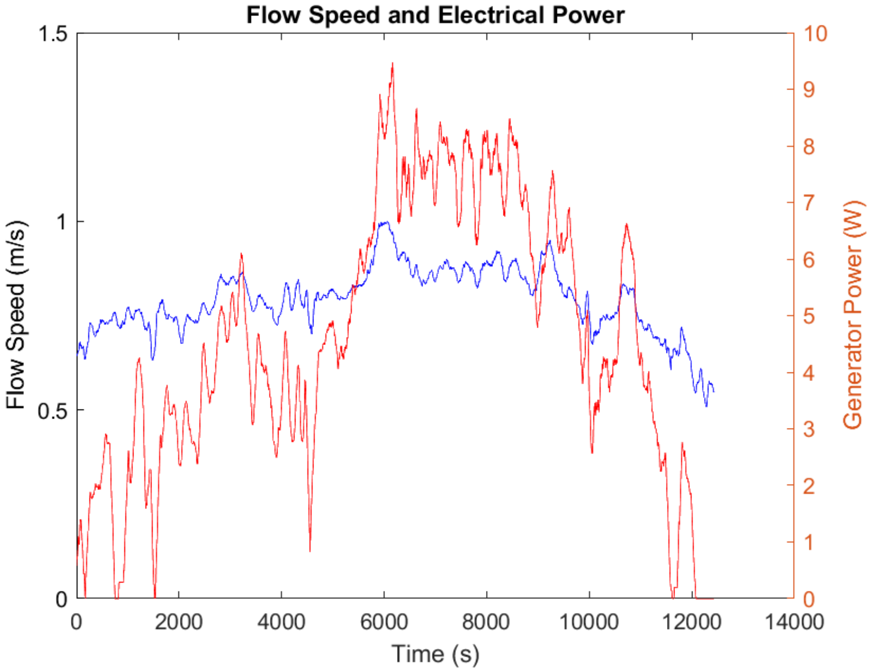

Figure 114: Flow speed vs electrical power – field test 01/19/24

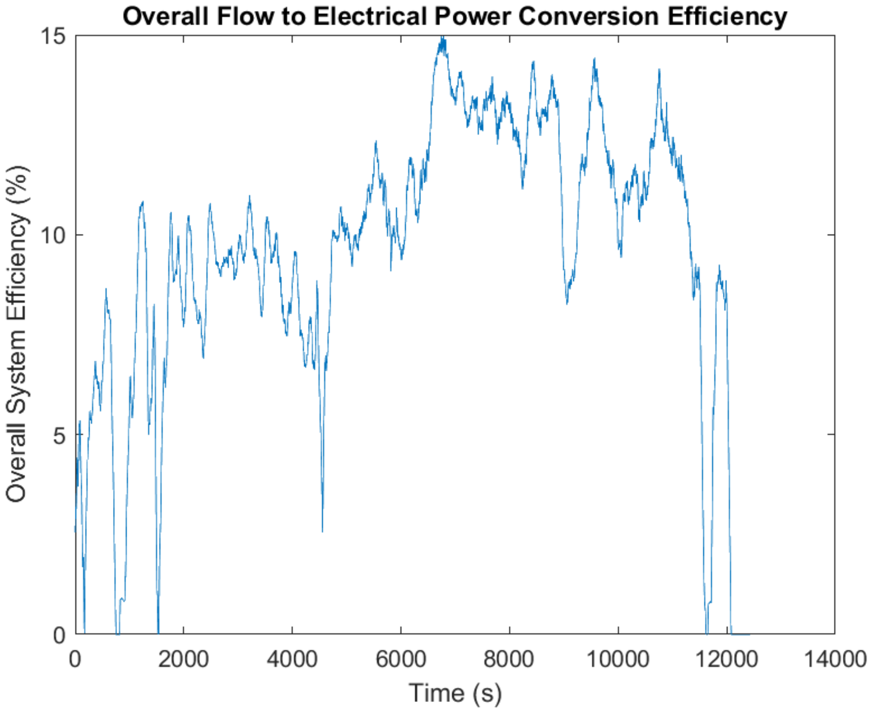

Figure 115: Overall system efficiency - from flow to electrical power – 01/19/24

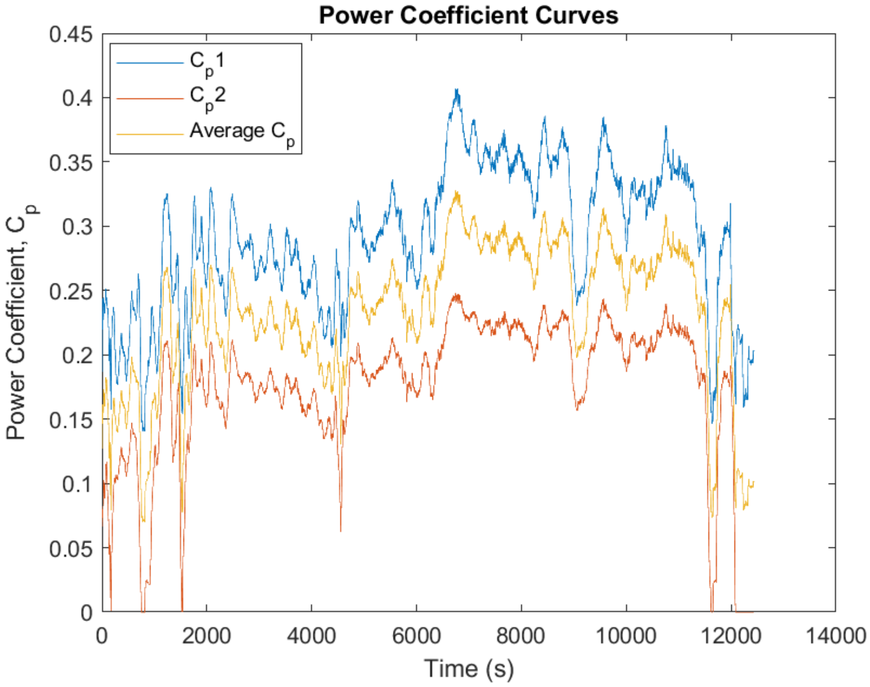

Figure 116: Power coefficient curves obtained via two calculation methods, and the resulting average curve - field test 1/19/24

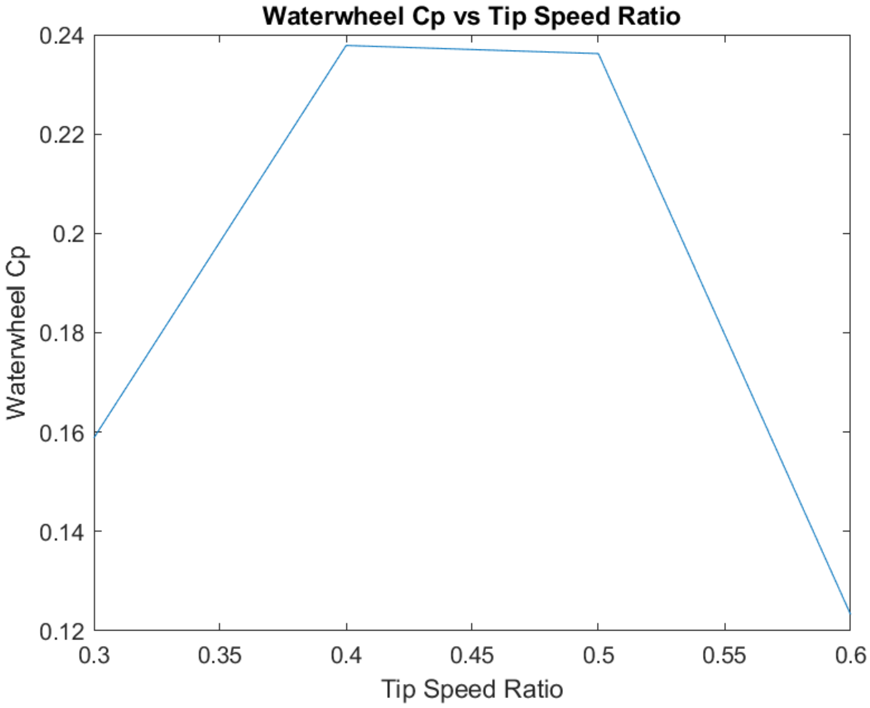

Figure 117: Resulting Cp curve - field test 01/19/24

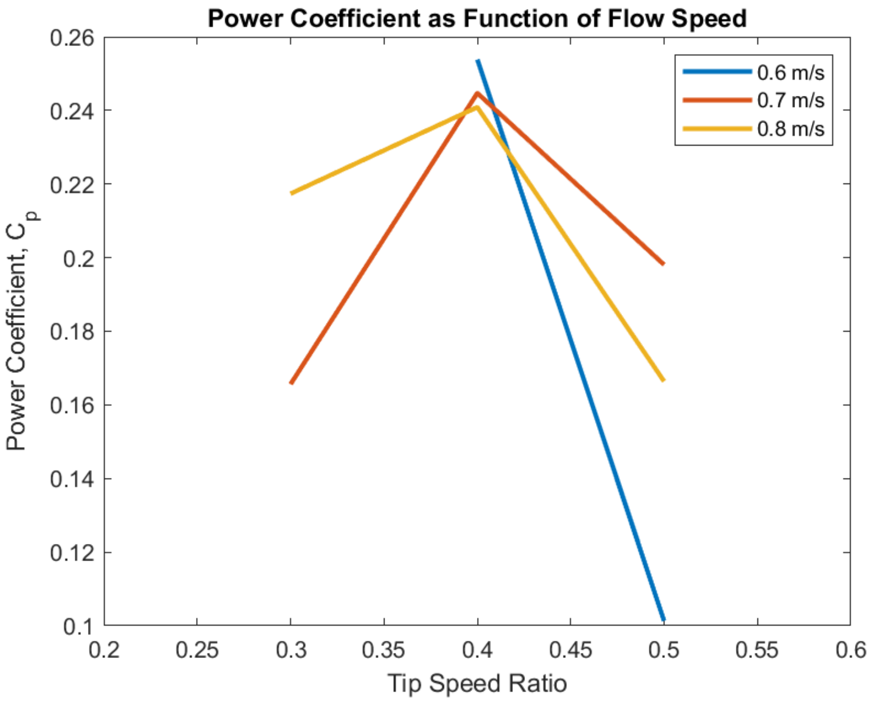

Figure 118: Cp vs TSR curves per flow speed – 01/19/24

6.6 Field Test (01/24/2024)

For this field test day, the 11-blade, full submergence waterwheel was tested, and the speed control performed relatively well, as illustrated in Figure 119. Figure 120 shows the flow speed and output electrical power for that test day, with output power peaking at close to 25W, while Figure 121 displays the overall system efficiency in converting flow power to electrical power. The Cp curves are displayed in Figure 122, which allows for the Cp vs TSR plot displayed in Figure 123 and the turbine performance per flow speed plot displayed in Figure 124.

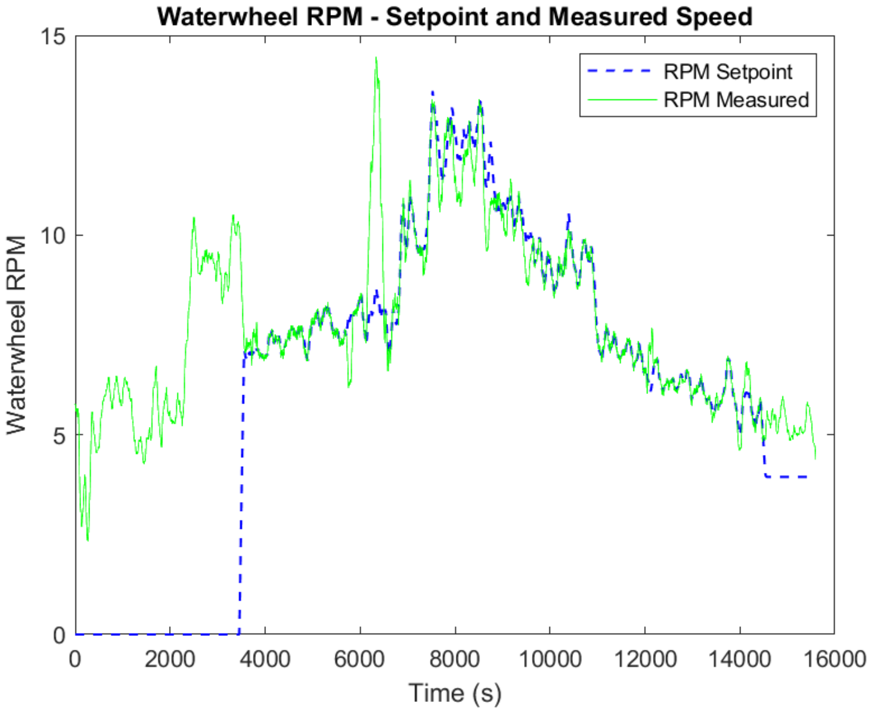

Figure 119: Waterwheel speed - setpoint vs measured – field test 01/24/24

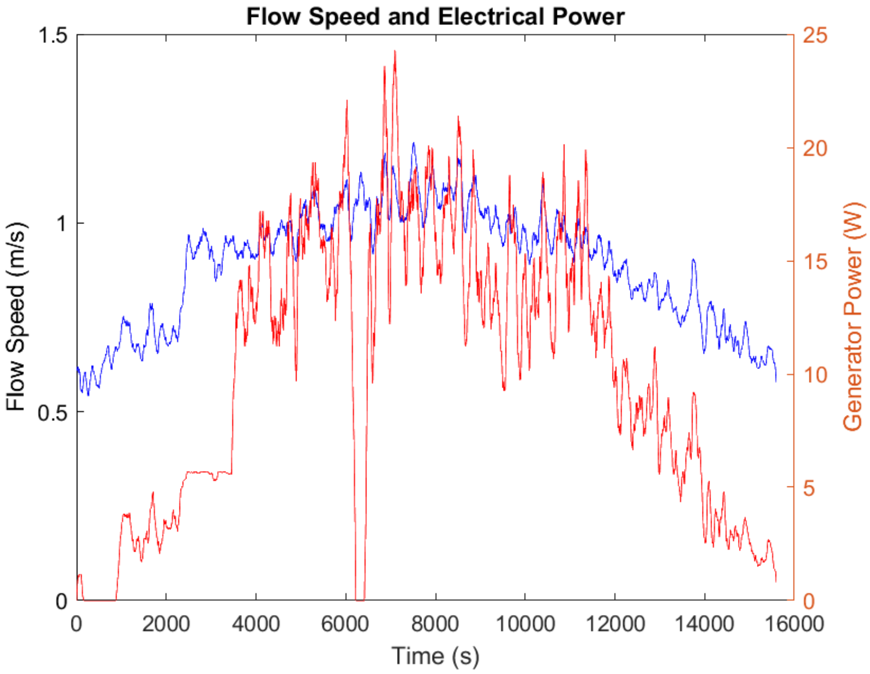

Figure 120: Flow speed vs electrical power – field test 01/24/24

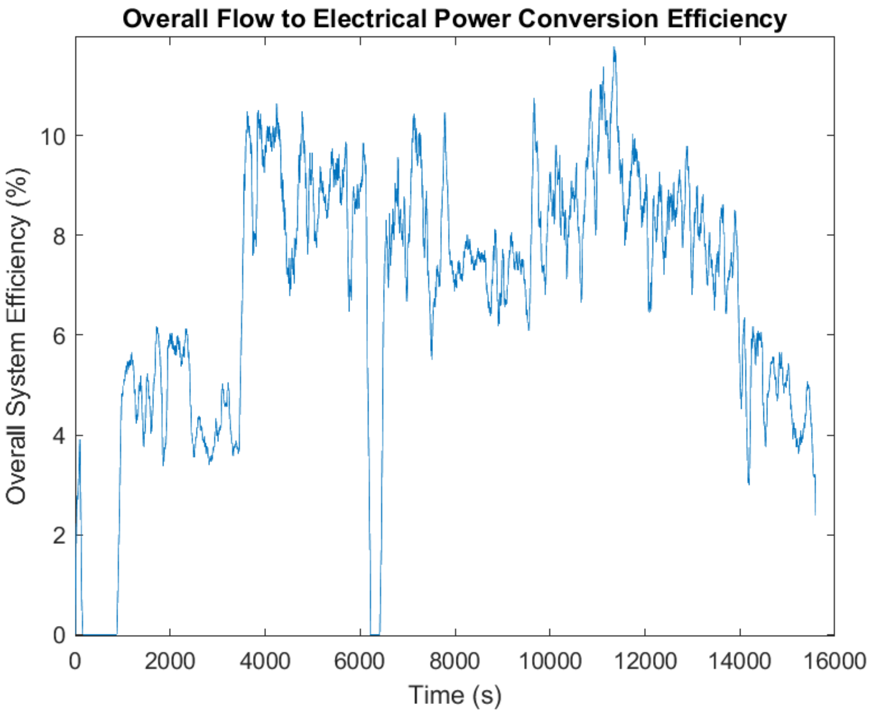

Figure 121: Overall system efficiency - from flow to electrical power – field test 01/24/24

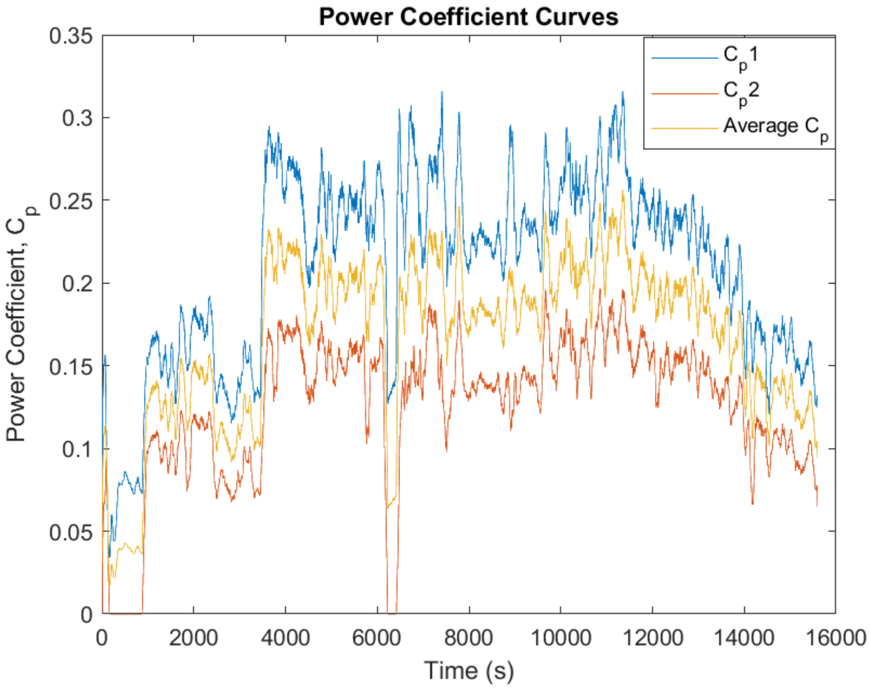

Figure 122: Power coefficient curves obtained via two calculation methods, and the resulting average curve - field test 1/24/24

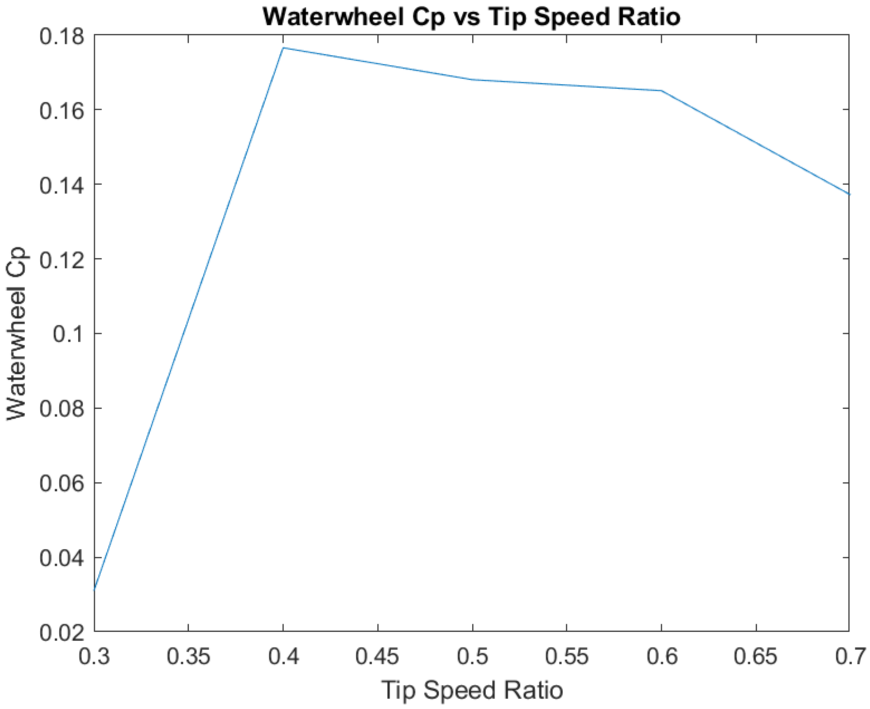

Figure 123: Resulting Cp curve - field test 01/24/24

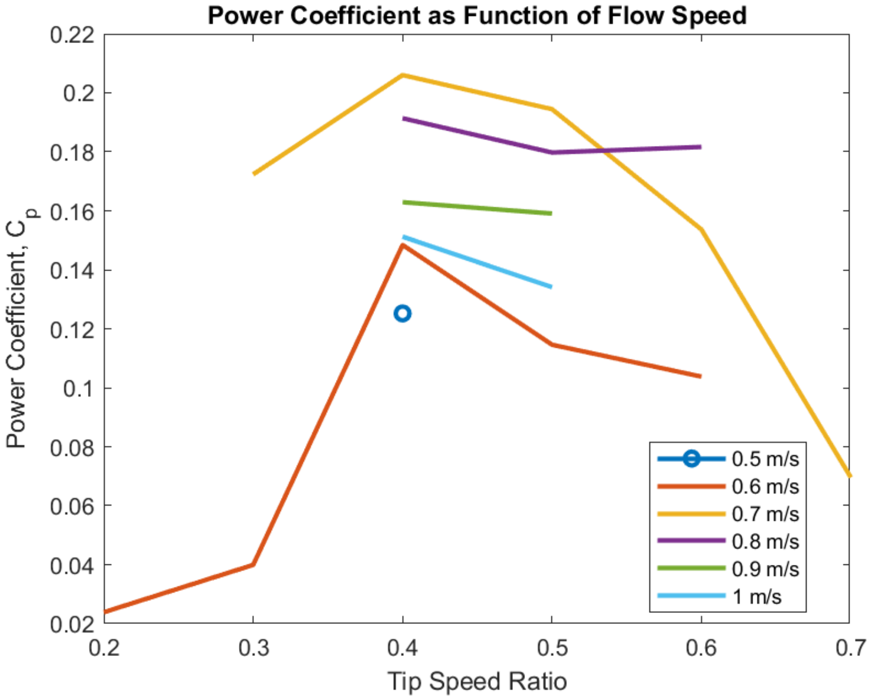

Figure 124: Cp vs TSR curves per flow speed – 01/24/24

6.7 Field Test (01/31/2024)

The 11 blade half-submergence configuration yielded negligible results since low flow was experienced during test day.

6.8 Summary of Field Tests – Round 2

The summary of the field tests alongside observations can be found on Table 7 below. On the “Note” row, the yellow cells indicate test days where speed control performance was relatively satisfactory, whereas the red cells indicate poor or no speed control. As previously mentioned, the tests for the 11-blade, half-submergence turbine obtained no data due to low flow speeds on test day. It can be noticed that, for both days where speed control was unsuccessful, the average flow speed was high, causing the wheel to rotate faster. For the main load demand controller running at a frequency of 0.5 Hz, the speed of the turbine might have been excessively fast for the controller to react in time.

Table 7: Summary of field test results

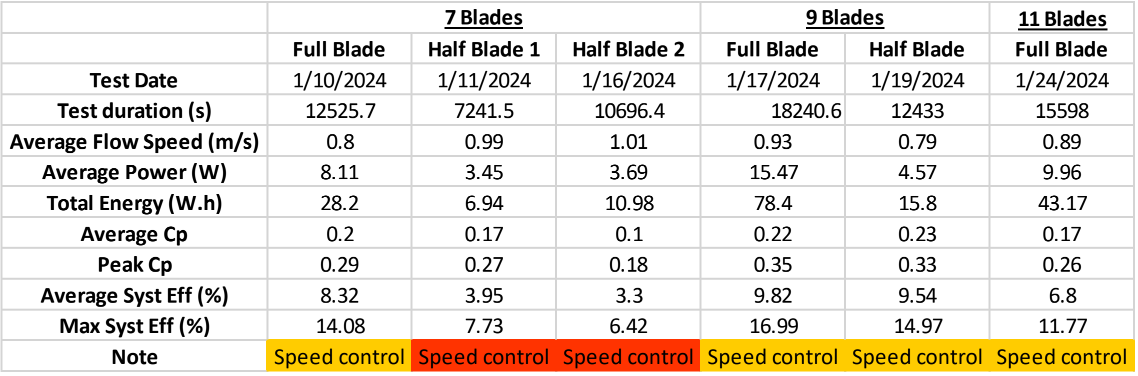

	7 Blades			**9 Blades**		**11 Blades**
	Full Blade	**Half Blade 1**	**Half Blade 2**	**Full Blade**	**Half Blade**	**Full Blade**
Test Date	1/10/2024	1/11/2024	1/16/2024	1/17/2024	1/19/2024	1/24/2024
Test duration (s)	12525.7	7241.5	10696.4	18240.6	12433	15598
Average Flow Speed (m/s)	0.8	0.99	1.01	0.93	0.79	0.89
Average Power (W)	8.11	3.45	3.69	15.47	4.57	9.96
Total Energy (W.h)	28.2	6.94	10.98	78.4	15.8	43.17
Average Cp	0.2	0.17	0.1	0.22	0.23	0.17
Peak Cp	0.29	0.27	0.18	0.35	0.33	0.26
Average Syst Eff (%)	8.32	3.95	3.3	9.82	9.54	6.8
Max Syst Eff (%)	14.08	7.73	6.42	16.99	14.97	11.77
Note	Speed control	Speed control	Speed control	Speed control	Speed control	Speed control

7. WATERWHEEL ANALYTICAL TORQUE ADJUSTMENT

Previously, the torque equation for a turbine blade was written as Equation (36), and a numerical approach was taken to evaluate the expression and come up with a response surface and a polynomial fit, considering blades at different positions and rotating at different TSRs. Here, another model is developed, this time without interference of blades on the flow, a key assumption on the first model (see Appendix I for details). Equation (36) has a validity region, since it squares the difference and cannot account for cases where $r > Usin\theta/\omega$. Those are cases where the blade enters the water and its tangential speed at a given distance from the center of the turbine is greater than the flow speed perpendicular to the blade surface, which results in a drag force opposing the rotation of the turbine. This phenomenon is a function of the underwater depth of its blades – the deeper the turbine, the greater the angle between the flow and the vector normal to the blade surface as it enters the flow. If the depth reaches the turbine radius, the blades enter the flow at a 90° angle with respect to the flow direction, resulting in maximum drag against the turbine motion. Details on the evaluation of the validity region can be seen on Appendix C

After considering the validity region acceptable, the blade torque equation is then rewritten as:

$$T_b = \frac{\rho b C_d r_1^2 U^2}{24}[6sin^2(\omega t + \psi_b)(1 - \gamma(t)^2) - 8\lambda sin\,(\omega t + \psi_b)(1 - \gamma(t)^3) + 3\lambda^2(1 - \gamma(t)^4)]$$

The total torque produced by the waterwheel can be calculated as the sum of torques of all blades underwater, or:

$$T_{ww} = \sum_{n=1}^{N_w} T_{bn}$$

Since the above summation is complex to evaluate analytically, a MATLAB script was developed to study the resulting function as a means to find a more user-friendly equation to be fit to field test data and used to estimate performance of waterwheel with different configurations. To illustrate the results, the 7-blade full-submergence configurations is used. Figure 125 shows the torque characteristics obtained by running the torque model over 5 seconds while varying the wheel's TSR for a flow speed of 1.2 m/s. Proceeding in a similar fashion for the complete flow speed range and averaging the torques, Figure 126 is obtained, where the average torque surface for the 7-blade, full-submergence turbine is shown. Figure 127 shows the Cp curve obtained by the torque model for that same configuration. It can be noticed that the optimal TSR for maximum Cp is 0.4, which will be used as speed setpoint for field tests. The curve also agrees with earlier analysis, which concludes that, contrary to lift-based machines, the power coefficient of drag-based machines does not depend on flow speed, as long as turbulence and other effects are negligible. Figure 128 shows the overall Cp curve format and its maximum value.

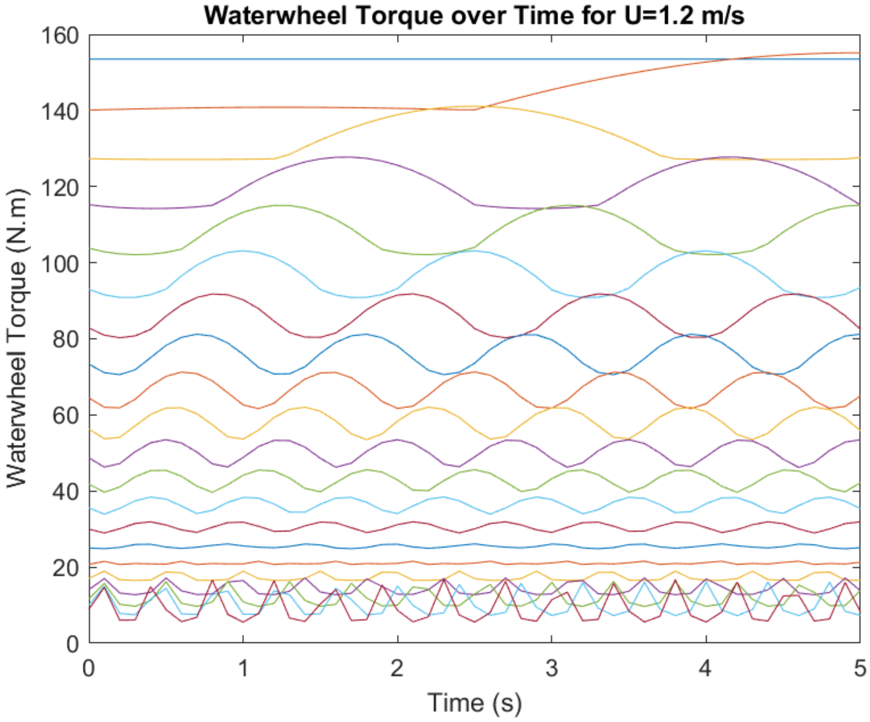

Figure 125: Waterwheel torque for tip speed ratios varying from 0.05 to 1 at flow speed of 1.2 m/s

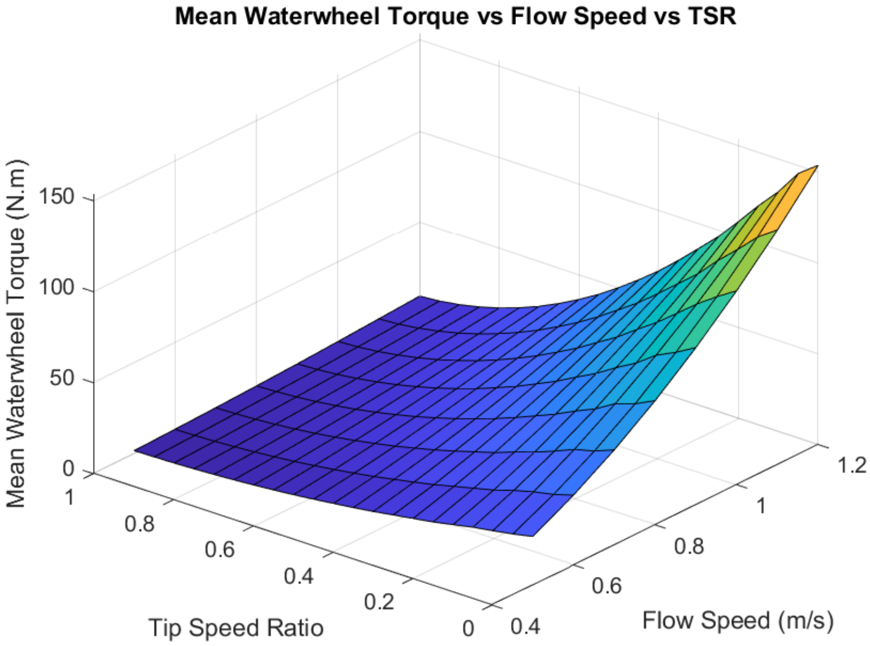

Figure 126: Mean waterwheel torque vs flow speed and TSR for the 7-blade, full-submergence configuration

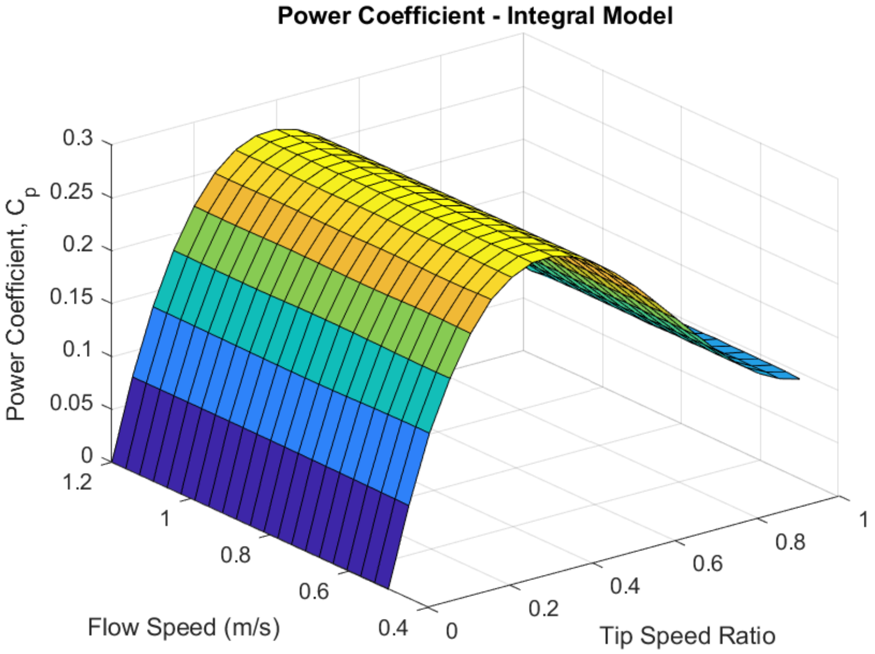

Figure 127: Cp curves for varying flow speeds for the 7-blade, full-submergence configuration

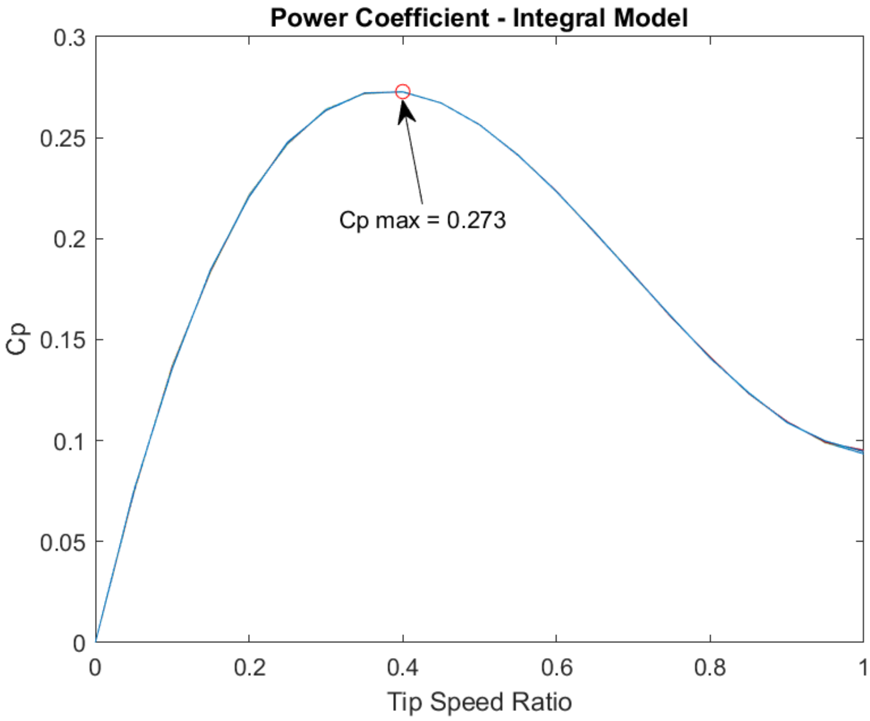

Figure 128: Maximum power coefficient obtained through integration

After evaluating the torque model, two functions were fit to the mean torque surface data. The first function is a polynomial function to be implemented on the test bench. The second function is based on the drag force model on a flat plate, due to its user-friendly structure. Therefore, obtaining the above-mentioned equations for the 7-blade, full-submergence configuration, and proceeding in a similar manner for the other configurations, the equations are as follows, with Table 8 displaying all coefficients:

$$T_{ww,poly} = a\lambda^3 + bU\lambda^2 + cU^2\lambda + d\lambda^2 + eU\lambda + fU^2 + g\lambda + hU + k \tag{64}$$

Table 8: Coefficients for the torque model polynomial

		Polynomial Coefficients									R²
# Blades	Sub	a	b	c	d	e	f	g	h	k	
7	Full	19.02	154.3	-104.9	-90.43	-152.2	96.19	72.66	22.88	-10.32	0.9996
	Half	14.38	66.16	-44.66	-47.21	-68.13	39.1	34.7	11.83	-5.109	0.9968
9	Full	35.72	193.6	-133.4	-130.6	-193	122.7	97.87	30.15	-13.65	0.9986
	Half	32.91	78.16	-58.79	-81.22	-76.65	51.24	50.86	11.28	-6.256	0.9939
11	Full	8.693	253.8	-164.4	-112.7	-254.8	150.7	105	40.9	-16.37	0.9998
	Half	-	-	-	-	-	-	-	-	-	-

For the drag-based model, an initial function was obtained from the mean torque surface as:

$$T_{ww,drag} = KU^2 n_b \delta (1-\lambda)^2 \tag{65}$$

$$K = \frac{\rho b C_d r_1^2}{24}$$

Where:

- K: constant obtained from integration of torque on single blade
- n_b: number of blades
- δ: fit factor $[blade^{-1}]$

After fitting the model to the mean polynomial torque surface obtained through integration, the calculated fit factor for each configuration is given in Table 9.

Table 9: Fit factor for drag-based model considering number of blades and submergence

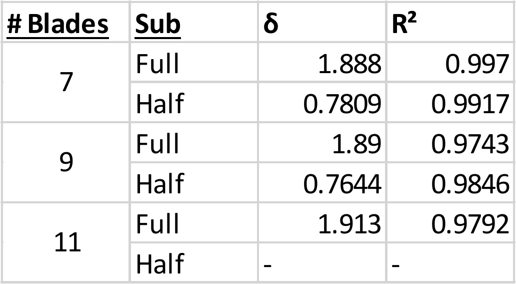

# Blades	Sub	δ	R²
7	Full	1.888	0.997
	Half	0.7809	0.9917
9	Full	1.89	0.9743
	Half	0.7644	0.9846
11	Full	1.913	0.9792
	Half	-	-

When the obtained drag-based model was fit to the field test torque data, only the test days with a higher level of speed control (highlighted in yellow in Table 7) allowed the model to better described the measured torques during tests. The days with low or no speed control presented torque readings that were completely different than what was predicted by the model. The main reason behind that is the accuracy of the generator torque and PTO efficiency models used to calculate the turbine torque, which were obtained through bench testing – for cases where no current is being demanded from the generator, the models cannot describe torque and efficiency as well as when load is being demanded, simply due to the number of adjacent data points for cases where electrical current is demanded, which contributes to the accuracy of the models in those situations. The drag-based model was then plotted alongside field tests data, compared to the actual readings and adjusted for higher accuracy.

The following plots show the measured torques during field tests, the fit and the adjusted torque models (drag models). The adjusted model is simply an updated value of δ (called δ^*) that best describes the torques measured during field tests. Figure 129, Figure 130, Figure 131 and Figure 132 display the measured, drag model and adjusted drag model torques for the test days with reasonable speed control, while Table 10 shows the summary of goodness of fits of both models. The fit model is a simplified version of the analytical (integral) model, written in the form of the drag torque on a plate, whereas the adjusted model is the fit model adjusted to the field test torque numbers. The torques obtained during field tests were calculated based on mathematical models of the generator torque and PTO efficiency obtained through bench tests, and are prone to some inaccuracy. Therefore, the adjusted model will not, by definition, have a high level of agreement with field data. For the drag model, the drag coefficient was approximated to that of a flat plate, or $C_d = 1.2$.

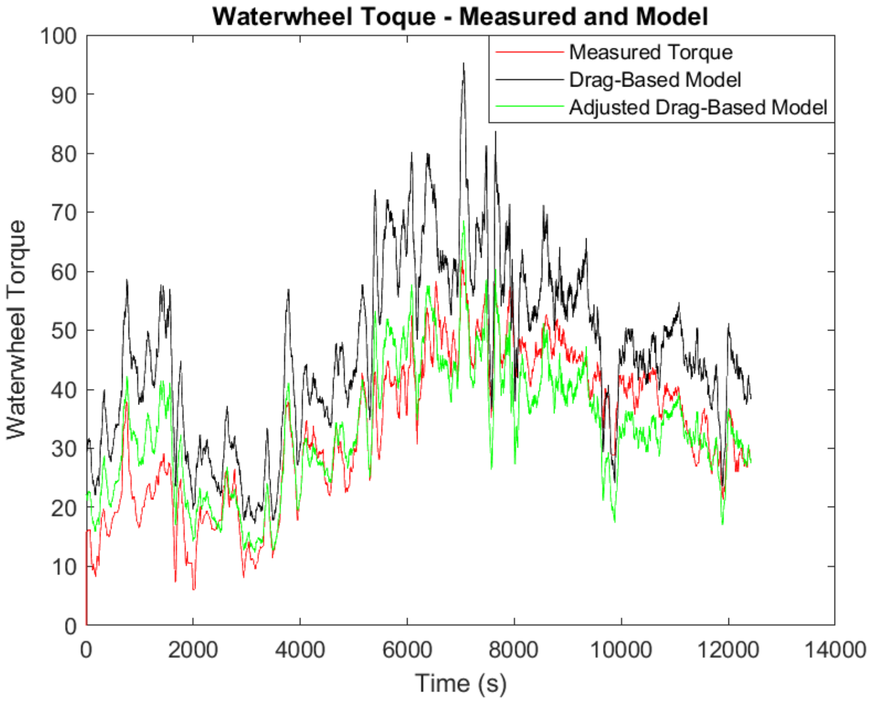

Figure 129: Measured, drag model and adjusted drag model torques for the 7-blade, full-submergence configuration – field test 01/10/24

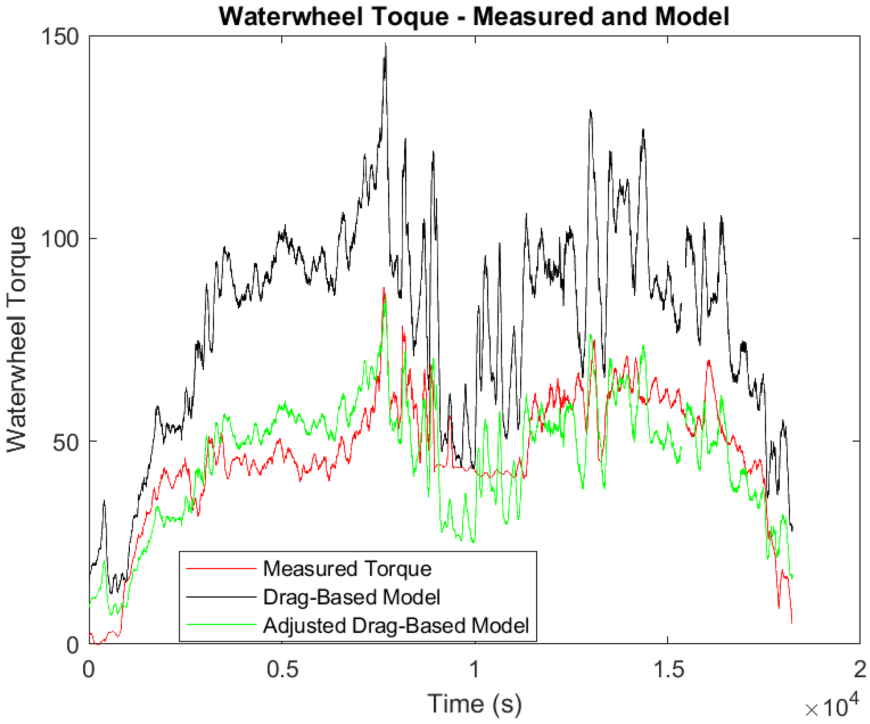

Figure 130: Measured, drag model and adjusted drag model torques for the 9-blade, full submergence configuration - field test 01/17/24

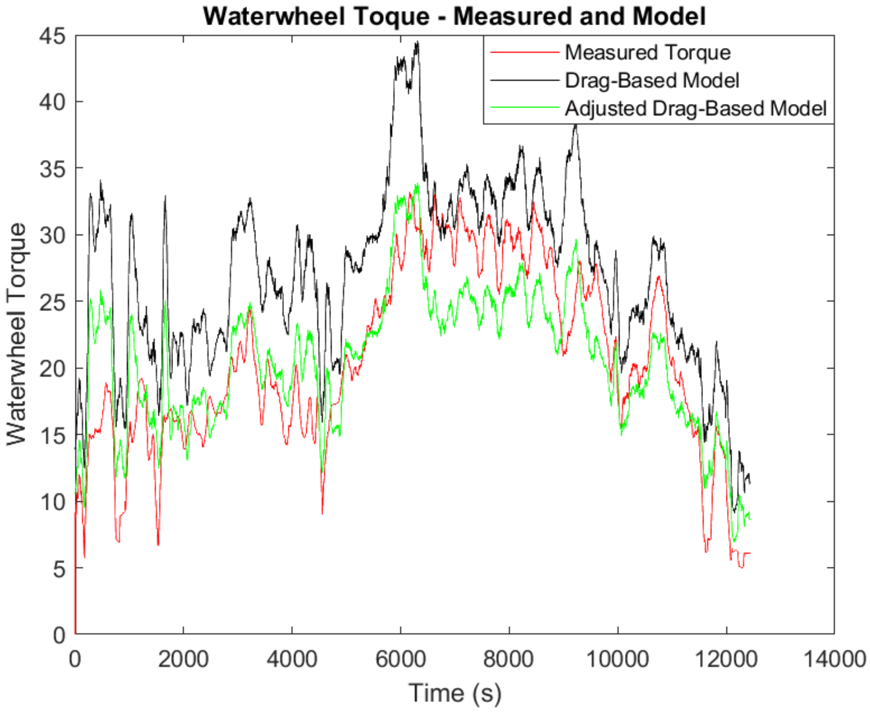

Figure 131: Measured, drag model and adjusted drag model torques for the 9-blade, half-submergence configuration – field test 01/19/24

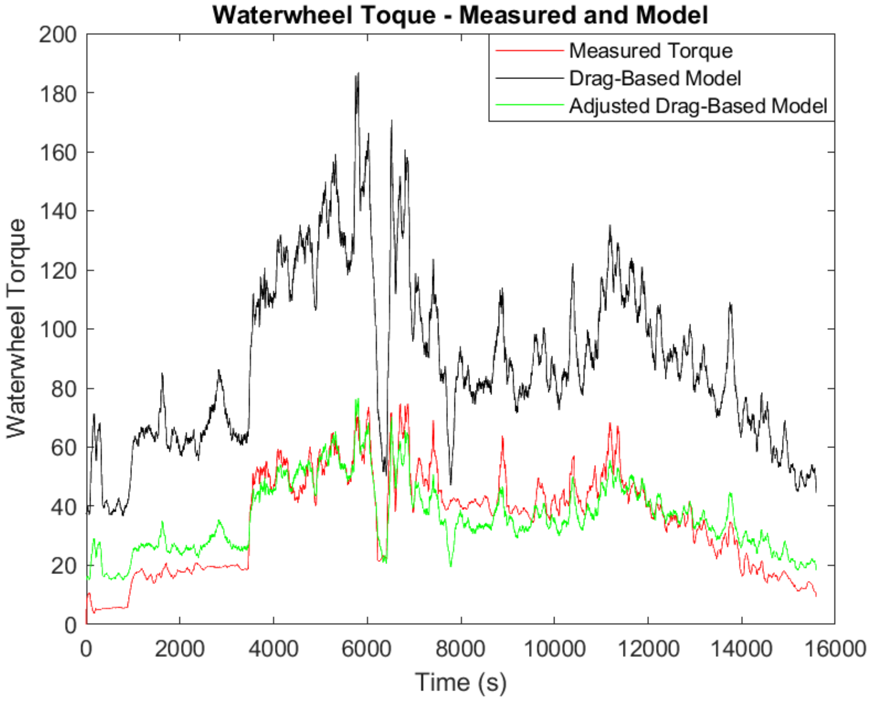

Figure 132: Measured, drag model and adjusted drag model for the 11-blade, full-submergence configuration – field test 1/24/24

Table 10: Goodness of fit for fit and adjusted turbine torque drag models

Test Date	# Blades	Sub	Fit Factor δ	Adjustment Factor δ*	Adjusted R²	
					Fit Drag Model	Adjusted Drag Model
1/10/2024	7	Full	1.888	1.359	-0.399	0.774
1/17/2024	9	Full	1.890	1.096	-4.11	0.638
1/19/2024		Half	0.764	0.581	-0.187	0.717
1/24/2024	11	Full	1.913	0.784	-10.113	0.776

Once again, the fit factor is used to better match the drag-based model to the torque surface obtained by analytical integration followed by numerical evaluation (i.e., it represents a theoretical model), while the adjustment factor adjusts the drag-based model to the torque data obtained during tests. After analyzing the results, it can be noted that the fit drag model (or theoretical model) overestimates torques for all configurations, since the adjustment factor δ^* is lower than the fit factor δ for all scenarios. It is also possible to notice that, as the number of blades increases, the theoretical torque model tends to overestimate torques, especially for the 11-blade wheel, which indicates the increase in flow blockage effects by neighboring blades.

Based on the results and the goodness of fit of the models, it is possible to conclude that, assuming a satisfactory speed control occurs, the waterwheel torque can be estimated by the adjusted drag model, which allows for the estimated waterwheel power and performance to be evaluated as:

$$C_{p,est} = \frac{T_{ww,model}\omega_{ww}}{P_{flow}} = \frac{KU^2 n_b \delta^* (1-\lambda)^2 \omega_{ww}}{1/2\rho A U^3} \tag{66}$$

By substituting for K and using the TSR definition in ω_{ww}:

$$C_{p,est} = \frac{n_b r_1 \delta^* C_d \lambda (1-\lambda)^2}{12d}$$

taking the constant terms as K_{Cp} and rewriting the expression for $C_{p,est}$:

$$K_{Cp} = \frac{n_b r_1 \delta^* C_d}{12d}$$

$$C_{p,est} = K_{Cp} \lambda (1-\lambda)^2 \tag{67}$$

After obtaining the estimated Cp expression, by plugging in the constants and plotting the estimated Cp vs TSR, the curves illustrated in Figure 133 can be obtained. The curves show that the 7-blade, full submergence configuration is expected to produce the highest amount or power ($C_{p,max} \cong 0.28$), followed by the 11-blade, full submergence configuration ($C_{p,max} \cong 0.25$), while the 9-blade, half submergence configuration outputs the lowest amount of power ($C_{p,max} \cong 0.16$). Note that the expression for the estimated power coefficient gives an optimal TSR of 0.3.

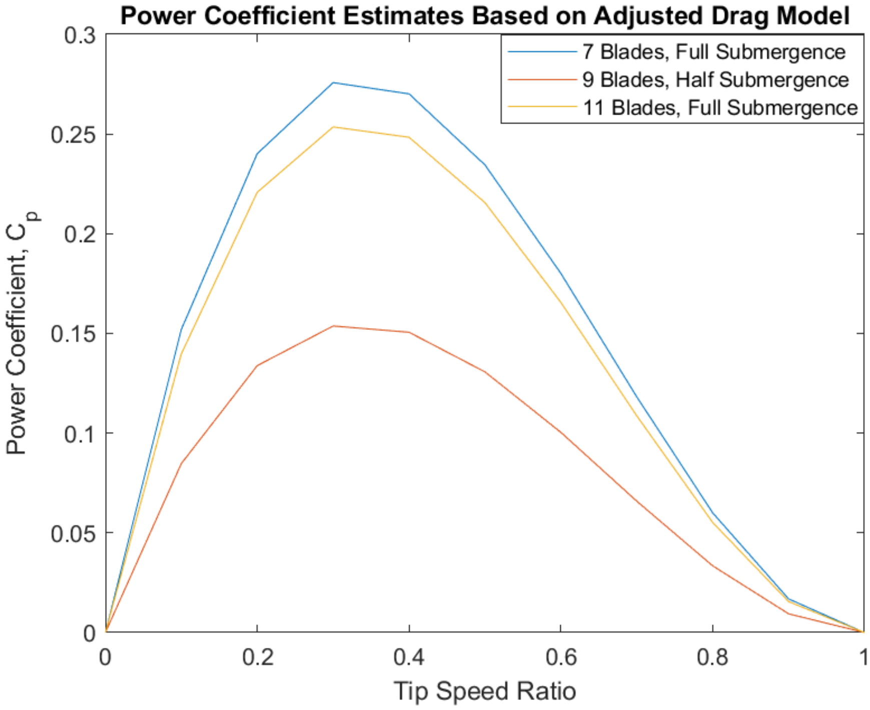

Figure 133: Plots of estimated Cp curves for 7-blade-full-submergence, 9-blade-half-submergence and 11-blade-full-submergence waterwheels

8. BENCH TEST – ROUND 2

Field tests allowed for a more accurate waterwheel torque model, both described in previous section. To implement the updated control strategy, an improved PI controller is derived based on the polynomial numerical model developed in previous section. The proportional gain Kp is taken as the derivative of the waterwheel torque with respect to its TSR, or:

$$K_p = \frac{dT_{ww}}{d\lambda}|_{U_0,\lambda_0} = 3a\lambda_0^2 + 2\lambda_0(bU_0 + d) + U_0(cU_0 + e) + g \qquad (68)$$

Where the constants take the values described in the polynomial coefficients table, Table 8. Taking the flow speed as constant, the gain Kp is recalculated every control loop iteration, which runs every second. Therefore, based on the tip speed ratio of the wheel and the flow speed, a new value for Kp is calculated, while Ki is set to -30 as before. During bench testing, it was noticed that the torque loads for the proportional gain described above were too large, causing further instabilities. Thus, the final proportional controller was written as:

$$K_p = K_{p0}/2$$

The error tolerance was set to ±8%, which means that if the turbine speed is within 8% of the setpoint, the primary controller will not perform any further actions to adjust the load demand, while the secondary controller adjusts the PWM output to meet the generator current demand set by the primary controller. The test bench Teensy board was programmed with the updated waterwheel torque model, running at 4Hz. It was also programmed to receive information regarding the CVT ratio on the PTO and calculate its acceleration based on that parameter and the calculated equivalent inertial resulting from the total gear ratio of the PTO reflected on the waterwheel shaft**.**

Figure 125 shows the performance results from the bench test with the updated controllers and proportional gain. The turbine speed begins its control phase peaking its speed but settling down around its setpoint for the first and second flow speed step, but oscillates considerably on around its setpoints on the second step (1 m/s). At the third step (0.8 m/s) it behaves smoothly, without major jerks. On the fourth step (1 m/s) it begins oscillating once again, but the oscillations decrease on the fifth step (0.9 m/s). The peak in acceleration is a clear indicator that the torque sensor saturation plays a critical role and contributes to the instabilities significantly, as it causes the calculated DC motor acceleration to increase much more than what was expected. Figure 126 shows the error and the upper and lower error threshold of ±8%. It is clear that, even though the oscillations are evident, the turbine speed is maintained within that range, apart from peaks on its speed when the flow speed steps up or down. Lastly, Figure 127 shows the system performance for another bench test, where the flow speed was increased from 0.8 to 0.9 and 1m/s and the TSR setpoint was kept at 0.4. It is clear the relationship between the increase in flow speed (thus increase in load), the increase in instabilities and increase in the corrective actions of the secondary controller, as well as the amplitude of those actions. The main reason for those increasingly higher amplitudes is the saturation of the torque sensor, which is a hardware issue that could not be overcome.

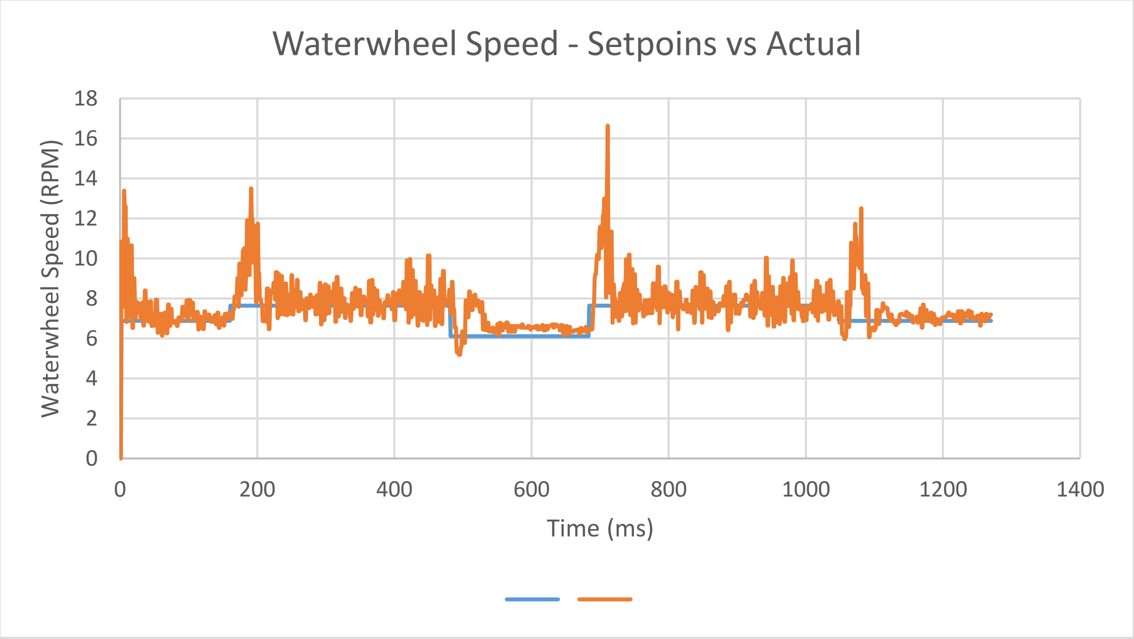

Figure 134: Waterwheel speed for TSR of 0.4 and flow speed step inputs: 0.9, 1, 0.8, 1 and 0.9 m/s

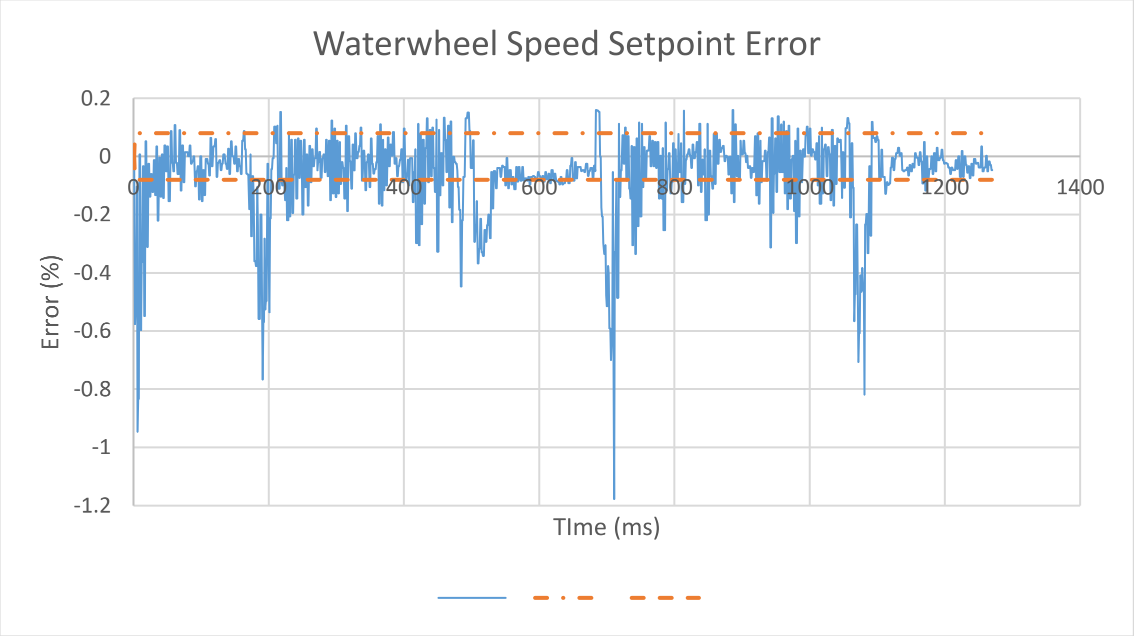

Figure 135: Waterwheel speed error, upper and lower error threshold limits

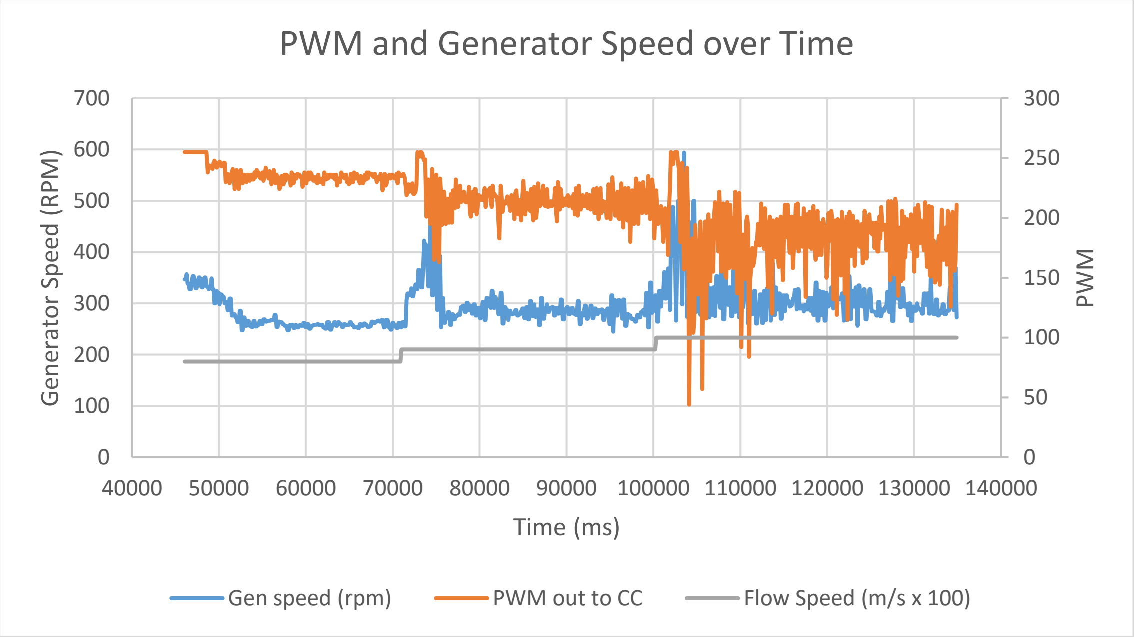

Figure 136: Generator speed and PWM per flow speed step input: 0.8, 0.9 and 1 m/s

As mentioned previously on the first bench test section, two main factors contribute significantly to the instability of the system: charge controller auto-regulation and torque sensor maximum reading. While the first one is an inherent characteristic of the current system, the second one is attributed to the test bench, which limits the tests on the controllability of the system when flow speeds of 1m/s and above are used. Although those factors pose increased difficulty in assessing the performance of the control logic, the overall performance of the control logic is satisfactory given the constraints. However, due to the instabilities presented and the direct relationship between a higher proportional gain and the amplitude of the instabilities, it was decided to remove the proportional gain and have the controller operate as an I-controller only. To further validate this method, field tests were conducted and the ability of the system to maintain a specific speed setpoint was evaluated.

9. FULL SYSTEM CONTROL

During the field tests described previously, the control system could only regulate the torque load on the turbine shaft, while the CVT ratio was controlled by the user when necessary. Those tests provided very important insights on how to integrate CVT and torque load control as well as implement the logic behind that integration as the main umbrella under which the complete PTO control takes place. The complete decision-making structure of the control system involves integrating the control of the CVT and the torque load on the turbine shaft. In the ideal scenario, operating setpoints for the CVT would be set based on flow speed, allowing for precise gear selection depending on flow conditions. However, since those setpoints are not known, an algorithm was developed with the goal of looking for a CVT ratio that allows efficient power production. The integration of CVT control and torque control comprises the full power generation system control, targeting efficient power production over a broad range of available flow power, with three distinct operating stages. Stage 1 looks for satisfactory conditions to begin producing power. Stage 2 produces electrical power while it looks for satisfactory conditions to begin TSR control. Stage 3 produces electrical power while controlling the speed of the turbine via generator current modulation. More details on those stages next.

Based on previous field tests, conditions were set to transition between stages of operation. The parameter used to transition between stages is the generator voltage, and the upper and lower threshold values were selected based on previous field tests and the performance of the system during those tests. To transition from Stage 1 to

Stage 2 and from Stage 2 to Stage 3, the average generator voltage has once again to reach values above 16V. To transition from Stage 3 to Stage 2, the average generator voltage has to reach values below 7.5V. To transition from Stage 2 to Stage 1, the above generator voltage has to reach values below 7V. The upper threshold voltage value of 16V was selected based on observations on voltage drop during previous field tests. When the charge controller is activated at minimum load, the generator voltage drops significantly. It was previously observed that, if the charge controller is activated with minimum load at voltage values below 13V, the voltage drop brings it close to 7V, which is the cutoff setpoint for the charge controller to self-disable.

The first developed version of the full system control algorithm kept track of the generator voltage, shifting the CVT ratio in a constant attempt to reach the upper threshold of 16V to transition between stages, with no regards to the waterwheel speed setpoint. If, upon an increase in ratio and after averaging the output voltage for a specific time, that voltage increased, the controller kept the direction of CVT ratio change (in that case continue to increase the ratio). However, if, upon an increase in ratio and after averaging the output voltage for a specific time, that voltage decreased, the controller switched the direction of CVT ratio change (in that case it would decrease the ratio for next iteration). The voltage thresholds that switch between stages remain the same. Figure 128 illustrates the behavior of that strategy, obtained by bench top testing.

On Stage 1, the system begins operation at a low flow speed of 0.6m/s and the CVT begins looking for higher output voltages by shifting its ration via servo motor and averaging the voltage output for a specific time before deciding whether to keep its direction of change or reverse it. Once it reaches 16V it enters Stage 2 and the charge controller is enabled (“CC Status” on Figure 128 shows the number 1, meaning it is enabled) with PWM kept at 255, which means minimum load. On Stage 2 the CVT continues to seek 16V while minimum load is applied to the turbine shaft and power is produced. However, even with an increase in flow speed to 0.7m/s, the system still cannot find 16V to enter the next stage, which causes the CVT controller to reach its search time-out and hold the CVT in place for a specific time before resuming the search. With an increase in flow speed to 0.8m/s and resuming the CVT search, the system finally finds 16V and the control system transitions to Stage 3, where speed control begins (note that the prior stages have no speed control) via modulation of generator current. With a decrease in flow speed back to 0.7m/s, the controller requests lower torque load on the turbine shaft to maintain its speed, which the charge controller alone cannot do, causing the CVT to decrease its ratio. With another decrease in flow speed to 0.6m/s, the control system detects a low voltage of 7.5V and transitions back to Stage 2, with the CVT back on its search for 16V. After another increase in flow speed to 0.8m/s, the system enters Stage 3 and speed control starts again.

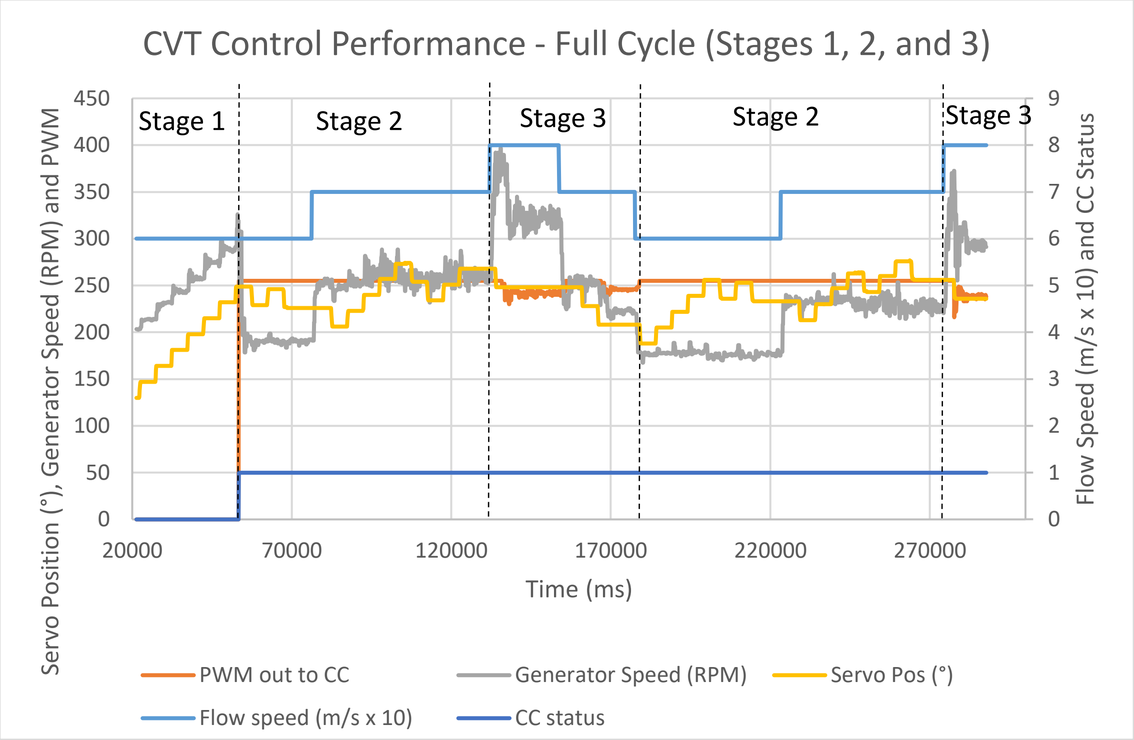

Figure 137: CVT control performance throughout the complete automation cycle (Stages 1, 2 and 3)

The algorithm, however, did not work as expected (as it will be explained in the coming field test section), which lead to the development of the latest algorithm. On that algorithm, the three stages have as a goal to maintain the turbine running at a specific TSR set by the user until conditions for the next stage are met. The three stages were modified and are described below.

Stage 1 utilizes the CVT to control the speed of the waterwheel and maintain it around its setpoint plus or minus a certain tolerance. During this stage the flow speed is not fast enough to enable the charge controller at minimum load without dropping the generator voltage below the minimum necessary to operate that controller. It can be argued that a higher speed setpoint would yield a higher voltage output, which allows the charge controller to be enabled. However, it is not known if the wheel can produce enough torque at higher speed setpoint to operate the system at minimum load under such low flow speeds. It was then decided that Stage 1 is solely dedicated to maintaining the speed setpoint of the wheel, with a TSR setpoint of 0.4 as optimal TSR, as obtained from modeling. It is important to notice that, since there is no power being produced, it is not viable to operate the CVT constantly as it's servo motor draws power. Thus, Stage 1 operates with a large speed setpoint error tolerance to avoid excessive use of the servo motor. The control logic during this stage is very simple and consists of increasing or decreasing the servo motor's position by a fixed angular displacement if the speed of the turbine falls outside the error tolerance, depending on the sign of the error. Although this is not an optimal control logic, it proved itself sufficient for proof-of-concept, as it will be discussed in the next field test section. Ideally a more robust control strategy combined with an optimized decision-making process should be implemented to avoid unnecessary energy expenditure when operating on Stage 1, while keeping track of the overall flow speed trend. When flow speed increases to a point where the generator voltage reaches average values above a specific threshold, the system migrates to Stage 2, which enables the charge controller and places a minimum load on the turbine.

Stage 2 is still reliant on the CVT to control the speed of the turbine around its setpoint, but with a fast enough flow speed that the charge controller can be activated and a minimum load can be placed on the turbine, allowing for power generation. This stage is similar to Stage 1, but now power is produced. The same large speed setpoint error tolerances are applied during this stage as well as the same simplified control algorithm. Although power is being produced, it is still important to be mindful about when to operate the CVT's servo motor, as it has an inherent cost to it. When flow speed increases to a point where the generator voltage reaches average values above a specific threshold, the system migrates to Stage 3, which enables waterwheel speed control via the modulation of the generator current demand (i.e., controlling torque load via electrical current) in conjunction with CVT ratio control.

Stage 3 varies the generator electrical current to vary the torque load on the turbine and thus control its speed around the setpoint, with CVT ratio control being used as support for situations where the torque demand reaches certain extremes. During this stage, the control algorithm utilized an I-controller to relate error signals to torque demand, which is then related to current demand and PWM output to the charge controller. This allows for effective control of turbine speed while the CVT position is held fix. As showed in previous sections, high PWM values mean low electrical current demand and low torque load, whereas low PWM values mean high electrical current demand and high torque load. When PWM values remain above a certain threshold for a specified time interval (that threshold was set to 250 with a 5-second interval), this means that the torque load demand on the turbine cannot be met by the charge controller alone, and the CVT ratio control is activated to move the servo motor position back by a specified decrement, causing a decrease in CVT ratio, which decreases the reflected load on the turbine shaft. This action gives back the system the ability to control the turbine speed via current demand modulation only. Conversely, when PWM values remain below a certain threshold for a specified time interval (that threshold was set to 100 with a 5-second interval), this means that, although the torque load demand on the turbine can be met by the charge controller alone, the system is not operating at an efficient range, since the generator is more efficient when it operates at a higher speed. The CVT ratio control is then activated to move the servo motor position forward by a specified decrement, causing an increase in CVT ratio, which increases the reflected load on the turbine shaft. This action allows for higher PWM numbers and therefore lower current demand, resulting in higher operating efficiency. As the flow speed begins decreasing, the control system begins demanding less torque load, causing the CVT to shift down several times over the operating time, until the average generator voltage reaches values below a specific threshold, causing the system to transition back to Stage 2. With continued decrease in flow speed, the system then transitions to Stage 1 and the cycle repeats itself.

10. FIELD TEST – ROUND 3

Field tests for full system control took place in two non-consecutive days, with the first iteration of the control algorithm tested on the first day for a 7-blade, half submergence waterwheel, and the second iteration of the control algorithm tested on the second day fir a 9-blade, full submergence waterwheel.

10.1 Field Test (02/27/2024)

Field test was performed on the 7-blade, half submergence turbine, which resulted in poor overall performance stemming from two sources: turbine speed control and CVT ratio control (data processing utilized moving averages for all data and a window size of 800 samples). For the CVT ratio control, the fact that the algorithm only tracked voltage resulted in a decrease in the ratio throughout the test. The algorithm picked disturbances on flow speed and output voltage drops as information on which to decide whether to increase or decrease the ratio, resulting in low operating ratios, which culminated with the turbine operating at high speeds and the generator operating at low speed, the exact opposite of what is desired. As for turbine speed control, the integral gain of -30 was too high for the averaging time and sampling frequency used (1s and 10Hz respectively), causing the control system to react suddenly with spikes in torque demand, resulting in unstable behavior and inability to operate within error tolerance. Figure 138 shows the discrepancy between speed setpoint and actual turbine speed. Figure 139 shows the generator output voltage and waterwheel speed over time. It can be noticed that the generator voltage does not reach 16V, even with the turbine operating at high speeds, which reflects the low CVT ratio resulting from poor performance of the control algorithm. Figure 140 shows the position of the servo motor and the respective CVT ratio over time, as well as the moments where the user had to send manual commands to reset the servo position. It is noticeable that the operating ratios did not surpass 0.9, which means that the total gear ratio is less than the ratio of the fixed gearbox alone (1:35), which would be expected at low flow speeds. However, only high flow speeds can bring the waterwheel up to such speeds of up to 12rpm, as the ones seen here. Furthermore, the arrows point to moments during field testing that the user manually reset the servo position to a higher setpoint, which correlates to higher gear ratio. However, the algorithm was not able to search and maintain a proper ratio for power generation and kept decreasing the CVT ratio and therefore the overall gear ratio of the PTO. Lastly, Figure 141 shows electrical power output and the total system efficiency converting flow power into electrical power. The efficiency is considerably below expected performance values, especially when compared to previous test for the 7-blade, half submergence wheel. Although previous test had the CVT manually set by the user, the discrepancy in overall efficiency illustrates the importance of properly setting the gear ratio of the PTO.

After analyzing the results of the abovementioned field test, modifications to the control algorithm were made as covered in previous section. The stages of operation remained the same, but with changes in criteria to control CVT ratio: from tracking generator output voltage, to tracking turbine speed setpoint, maintaining it within a certain error tolerance. The integral gain was also modified from -30 to -10 for the same averaging time of 1 second. Position limits for the servo motor were also set.

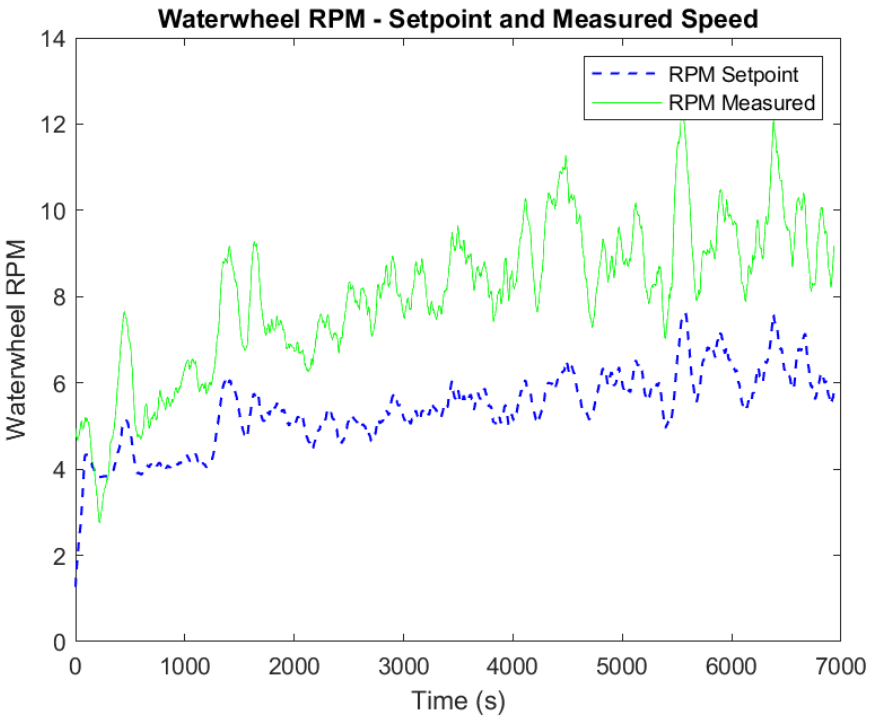

Figure 138: Waterwheel speed - setpoint vs measured – field test 02/27/2024

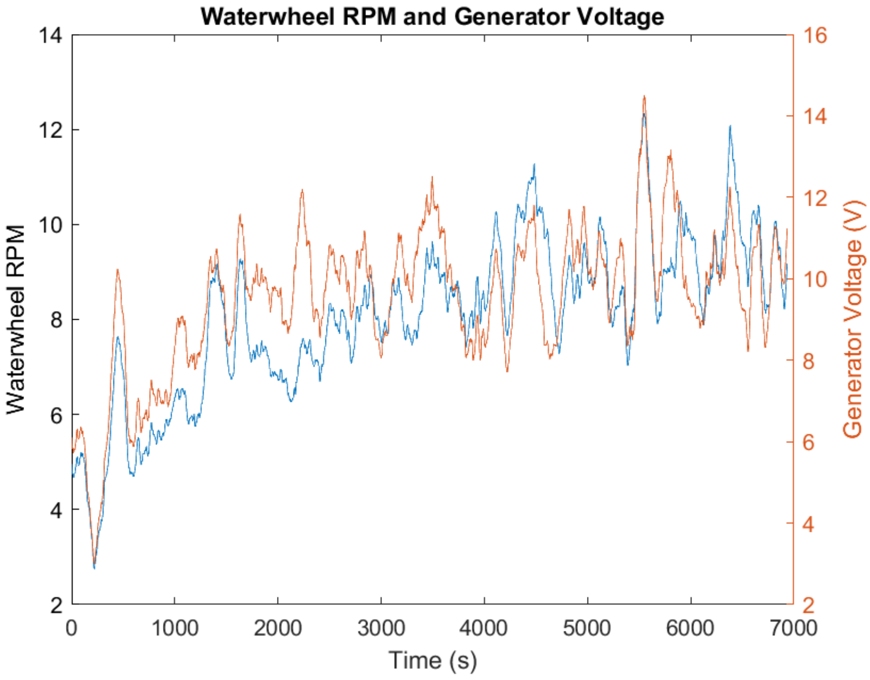

Figure 139: Waterwheel speed and generator voltage output - field test 02/27/2024

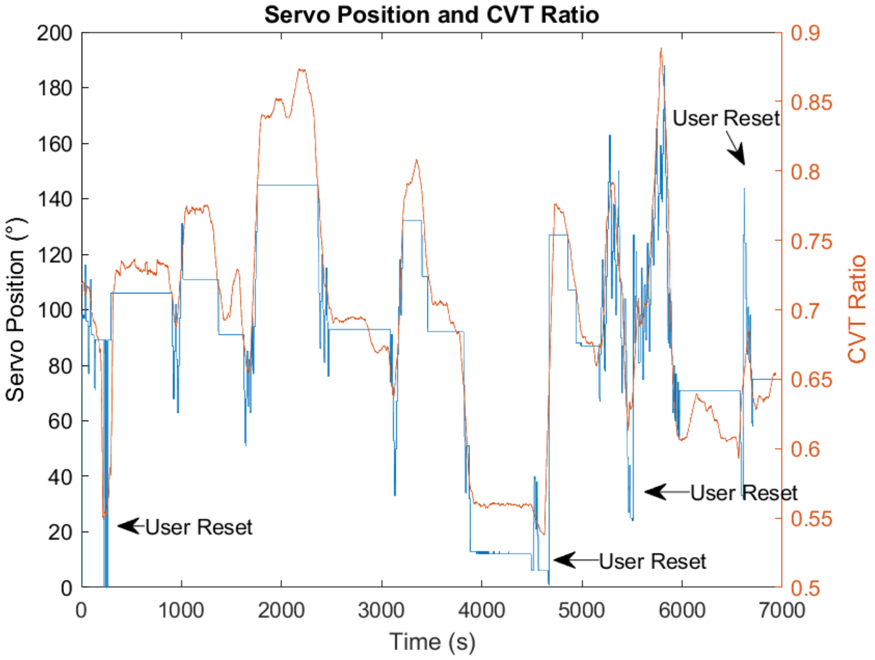

Figure 140: CVT's servo motor position and CVT ratio, with arrows indicating manual reset commands by the user - field test 02/27/2024

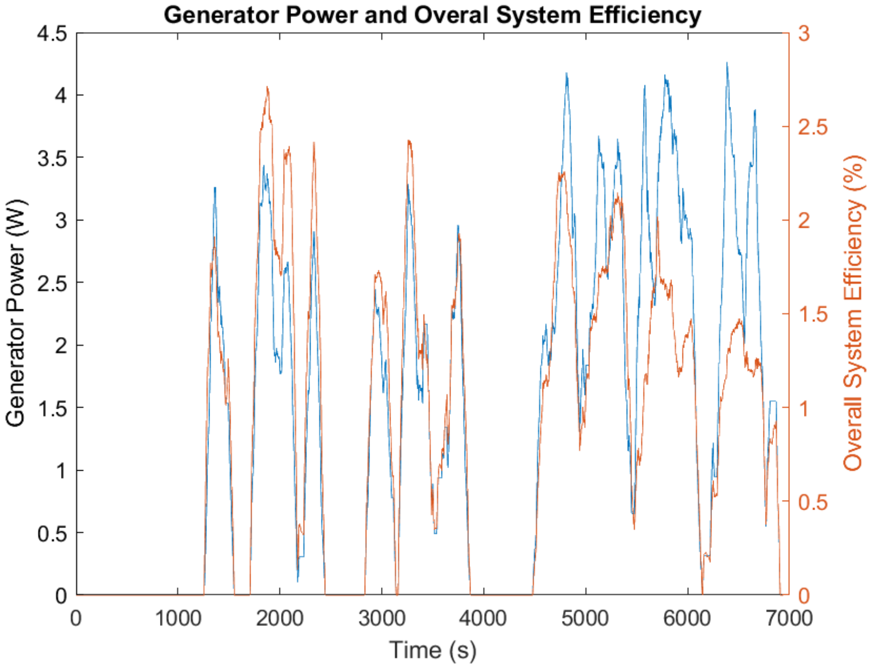

Figure 141: Generator power output and total system efficiency -field test 02/27/2024

10.2 Field Test (02/29/2024)

Field test was performed on the 9-blade, full submergence turbine, with updated control algorithm, and the results were overall satisfactory (data processing utilized moving averages for all data but charge controller status, and a window size of 800 samples). While operating on Stage 3, the TSR control algorithm displayed some instabilities during short sections of testing, which can be seen on Figure 142, which shows the turbine speed setpoint and its actual speed. The reasons for such unstable behavior are not yet known, but it is suspected that the integral gain and the averaging time used were suitable values, and the source of such behavior lies within the overall architecture of the field test code and loops. Despite those instabilities, the overall TSR control algorithm worked well and the stages of operation were successfully deployed sequentially, with no user interference.

Figure 143 shows the behavior of some of the main variables during field test, where the upper plot displays generator voltage, PWM and charge controller status (0 – charge controller disabled; 100 – charge controller enabled), and the lower plot displays flow speed and CVT's servo position. PWM is plotted using the same moving average used on the other datasets, but in next figures it will be plotted as raw values. Minimum and maximum position limits were set for the servo motor as 100° and 295°. The lower limit was set to 100° based on observations during previous field tests and the realization that servo positions under 100° do not allows for any power production and result in a larger number of iterations operating the servo motor to arrive at usable ratios. The 295° limit was set based on the fact that, given the mechanical characteristics of the PTO, moving the servo to positions beyond that maximum limit significantly increase the chances of the servo reaching over torque due to the meshing of the gears. To exit that mode, a full power cycle is required and perhaps even removing the servo, manually setting the CVT ratio to lower values and mounting the servo back on.

On the top plot it can be noticed that the system spends almost no time operating on Stages 1 and 2 and promptly moves on to Stage 3 after reaching 16V from Stage 2. The charge controller is enabled and the PWM varies, which means that the controller is performing TSR control at Stage 3. It can be noticed that, as flow speed increases, so does the CVT ratio, represented by the servo position, until it reaches its maximum value. The PWM decreases with increase in flow speed, meaning more power is drawn from the generator. That behavior is more evidenced when the servo reaches its maximum position, which means that, for a required torque load, the servo can no longer increase the reflected inertia on the turbine shaft, which causes the PWM to drop more consistently. It can be noticed that the charge controller status displays some oscillations at specific points in time, which indicate the instabilities on the control system and/or the turbine being hit by wakes cause by passing boats at the time of testing. As the flow speed begins to decrease, so does the servo position and the overall torque demand, which can be seen by the increase in PWM.

At a certain flow speed, the controller begins alternating between Stages 3 and 2, in an attempt to control the speed of the wheel while producing power. That alternating behavior cannot be clearly seen since the PWM plotted is a moving average of the raw PWM values. In reality, the PWM oscillates when in Stage 3 and remains constant at 255 in Stage 2. As the flow speed drops further down, the controller alternates between Stages 2 and 1, until it finally settles on Stage 1, where no power is produced and the turbine speed setpoint is controlled with the CVT's servo only. Stage 1 can be clearly seen due to the frequent operation of the servo motor maintaining the wheel within its setpoint.

Figure 144 shows the first 3 minutes of operation, where it can be clearly seen that the controller spends only about 20 seconds on Stage 1 and moves on to Stage 2, where it alternates between Stage 2 and 3 until it stabilizes on Stage 3. It can also be noticed the convergence between the turbine speed setpoint and the measured speed. The transient effect occurs due to the fact that the CVT's servo is positioned at its lower limit when the test begins, and only changes its position every 3 seconds, after averaging the turbine speed error. When the servo finds a position, the controller enters Stage 3 and begins using current demand to control the turbine speed. Notice that the PWM shown are the raw values, with no moving average filter.

Figure 145 shows the system operating at a few minutes over the half mark of the entire test duration, where the PWM is plotted as raw values. It is noticeable how the waterwheel follows its setpoint relatively well, as well as the actuation of the servo motor. The servo increases due to a prior action that was held on due to the actuation time-out (when the servo is actuated more than a specific number of times). It then comes back down due to lower torque demand and the fact that the current modulation alone cannot generate such low torque. The fact that large wakes hit the turbine and caused large disturbances also contributed to actuations on the servo motor that were not supposed to happen. However, those actuations were seldom.

Lastly, Figure 146 shows the last 50 minutes of test time, where the system operates at Stage 3. It is possible to notice the change in CVT ratio on Stage 3 as the controller requests less torque load due to a decrease in flow speed and current demand alone cannot provide such low torque. The controller then begins alternating between Stages 3 and 2 and finally stabilizes at Stage 2, where the PWM is held at

255 throughout the entirety of that stage and the turbine speed is controller via CVT only. At the last minutes of testing, the controller begins alternating between Stages 2 and 1 before the test is wrapped.

To further process the data, the main instability, shown in Figure 142 by the main trough on the measured turbine RPM, is removed from the set, since it is known that it represents a glitch in the dataset. Figure 147 shows the turbine RPM readings without the instability region. Figure 148 and Figure 149 show the Cp curves obtained during the test.

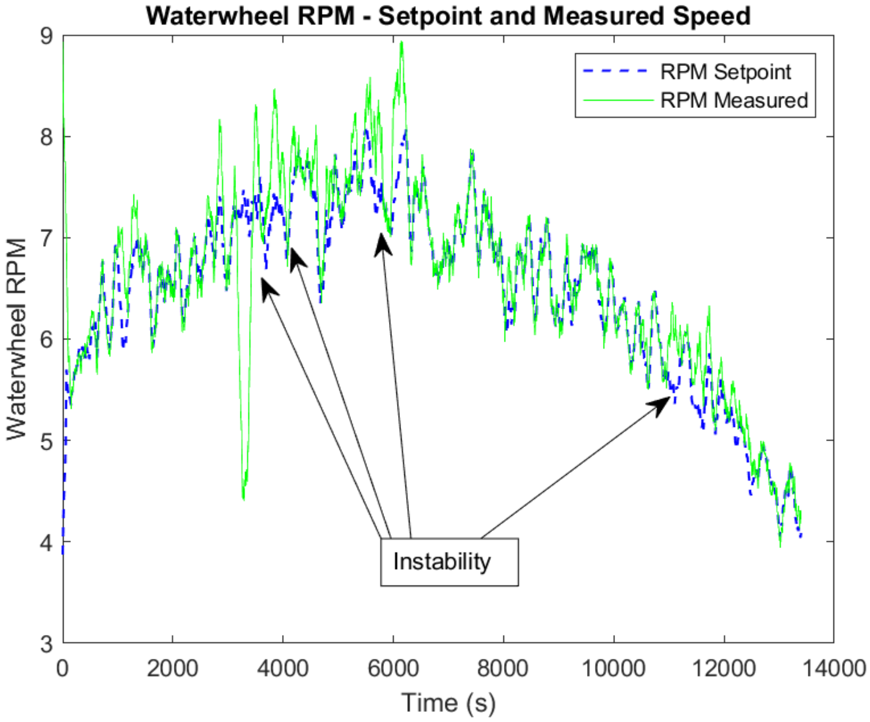

Figure 142: Waterwheel speed - setpoints vs measured - field test 02/29/2024

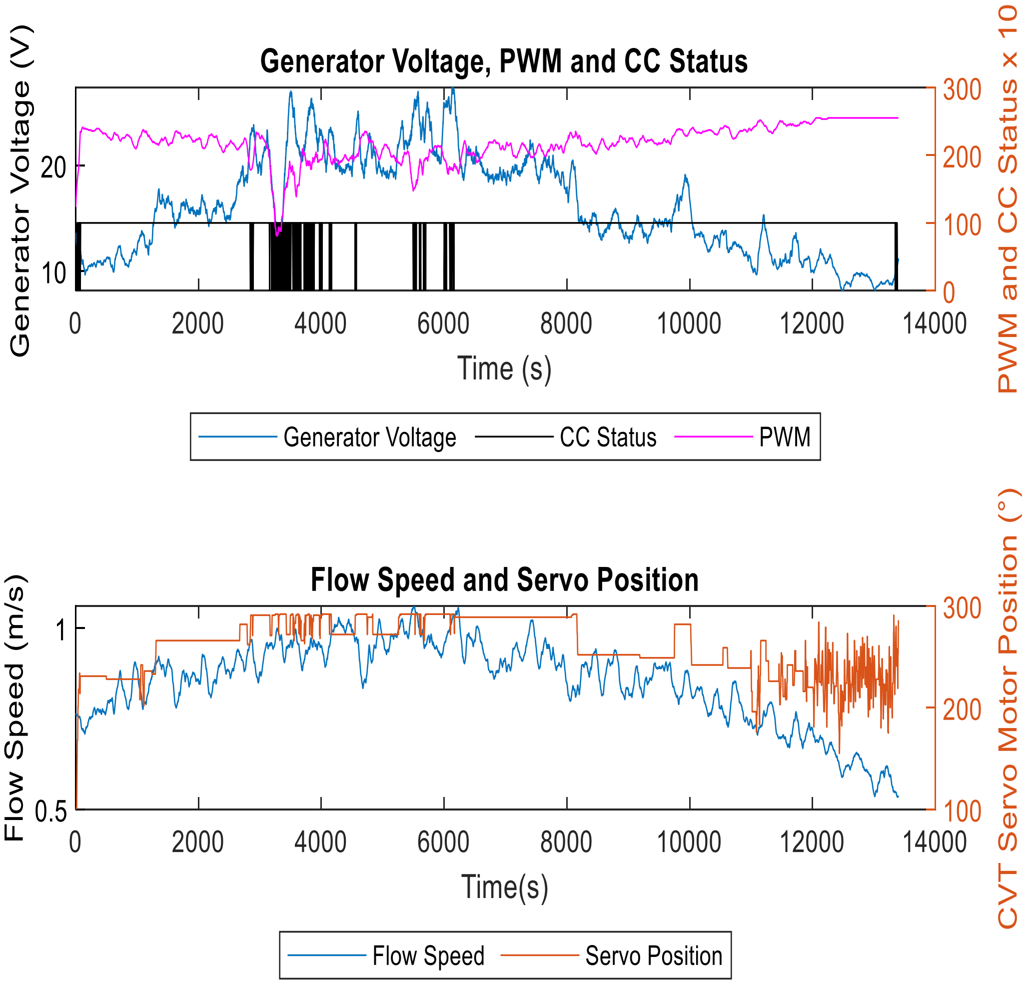

Figure 143: Subplot 1 - Generator voltage, PWM and CC status; subplot 2 - Flow speed and CVT servo motor position - field test 02/29/2024

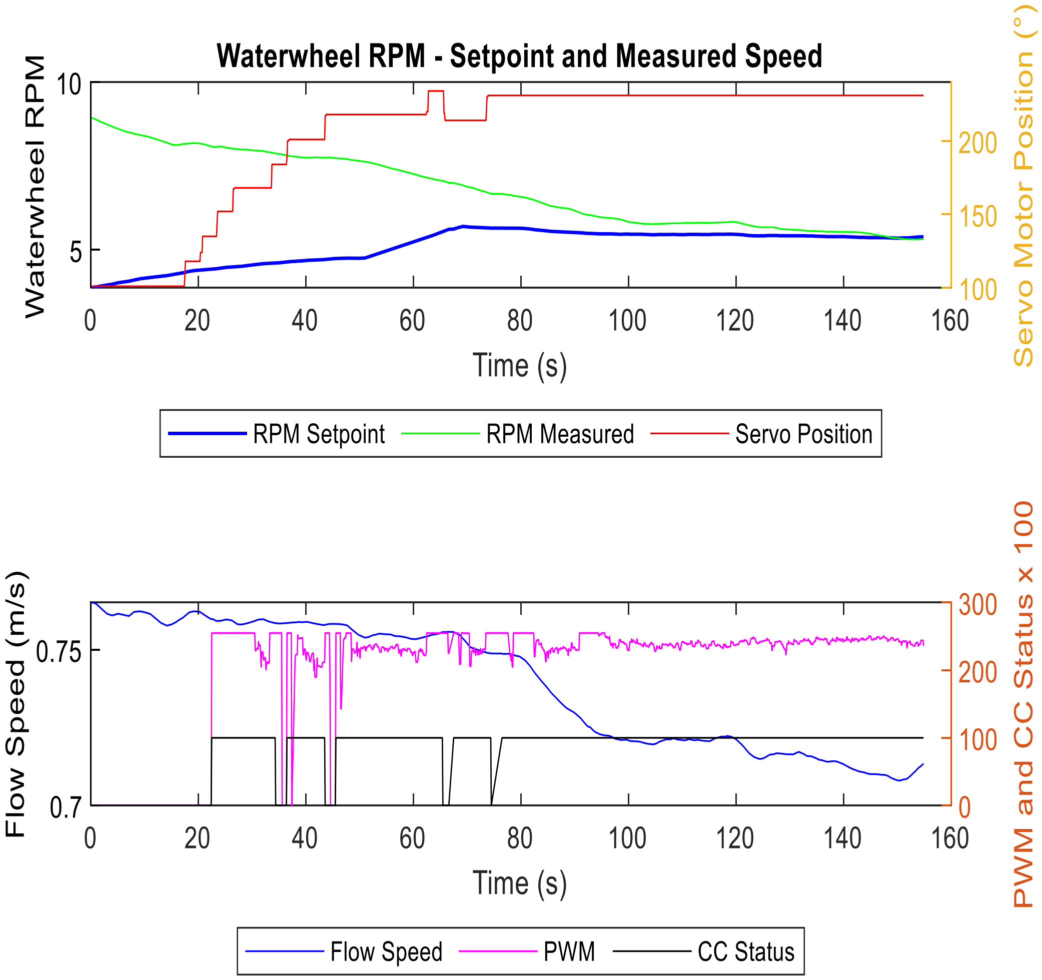

Figure 144: First 3 minutes of operation - field test 02/29/2024

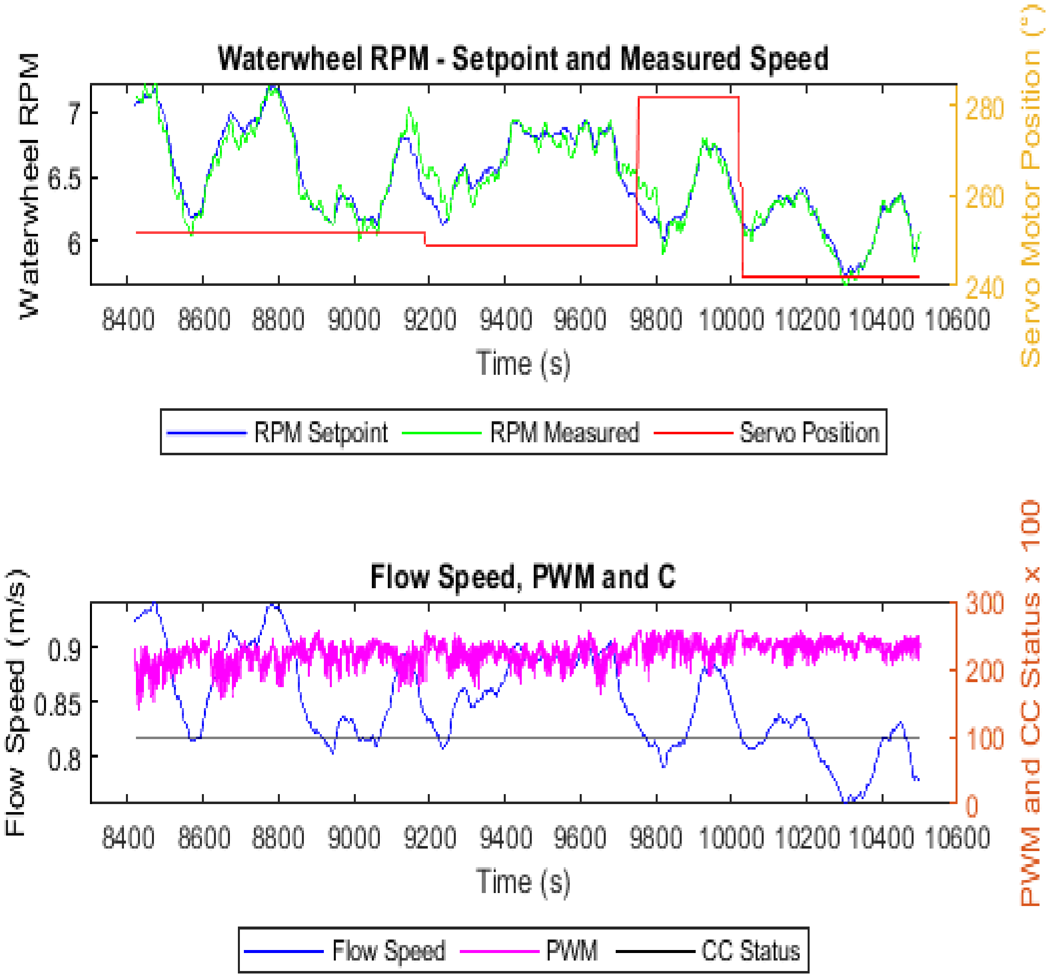

Figure 145: Operation at approximately a few minutes over half the total test time length - field test 02/29/2024

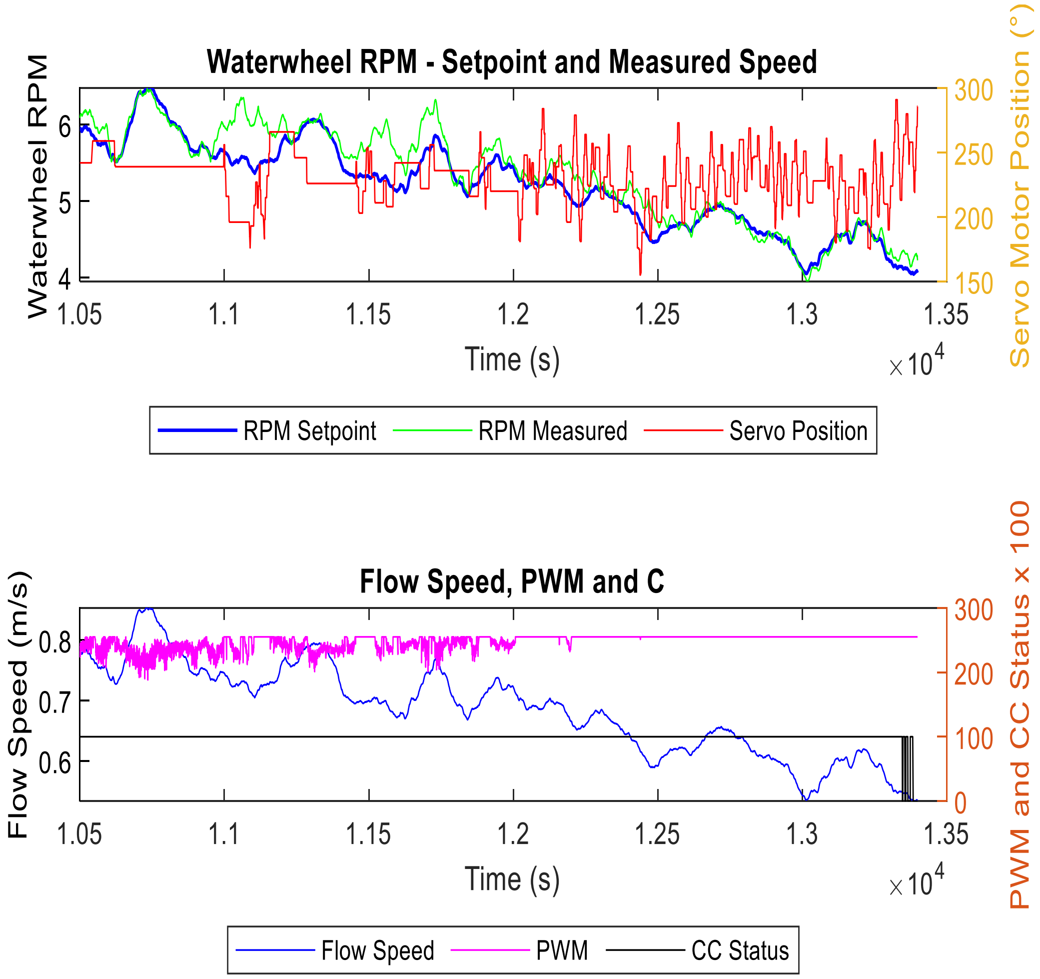

Figure 146: Last 50 minutes of test time - field test 02/29/2024

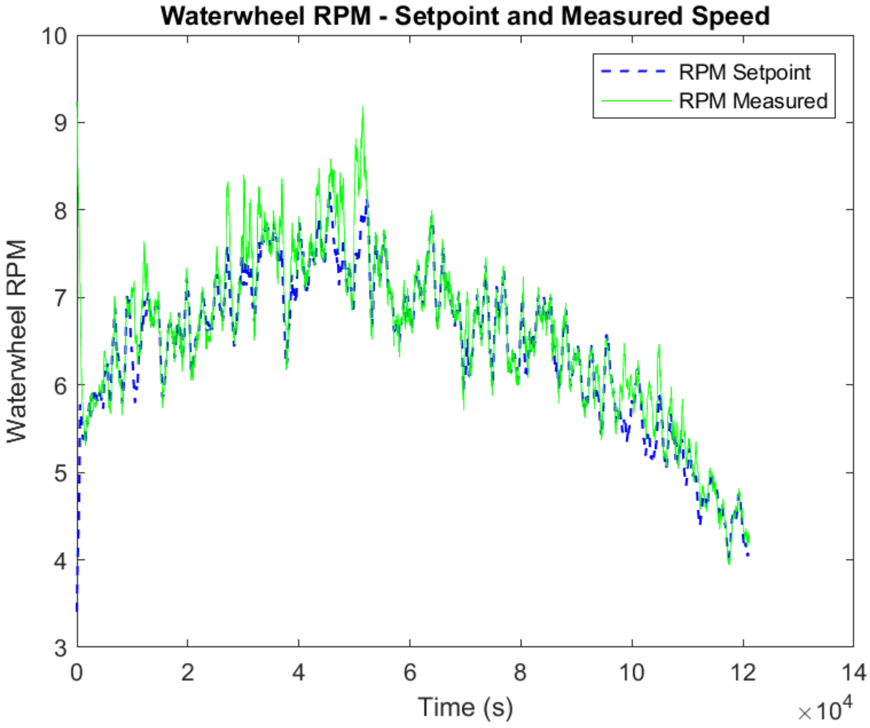

Figure 147: Waterwheel speed - setpoints vs measured, instability removed - field test 02/29/2024

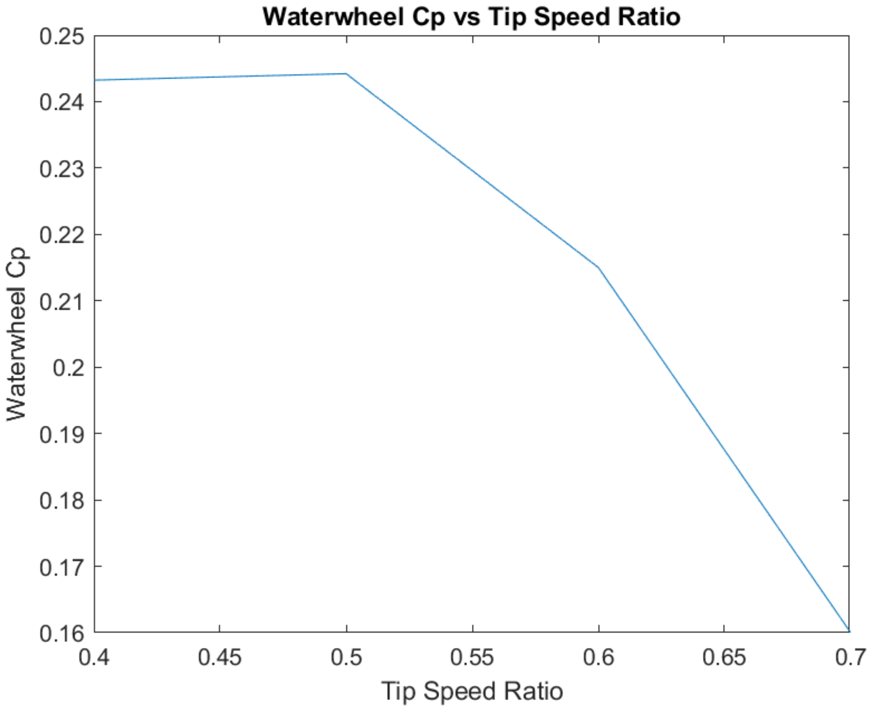

Figure 148: Resulting Cp curve - field test 2/29/24

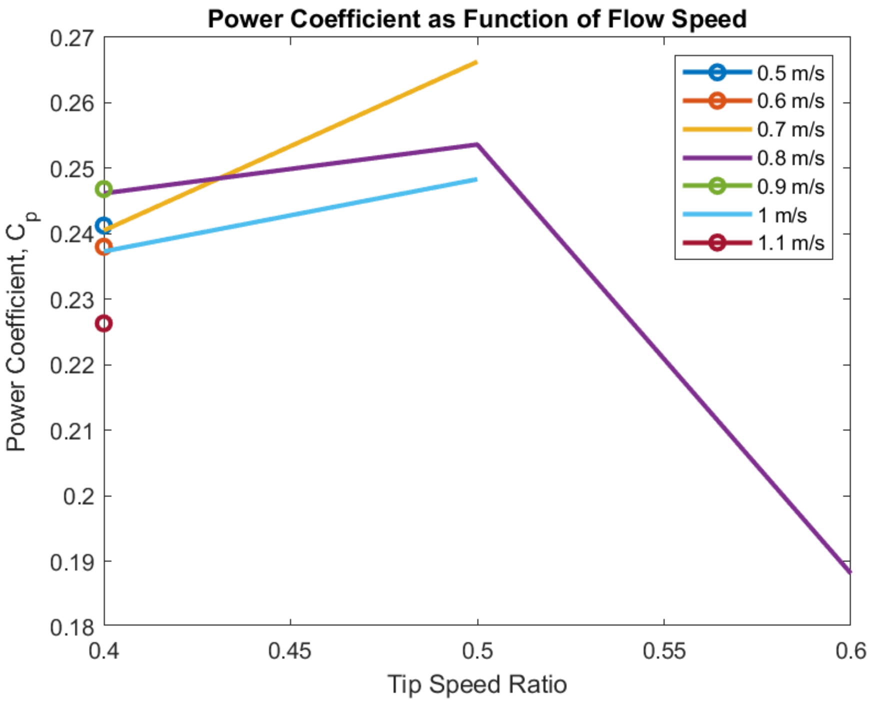

Figure 149: Cp vs TSR curves per flow speed – field test 02/29/24

Looking at the net power produced, it is important to take into account the total power utilized to operate the servo motor when changing CVT ratios. Knowing that the power consumed by the servo is approximately 6W, it is possible to calculate the total energy used during field test to actuate it and, by computing the total energy output of the system, calculate the net energy produced. The total servo energy expended was computed as:

$$E_s = \int_{t_0}^{t_f} P_s dt$$

Thus, by computing those values, Table 11 shows the results.

Table 11: Comparison between total energy output and servo energy consumed

Servo Energy (W.h)	Energy Out (W.h)	Net Energy (W.h)	Efficiency
0.35	36.92	36.57	99.1%

The energy consumed by the servo motor is minimal in this scenario, yielding high efficiency when comparing energy produced versus consumed. This was only possible because the system operated on Stage 1 for a short duration. Had the system been deployed at a lower flow speed or the test extended for longer, the controller would spend more time on Stage 1, thus operating the servo more frequently. On that stage it is important to come up with an optimized operation strategy to minimize actuation of servo motor. More on that topic later.

One option to decrease the actuation frequency of the servo is to find the servo position setpoints found by the controller during field tests and utilize those points as reference for next deployments. Based on the performance of the system, the points found to be candidate position setpoints for the servo are displayed in Figure 150. Those points were obtained by analyzing the average position of the servo at each flow speed range. Those points are particular to the 9-blade, full submergence turbine utilized on the test, and can differ if a different turbine and/or submergence level are used.

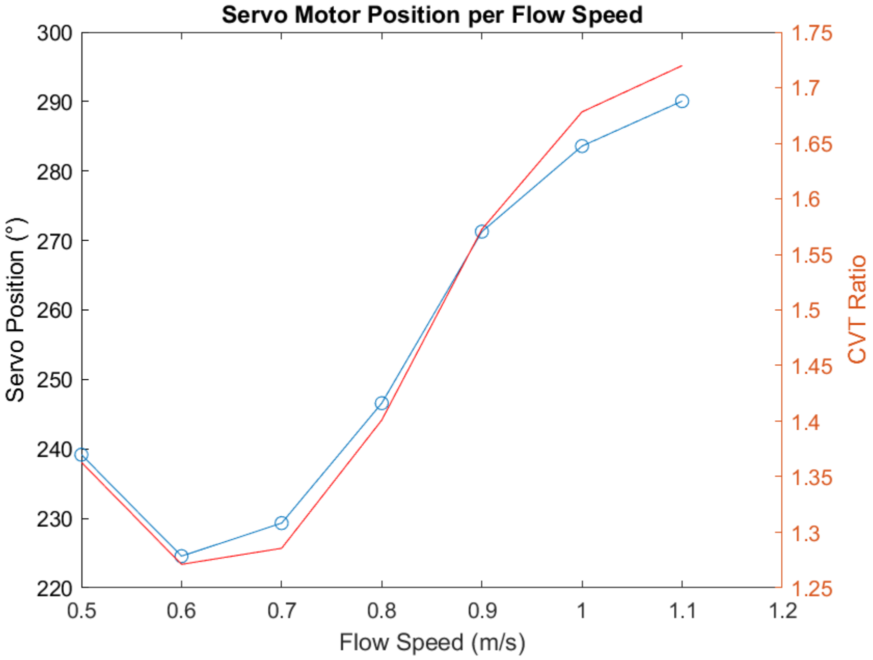

Figure 150: Servo motor position setpoints based on flow speed - field test 02/29/2024

The torque models fit to the turbine torque curve are the theoretical drag-based model (derived by fitting the drag-based torque equation to the torque surface obtained through analytical integration and numerical evaluation) and the adjusted drag-based model. Figure 151 displays the measured turbine torque and both drag and adjusted drag models. For this configuration, the theoretical torque model once again overestimated the torques and some adjustment was needed. The adjusted model describes the torques well, with a high R^2. The goodness of fit coefficients are shown in Table 12.

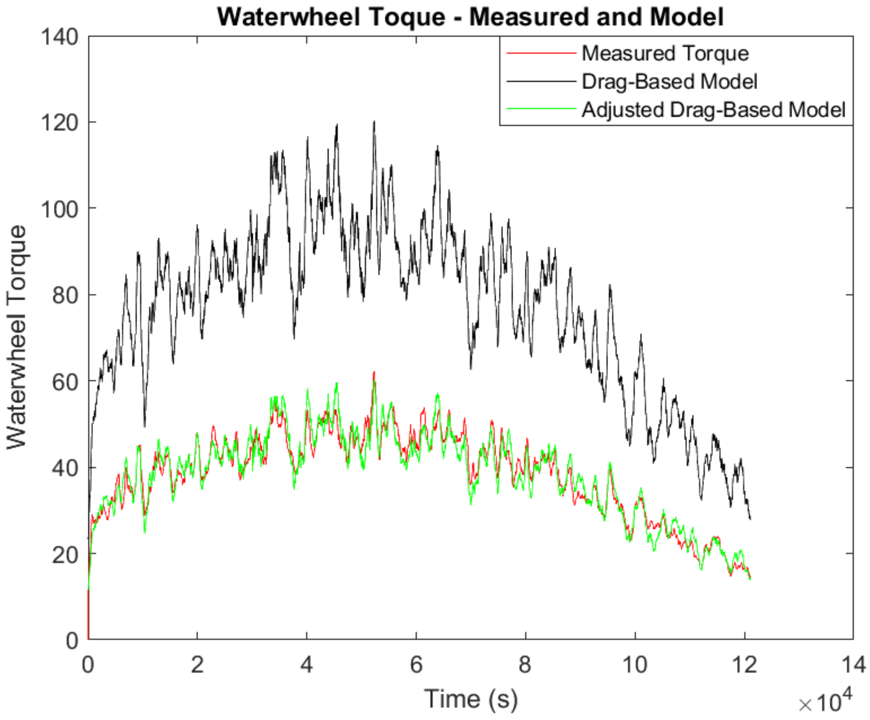

Figure 151: Waterwheel torque - measured versus model values

Table 12: Implementation of each model to fit turbine torque data - field test 02/29/2024

Test Date	# Blades	Sub	Fit Factor δ	Adjustment Factor δ*	Adjusted R^2	
					Fit Drag Model	Adjusted Drag Model
2/29/2024	9	Full	1.89	0.945	-14.848	0.934

11 RESULTS

Torque model results – for the turbine's 7, 9 and 11 blade configurations at full submergence, and for the turbine's 9-blade, half submergence, simplified torque models were obtained based on the drag model. Two approaches were taken:

1) Integrate the drag force along the blade, calculate its torque and sum the torques of all blades to find the resultant torque produced by the waterwheel. Evaluate the function numerically due to its complexity, using MATLAB, and fit a drag-based model to that surface, utilizing a fit factor δ to adjust the model to the surface. That fit model is the plotted against test data to verify how well the analytical model agrees with test data.

2) The same drag-based model is used, but an adjustment factor δ^* is used to adjust the model to the test data.

The resulting models with their respective factors δ and δ^* are then compared against field data via the goodness of fit R^2. Table 13 summarizes the results for both models under all scenarios where speed control was satisfactory.

Table 13: Performance of analytical drag model and adjusted drag model

Test Date	# Blades	Sub	Fit Factor δ	Adjustment Factor δ*	Adjusted R²	
					Fit Drag Model	Adjusted Drag Model
1/19/2024	9	Half	0.764	0.581	-0.187	0.717
1/10/2024	7	Full	1.888	1.359	-0.399	0.774
1/17/2024	9	Full	1.89	0.94	-4.11	0.638
2/29/2024	9	Full	1.89	0.945	-14.848	0.934
1/24/2024	11	Full	1.913	0.784	-10.113	0.776

For all test scenarios, the analytical torque model overestimates the produced torque, especially at a higher number of blades, which indicates the inability of the model to account for blade interference in the flow speed. Furthermore, it can be noted that the adjustment factor $\delta^*$for the full-blade submergence cases decreases as the number of blades increase, which means that the effects of flow blockage by neighboring blades become less negligible with increased number of blades. By fitting a function that describes δ^* in terms of the number of blades on the waterwheel:

$$\delta^*(n_b) = 14.52 n_b^{-1.231} \tag{69}$$

$$R^2 = 0.982$$

The resulting curve is illustrated in Figure 152 and it allows for torque and power estimations for a number of blades in between the configurations tested, plus a short extrapolation on either side of the curve, although results may differ more than what is depicted in the plot. With all adjustment factors at hand, the estimated Cp curves can be plotted for all tested configurations, with peak Cp results shown in Table 14 and Cp curves shown in Figure 153. The waterwheel configuration that yields the highest maximum Cp is, therefore, the 7-blade configuration, followed by the 9 and 11 with equal peak Cp values.

Table 14: Resultant maximum Cp per number of blades and submergence

Number of Blades	Sub	Max Cp
9	Half	0.15
7	Full	0.28
9	Full	0.25
11	Full	0.25

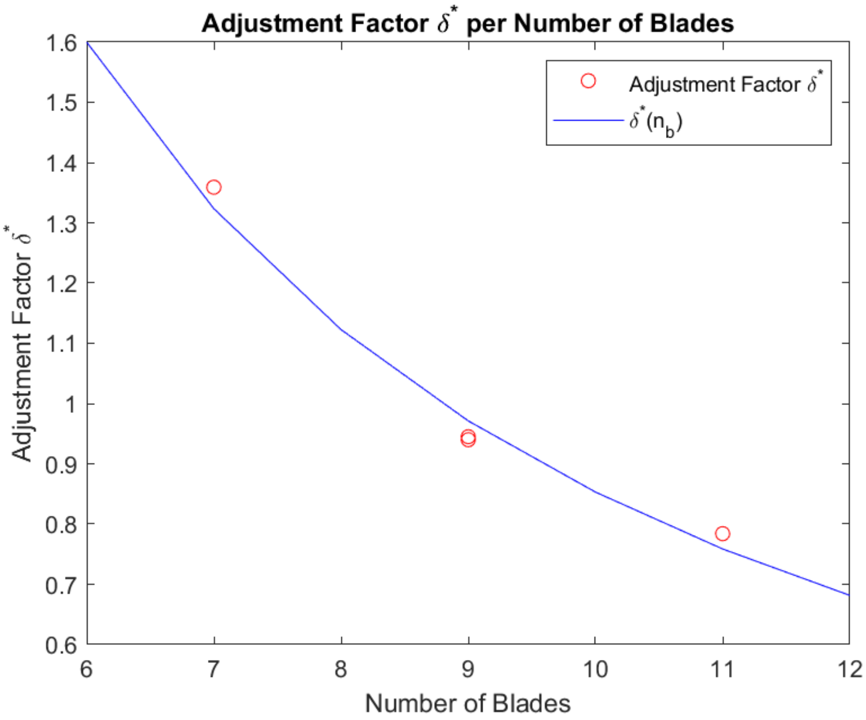

Figure 152: Adjustment factor as function of number of blades

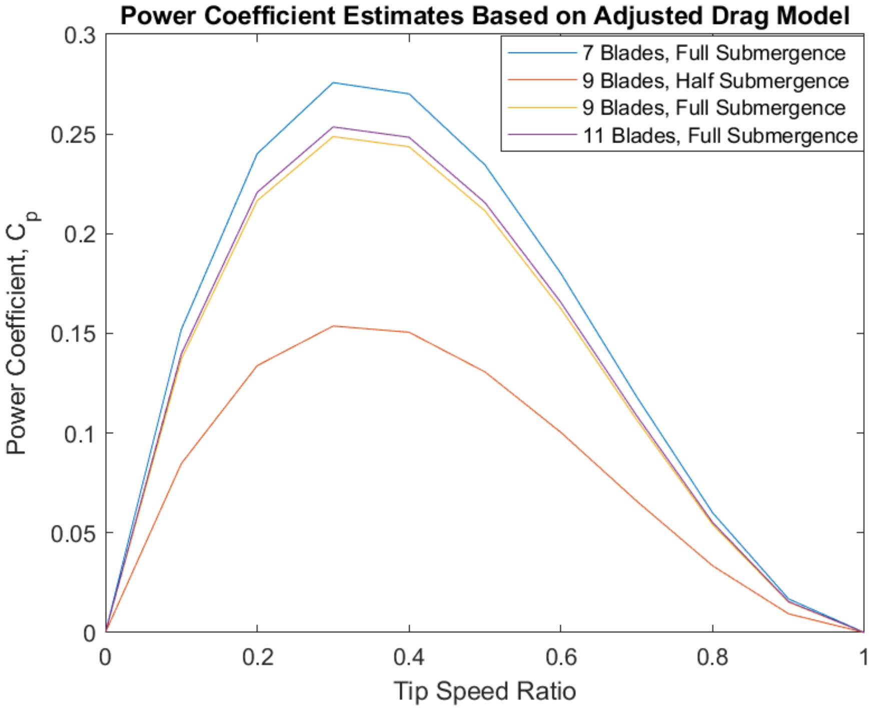

Figure 153: Estimated Cp curves for all tested waterwheel configurations

The estimated Cp can then be rewritten as:

$$C_{p,est} = \frac{14.52 n_b r_1 n_b^{-1.231} C_d \lambda (1-\lambda)^2}{12d}$$

Taking the ratio between blade depth over wheel radius as $\kappa = d/r_1$:

$$C_{p,est} = \frac{1.21 n_b^{-0.231} C_d \lambda (1-\lambda)^2}{\kappa} \tag{70}$$

Therefore, the above expression for Cp can be utilized to estimate power delivery of a waterwheel that contains from 7 to 11 blades at full submergence, and can give insightful information regarding a wheel with 6 or 12 blades at full submergence.

Taking the optimal TSR to be 0.3, as estimated in Figure 153, the maximum Cp based on number of blades can be evaluated as shown in Figure 154.

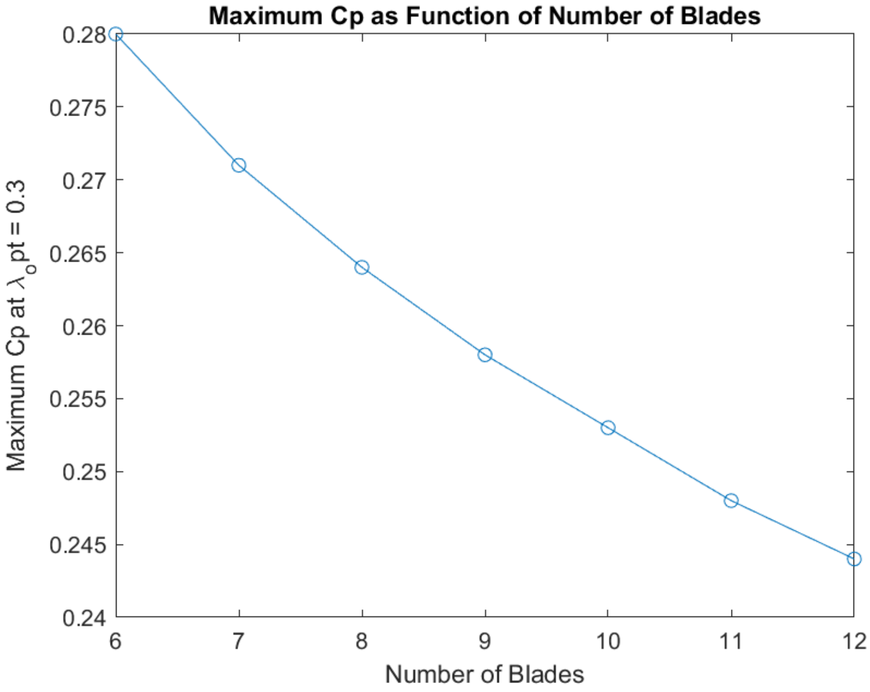

Figure 154: Maximum Cp per number of blades at full submergence

Based on the obtained expression for power coefficient, the turbine torque as a function of the number of blades can be obtained as:

$$T_{ww,m} = 0.6\rho b C_d n_b^{-0.231} r_1^2 U^2 (1-\lambda)^2 \tag{71}$$

Power can then be obtained as:

$$P_{ww,m} = 0.6\rho b C_d n_b^{-0.231} r_1 U^3 \lambda (1-\lambda)^2 \tag{72}$$

12. DISCUSSION

Although not explicitly shown in this work, the numerical models developed taking as a basic governing law the drag force on a plate caused by a passing flow do agree with results presented by (Olivier Cleynen 2018). As the results suggest, increase in depth of submergence of the waterwheel, leads to increase in the value of the power coefficient up to a certain limit. If the submergence depth is increased beyond that limit, the blades entering and leaving the flow generate negative power, which means that they oppose the flow and cause a braking effect. Figure 52 and Figure 53 show the negative power coefficient as the TSR nears 1. Therefore, there is an optimal operating submergence depth which yields maximum power coefficient.

The models suggest that the power coefficient is higher for the 7-blade turbine configuration, followed by 9 and 11, all operating at full blade submergence. After deriving an expression for the adjustment factor, finding an expression for C_p as a function of the number of blades and plotting Figure 154, it can be estimated that the 6-blade configuration yields the highest C_p. That result agrees with (S K Teoh 2022), who compared the performance of a waterwheel with 4, 6 and 8 blades, and found the 6-blade turbine to yield the highest power coefficient of the group.

(Quaranta 2018) concluded that the maximum expected C_p values range from 0.3 to 0.4 at a TSR 0f 0.5. It was also concluded that the waterwheel power can be improved by using curved blades, which also agrees with the findings in (S K Teoh 2022). The current work, based on numerical modeling, found the maximum C_p to be 0.28 for the 6-blade turbine, which is close to the lower range suggested by (Quaranta

2018). The optimal TSR in this study was found to be between 0.3 and 0.4, which is a bit under the range proposed by that study.

(Müller, Jenkins and Batten 2010) found a maximum C_p value of 0.42 at a TSR between 0.4 and 0.55. Although the maximum power coefficient found in the model-based study was 0.28, the TSR range at which that maximum is found resonates with that found in that study.

(Al-Dabbagh 2018)investigated the performance of a 12-blade waterwheel equipped with curved blades, through CFD, with flow speeds of 1m/s and 2 m/s. and TSR values of 0.2, 0.4, 0.6, 0.8 and 0.9. The results showed a maximum power coefficient of 0.15 at a TSR of 0.42 and flow speed of 2m/s. All other power coefficient values for both flow speeds were similar. Those results agree partially on the optimal TSR, although the maximum power coefficient obtained was 0.15, much lower than what the model developed in this work would predict ($C_p = 0.245$). The power coefficient for both flow speeds were similar, which agrees with the model in this work, suggesting that the power coefficient is a function of the drag coefficient and not flow speed.

(Nguyen Manh Hung 2018)conducted CFD and laboratory-based experimental studies on a waterwheel equipped with 3, 6, 9, 11 and 12 flat blades and solid disk plates on the laterals of the turbine and a bottom clearance of 0.15m. The setup also included local flow speed augmentation profiles to locally increase flow speed and decrease environmental effects of the turbine in river beds. For the CFD study, a three-dimensional model of the turbine within a domain of flow fields was elaborated. Mesh refinement tests were caried out utilizing a tetrahedral mesh to determine minimum number of mesh elements to preserve accuracy and save computational time. The study found that all tests, both experimental and numerical (with the exception of the 3-blade turbine), found maximum power coefficients at a TSR of 0.4. The 6-blade turbine showed the best performance, with a C_p value of 0.424, followed by the 9-blade turbine ($C_p = 0.41$), 11-blade turbine ($C_p = 0.387$), 12-blade turbine ($C_p = 0.373$) and 3-blade turbine ($C_p = 0.3$). The higher C_p values can be explained due to both the lateral discs on the turbine (partially blocking sideways flow of water) and the bottom effect, constraining the flow. The highest performing blades agreed with what was concluded in this work, meaning that both studies found the 6-blade turbine to be the most efficient, followed by the 9, 11 and 12-blade turbine. Although (Nguyen Manh Hung 2018) did not test a 7-blade wheel configuration, by analyzing the trend it can be concluded that the results agree.

Instabilities on the speed controller, described in Chapter 5, might have a direct relationship with sampling rate, in which the controller developed in this work had undersampling issues. The controller integral gain needs to be adjusted based on the sampling frequency, which was not possible to achieve in this work. Sampling frequencies based on turbine speed, with proper integral gains, could have increased the performance of the controller.

The increase in blade curvature has the potential to impact power production. A higher degree of curvature can increase the drag coefficient, which was demonstrated to affect the power coefficient linearly. It can also decrease the water build-up on the blade at the end of the stroke, when braking effects can occur, especially at greater blade submergence depths.

Friction on bearings and seals, as well as losses in gear meshing, decrease the mechanical efficiency of the PTO and the overall power conversion efficiency of the complete system. Tighter design and manufacturing tolerances have the potential to increase system performance, especially if paired with a stiffer PTO frame.

Limitations of this study include lack of measurement of shaft torque during field tests. Although mathematical models for the torque were obtained through bench tests, those models are not highly accurate and serve only to estimate the torque on the turbine. The torque sensor utilized on the benchtop tests had a low saturation point, which considerably limited the ability to carry further tests at higher flow speeds due to unstable behavior. Period of field testing was limited to a small fraction of the year due to the requirement that in-water tests not be conducted during the turtle nesting season in South Florida, which impacted the ability to carry out further field tests.

13. CONCLUSION AND FUTURE WORK

This work has successfully resulted in the development of field-validated torque, power and power coefficient models that characterize the operation of an undershot waterwheel deployed from a floating platform as functions of the number and submergence levels of the turbine of blades. Those developed models can be utilized in guiding the future design of waterwheels, based on the local available flow conditions and target power generation requirements.

The waterwheel equipped with a PTO containing a B-CVT was bench and field tested and its power generation assessed. There seems to be no field tests of a PTO equipped with a CVT, in addition to control strategies to actuate the CVT and combine it with electrical current modulation. Furthermore, the turbine performance was characterized, modeled and validated utilizing the abovementioned PTO as the power conversion component.

Based on field-validated torque models and numerical modeling, the 7-blade configuration displayed the highest performance, followed by the 9-blade and 11-blade configurations. However, field tests data suggest that, among the configurations tested, the 9-blade, full submergence waterwheel yielded the highest performance, followed by the 7-blade, full submergence, and 11-blade, full-submergence configurations. Although no conclusion can be drawn regarding the optimal waterwheel configuration for highest performance, the 11-blade configuration displayed the lowest performance, through both numerical model and field tests. Upon extrapolation of the numerical model results, the model for the power coefficient C_p that has been developed suggests that, in fact, a waterwheel with six blades would have the optimal performance, whereas one with 12 blades would have the least desirable performance. Moreover, desired CVT ratio setpoints for a range of flow speeds were determined for the 9-blade wheel configuration.

An overall turbine speed control strategy was developed, implemented and validated, based on 3 operating stages. Stage 1 utilizes the CVT actuation to control the turbine speed. Stage 2 is analogous to Stage 1, but with minimum load on the waterwheel shaft (i.e., power is produced). Stage 3 holds the CVT in its last position and begins controlling the turbine speed via electrical current modulation. The CVT is used as a mechanism for dynamically adapting the torque load range, whereby its ratio is increased if torque loads are too high, and decreased if torque loads become too low.

The MHK platform and its subsystems performed robustly over all test rounds and was repeatable, fulfilling its mission to produce power and withstand wakes.

For future work, it is recommended that the drag coefficient be increased, as the power coefficient has a linear relationship with that coefficient, with potential enhancing effects on power production.

To better control the torque load on the turbine shaft, the charge controller should be sourced such that full control can be attained over it. If such component does not exist, it is recommended that one be designed and manufactured, as torque control is paramount for optimal operation of turbines. Furthermore, Stage 1 of the full system controller should be further developed to capture the trends of flow speed and use those trends in deciding whether the CVT should be operated or not, in order to save power.

Further investigation of the effects of turbine depth of operation should be carried out, as it clearly has an effect on its ability to produce power. It is suspected, based on the results of this work and previous work in literature, that the power coefficient of a waterwheel increases as the depth increases, reaches a maximum and begins decreasing. That effect is expected since the deeper the turbine operates, the greater is the entry splash and water build-up when the blades enter and exit the water respectively.

On the mechanical side, the PTO design should be reviewed for higher stiffness, improved gear meshing and overall tighter tolerances for improved efficiency. The current version has considerable play on the meshing of gears at the input and output of the CVT, which impacts efficiency. Low stiffness also subtracts from overall efficiency, as part of the power captured is spent twisting the frame of the PTO. Furthermore, a more permanent and waterproof housing should be implemented to avoid water leakage and corrosion of the internal components. The CVT should be reevaluated for efficiency, as its ratio drops upon increase in load demand. If that is an inherent characteristic of that components, a more suitable option should be sought.

Scalability and cost analysis should be carried out to assess turbine sizes and expected costs for specific power production targets and available flow speeds. The MHK turbine and PTO system should be cost-effective, allowing not only for significant power production but low cost per kilowatt-hour. If those criteria are satisfied, the technology’s potential to enter the market is significantly increased. To achieve low power cost, the mechanical design has to be reevaluated not only for precision and efficiency, but for ease of manufacturing.

14. APPENDIX

Appendix A – Numerical Model

Figure 155 shows a more detailed, realistic model of the wheel, where the depth of the blade underwater changes at each instant in time as well as the flow speed component acting on it, where:

- r_d: dry radius
- h: underwater section of blade, measured radially
- d: underwater depth of wheel

$$r_d(\theta(t)) = (r_1 - d)/sin\,(\theta(t)) \tag{73}$$

$$h(\theta(t)) = r_1 - r_d(\theta(t)) \tag{74}$$

To consider the blade angle, substituting the flow speed U by its component normal to the blade $Usin\theta$ on the blade torque equation, the following expressions can be obtained.

$$T_B = \frac{\rho b C_d r_1^2 U^2}{6\lambda}\Big[(sin\theta - \lambda\gamma)^3\gamma - (sin\theta - \lambda)^3 + \frac{1}{4\lambda}((sin\theta - \lambda\gamma)^4 - (sin\theta - \lambda)^4)\Big]$$

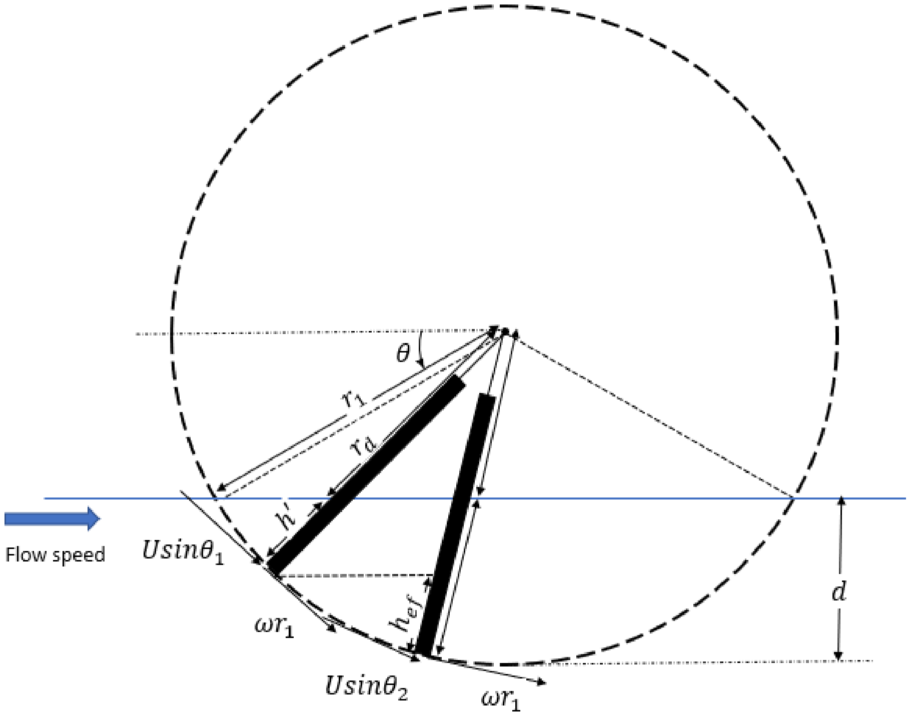

Figure 155: Blade shadowing effect and effective blade height

Due to increased complexity of the torque model, a numerical model is developed to estimate the exerted torque on the waterwheel by the incoming flow assuming certain conditions which may not hold entirely true in real world applications. One of the main assumptions on this model relates to flow leakage through the sides and bottom of wheel. The method used to develop the model essentially assumes that the blade is immersed in a closed channel, with no room for water to go around the blades. In reality however, a fraction of the flow will certainly go around the blades. Another important assumption pertains to the effective flow acting on the blade, based on the work of (F. and Liu 2012). For the current model it is considered that the flow acting on blades on the shadow region (behind other blades) but on the first half of the stroke will experience a decreasing flow speed, beginning at the horizontal line that connects the tip of the front blade to the surface of the blade on the shadow region (Figure 156), and ending at the mean water level. The model will be compared to real-world results after the field-testing phase and refined for further investigation. The following assumptions are used for the development of the model, with the aid of Figure 156 and Figure 157 to illustrate each parameter:

1) Full flow speed acts only on blade surface exposed to it. Portions of blades under shadow regions (i.e., behind other blades) are assumed to experience a decreasing flow speed that varies with the square of the distance to the center of the wheel, reaching a lower limit of 66% of the flow speed at the portion of the blade interfacing with the surface (G.A.M. van Kuik 2015).

2) Blades that are past 90° have 66% of the incoming flow speed acting on them (G.A.M. van Kuik 2015).

3) Flow "leakage" through top/bottom and sides of blades is not considered in the model, but will be accounted for when comparing field test results with model results in an effort to adjust the model to real world performance.

4) The impact of the number of blades on the performance of the wheel cannot be accounted for in the model, but that effect will be taken into account when comparing field test results with model results in an effort to adjust the model to real world performance.

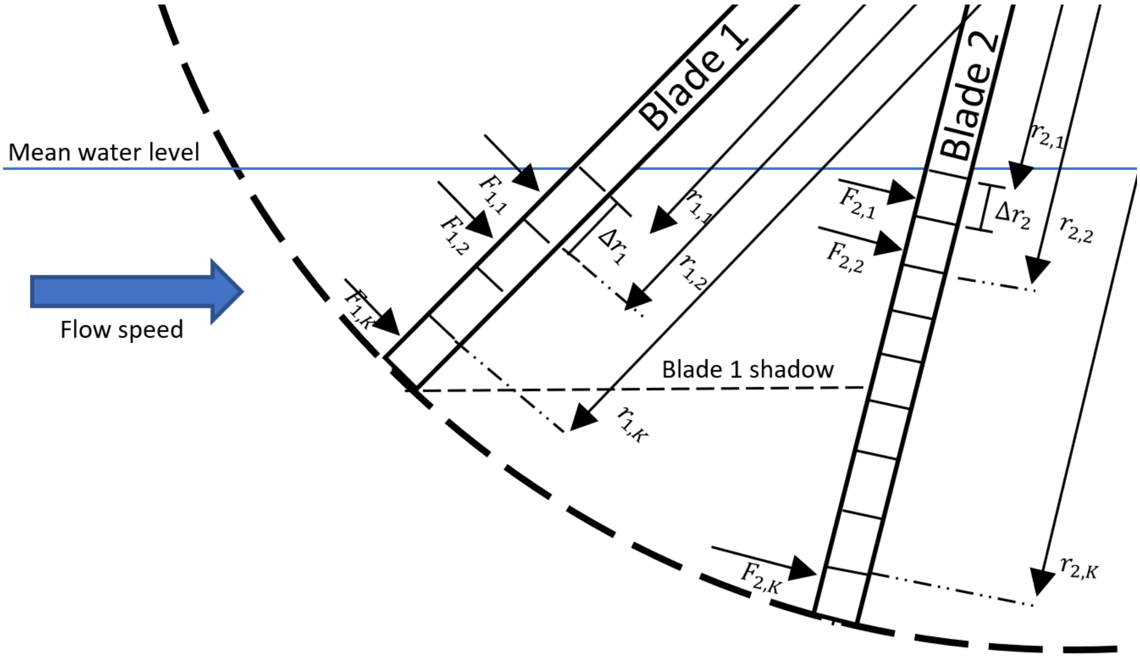

Figure 156: Detailed schematic of numerical model for waterwheel torque

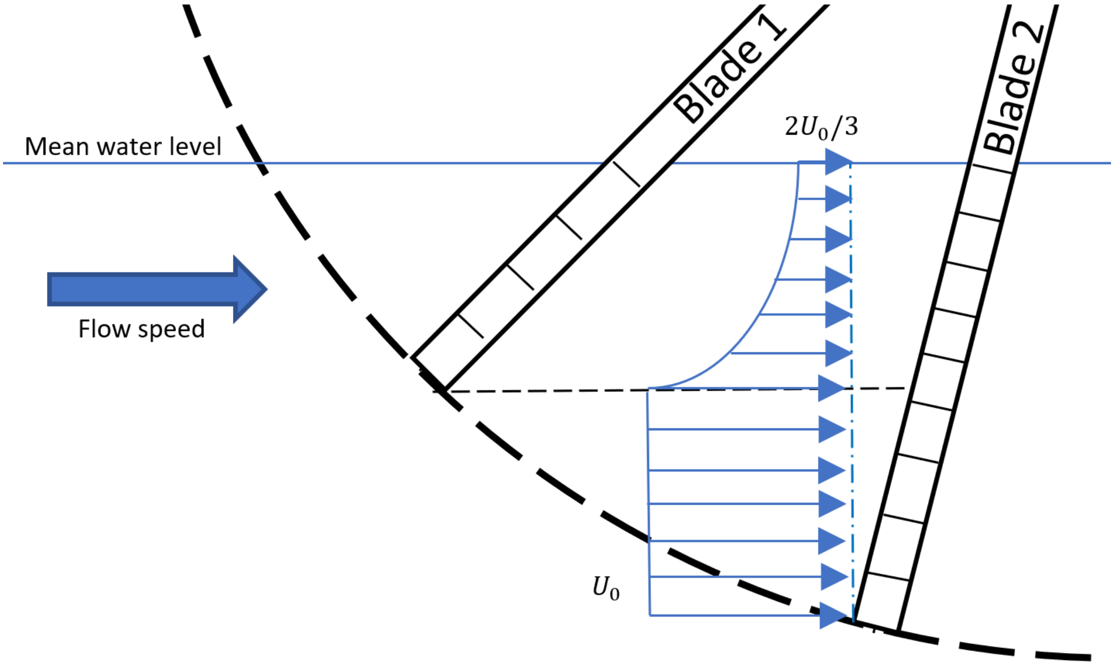

Figure 157: Flow speed profile acting on blade - model assumption

The model makes a clear distinction between which blades are at the front section of the stroke ($\theta_n \leq 90°$) and the ones that lie on the back section of the stroke ($\theta_n \geq 90°$) and adjusts the flow speed and effective height accordingly, based on the assumptions for the model. For this section, it is helpful to refer to Figure 155 for visual aid due to the trigonometry applied to the waterwheel geometry. The underwater section of each blade is calculated as:

$$r_{d,n} = \frac{r_1 - d}{sin\theta_n} \tag{75}$$

$$h'_n = r_1 - r_{d,n} \tag{76}$$

For the blades that lie in the front section of the stroke ($\theta_n \leq 90°$), the blade height subjected to the full flow speed is obtained as:

$$h_{eff,n} = r_1(1 - sin\,(\theta_{n-1})/sin\,(\theta_n)) \tag{77}$$

For all the blades, the blade elements are obtained as:

$$\Delta r_n = \frac{r_1 - h'_n}{K} \tag{78}$$

Where:

- θ_{n-1}, θ_n : angle of each individual blade

- $r_{d,n}$: “dry” radius of “n-th” blade – radial distance to blade portion outside the water

- h'_n: underwater section of "n-th" blade – radial distance from tip of blade to water surface for submerged blade.
- $h_{eff,n}$: effective section of "n-th" blade subjected to full flow speed (not on the shadow region)
- Δr_n: length of each blade element of "n-th" blade.
- K: total number of elements on blade

The flow speed profile is calculated based on where the torque is being calculated on the blade. If the torque is being calculated for an element at the shadow region of the blade, the model considers a quadratic function that describes the flow speed acting on the blade, which decreases as the radial distance to the center of the wheel decreases (Figure 157). The flow speed at the shadow region is given by the equation below, obtained by fitting a second-order polynomial of the flow speed as a function of the radius.

$$U(r) = ar_n^2 - br_n + c$$

The boundary conditions used were:

* At $r_n = r_1 - h'_n \;\rightarrow\; U(r_1 - h'_n) = U_0/3$ (flow speed at mean water surface)

* At $r_n = r1 - h_{eff,n} \;\rightarrow\; U\left(r_1 - h_{eff,n}\right) = U_0$ (flow speed at unobstructed blade surface)

* At $r_n = r_1 - h'_n \;\rightarrow\; dU/dr_n = 0$ (slope of flow speed function at mean water surface)

The resulting flow speed profile equation at the shadow region was obtained as:

$$U(r_n) = \frac{U_0}{3\left(h_n' - h_{eff,n}\right)^2}\left(2r_n^2 - 4(r_1 - h_n')r_n + \left(h_n' - h_{eff,n}\right)^2\left(1 + 2\left(\frac{r_1 - h_n'}{h_n' - h_{eff,n}}\right)^2\right)\right) \tag{79}$$

The torque on each blade is computed by a routine similar to numerical integration, where each blade under flow effect is subdivided into small elements and the torque on each section is calculated as the force on each section times the distance from the section to the center of the wheel:

$$T_k = F_k r_k$$

$$T_k = 1/2\rho b C_d \Delta r_n (U sin\theta_n - \omega_r r_k)^2 r_k \tag{80}$$

And

$$r_k = r_{k-1} + \Delta r_n$$

The torque on each blade is then calculated as the sum of torques on each blade element, and the total torque on the waterwheel is calculated as the sum of the torques on each blade underwater:

$$T_n = 1/2\rho b C_d \Delta r \sum_{k=1}^{K} (U sin\theta_n - \omega_r r_k)^2 r_k$$

The total torque on the waterwheel is calculated as the sum of the torques on each blade underwater:

$$T_{WW} = \sum_{n=1}^{N_w} T_n$$

$$T_{WW} = 1/2\rho b C_d \Delta r \sum_{n=1}^{N_w} \sum_{k=1}^{K} (Usin\theta_n - \omega_r r_k)^2 r_k \tag{81}$$

Where:

- r_k: distance from each element to center of wheel
- N_w: number of blades underwater

The same number of elements is always applied to all blades, which causes the length of each element to change depending on which blade the model is calculating the torque on and the angle of each blade, since the underwater section of each blade is different and changes over time. To verify the adequate number of blade elements, a mesh refinement test is conducted to verify the minimum number of elements that yields adequate precision without sacrificing computational cost. Thus, as the number of elements was increased, the waterwheel torque at no speed was analyzed and the increment in precision was related to the increase in the number of elements, as shown in Figure 158. When the number of elements approaches 20, the increase in mesh size from 20 t o22 causes an increment in precision of 0.4%, which is considered precise enough for the model. Therefore, a mesh size with 20 elements should be sufficient to result in satisfactory precision.

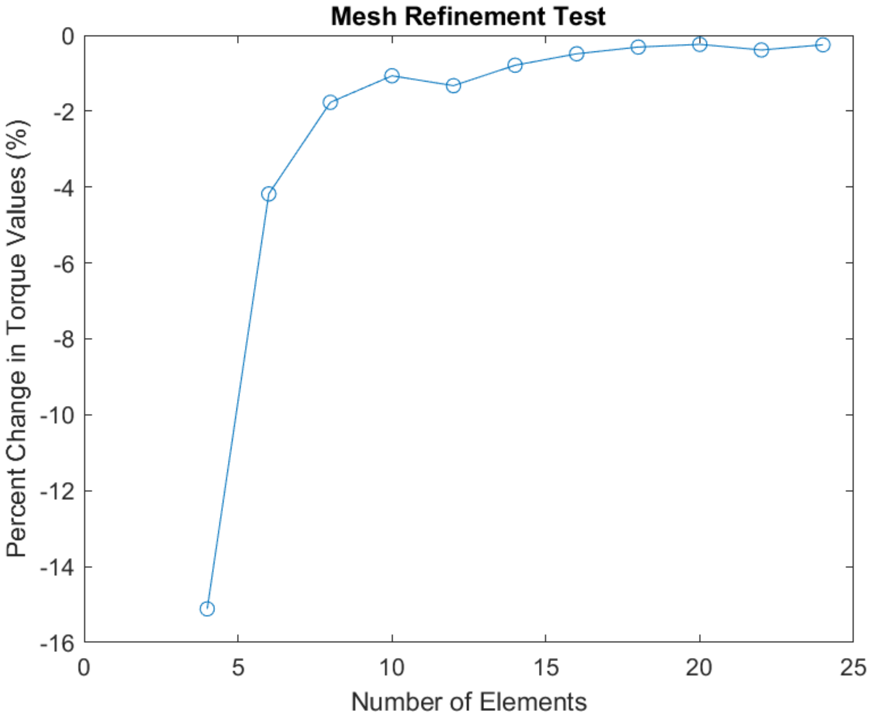

Figure 158: Mesh refinement test

The model simulates the waterwheel behavior as a function of time, which means that the abovementioned calculations are performed at each time step, since the angle of the blades change with time. Since the torque on the blade is sinusoidal, the average torque on the waterwheel over time is obtained by calculating the mean torque over the simulation time:

$$\overline{T_{WW}} = \frac{T_{WW}}{t_{sim}} \tag{82}$$

The waterwheel power is calculated by multiplying its average torque by its angular speed, while its power coefficient is calculated by dividing the waterwheel power by the flow power.

$$P_{ww} = \overline{T_{WW}}\omega_{ww}$$

$$C_p = \frac{P_{ww}}{P_f}$$

Appendix B – Bench Test Programming and CVT Slip

To emulate the waterwheel, the DC motor has to behave as such. However, the only effective control over that motor is speed control via PWM. Therefore, a comparison between the model torque and the torque measured on the test bench via torque sensor takes place and that difference in torque (i.e., the resultant torque) divided by the equivalent system inertia caused the motor to accelerate or decelerate. The calculation frequency was set to 4Hz, which yields a time step of 0.25s. In mathematical terms:

$$\dot{\omega}_{ww} = \frac{T_{ww,mod} - T_s}{J_{eq}} \tag{83}$$

$$\omega_{ww,1} = \omega_{ww,0} + \dot{\omega}_{ww} t_s \tag{84}$$

$$N_{ww,1} = \frac{\pi}{30} \omega_{ww,1} \tag{85}$$

$$PWM = \frac{N_{ww,1}}{40} \cdot 255 \tag{86}$$

Where:

- 40: maximum DC motor speed at a PWM of 255
- $N_{ww,1}$ waterwheel speed at current iteration in RPM
- $\omega_{ww,1}$ and $\omega_{ww,0}$: waterwheel speed in rad/s at current and previous time steps
- $\dot{\omega}_{ww}$ waterwheel acceleration calculated for current time step
- J_{eq}: equivalent inertia reflected on waterwheel shaft

The user sets the desired flow speed on the test computer and activates the "Waterwheel mode" to initiate the emulation. The user has the ability to change the set flow speed and also reprogram the waterwheel model to reflect different configurations, such as the number of blades and the operating depth.

A characteristic of the system that affects the overall performance of the PTO is the inverse relationship between the CVT ratio and the torque load. Despite the fixed position of the servo motor (which controls the CVT ratio), when torque load increases the CVT ratio begins to decrease. Figure 159 shows the initial CVT ratio of 1.9 and its decrease as the current demand increases. This peculiarity should be addressed in future iterations of the PTO or in other renewable energy applications, since high performance is paramount to bringing costs down.

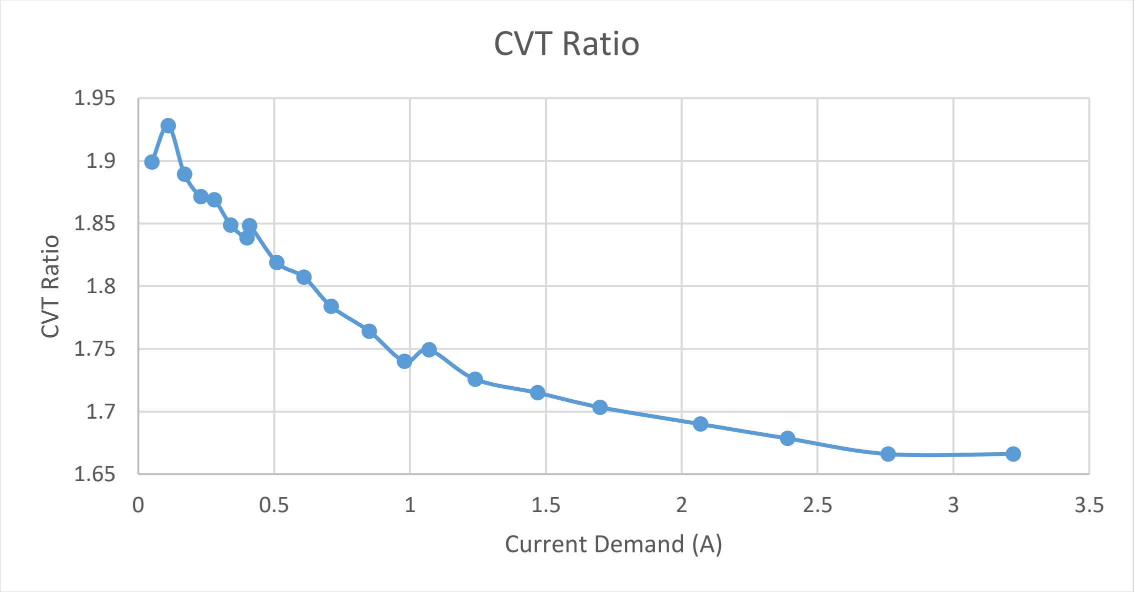

Figure 159: Decrease in CVT ratio with increase of current demand

Appendix C – Evaluation of Validity Region of Analytical Torque Expression

. In order to have the Equation (36) equation valid:

$$r < Usin\theta_{b,min}/\omega$$

$$\frac{r}{r_1} < Usin\theta_{b,min}/\omega r_1$$

$$\gamma < sin\theta_{b,min}/\lambda$$

The sine of the minimum blade angle when entering the water can be written as $1 - d/r_1$, which gives

$$\gamma < (1 - d/r_1)/\lambda$$

Taking the ratio between blade depth over wheel radius as $\kappa = d/r_1$:

$$< (1 - \kappa)/\lambda \tag{87}$$

Therefore, if the above expression is satisfied, the torque equation is valid. Figure 160 shows the validity region for the configurations studied in this work, where the maximum depth equals half the turbine radius and the maximum expected tip speed ratio is 0.7. When those conditions are examined, only when the torque model integral is evaluated at a radial distance of 80% of the turbine radius is when the validity of the torque model is not satisfied. At lower TSR, the torque model is valid for the whole range of depths and radii. It was then concluded that the torque model can be used throughout the entire spectrum of waterwheel depths and tip speed ratios (as previously mentioned, based on field tests, it was assumed that a TSR of up to $\lambda = 0.7$ is possible).

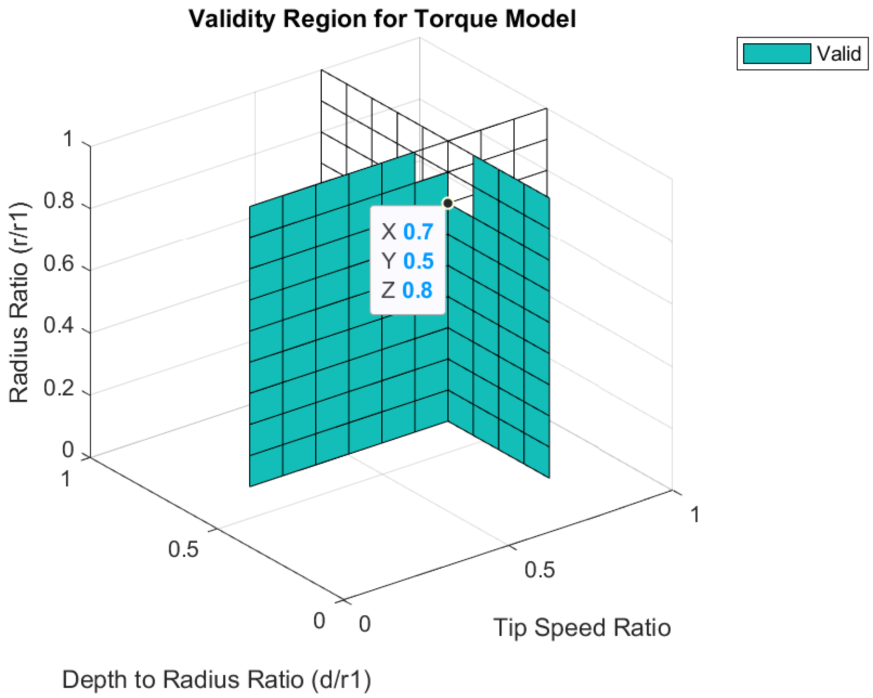

Figure 160: Validity region for torque model considering dimensionless parameters gamma, kappa and TSR

By solving the torque integral, the expression for the blade torque is:

$$T_b = \frac{\rho b C_d r_1^2 U^2}{24}[6sin^2\theta_b(1-\gamma^2) - 8\lambda sin\theta_b(1-\gamma^3) + 3\lambda^2(1-\gamma^4)] \tag{88}$$

However, the blade angle varies with time and the torque equation is rewritten as:

$$T_b = \frac{\rho b C_d r_1^2 U^2}{24}[6sin^2(\omega t + \psi_b)(1-\gamma^2) - 8\lambda sin\,(\omega t + \psi_b)(1-\gamma^3) + 3\lambda^2(1 - \gamma^4)]$$

Furthermore, the dimensionless parameter gamma varies in time since $\gamma = r_0/r_1$ and $\mathrm{r_0 = f(t)}$. The parameter $\mathrm{r_0}$ can be written as:

$$\mathrm{r_0 = r_1 - \frac{1}{sin\theta_b}\left[d - r_1 + \frac{(r_1 - d)sin\theta_b}{sin\theta_{min}}\right]} \tag{89}$$

Where θ_{min} is the minimum angle at which the blades contact the water. Once again, since the position of the blade varies with time and dividing both sides by $\mathrm{r_1}$ and using the dimensionless parameter $\mathrm{\kappa = d/r_1}$:

$$\gamma(\mathrm{t}) = 1 - \frac{1}{\sin\,(\omega\mathrm{t} + \psi_\mathrm{b})}\left[\kappa - 1 + \frac{(1-\kappa)\sin\,(\omega\mathrm{t} + \psi_\mathrm{b})}{\sin\theta_{\mathrm{min}}}\right] \tag{90}$$

The above result yields the analytical approach considerably complex to solve. MATLAB is used to evaluate the expression numerically.

15. REFERENCES

A. S. Mahdi, A. K. Mahamad, S. Saon, T. Tuwoso, Hakkun Elmunsyah, S. W. Mudjanarko. 2019. "Maximum power point tracking using perturb and observe, fuzzy logic and ANFIS." SN Applied Sciences (Springer Link). doi:https://doi.org/10.1007/s42452-019-1886-1.

A.H. Day, A. Babarit, A. Fontaine, Y.-P. He, M. Kraskowski, M. Murai, I. Penesis, F. Salvatore, H.-H. Shin. 2015. "Hydrodynamic modelling of marine renewable energy devices: A state of the art review." Ocean Engineering (Elsevier) 46-69. doi:https://doi.org/10.1016/j.oceaneng.2015.05.036.

Ackerman, Evan. 2021. IEEE Spectrum. https://spectrum.ieee.org/underwater-manta-kites-tidal-power-harvesting#toggle-gdpr.

Al-Dabbagh, Mohammad A. 2018. "Investigation the Performance of Stream Water Wheel Turbines using CFD Techniques." The Eurasia Proceedings of Science, Technology, Engineering & Mathematics (EPSTEM). ISRES Publishing. 354-360.

n.d. Analog Devices. https://www.analog.com/en/products/lt8491.html?doc=LT8491.pdf#product-samplebuy.

Anderson, Margo. 2019. IEEE Spectrum. https://spectrum.ieee.org/alphabets-makani-tests-wind-energy-kites-in-the-north-sea.

Baoshou Zhang, Baowei Song, Zhaoyong Mao, Wenlong Tian, Boyang Li. 2017. "Numerical investigation on VIV energy harvesting of bluff bodies with different cross sections in tandem arrangement." Energy (Elsevier) 723-736. doi:https://www.sciencedirect.com/science/article/pii/S0360544217308083?via%3Dihub.

Dhanak, Manhar. 2023. "WAM-V." Dania Beach.

n.d. Engineers Edge. https://www.engineersedge.com/fluid_flow/long_semicircular_concave_surface_drag_14037.htm.

F., Yoosef Peymani, and Yucheng Liu. 2012. "Development of an Analytical Model to Predict the Performance of Paddle Wheel in Generating Electricity and Its Validation Using Computational Fluid Dynamics (Cfd)." IEEE Green Technologies Conference (IEEE-Green). IEEE. doi: 10.1109/GREEN.2012.6200972.

G.A.M. van Kuik, J.N.Sørensen, V.L.Okulov. 2015. "Rotor theories by Professor Joukowsky: Momentum theories." ProgressinAerospaceSciences. Elsevier. 1-18.

Hall, Adam. 2022. Design, Simulation and Testing of a CVT Based PTO and Controller for a Small Scale MHK-Turbine in Low Flow Speed. M.Sc. Thesis, Boca Raton: Florida Atlantic University.

Henderson, Edward. 2023. "LT8491 Battery Charge Controller Evaluation Board - Modifications for Current Demand Control."

José F. Gaspar, Peter K Stansby, Miguel Calvário, C. Guedes Soares. 2021. "Hydraulic Power Take-Off concept for the M4 Wave Energy Converter." Applied Ocean Research (Elsevier). doi:https://doi.org/10.1016/j.apor.2020.102462.

K.E. Johnson, L. J. Fingersh, M.J. Balas, L.Y. Pao. 2003. "Methods for Increasing Region 2 Power Capture on a Variable Speed HAWT." ASME Wind Energy Symposium. Reno.

Kackenmeister, Katie. 2021. EurekAlert! https://www.eurekalert.org/news-releases/863042.

M. J. Khan, G. Bhuyan, M.T. Igbal, J. E. Quaicoe. 2009. "Hydrokinetic energy conversion systems and assessment of horizontal and vertical axis turbines for river and tidal applications: A technology status review." Applied Energy (Elsevier) 1823-1835. doi:https://doi.org/10.1016/j.apenergy.2009.02.017.

Manwell, J. F, J. G Mcgowan, and A. L Rogers. 2009. Wind Energy Explained: Theory, Design and Application. Wiley.

Maura, Shunsuke, Naoyuki Hara, Hiromichi Akimoto, and Keiji Konishi. 2019. "Torque Control of the Floating Vertical Axis Wind Turbine with a Frictional Power Take-off System." International Automatic Control Conference (CACS). IEEE. doi:10.1109/CACS47674.2019.9024733.

Michael M. Bernitsas, Y. Ben-Simon, Kamaldev Raghavan, E. M. H. Garcia. 2008. "The VIVACE Converter: Model Tests at High Damping and Reynolds Number Around 10^5." J. Offshore Mech. Arct. Eng. (ASME). doi:https://doi.org/10.1115/1.2979796.

Min-Hsiung Yang, Zhong-Ting Gu, Rong-Hua Yeh. 2023. "Numerical and experimental analyses of the performance of a vertical axis turbine with controllable-blades for ocean current energy." Energy Conversion and Management (Elsevier). doi:https://doi.org/10.1016/j.enconman.2023.117009.

n.d. Missouri Wind and Solar. https://windandsolar.com/skymax-legacy-permanent-magnet-generator/.

Müller, Gerald, R. Jenkins, and W. M. J. Batten. 2010. "Potential, performance limits and environmental effects of floating water mills." 707-712.

n.d. Nasa. https://www.grc.nasa.gov/www/k-12/VirtualAero/BottleRocket/airplane/shaped3.html#:~:text=A%20flat%20plate%20has%20Cd,typical%20airfoil%20has%20a%20Cd%20%3D%20.

Nguyen Manh Hung, Jeong Haechang, Yang Changjo. 2018. "A study on flow fields and performance of water wheel turbine using experimental and numerical analyses." Science China Technological Sciences (CrossMark). doi:https://doi.org/10.1007/s11431-017-9146-9.

Niassati, N., M. Mohseni, H. Amiri, K. Seyedtabaei, and A. Hajihosseinlu. 2012. "A new maximum power point tracking technique for wind power conversion systems." International (EPE-PEMC) Power Electronics and Motion Control Conference. IEEE. doi:10.1109/EPEPEMC.2012.6397311.

Olivier Cleynen, Emeel Kerikous, Stefan Hoerner, Dominique Thévenin. 2018. "Characterization of the performance of a free-stream water wheel using computational fluid dynamics." Energy (Elsevier) 1392-1400. doi:https://doi.org/10.1016/j.energy.2018.10.003.

Ouhrouche, Jogendra Singh Thongam and Mohand. 2011. "MPPT Control Methods in Wind Energy Conversion Systems." Fundamental and Advanced Topics in Wind Power (Intech). https://cdn.intechopen.com/pdfs/16255/intech-mppt_control_methods_in_wind_energy_conversion_systems.pdf.

Pengyingkai Wang, Li Sui, Gengchen Shi, Guohua Liu. 2016. "Performance of pre-deformed flexible piezoelectric cantilever in energy harvesting." AIP Advances (AIP Publishing). doi:https://doi.org/10.1063/1.4948697.

Peter Avram, Robert Shaun McKee, Tolga Tuzun, Brandon Geiger. n.d. University of Michigan Library. https://deepblue.lib.umich.edu/bitstream/handle/2027.42/61915/me450?sequence=1.

n.d. Power Take Off Generators. https://www.amazon.com/Marsrock-Permanent-Generator-Alternator-Horizontal/dp/B094QL4QZG.

Quaranta, Emanuele. 2018. "Stream water wheels as renewable energy supply in flowing water:Theoretical considerations, performance assessment and design recommendations." Energy for Sustainable Development (Elsevier) 96-109. doi:https://doi.org/10.1016/j.esd.2018.05.002.

Richard C. Dorf, Robert H. Bishop. 2011. Modern Control Systems. Pearson.

n.d. Robotis Dynamixel-xc430-w150-t. https://www.robotis.us/dynamixel-xc430-w150-t/.

S K Teoh, S Y Wong, C H Lim, S S Leong & S W Khoo. 2022. "Investigation of design parameters on self-floating water wheel for micro-hydropower generation." International Journal of Green Energy (Taylor & Francis) 931-940. doi:https://doi.org/10.1080/15435075.2021.1975123.

Scott Baker, Andrew Cornett. 2015. "3D Modelling and Optimization of a Hydrokinetic Power Generation Barge." 11th European Wave and Tidal Energy Conference.

n.d. Tethys Engineering. https://tethys-engineering.pnnl.gov/technology/cross-flow-turbine.

n.d. Tethys Engineering. https://tethys-engineering.pnnl.gov/technology/oscillating-hydrofoil.

n.d. TUDelft. https://www.tudelft.nl/en/me/about/departments/delft-center-for-systems-and-control/research/data-driven-control/hydraulic-wind-turbines.

Van Bang Nguyen, Dalibor Rozehnal. 2017. "Determination of performance parameters of vertical axis wind turbines in wind tunnel." Dynamics of Civil Engineering and Transport Structures and Wind Engineering – DYN-WIND’2017. MATEC Web of Conferences. doi:https://doi.org/10.1051/matecconf/201710700076.

n.d. Verdant Power. Accessed 2023. https://verdantpower.com/technology/.

n.d. Vortex Hydro Energy. https://www.vortexhydroenergy.com/technology/how-it-works/.

Wang, Quincy, and Liuchen Chang. 2004. "An intelligent maximum power extraction algorithm for inverter-based variable speed wind turbine systems." IEEE Transactions on Power Electronics (IEEE) 1242-1249. doi:10.1109/TPEL.2004.833459.

Watson, David. n.d. FT Exploring Science And Technology. https://www.ftexploring.com/wind-energy/wind-power-coefficient.htm.

Yucheng Liu, Yoosef Peymani. 2012. "Evaluation of Paddle Wheels in Generating Hydroelectric Power." Proceedings of the ASME 2012 International Mechanical Engineering Congress & Exposition. Houston: ASME. doi:10.1115/IMECE2012-85121.